



Mechanisms of regional morphogenesis along the gastrointestinal tract

Citation

Gill, Hasreet Kaur. 2023. Mechanisms of regional morphogenesis along the gastrointestinal tract. Doctoral dissertation, Harvard University Graduate School of Arts and Sciences.

Permanent link

<https://nrs.harvard.edu/URN-3:HUL.INSTREPOS:37375830>

Terms of Use

This article was downloaded from Harvard University's DASH repository, and is made available under the terms and conditions applicable to Other Posted Material, as set forth at <http://nrs.harvard.edu/urn-3:HUL.InstRepos:dash.current.terms-of-use#LAA>

Share Your Story

The Harvard community has made this article openly available.
Please share how this access benefits you. [Submit a story](#).

[Accessibility](#)

HARVARD UNIVERSITY
Graduate School of Arts and Sciences




DISSERTATION ACCEPTANCE CERTIFICATE


The undersigned, appointed by the
Department of Molecular and Cellular Biology
have examined a dissertation entitled
**Mechanisms of regional morphogenesis along the
gastrointestinal tract**

presented by **Hasreet Kaur Gill**

candidate for the degree of Doctor of Philosophy and hereby
certify that it is worthy of acceptance.

Signature  _____


Typed name: Prof. **Nancy Kleckner**

Signature  _____
JessicaWhited (Apr 19, 2023 09:54 EDT)

Typed name: Prof. **Jessica Whited**

Signature  _____

Typed name: Prof. **Maxwell Heiman**

Signature  _____
Olivier Pourquie (Apr 19, 2023 09:29 EDT)

Typed name: Prof. **Olivier Pourquie**

Date: April 19,2023

Mechanisms of regional morphogenesis along the gastrointestinal tract

A dissertation presented

by

Hasreet Kaur Gill

to

The Department of Molecular and Cellular Biology

In partial fulfillment of the requirements for the degree of

Doctor of Philosophy

in the subject of

Biology

Harvard University

Cambridge, Massachusetts

April 2023

© 2023 Hasreet Kaur Gill

All rights reserved

Mechanisms of regional morphogenesis along the gastrointestinal tract

ABSTRACT

Distinct compartments along the gastrointestinal tract perform complementary digestive processes that sustain life. In vertebrates, the esophagus, small intestine, and large intestine originate from a common primordial gut tube, but eventually adopt unique forms consistent with their roles in digestion. Despite our extensive knowledge of conserved molecular factors that specify anteroposterior gut regions, the physical processes that differentially shape them are virtually unknown. Furthermore, how these regional genes regulate mechanical forces to confer distinct morphologies is poorly understood. This thesis presents three sets of findings from the developing chick gut that address how intestinal identity regulates form.

First, we asked how compartments achieve specialized tube dimensions. By combining smFISH, cell division and density measurements, and predictions from a two-step mathematical model of reaction-diffusion based patterning followed by growth, we found that volumetric growth parameters predict growth trajectories well, but gene expression data do not match model predictions. Explant experiments instead suggest that differential sensitivities to Bmp and Shh signaling along the gut define muscle patterns. Thus, both morphogen patterning and growth are important for specifying early gut tube dimensions.

Proper morphogenesis of the gut epithelium is important for function in all compartments, so we next asked how the esophagus and large intestine develop distinct lumen wrinkling patterns from the midgut by measuring growth and mechanical parameters during initial epithelial diversification. Systematic simulations incorporating these data show that spatiotemporal geometries, stiffnesses, and growth rates control both primary and secondary, multiscale buckling patterns found in the foregut and hindgut.

Finally, gut compartment identities are demarcated early in development via Hox genes, which are highly conserved, master regulators of spatial patterning in the embryo that were discovered 30 years ago in vertebrates; yet, how these factors trigger regional morphogenesis is still a mystery. We combined mechanical measurements and mathematical modeling to demonstrate that the posterior Hox gene *Hoxd13* regulates biophysical phenomena that shape the hindgut lumen. We further show that *Hoxd13* acts through the TGF β pathway to thicken, stiffen, and promote isotropic growth of the subepithelial mesenchyme; together, these features generate hindgut surface patterns. TGF β , in turn, promotes collagen deposition to affect mesenchymal geometry and growth. We thus identify a cascade of events downstream of genetic identity that direct posterior intestinal morphogenesis.

Table of contents

<i>Title page</i>	<i>i</i>
<i>Copyright page</i>	<i>ii</i>
ABSTRACT	iii
<i>Table of contents</i>	v
<i>Acknowledgements</i>	ix
<i>List of Figures</i>	x
<i>List of Tables</i>	xi
<i>Abbreviations</i>	xii
INTRODUCTION	1
Origin of the regionalized digestive tube	1
Evolution of intestinal compartments	1
Patterning positional identity along the early gut	3
Anatomy and physiology of gut compartments	6
Epithelial structure and turnover in the esophagus	6
Architecture of the intestinal epithelium	8
Morphogenesis of the gut	10
Patterning the gut cross-section with Hh and Bmp	10
Elongational growth of the small intestine	13
Physical forces in intestinal growth and shaping	16
Summary & motivation	18
Chapter 1: Radial and axial geometry in early gut tube development	19
Attributions	19
Background	19
Results	22
Development of different tube dimensions along the early gut	22
Hh and Bmp signaling landscapes vary across space and time	23
Mismatch between measured and predicted morphogen levels fit to radial geometries	27
<i>Ex vivo</i> morphogen perturbations indicate regional differences in Bmp sensitivity	29
Differential growth is driven by cell division and changes in cell density	32
Relative growth of the mesenchyme in each region predicts radial geometries	34
Oriented mesenchymal cell divisions do not explain differential tube elongation	37
Conclusions	38
Chapter 2: Divergent epithelial bucking across gut regions	41
Attributions	41
Background	41

Results.....	42
Unique epithelial shapes along the gut anteroposterior axis	42
Foregut and hindgut lumens develop multiscale buckling patterns	46
Differences in smooth muscle constraints do not explain morphological differences	47
Width ratio increases and radius ratio decreases from the foregut to hindgut	48
The inner modulus ratio decreases positionally from the foregut to hindgut.....	50
Major ECM components vary in abundance and alignment between regions.....	52
Development of a computational model to capture buckled morphologies.....	53
Relative endodermal thinning drives primary and secondary wrinkling in the foregut	56
Early hindgut creasing patterns are consistent with geometric and material properties	59
Multiscale hindgut buckling requires stabilization of inner creases	60
Foregut inner layers experience axial pre-stretch	63
Sox9 and phospho-Smad staining patterns correlate with post-buckling motifs	65
Conclusions	68
Chapter 3: Genetic and biochemical control of physical forces in hindgut morphogenesis	70
Attributions	70
Background	70
Results.....	72
Distinct biaxial buckling instabilities in mid- and hindgut epithelia.....	72
The developing hindgut and midgut are unique in growth and mechanical properties.....	73
3D numerical simulations of lumen wrinkling capture mid- and hindgut morphologies.....	77
Cuff formation lacks hallmarks of mesenchymal clustering and requires circular constraint	80
Hoxd13 misexpression transforms midgut luminal folding a hindgut-like pattern	83
Hoxd13 modulates mechanical properties of the developing gut tube	86
Noggin misexpression generates sulci and promotes mesenchymal thickening and stiffening.....	88
Mesenchymal TGF β signaling is upregulated in the hindgut and midgut + Hoxd13.....	89
Modulating TGF β signaling toggles the lumen between mid-and hindgut forms	92
TGF β activation is necessary and sufficient to promote hindgut mechanical properties.....	95
TGF β signaling promotes equibiaxial inner layer differential growth.....	95
Simulated explant morphologies follow endogenous trajectories in the parameter space.....	96
TGF β alters mesenchymal geometry through modulation of the ECM	97
Orientation of ECM, but not muscle, correlates with stiffness of the mesenchyme	101
Myofibroblast-related genes are upregulated in subepithelial cell layers.....	102
Conclusions	106
DISCUSSION.....	108
Positional trends in the gut morphogenic landscape	108
Changes in growth and material properties from the foregut to hindgut.....	109
Tuning regional responses to Shh and Bmp signaling.....	111
Properties shared between the foregut and hindgut	112
From regional gut identity to specialized morphology	112
An instructive role for Hoxd13 in hindgut morphogenesis.....	114
TGF β regulation of cells and extracellular matrix in the gut mesenchyme.....	116
Molecular and functional consequences of gut morphogenesis	118
Axial buckling and pre-stretch in the foregut.....	119
Hindgut isotropic growth, creasing, and large-scale wrinkling	121

Perspectives and future work.....	123
MATERIALS & METHODS.....	125
Experimental	125
Use of chicken embryos	125
Chick intestinal electroporation	125
Lumen surface imaging	126
Section immunostaining	126
Whole mount immunostaining and tissue clearing	128
EdU/BrdU labeling.....	128
Differential growth measurements.....	129
Modulus measurements	129
Fluorescence in situ hybridization (FISH)	130
Single molecule FISH	130
Quantitative PCR.....	132
RNA sequencing library preparation	133
Chick intestinal explant culture.....	134
Light-seq spatial RNA sequencing	135
Data analysis	136
Radial and axial geometry measurements.....	136
EdU/BrdU quantification.....	136
FISH and immunostain quantification.....	138
Nucleus and division orientation measurements	138
Surface wrinkling quantification	139
Muscle and ECM orientation analysis.....	139
Fold morphology measurements.....	140
Differential growth calculations.....	141
Modulus calculations	141
RNA sequencing and data analysis.....	143
Simulations.....	144
Radial muscle patterning and growth	144
2D foregut and hindgut epithelial folding.....	145
3D hindgut and midgut lumen wrinkling	146
APPENDIX 1: Supplementary materials for Radial and axial geometry in early gut tube development.....	150
Extended Figures 1-3.....	150
Calculating contributions of cell density and proliferation to volumetric growth.....	153
Reaction-diffusion model of muscle patterning with differential growth	155
Simple model without growth	155
Change to dimensionless variables	156
Steady state solution in 1D	157
Steady state solution in 2D with radial symmetry	159
Incorporating growth	162
Convergent extension	163
APPENDIX 2: Supplementary materials for Divergent epithelial buckling across gut regions	164
Extended Figures 4-8.....	164

2D model of primary and multiscale buckling in the fore- and hindguts	169
Basic model and growth description.....	169
Constitutive relations and stresses	170
Governing equations and boundary conditions.....	171
<i>APPENDIX 3: Supplementary materials for Genetic and biochemical control of physical forces in hindgut morphogenesis</i>	173
Extended Figures 9-18.....	173
3D model of biaxial buckling instabilities in the midgut and hindgut.....	182
REFERENCES	184

Acknowledgements

I first want to thank Cliff for his kindness, support, and mentorship over the past several years. I also appreciate members of the Tabin lab for making it a great place to complete my PhD. I am grateful for years of guidance and support generously offered by Nandan Nerurkar and Tyler Huycke, especially during the COVID-19 pandemic. I also want to thank my committee members Nancy Kleckner, Olivier Pourquie, Max Heiman, and Jessica Whited for suggestions and helpful discussions. I have had the pleasure of working with excellent collaborators over the years, including David Sprinzak, Shahar Kasirer, L. Mahadevan, and Sifan Yin.

I am thankful for the like-minded friends I made from being a part of Science in the News (SITN), Harvard Graduate Student Union (HGSU-UAW), and HMS Genetics DEI initiatives. Finally, I want to thank my partner Brett for his constant support over the course of my PhD, and my parents for supporting my interest in science from a young age.

This dissertation is dedicated to the memory of my grandfather, Sdr. Bhupinder Singh Gill, who was always a loving and supportive presence in my life.

List of Figures

Figure 1. Radial and axial growth patterns along the early gut.....	24
Figure 2. Shh and Bmp signaling across compartments and corresponding model predictions. 26	
Figure 3. Shh and Bmp explant perturbations in the foregut and hindgut	30
Figure 4. Differential growth via cell division and expansion of intercellular spaces	35
Figure 5. Oriented cells and divisions do not correlate with elongation rates	37
Figure 6. Regional gut epithelia develop distinct folding patterns.....	44
Figure 7. Muscle layer orientations are consistent along the gut.	49
Figure 8. Spatiotemporal evolution of gut inner tissue mechanical properties.....	51
Figure 9. Numerical model of cylindrical bilayer morphogenesis.	55
Figure 10. Simulated foregut period-double wrinkles via anisotropic radial growth profiles.	58
Figure 11. A three-phase model capturing multiscale buckling in the hindgut lumen.	61
Figure 12. Longitudinal tension from differential growth in the foregut.	64
Figure 13. Patterns of Bmp signaling and Sox9 activation correlate with postbuckling motifs... 67	
Figure 14. Hindgut-specific morphological features are replicated with <i>Hoxd13</i> misexpression 74	
Figure 15. Mechanical properties of the hindgut are regulated by <i>Hoxd13</i> activity.....	78
Figure 16. Cuffs require static circumferential compression and cyclic contractions to form	81
Figure 17. Markers for villi mesenchymal clusters do not prefigure or localize to cuffs	82
Figure 18. TGF β signaling is upregulated in the hindgut and RCAS- <i>Hoxd13</i> mesenchyme.....	91
Figure 19. TGF β perturbations capture mid- and hindgut morphologies and mechanics	94
Figure 20. Lumen morphology depends on TGF β -induced collagen remodeling.	99
Figure 21. A genetic and mechanical model of differential intestinal morphogenesis.....	100
Figure 22. Fibrillin fiber orientation correlates with mesenchyme modulus	103
Figure 23. Subepithelial differentially expressed genes include myofibroblast-related factors 105	
Extended Figure 1. qPCR results for muscle patterning and differentiation genes	150
Extended Figure 2. Endogenous and explant Bmp activation during muscle patterning	151
Extended Figure 3. Unique cell shapes and ECM properties in the early fore- and hindguts....	152
Extended Figure 4. Wrinkle morphology and lack of stepwise buckling in the foregut.....	164
Extended Figure 5. Endodermal surface creasing in the hindgut.....	165
Extended Figure 6. Anteroposterior trends in mechanical properties along the gut	166
Extended Figure 7. Anisotropic stiffness in the foregut inner composite.....	167
Extended Figure 8. ECM organization across compartments.....	168
Extended Figure 9. <i>Hoxd13</i> endogenous and ectopic expression levels.....	173
Extended Figure 10. Additional quantifications of mid/hindgut and midgut+ <i>Hoxd13</i> lumens .	174
Extended Figure 11. Modulus and width parameters in the intestine and midgut+ <i>Hoxd13</i>	175
Extended Figure 12. <i>Noggin</i> misexpression in the midgut phenocopies RCAS- <i>Hoxd13</i>	176
Extended Figure 13. Enrichment of TGF β genes in the hindgut and with <i>Hoxd13</i> expression ..	177
Extended Figure 14. Hindgut expression of <i>Hoxd13</i> and putative downstream gene <i>Inhba</i>	178
Extended Figure 15. NCC aggregation and endothelial expansion with <i>Hoxd13</i> expression.....	179
Extended Figure 16. TGF β modulation effect on gut morphology, growth and mechanics	180
Extended Figure 17. Collagen dysregulation in the hindgut.....	181
Extended Figure 18. Lumen morphology becomes hindgut-like in the distal small intestine ...	181

List of Tables

Table 1. Model parameters for Shh-Bmp morphogen patterning	28
Table 2. Results and model predictions for amount of muscle after explant perturbations	31
Table 3. Growth rates for model predicting radial geometry over time	36
Table 4. Primers for qPCR amplification of <i>Hox</i> genes	132
Table 5. Geometries and mechanical properties of 2D numerical models.	146
Table 6. Measured values used to determine lumen wrinkling model parameters.	148
Table 7. 3D midgut, midgut + <i>Hoxd13</i> , and hindgut simulation parameters.	149

Abbreviations

GI	Gastrointestinal
AP	Anteroposterior
DV	Dorsoventral
LPM	Lateral plate mesoderm
ISC	Intestinal stem cell
SMA	Smooth muscle actin
S/HH	Sonic/hedgehog
BMP	Bone morphogenetic protein
TGF β	Transforming growth factor β
ECM	Extracellular matrix
NC/C	Neural crest / cell
DEG	Differentially expressed gene
FISH	Fluorescence in situ hybridization
FWHM	Full width half max
DE	Definitive endoderm
VE	Visceral endoderm
SBS	Short bowel syndrome
PS	Primitive streak
HA	Hyaluronic acid

INTRODUCTION

Origin of the regionalized digestive tube

During his study of calcareous sponge development in the late 1800s (Die Kalkschwämme), Ernst Haeckel developed his famous “gastraea” theory, which proposed that the endodermal gut is homologous among all animals (Levit et al., 2022; Steinmetz, 2019). Accordingly, he argued that the successive morphological steps of vertebrate gastrulation replay the origin and evolution of the gut. Though there is evidence to refute the universality of an exclusively endodermal metazoan gut tube, this idea is still conceptually useful for understanding how different regions along the gastrointestinal (GI) tract acquire their identities. In fact, if we consider classical studies and modern molecular analyses of both the earliest moments of vertebrate gut formation and the simple digestive systems of earlier-branching animal taxa, it is clear that regionalized genetic and cellular identity along the gut is inherent to—and as ancient as—the gut itself (Annunziata et al., 2019; Annunziata & Arnone, 2014).

Evolution of intestinal compartments

The primitive intestine likely evolved over 600 million years ago, with a transition to extracellular digestion in the common ancestor of Cnidaria, Ctenophora and Bilateria (Hartenstein & Martinez, 2019a; Steinmetz, 2019). Since intracellular digestion as in Poriferans (sponges) is limited by cell size and the availability of subcellular lysozymes, extracellular digestion allows for the breakdown and uptake of nutrients from more complex food sources. It

is thus thought to be a crucial innovation in animal evolution, as the ability to process larger macromolecules likely satisfied the higher energetic costs of more intricate body plans.

(Hartenstein & Martinez, 2019b) The appearance of predominantly extracellular digestion, in all cases except Placozoa (a sister group to Bilateria), corresponded to the appearance of a through-gut—a tubular digestive tract with either common or two separate oral and anal openings (Hejnal & Martindale, 2008; Hejnal & Martín-Durán, 2015). This vital moment in evolutionary history is also when a form of physiological regionalization along the digestive apparatus likely emerged, although it has been argued that even single-celled protozoans display a form of digestive compartmentalization (Blum et al., 2014).

Extracellular digestion requires both secretory and absorptive cell types, and thus necessitates a means of organizing them along the body. In *Trichoplax adhaerans*, a tiny marine placozoan species, the gut is not a tube but rather a blind-ended invagination (C. L. Smith et al., 2015; C. L. Smith & Mayorova, 2019). *Trichoplax* wraps its lower endodermal epithelium over small prey like algae and secretes enzymes to perform extracellular digestion. Despite lacking a gut tube and an axis of symmetry, its 3 digestive cell types display a rudimentary spatial arrangement that facilitates the breakdown and absorption of nutrients.

All polyp- and medusa-stage Cnidarians (jellyfish) digest prey within tubular gastrovascular cavities via gland cells that secrete digestive enzymes; partially digested material is then trafficked through the cavity to absorptive gastrodermal cells, which also contain lysozymes for full nutrient breakdown (Steinmetz, 2019). The mouth region is exclusively lined with gland cells that are generally absent from the ‘epitheliomuscular’ body column, with a complementary distribution of phagocytic cells—in other words, the gut develops an exocrine

anterior portion and absorptive posterior portion (Berking, 2007; Steinmetz, 2019). Some subgroups also possess morphological adaptations, such as ‘gastric filaments’ near the mouth that project into the body cavity and carry a higher proportion of enzyme-secreting cells. Sea anemones, or Anthozoans, present folds along the cavity wall that subdivide the space and separate different cell types.

Clearly, the formation of intestinal compartments with functional adaptations is not only evolutionarily ancient—remarkably, gut regions also share morphological and physiological features across distant phyla. It is therefore not surprising that many of the key molecular determinants of regional identity are also highly conserved. This is true even in the case of the sea anemone *Nematostella vectensis*, which expresses orthologs of bilaterian foregut endoderm markers in its ectodermally-derived pharyngeal lining (Steinmetz et al., 2017). Moving forward in evolutionary time to protochordates and sea urchins, molecular regulators like *Cdx*, *Hox* genes, *Pdx1*, and Wnt signaling pattern morphologically distinct foregut, midgut, and hindgut domains, as in vertebrates (Annunziata & Arnone, 2014; Nakayama et al., 2019).

Patterning positional identity along the early gut

Anteroposterior identity in the gut endoderm is established at least as early as gastrulation. In chick and mouse embryos, gastrulation starts with the formation of the primitive streak (PS); mesendoderm precursor cells of the epiblast e/ingress through the PS to form either endoderm or mesoderm (Bardot & Hadjantonakis, 2020). This initial fate decision depends in a dose-dependent way on Wnt-mediated regulation of Nodal signaling, and the AP position at which cells migrate into the streak determines their ultimate placement along the

gut tube (Fleming et al., 2013; Probst et al., 2021). The first cells to migrate through travel anteriorly to become foregut endoderm; later migrating cells move laterally and posteriorly to form mid- and hindgut endoderm. By the end of gastrulation, an internal mesoderm layer is sandwiched between a sheet of endodermal cells and the ectoderm (Lewis & Tam, 2006; Nowotschin et al., 2019). Then, to form a gut tube, the anterior and posterior ends of the endoderm fold to form the anterior and posterior intestinal portals (AIP and CIP, respectively). The endoderm closes into a tube in a proximal-to-distal manner, and splanchnic lateral plate mesoderm wraps around it to form the complete initial GI tract.

At this point, though the gut is morphologically nondescript along its length, AP subregions have already been defined. In the mouse, core transcription factors, including conserved FoxA and GATA factors, drive PS-ingressing cells toward an endodermal fate (Boyle & Seaver, 2010). All of these factors were thought to be regulated by Wnt/Nodal, which is ubiquitously needed for mesendoderm specification in vertebrates. However, Sox17, another essential driver of endodermal fate that contributes to the posterior gut, is expressed in presumptive definitive endoderm cells prior to egression and appears independently of Wnt signaling (Engert et al., 2013; Viotti et al., 2014). Together with the finding that FoxA2-expressing cells that contribute to anterior parts of the gut are also present prior to egression, this result further underscores the extent to which molecular identity prefigures intestinal patterning. In fact, By the end of chick and mouse gastrulation, the endoderm is roughly divided into anterior and posterior domains. The anterior expresses transcription factors Hhex, Sox2, and Foxa2 and the posterior expresses Cdx transcription factors, most notably Cdx2/A. Pdx1 is also expressed in the presumptive midgut endoderm (Spence et al., 2011).

Both using a candidate gene expression approach looking at known regional transcription factors, as well as via unsupervised clustering of single cell transcriptomes, it has been shown that rudimentary organ boundaries are established by E8.5 in the mouse, just prior to formation of the bi-layered gut tube (Nowotschin et al., 2019; Sherwood et al., 2009). Yet, even though the endoderm that makes up anterior and posterior regions of the gut already harbors intrinsic positional identity, cell fates are still plastic for a time. Pioneering grafting studies in the chick by Nicole Le Douarin showed inductive influences from the adjacent lateral plate mesoderm (LPM) define positional identity along the AP axis (Douarin, 1975). Ultimately, assays like *in vitro* germ layer explants have shown that the gut is patterned through reciprocal crosstalk between the endoderm and mesenchyme during tube closure, when tissues are in closer proximity, involving a combination of Wnt, Bmp, RA, and FGF signals (Grapin-Botton, 2005; Wells & Melton, 2000; Zorn & Wells, 2009). Each of these factors, in fact, promotes hindgut identity; Wnt and FGF4 activate the ParaHox gene *Cdx2*, which suppresses anterior fate (Sherwood et al., 2011; Wells & Melton, 2000). The importance of these genes has also been demonstrated for the purpose of constructing organoids—formation of colonic organoids requires Bmp activation, which stimulates expression of posterior Homeobox (Hox) genes (Múnera et al., 2017).

Indeed, as we will discuss in Chapter 3 (Background), Hox genes play important roles in fate specification along the gut AP axis. Hox gene expression in both the mesoderm and, to a lesser extent, the endoderm forms a combinatorial code that defines regional identity, demonstrated by expression mapping and mouse mutant studies (J. Aubin et al., 2002; Boulet & Capecchi, 1996; Grapin-Botton, 2005; Kondo et al., 1996). Hox genes are expressed in a colinear

fashion in the lateral plate mesoderm from gastrulation onward, and they are both upstream and downstream of morphogen pattern mechanisms (Beck, 2002). For example, Hoxd control of FGF10 is important for development of the cecum (Zacchetti et al., 2007).

Anatomy and physiology of gut compartments

Mature gut compartments perform vital and complementary roles in digestion that together ensure efficient processing of food. As development progresses, each region defined and shaped by the molecular factors described above adopts unique macroscale dimensions and a specialized mucosal, or inner endodermal, surface morphology that facilitates its function (Thompson et al., 2018). Along the gut, the epithelium is critical for secreting mucus and absorbing water and nutrients, as well as for protection against pathogens and mechanical insults (Bonis et al., 2021; Peterson & Artis, 2014). Though the stomach and other accessory organs that develop from the endoderm are critical components of the digestive apparatus, here we will focus on properties of the basic gut tube derivatives: the esophagus, small intestine, and large intestine.

Epithelial structure and turnover in the esophagus

The esophagus is the site of food intake into the GI tract, and primarily develops broad axial ridges that extend along its length (Ménard, 1995; Wake, 1978). This morphology is strikingly conserved across vertebrate taxa: birds, mammals, and reptiles all display some degree of longitudinal folding, which is often also present in the stomach as “rugae”.

Esophageal folds occur on a much larger length scale than villi and are thought to permit

circumferential distension and accommodate a food bolus without rupture (Liao et al., 2007; Soliman & Madkour, 2021a). In humans and other mammals, orthogonal circumferential folds have only been reported in the context of esophageal disease, where axial folds also become reduced in depth and number, or as transient occurrences in healthy samples (Gohel et al., 1978; Levine & Rubesin, 2005).

The epithelium of the esophagus in vertebrates is initially cuboidal, pseudostratified and, in contrast to the simple columnar epithelium that lines the intestine, progressively transforms into a stratified squamous epithelium over the course of development (Y. Zhang et al., 2021). This process involves the initial thinning of the pseudostratified layer into a single sheet, which then becomes a bilayer briefly, before expanding via stratification. The mouse esophagus forms 4-6 squamous epithelial cell layers that are covered in a final layer of keratin on the luminal side, while the human esophagus forms 20-30 cell layers and lacks a keratin layer (Shibata et al., 2019). The mechanism of mucosal self-renewal in the mature esophagus is also distinct from the intestine, as it relies on a basal layer of proliferating progenitors instead of crypts housing intestinal stem cells (ISCs). Studies in the mouse have shown that regulation of BMP signaling is important for differentiation of keratin-8 positive columnar cells into keratin-5 and -14 positive squamous cells (P. Rodriguez et al., 2010). Importantly, constitutively active *Bmpr1a* suppresses the initiation of stratification altogether, whereas *Bmpr1a* deletion leads to aberrant expansion of the progenitor cell type and impaired differentiation, indicating that a sharp spatiotemporal switch in BMP activation is key to epithelial reorganization and expansion (P. Rodriguez et al., 2010).

Unlike the small and large intestines, which have mucin-secreting goblet cells distributed across their epithelial surfaces, the esophagus sequesters these cells in glands that form at late fetal stages from foregut endoderm (Long & Orlando, 1999). In addition to mucus, glands secrete neutralizing substances like bicarbonate, as well as growth factors and hormones. Importantly, gland cells are cuboidal, and the aberrant appearance of cuboidal cells in the epithelium is a hallmark of a rare but significant form of esophageal cancer, Barrett's esophagus (Garman, 2017). Gland cells have been shown to initiate cancerous growth, making them important targets for understanding the appearance and progression of this condition (Nie et al., 2017).

Architecture of the intestinal epithelium

In the small intestine, long, finger-like epithelial structures called villi are tightly packed and extend into the lumen to maximize surface area for nutrient absorption. Each villus has multiple associated crypts—invaginations that house intestinal stem cells (ISCs)—and along the crypt-villus axis, slow-cycling ISCs give rise to absorptive and secretory cell types with highly reproducible spatial organization (reviewed in Bonis et al., 2021; de Santa Barbara et al., 2003; Gehart & Clevers, 2018). Briefly, ISCs exist at the very bases of crypts sandwiched between Paneth cells, which secrete antimicrobial compounds into the lumen, as well as niche factors like EGF and Wnt. Above the stem cell compartment is a series of transit amplifying cells, which are fast-cycling absorptive progenitors. Amongst differentiated cell types are enterocytes, the most common absorptive cells in the small intestine, goblet cells, which secrete mucus, and

enteroendocrine cells, which secrete hormones (Bonis et al., 2021). The architecture of the small intestinal epithelium is thus crucially tied to its purpose.

The mucosal surface of the large intestine, or colon, is often reported to be like that of the small intestine, but devoid of villi and thus “flat” (De Santa Barbara et al., 2003; Gehart & Clevers, 2018; Kostouros et al., 2020). Accordingly, though it shares crypts and ISCs that renew the epithelium, the collection of cell types in the colon was thought to be simply a subset of those in the small intestine, though with a more extensive population of secretory goblet cells. However, many have noted the appearance of reticulated surface folds and/or structures analogous to villi—“colonic villi” or “cuffs”—that sometimes disappear with distension (Bell & Williams, 1982; Gehart & Clevers, 2018; Kostouros et al., 2020; Mahoney et al., 2008; Pandit et al., 2018; Rubio, 2020; Wake, 1978). These outgrowths are similar to villi in the embryo and become relatively flatter after birth for humans, but persist in chicks. In addition, recent work has shown that the colon exhibits a wide array of absorptive and secretory cell types analogous to those of the small intestine, which can also assume reproducible positions relative to the crypt and inter-crypt epithelial folds (Birchenough et al., 2016; Parikh et al., 2019). For example, a “sentinel” goblet cell first discovered in the colon sits at the crypt opening and promotes coordinated mucus secretion in response to an insult (Birchenough et al., 2016).

Interestingly, crypts form after birth in mice but before birth, during the appearance of “colonic villi”, in humans (Kostouros et al., 2020). Crypts can also form in organoids in the absence of a creased or folded architecture, but it is often difficult to assess the fidelity of an organoid system to its *in vivo* counterpart (Sprangers et al., 2020). It is therefore unclear whether human large intestinal crypts rely on any architectural features of the mucosal surface.

Altogether, large intestinal morphogenesis and cell type specialization is less well characterized, though these features are of great interest for understanding, preventing, and ameliorating the effects of colon cancer.

Morphogenesis of the gut

Despite our wealth of knowledge surrounding molecular underpinnings of regional features, especially in the epithelium, the morphogenetic processes that differentially shape compartments along developing GI tract are much less clear. Three characteristics, in particular, show positional variation and are vital for GI function: the radial pattern of concentric smooth muscle, tube length, and morphology of the epithelium.

Patterning the gut cross-section with Hh and Bmp

Smooth muscle is needed for both gut physiology and morphogenesis. Proper radial patterning of the first circumferential muscle layer drives differentiation of longitudinal muscle, and the coordinated contractions of these layers generate the peristaltic movements that passage food through the GI tract (Huycke et al., 2019). Furthermore, muscle constraints and geometric properties of gut tissue layers are important determinants of lumen shaping and elongational growth (Khalipina et al., 2019; Shyer et al., 2015; Y. Yang et al., 2021). Another vital phenomenon that occurs at roughly the same time as muscle formation is separation of the common foregut into nascent esophageal and tracheal tubes, or respiratory-esophageal separation (RES). Failed separation leads to the congenital defect of esophageal atresia (EA) and/or tracheoesophageal fistula (TF) (Ginzal et al., 2023; Rosekrans et al., 2015). EA/TF

requires surgical intervention, as the esophagus can develop a discontinuity and/or retain aberrant connections to the airway tube.

In addition to other signals and transcription factors, at the heart of the mechanisms driving these two events is a common reliance on the Shh and Bmp pathways. Though many studies identified a key role for the Hh pathway activation (mediated by both Shh and Ihh) in gut smooth muscle patterning, conflicting reports made a definitive mechanism elusive. Tissue recombination experiments in the chicken, where the mesenchyme of the gizzard was cultured with the endoderm in various configurations (e.g. mediolaterally flipped, endoderm on both edges, no endoderm), showed a zone of muscle inhibition adjacent to the endoderm in all cases, which was revealed to be a consequence of Hh-driven repression using cyclopamine, bead implantation and FISH analysis (Sukegawa et al., 2000). Mouse genetic studies, however, showed that Shh and Ihh mutants have reduced smooth muscle (Mao et al., 2010; Ramalho-Santos et al., 2000).

Recent work from our lab demonstrated using in vitro cultures and gene expression analysis that these contradictions can be explained by dose-dependence and downstream regulation of Bmp signaling, which has been known to inhibit smooth muscle formation in the chick (De Santa Barbara et al., 2005; Huycke et al., 2019; D. M. Smith et al., 2000). At high concentrations in the mesenchyme immediately next to the endoderm, Hh signaling activates expression of the master myogenic transcription factor Myocardin (Myocd), but also Bmp signaling via Bmp4 upregulation, which locally suppresses muscle differentiation by inhibiting Myocardin and two additional MRTF transcription factors (Huycke et al., 2019). Further away from the endoderm, however, the Hh signal concentration attenuates to a level that is below

the threshold for Bmp activation, but still sufficient for upregulation of Myocd, leading to the appearance of smooth muscle actin-positive cells. Bmp2/7 secreted by the mesothelium suppresses muscle from the opposite side of the mesenchyme. Smooth muscle therefore appears as a radially patterned ring with its geometry set by the length scale of Hh, Bmp, and Myocd/Mrtf reaction-diffusion dynamics. To induce differentiation of the outermost longitudinal layer, the circumferential layer and enteric neurons migrating along its outer surface secrete Bmp inhibitors, releasing Bmp-mediated suppression of muscle, which allows the outer layer to differentiate.

A complete picture of early gut patterning requires also noting the signals involved in RES in the early foregut tube. At around E9.5-11 in the mouse, 4-6 weeks of gestation in the human, and between E2.5-3.5 in the chick, the anterior endoderm undergoes an invagination at its DV midline to split the foregut tube into the dorsal esophagus and ventral trachea (Fausett & Klingensmith, 2012; Y. Zhang et al., 2021). The dorsal marker and essential regulator of esophagus endodermal fate is Sox2, while Nkx2.1 promotes ventral, airway endodermal fate (Graham et al., 2003; Que et al., 2007). Low Bmp activity in the presumptive esophageal mesenchyme appears in this context as well, as Bmp activates Nkx2.1 expression (Domyan et al., 2011). In the absence of Bmp signaling through deletion of its receptors, RES is lost, and the entire foregut is Sox2-positive. Complementing this expression pattern is Noggin expression in the dorsal mesenchyme; failed RES in the Noggin mutant is rescued by Bmp4 and Bmp7 deletion (Que et al., 2006). Additionally, though Shh is expressed in both compartments, it is more highly enriched on the ventral side (Y. Zhang et al., 2021). Therefore, biochemical

patterning of RES involves separating two domains of Bmp and Shh signaling along the DV axis, where both are enriched ventrally.

Elongational growth of the small intestine

The mechanism driving midgut elongation has been of considerable interest, in part because of short bowel syndrome (SBS), a condition where the small intestine is truncated and unable to absorb water and nutrients (Sugimoto et al., 2021). Lengthening of the midgut is thus clearly essential to its function, but a comprehensive understanding of how it is first achieved in the embryo has been elusive. However, three types of studies have shed light on how the gut elongates: the first concerns regulation of proliferative growth in the mesenchyme, the second deals with oriented cell behaviors and divisions in the pseudostratified gut epithelium, and the third includes studies about mesenchymal growth anisotropy.

Both Fgf and Shh signaling have been implicated in the regulation of mesenchymal proliferation and, in turn, gut length in the mouse. Null mutants for endodermally-expressed Fgf9 and mesodermally-expressed Fgfr1/2 develop guts that are considerably shorter than normal—but, interestingly, not different in diameter—due to decreased mesenchymal proliferation (Geske et al., 2008). Subsequent stains for pErk1/2 (a downstream readout of Fgf activation), alpha smooth muscle actin/desmin (markers used to assess myofibroblast differentiation), pSmad2/3 (a readout of Tgf β signaling), and TGF β inhibitors revealed that only a subset of mesenchymal cells respond to the Fgf9, and that these cells suppress local activation of myofibroblast differentiation via TGF β . Aberrant differentiation of these cells with

Fgf9 loss, via a specialized mesenchymal subtype that receives the Fgf signal, leads to a slower mesenchymal proliferation rate and a shorter gut (Geske et al., 2008).

Shh and Ihh double mutants also show defects in mesenchymal proliferation without affecting apoptosis (Mao et al., 2010). When intestinal mesenchyme progenitors were treated ex vivo with recombinant versions of various important signaling proteins in the gut, Shh induced the most dramatic increase in proliferation index. Naturally, blocking Hh signaling shortens the gut. It is well-established that Hh signaling is transduced by the primary cilia of mesenchymal cells; therefore, cilia mutants would also be expected to have shorter guts due to abrogated Hh activation, as shown in a recent study (Y. Yang et al., 2021). Activation of YAP signaling rescues the short gut phenotype in cilia mutants by restoring proliferation rate—along with the loss of YAP activation in these mutants, the authors interpreted this to mean Hh modulates YAP to affect proliferation rate, which allows for proper gut growth and elongation.

It is obvious that proliferation will affect gut extension, but understanding how growth anisotropy is achieved is more difficult. Why is new mass added through cell division directed rostrocaudally instead of radially or circumferentially? Studies investigating the role of non-canonical Wnt signaling have begun to shed light on this question. Non-canonical Wnt is the most prominent pathway involved in oriented cell behaviors during morphogenesis, as Wnt ligands can act as attractive cues for endodermal and mesenchymal cells as part of the PCP pathway (Jones & Chen, 2007). Mutations leading to loss of either mesenchymal Wnt5a or Ror2 (a Wnt5a receptor) lead to short gut phenotypes like those with Fgf9 and Hh mutants (Cervantes et al., 2009; Yamada et al., 2010). However, one key difference is that the mesenchyme becomes thicker as well, indicating a defect in coordinating directional growth.

Recent work employing elegant cell tracking and live imaging showed that gut shortening in the Wnt5a mutant results from defects in the reintegration of post-mitotic sister cells into the pseudostratified epithelium. Pseudostratified epithelial cells all retain apical and basal attachments, and migrate to the apical surface to divide, after which the new daughter cell or both cells must attach or re-attach to the basal ECM (S. Wang et al., 2018). Selective loss of Wnt5a in the mesenchyme using a tissue-specific Cre driver showed that cells fail to form filopodia directed toward to the basal membrane, toward the Wnt attractive cue, and are thus extruded, leading to decreased cell numbers in the endoderm.

Despite this study revealing a role for oriented cell behaviors in elongation, the question of anisotropy remains, as the thickness of the endoderm appears unaffected by Wnt5a loss; decreased cell numbers somehow preferentially lead to axial shortening rather than radial thinning. One possible explanation may come from the mouse esophageal and tracheal mesenchyme, where subepithelial “smooth muscle progenitors” were found to—as assessed by staining for the Golgi apparatus—orient themselves radially, toward the epithelium, in a Wnt5a-dependent manner (Kishimoto et al., 2018). Dissociated and plated wild-type mesenchymal cells migrated toward epithelial spheres embedded in Matrigel, while Wnt5a^{-/-} mesenchymal cells lost oriented movement. The authors proposed that radial orientation of these cells restricts radial expansion and promotes tube elongation. In both this case and the epithelial pathfinding story, however, the molecular partner to Wnt5a that facilitates directional movement is unknown.

In their 1958 study of intestinal development in the chick, Alfred and Jane Coulombre speculated that “...the onset of contraction in the smooth muscle restricts radial expansion of

the duodenum and initiates a period of relative elongation” (Coulombre & Coulombre, 1958). Recent studies have begun to test this intuitive hypothesis systematically, though it is still unclear whether muscle contractions promote intestinal elongation. In the chick, pharmacological suppression of muscle contraction leads to a thicker and shorter gut after ex vivo culture for several days (Khalipina et al., 2019). However, it is unclear from the methodology used whether the change in gut dimensions is a result of dampened longitudinal growth, or simply the elastic response that occurs in the first ten minutes after drug treatment. Partial ablation of smooth muscle formation using diphtheria toxin driven by Myh11 regulatory elements leads to a modest reduction in gut length, but culturing the mouse gut with a ROCK inhibitor did not affect elongation, so the observed result is a result of disrupting static rather than cyclic muscle constraint (Y. Yang et al., 2021). Altogether, the mechanism of preferential axial growth, and the coordinated role of both physical forces and biochemical signals in mediating it, is still unclear.

Physical forces in intestinal growth and shaping

In the chick and mouse, theoretical and experimental studies have outlined several events during intestinal development driven by mechanics, in some cases even bridging physical forces to molecular regulators. Looping of the entire gut is driven by differential growth between the gut tube and mesentery, which is mediated by BMP signaling (Nerurkar et al., 2017; Savin et al., 2011), and formation of the hindgut tube is driven by a gradient of FGF signaling-driven contractility (Nerurkar et al., 2019). Rotation of the gut occurs through patterned deposition of HA in the dorsal mesentery, which cooperates with TGF β signaling to

generate a stiffness differential stiffness on the left-right axis, and smooth muscle layers are oriented by both static and cyclic strains (Huycke et al., 2019; Kurpios et al., 2008; Sanketi et al., 2022; Sivakumar et al., 2018). Additional studies in the chick have proposed roles for longitudinal tension and muscle contractility in intestinal elongation (Chevalier, De Witte, et al., 2018; Khalipina et al., 2019).

Villi in the developing chick small intestine form through a primarily mechanical mechanism, where sequentially forming smooth muscle layers drive orthogonal buckling instabilities. A circumferential layer and two subsequent longitudinal layers constrain inner endoderm and mesenchyme tissues until they fold—first into ridges, then zigzags that become increasingly compressed—to ease residual stress from differential growth (Shyer et al., 2013). As the epithelium buckles smoothly with the underlying mesenchyme, increased curvature concentrates Shh to induce Bmp and the formation of a villus cluster in the mesenchyme, which feeds back to suppress epithelial Wnt at villus tips. Wnt between villi activates Sox9, leading to ISC localization to the bases of villi (Shyer et al., 2015).

Chick midgut villi form through a mechanical process that, for the most part, can be described by treating tissues as continuous materials. However, the late stages of chick villi development and the mechanism of villi formation in the mouse suggest that local, cell level mechanics and growth behaviors are required for proper morphogenesis as well. In mice, subepithelial aggregation of mesenchymal clusters has been proposed to deform the overlying epithelium to initiate villus formation (Hughes et al., 2018; Karlsson et al., 2000; Walton et al., 2012, 2016). Also, in addition to work showing that apical invaginations via actomyosin initiate crypt formation, results from 2D and 3D *in vitro* cultures of crypts have also pointed to roles for

inflation-collapse dynamics and tissue tension in directing both crypt appearance and the movement of cells out of the stem cell niche (Houtekamer et al., 2022; Pérez-González et al., 2021; Tallapragada et al., 2021; Q. Yang et al., 2021). Furthermore, and perhaps most strikingly, it has been shown using photopatterned substrates that crypt curvature alone is sufficient to induce the formation of niche cell types, in part via mechanosensitive YAP signaling (Gjorevski et al., 2022).

Summary & motivation

It is clear from previous work that the initiation of regional specialization along the gut on a molecular level occurs far prior to morphological specialization, and that distinct epithelial morphologies and structures along the gut allow for correct intestinal function. Furthermore, there is substantial evidence supporting a role for local physical forces and large-scale differential growth strains in intestinal morphogenesis. Yet, as we learn more about mechanical contributions to morphogenesis, how they are encoded genetically still remains unclear. This is a fundamental problem in development across organisms, but especially in the complex organs of birds and mammals. The chick gut offers an opportunity not only to understand how gut regions are differentially shaped, as we explore in Chapters 1 and 2, but also to link regional genes to forces due to its extensively characterized molecular AP pattern (Chapter 3).

The work described herein begins the difficult task of traversing scales--subcellular gene regulation and biochemical signals, cells and extracellular matrix, and continuous multicellular tissues--to offer a comprehensive view into the appearance of form and function in the serially homologous segments of the gastrointestinal tract.

Chapter 1: Radial and axial geometry in early gut tube development

Attributions

Hasreet K. Gill devised the project with Tyler R. Huycke, planned, designed, and performed all experiments, and performed data analyses. Shahar Kasirer performed simulations and developed all theoretical and numerical method codes/formulations for modeling morphogen patterning and growth. Chaitra Prabhakara developed methods and wrote codes for radial geometry, cell density, and FISH pattern quantification, based on a method developed by Hasreet K. Gill and David Sprinzak (Huycke et al., 2019). Tyler R. Huycke designed and performed pilot experiments that initiated the project, including whole mount PH3 staining reported in Figure 5. David Sprinzak and Hasreet K. Gill developed code for proliferation quantification and equations for volumetric growth measurements. Emma R. West and Jiho Choi provided reagents and assistance with SABER-FISH experiments. Clifford J. Tabin and David Sprinzak supervised this project.

Background

Shortly after tubulogenesis, the nascent foregut, midgut, and hindgut share similar circumferences, tissue widths, and lengths. However, over the course the several days, each region adopts characteristic dimensions that ultimately constrain regional morphogenesis and reflect compartmental functions. These regions share tissue types and the molecular toolkit that patterns radial geometry, raising the question of how muscle patterns are diversified along the early gut.

AP gradients of signaling pathways are essential for proper regional patterning in early gut formation, raising the possibility of spatial differences in these factors affecting radial patterning as well. Bmp signaling has been shown to negatively regulate muscle differentiation along the entire chick gut, but differences in the endogenous levels of Bmp ligands, and in responsiveness to upstream and downstream genes, is variable, particularly in the foregut (D. M. Smith et al., 2000). Bmp4 is thought to be expressed in the gizzard only after muscle has already differentiated, at E7, while Bmp receptors Bmpr1a and Bmpr2 are absent altogether. Since Bmpr2 is required to form a Bmpr1a/b-Bmpr2 heterodimer that facilitates signal activation, this suggests low Bmp activity in the gizzard may be needed to permit formation of a thicker muscular layer. Shh is expressed along the entire gut endoderm, but its viral misexpression only activates Bmp4 expression in the more caudal parts, not in the foregut-derived gizzard (Roberts et al., 1995). Bmp4 overexpression induced expression of the pyloric sphincter marker Nkx2.5 only in the gizzard and not the intestine, further supporting an AP prepattern that determines how tissues will respond to Bmp activation. Though it is unclear from these initial studies what is happening in the more anterior primordial esophagus, it appears that Bmp signaling and activation by Shh is dampened in anterior parts of the gut, though it still affects muscle formation as in the midgut. Finally, Bmp signaling is important for development of both smooth muscle and the enteric ENS of the hindgut (De Santa Barbara et al., 2005). Unlike in the foregut where existing muscle is abolished via apoptosis by Bmp4, Bmp overactivation using a mutated form of the Bmp repressor Bapx1 leads to the persistence of undifferentiated mesenchyme in the hindgut, as we would expect from studies in the midgut.

As a complex regional mix of signals guides muscle differentiation, the gut tube also grows both radially and axially. Bmp and Shh signals affect both cell fate decisions and growth and apoptosis in the gut, ureter, and lung, raising the question of how these pathways affect regional cell-level growth through ECM expansion and proliferation, and how growth feeds back to signaling (Fu et al., 2004; Jeffery et al., 2005; Mamo et al., 2017; Yu et al., 2002). At the same time, little is known about the mechanism of regionally specialized growth anisotropy that parses growth along circumferential, radial, and axial directions, leading to differential elongation in distinct compartments along the gut. In other words, why does the large intestine elongate considerably less than the esophagus and small intestine?

Many studies have considered ways to model the interplay of reaction-diffusion based patterning and growth, such as through a variety of scaling laws or time-dependent field expansion via advection (Crampin et al., 1999; Rasolonjanahary & Vasiev, 2016; Sagner & Briscoe, 2017). However, in the case of a system that grows in three dimensions over the course of several days, the likely distinct timescales of reaction-diffusion patterning and tissue growth make such models less relevant. One similar case to the developing gut, however, is DV pattern scaling in the developing neural tube (Dessaud et al., 2008; Uygur et al., 2016). In Kicheva et al., 2014, the authors implement a two-step model of DV patterning via Shh and Bmp signaling, followed by domain size refinement via differentiation of motor neurons. In this first chapter, we adopt an analogous model to investigate the interplay of radial patterning and volumetric growth in sculpting initial tube dimensions along the gut. These distinct geometries both prefigure final macroscale dimensions and determine how the lumen will buckle in each region.

Results

Development of different tube dimensions along the early gut

To investigate how the foregut, midgut, and hindgut initially diverge in geometry, we first characterized tube dimensions over the course of muscle differentiation, from E4 to E7, using whole-gut samples and transverse sections. Consistent with an established anterior-posterior trend in intestinal development, the foregut is the first to close into a patent tube at around 3 days of development—the hindgut and midgut were therefore partially or just barely closed at E4 (Southwell, 2006). To visualize smooth muscle, we stained for the marker Smooth Muscle Actin, and observed that while the midgut and hindgut show traces of SMA-positive cells at E4, a true muscle layer does not appear until E5 in all regions (Figure 1A).

From tube closure onward, each region displays a unique radial growth trajectory. First, while the midgut and foregut maintain steady endoderm thicknesses, the hindgut endoderm thickens exponentially over 2 days (Figure 1A, C). Meanwhile, the midgut maintains its mesodermal width as well, even when smooth muscle differentiates within it, while the foregut and hindgut both experience gradual and drastic mesodermal thickening, respectively (Figure 1A, C). Examining the contributions of endoderm and mesoderm to radial thickness and growth reveals a spatiotemporal trend in tube wall growth, where the relative thickness of the mesoderm increases over the course of muscle differentiation in the foregut, and that of the endoderm increases in the hindgut (Figure 1F). In the midgut between these regions, relative thicknesses of the endoderm and mesenchyme remain relatively constant over time. Geometric properties of the muscle also show key regional differences. After its differentiation at E5, the center peak of the circumferential muscle layer progressively shifts outward from the

endoderm (Figure 1G). Though this change in position (normalized to the size of the mesoderm) appears between E5 and E6 in all regions, subsequent rates of radial expansion differ positionally; foregut muscle remains in its relative position, but muscle distance increases at the same rate and a slightly lower rate in the midgut and hindgut, respectively, between E6 and E7. Notably, hindgut muscle experiences the largest change in relative distance. Finally, though muscle appears to thin over time in all regions (Figure 1A), presumably to refine its boundaries, normalized FWHM measurements show that this only truly happens in the midgut and hindgut (Figure 1G). The foregut instead differentiates muscle at E5 at a defined width that is stable relative to mesoderm size throughout these stages.

To fully capture regional growth trajectories during early gut morphogenesis, we next needed to consider axial growth. While it is common knowledge that the small intestine elongates extensively compared to the esophagus and large intestine, we first found that the foregut elongates at a mildly faster rate than the midgut during early chick gut growth (Figure 1B). The hindgut, by contrast, grows very little in absolute length compared to the anterior gut compartments (Figure 1B, E). However, all three regions show a substantial relative increase in length specifically after muscle differentiation at E5 (Figure 1E).

Hh and Bmp signaling landscapes vary across space and time

Our measurements highlight both similarities and important geometric variations between regions that correlate with the formation and refinement of smooth muscle. We therefore

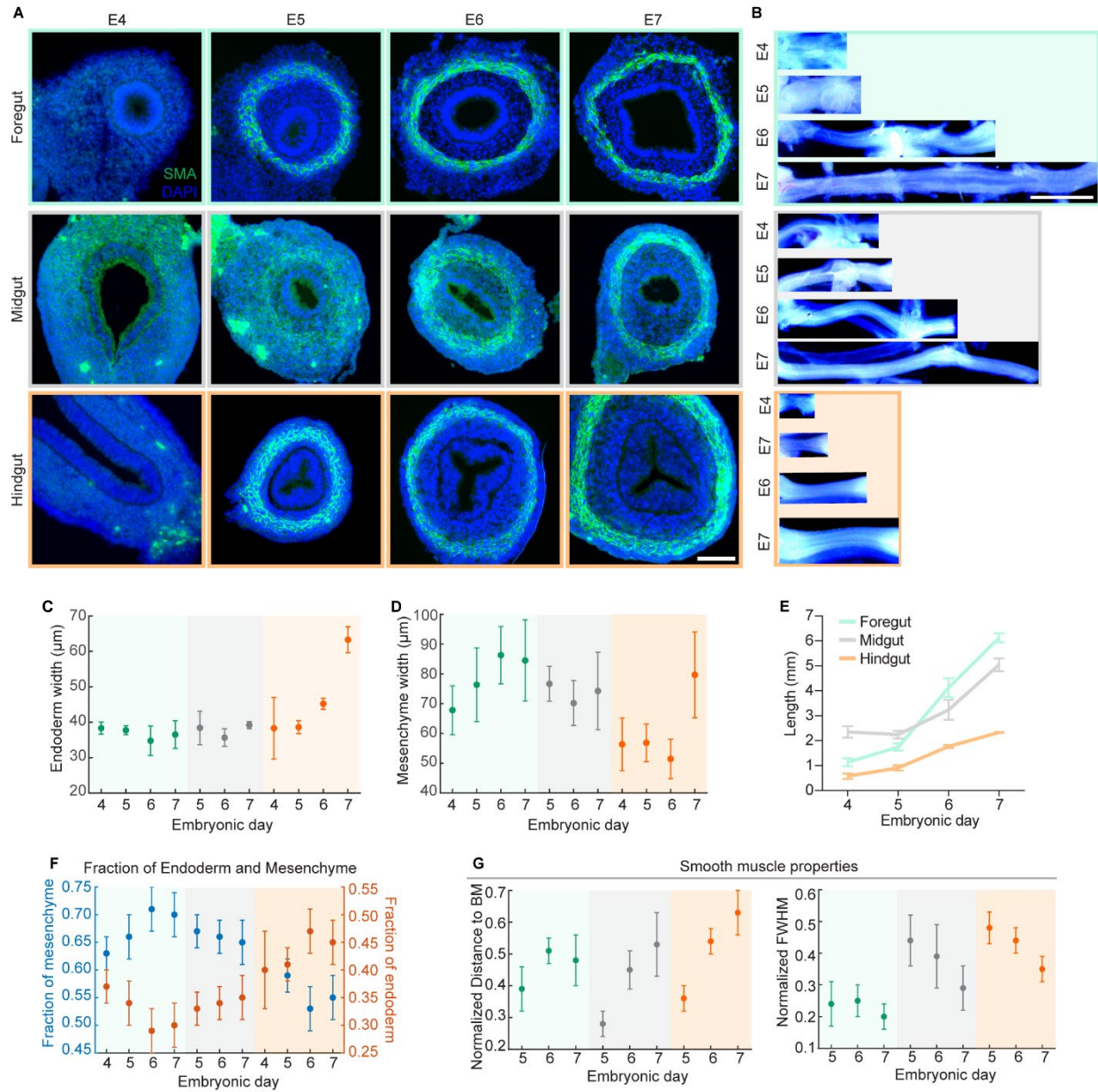


Figure 1. Radial and axial growth patterns along the early gut

(A) Transverse sections through the foregut, midgut, and hindgut stained for nuclei (DAPI) and smooth muscle (Smooth Muscle Actin, SMA) over the course of early muscle differentiation, E4-E7. Scale bar, 50μm. (B) Whole-tube images of each region in isolation from E4 to E7, where anterior is left and posterior is right. Scale bar, 1mm. (C) Measurements of endoderm and (D) mesenchyme width from E4-E7 in the hindgut and E5-E7 in the midgut, where left to right is anterior to posterior (green, foregut; gray, midgut; orange, hindgut). “Mesenchyme” here refers to the entire mesoderm, from basement membrane to outer edge (excluding the thin mesothelium). (E) Region length over time. (F) Fraction of endoderm and mesenchyme as a function of position, determined from parts C and D. (G) Smooth muscle peak distance from the endoderm (left) and muscle width (FWHM, right) over time as a function of position, normalized to the size of the mesoderm. For all plots, n=3 biological replicates; error bars, SEM.

hypothesized that differences in radial smooth muscle patterning may underlie both the temporal evolution of tissue width and tube elongation. For example, region-specific restrictions on radial expansion imposed by activators and inhibitors of smooth muscle differentiation could lead to preferential distribution of new mass on the longitudinal axis and, thus, differences in lengthening.

As described in Patterning the gut cross-section with Hh and Bmp, a classic activator-inhibitor morphogen patterning mechanism drives muscle differentiation and radial positioning, where Hh signal from the endoderm induces both “muscle-activating” *Myocd* and “muscle inhibitory” *Bmp4* expression in the mesoderm. Local *Myocd* suppression by Bmp signaling at high concentrations of Hh leads to zone of undifferentiated mesenchyme between the endoderm and muscle, and diffusion of Bmp2/7 from the mesothelium on the opposite end of the mesoderm sets the outer muscle boundary (Huycke et al., 2019). To ask whether differences in Hh or Bmp levels may tune radial geometry in different compartments, we used qPCR to first assess relative levels of muscle gene expression in the foregut and hindgut relative to the midgut. Qualitatively consistent with more prominent widening of the subepithelial mesenchyme, we primarily observe that Bmp4 levels are higher in the hindgut at E4 and E5 (Extended Figure 1; Figure 1E). However, despite forming a clear non-muscle mesenchyme layer, the foregut shows diminished relative Bmp4 expression at all time points while still prominently expresses muscle markers (Extended Figure 1; Figure 1A, E).

Our QPCR data suggested possible differences in Bmp4 activation by Hh in the foregut and hindgut. Though informative, these samples included the endoderm and were assessed

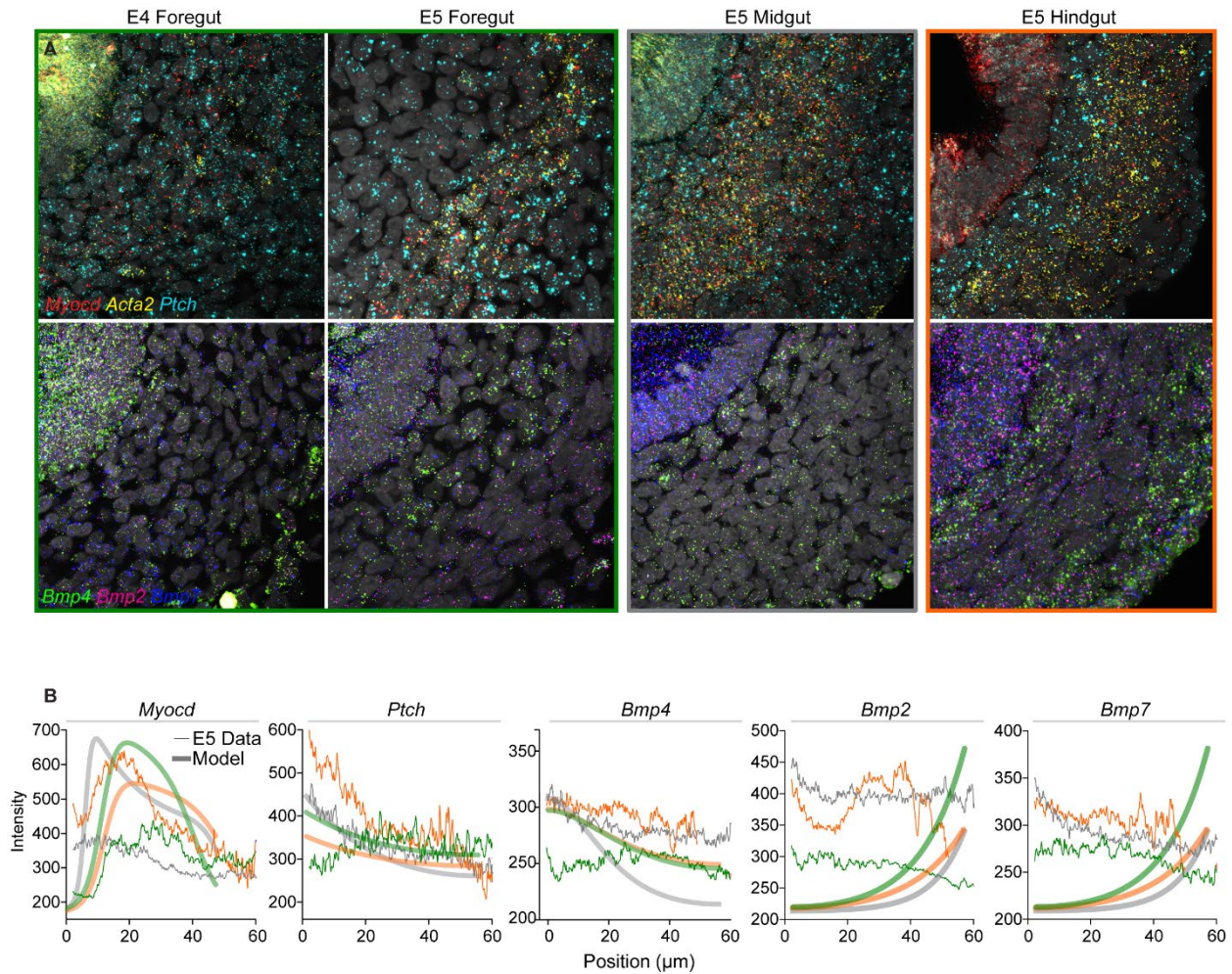


Figure 2. Shh and Bmp signaling across compartments and corresponding model predictions.

(A) SABER-FISH patterns across regions for (top) muscle differentiation genes *Myocd*, *Acta2*, Shh receptor and target *Ptch*, and (bottom) Bmp ligands. (B) Radial intensity quantifications for FISH patterns at E5, where the narrow solid line is measured from actual images and the thick lines correspond to predicted profiles from a reaction-diffusion model fit to initial muscle geometries. Colors correspond to boxes around images in A. To compare model curves to measurements, gray lines corresponding to midgut profiles were aligned to their predicted counterparts, and the other model curves for the foregut and hindgut were scaled accordingly.

relative to the midgut. To observe and quantify absolute levels of Hh target and Bmp gene expression in the mesoderm, we performed single-molecule FISH amplified by SABER (Kishi et al., 2019) at E4 and E5—the time frame when muscle differentiates. To first assess when a discrete muscle layer begins to form in each region, we examined expression of *Myocd* and *Acta2* (smooth muscle alpha actin) and found that *Myocd* expression already prefigures muscle

at a distance from the endoderm at E4 in the foregut, even though SMA is not yet detectable (Figure 2A, red signal). Accordingly, *Acta2* is only expressed in a few sparse cells (Figure 2A, yellow signal). This observation may explain why foregut muscle already appears as a distinct band at E5 and does not refine from a diffuse starting point as in the E5 midgut and hindgut (Figure 1G). Indeed, we did not observe a pattern in *Myocd* in these more posterior regions until E5 (Figure 2A). For this reason, subsequent comparisons of early muscle differentiation events were made at E4 in the foregut and E5 in the midgut and hindgut. To quantify expression patterns, we measured average signal intensity as a function of radial position from the basement membrane to the other edge of the tube at E5 for the midgut and hindgut and E4 for the foregut (FISH and immunostain quantification); intensity traces for muscle genes show clear peaks of expression corresponding to the nascent layers (Figure 2B).

We next found that *Ptch* expression, and thus Hh pathway activation, was highest in the hindgut and lowest in the foregut. Further examination of *Bmp2/4/7* expression indicated that, in fact, all genes are relatively lowly expressed in the foregut at E4, and, save for *Ptch*, all Bmp genes showed similar expression levels in the midgut and hindgut (Figure 2A-B). This result for Bmp ligands in the foregut is consistent with QPCR data and suggests that the foregut is able to suppress muscle subepithelially despite expressing less *Bmp*. High levels of Bmp ligands in the hindgut endoderm may explain why we saw higher hindgut *Bmp4* expression via QPCR.

Mismatch between measured and predicted morphogen levels fit to radial geometries

SABER-FISH images revealed relatively lower Bmp ligand expression in the foregut and higher Hh pathway activation in the hindgut via *Ptch* expression. Though we can make

qualitative predictions for how these differences would affect muscle patterns, for a quantitative measure of expected radial geometry, we developed a mathematical model of reaction-diffusion based muscle patterning in the gut (Reaction-diffusion model of muscle patterning with differential growth). We then performed a manual exploration of the parameter space to determine the relative morphogen levels that would predict the observed geometries (Table 1, Radial muscle patterning and growth).

Table 1. Model parameters for Shh-Bmp morphogen patterning

Region	η_{SHH}	η_{BMP2}	$\beta_{\max BMP4}$
Foregut	0.95	10	10
Midgut	1.4	5	10
Hindgut	0.76	5	2

Because the gut is radially symmetric, we confined our treatment to 1D for simplicity. Maintaining a constant field length, Shh signal diffuses in from the left side at a concentration η_{SHH} , and Bmp2/7 (treated as one entity) from the right side at $\eta_{BMP2/7}$. Shh activates Bmp4 at a concentration-dependent production rate β_{BMP4} . Several other parameters are defined and fit to midgut data, including degradation rates and diffusion coefficients, but only the above parameters were adjusted to fit radial geometry when muscle differentiates. When model predictions were overlaid with intensity traces, we observed that predictions based solely on expression levels fail to predict the data—*Ptch* expression is expected to be lowest in the hindgut, and *Bmp4* levels are predicted to be nearly equivalent between the foregut and hindgut (Figure 2B). This mismatch between the model and data therefore suggests that the

relative amounts of patterning gene expression do not explain differences between compartments.

***Ex vivo* morphogen perturbations indicate regional differences in Bmp sensitivity**

One possible explanation for these findings is that the foregut and hindgut have different sensitivities to the morphogens involved in muscle patterning, thus affecting how muscle differentiates independently of expression levels per se. To see whether downstream activation of Bmp signaling in the foregut is affected by its lower expression of Bmp ligands, we immunostained for phospho-Smad1/5/9 and examined nuclear localization of the signal, which indicates active Bmp signaling. While the midgut and hindgut show clear pathway activation via pSmad staining subadjacent to the endoderm at E5, the foregut shows the lowest pathway activity in this compartment relative to other regions and its own outer layers (Extended Figure 2A). However, the pSmad pattern in the foregut at E4 is quite similar that of other regions at E5, indicating that, even though it expresses *Bmp4* at relatively low levels at this time, the foregut still induces Bmp signaling as expected when it begins to differentiate muscle. This suggested that small amounts of Bmp4 may still be sufficient to suppress muscle because the mesoderm is more sensitive to Bmp. By the same token, we may expect that the observed high levels of Shh in the hindgut do not notably affect radial muscle pattern because the hindgut is less sensitive to Hh pathway activation.

To test whether the foregut and hindgut respond to changes in Hh and Bmp levels in line with differences in sensitivities, we observed muscle patterns in E4 guts cultured for 2 days with exogenous proteins and a pharmacological inhibitor of Hh signaling. First, incubation with

a concentration of the SMO inhibitor cyclopamine that abolishes muscle in the midgut also prevented muscle formation in the foregut (Figure 3). However, muscle was still able to differentiate in the hindgut. Similarly, while the intermediate concentration of Shh that expands muscle in the midgut also expanded muscle in the hindgut, a high concentration that prevents muscle formation via Bmp activation in the midgut fails to do so in the hindgut, and muscle still differentiates (Figure 3). The hindgut therefore appears to be less sensitive to Hh pathway perturbations. Analysis of pSmad patterns in these conditions show that the intermediate concentration of Shh does not appreciably affect Bmp pathway activity, but cyclopamine inhibits it, meaning Hh regulates Bmp in the hindgut as expected (Extended Figure 2B).

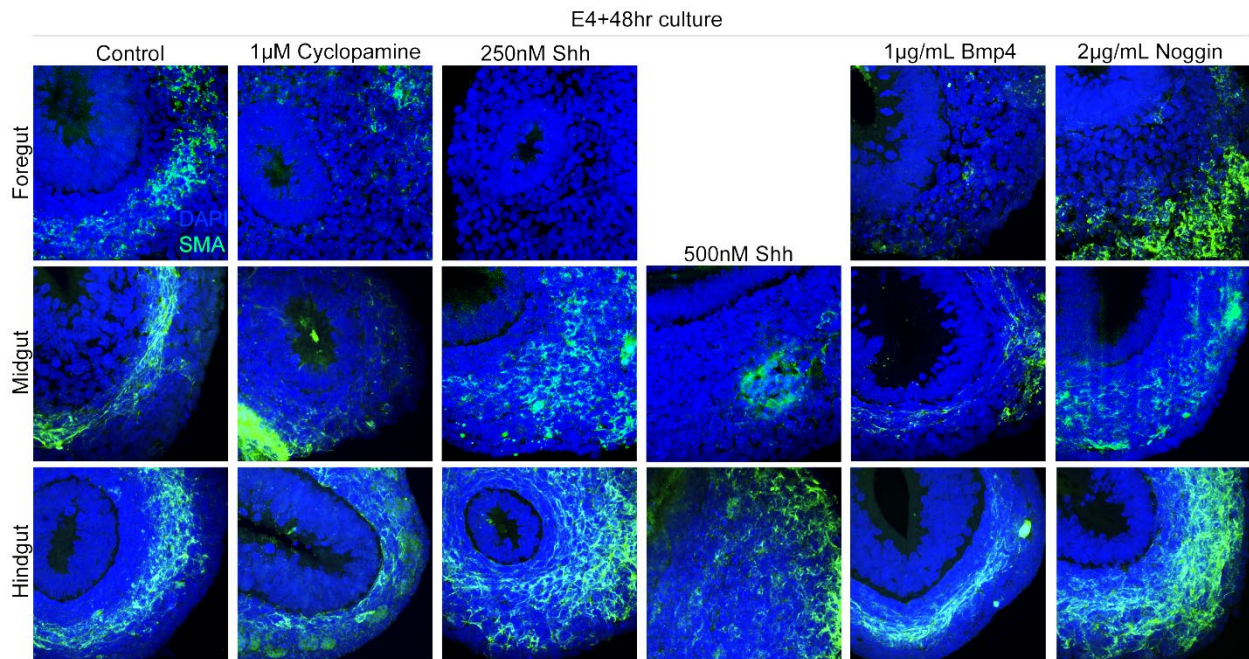


Figure 3. Shh and Bmp explant perturbations in the foregut and hindgut

Effects of explant perturbations performed at E4 for 48 hours on muscle patterning in the foregut, midgut, and hindgut. All images are of transverse sections stained with DAPI and SMA; the endoderm and lumen are roughly in the top right corner in each image.

We instead see the opposite effect in the foregut. The intermediate concentration of Shh is already sufficient to suppress muscle formation—Bmp is highly activated in this

condition, which we expect mediates this effect. In contrast to previous work showing that Shh does not activate Bmp signaling in the foregut-derived gizzard, Bmp activation is lost with cyclopamine treatment, again consistent with Hh regulation of Bmp (Figure 3) (Roberts et al., 1998a).

Next, when explants were treated with a concentration of Bmp4 that only allows for a small amount of muscle differentiation in the midgut, muscle was completely lost in the foregut and pSmad activation was dramatically expanded, consistent with high sensitivity to Bmp4 (Figure 3, Extended Figure 2B). In fact, in an experiment with E5 guts not shown here, even a quarter of the Bmp4 concentration used for the midgut was sufficient to abolish foregut muscle (Huycke, 2018). Once again, the hindgut showed the opposite result—a whole, discrete smooth muscle band was still present after treatment with Bmp4, indicating low sensitivity to Bmp as well. Finally, treatment with Noggin expanded muscle as expected in the hindgut, but still allowed for muscle differentiation a distance away from the endoderm in the foregut, possibly suggesting that the remaining amounts of Bmp ligand even after suppression by Noggin is sufficient to block muscle (Figure 3).

Table 2. Results and model predictions for amount of muscle after explant perturbations

Region	Medium Shh		High Shh		Less Shh (Cyclopamine)		Medium Bmp4		Less Bmp4 (Noggin)	
	Expt	Model	Expt	Model	Expt	Model	Expt	Model	Expt	Model
Foregut	None	Less	None	None	None	Less	None	Same	Same	Same
Midgut	More	More	None	None	Less	Less	Less	Less	More	Same
Hindgut	More	None	Less	None	Less	Less	Less	Same	More	More

Overall, it appears that levels of relevant gene expression alone do not explain differences in foregut and hindgut radial patterns, and that higher sensitivity to Bmp in the foregut and lower sensitivity to both Bmp and Shh in the hindgut may compensate for this discrepancy. As a further test of how well our model predicts gut behaviors, we introduced perturbations *in silico* to mimic explant experiments, and found that most failed to recapitulate observations (Table 2, Reaction-diffusion model of muscle patterning with differential growth). Further exploration of other model parameters is needed to determine the underlying mechanism, as well as gene expression analysis of other pathway regulators that may influence mesodermal sensitivity.

Differential growth is driven by cell division and changes in cell density

While the initial appearance of muscle is likely driven by the interaction of biochemical signals in space at a single time point, the subsequent reshaping of tube dimensions is likely more dependent on tissue growth because 1) muscle cells probably stop differentiating soon after the appearance of a muscle layer and 2) growth occurs on a longer timescale than morphogen patterning, so we would expect that it would have a dominating effect on geometry changes assessed over the course of days. Therefore, to further understand the development of distinct tissue layer widths and tube shapes during early regional morphogenesis, we next assessed differences in growth patterns between the foregut, midgut, and hindgut.

The most obvious source of new mass in the rapidly growing gut is proliferation, so we began by measuring proliferation rates between mesodermal tissue layers at the time when major differences in growth appear, E5. Though we also measured endoderm proliferation

rates, they were not appreciably different from mesenchyme division rates, and were thus ignored for simplicity. To determine division rates, we used an EdU/BrdU pulse labeling method to estimate average cell cycle length in each layer (Figure 4A; see also EdU/BrdU labeling, EdU/BrdU quantification). We first observed that overall division rate is faster in the foregut and slower in the hindgut (but only moderately) (Figure 4B). When we compared mesenchyme to muscle cell cycle lengths, we found that the muscle grows significantly more slowly in the midgut, consistent with previous work and expectations based on inner layer buckling (Huycke et al., 2019; Shyer et al., 2013). Surprisingly, however, mesenchyme and muscle division rates were not different in the foregut and hindgut. To calculate relative division rate (i.e., how much faster the mesenchyme grows than the muscle in each compartment), we divided muscle cell cycle length by mesenchyme cell cycle length for each sample. Resulting values indicate that the mesenchyme grows about 3x faster in the midgut by proliferation, but that there is no differential growth from proliferation in the foregut and hindgut (Figure 4C).

Another possible source of tissue growth is expansion of cell sizes or of intercellular spaces via ECM secretion. Since both of these mechanisms would lead to increased distances between nuclei, we next measured nuclear density in each layer and found that overall density in the mesoderm is lower in the foregut at both E5 and E7, while density is similar between the midgut and hindgut at E5, and slightly higher in the hindgut at E7 (Figure 4D). To assess the contribution of change in density to growth of the mesenchyme over the course of tube growth from E5 to E7, we compared relative density of the mesenchyme (muscle density divided by mesenchyme density) at E5 to E7 in each compartment. By E7, the foregut mesenchyme expands 1.3x more in the mesenchyme than the muscle, indicating that the mesenchyme grows

more than the muscle in the foregut via a differential decrease in cell density (Figure 4E). The midgut and hindgut instead showed a modest increase and decrease, respectively, in relative density.

To understand the differential evolution of tissue layer geometries over time between gut regions, we needed to next properly assess relative growth of the mesenchyme to muscle by considering both cell division and change in density. We therefore derived a formula for volume change ΔV (Calculating contributions of cell density and proliferation to volumetric growth):

$$\Delta V = V(t) \frac{\ln 2}{\tau} \Delta t - V(t) \frac{\Delta C}{C(t)}$$

where $\frac{\ln 2}{\tau} \Delta t$ is change in cell number over time t due to proliferation with cell cycle length τ

and $\frac{\Delta C}{C(t)}$ is the contribution of change in cell density (Figure 4F). To determine relative volume

change between the mesenchyme and muscle, we calculated $\Delta V_{\text{Mes.}} / \Delta V_{\text{Musc.}}$ and found that

differential growth is still highest in the midgut (4.2x), while foregut mesenchyme grows slightly more than muscle (1.3x), and tissue layer growth rates are identical in the hindgut (1.0x) (Figure 4F).

Relative growth of the mesenchyme in each region predicts radial geometries

To determine how these differences in growth rates are expected to affect development of the radial axis over time across compartments, we next added a second phase to our reaction diffusion model. After muscle differentiation according to morphogen patterning, we introduced growth by predicting the change in area ΔA for each layer based on relative growth

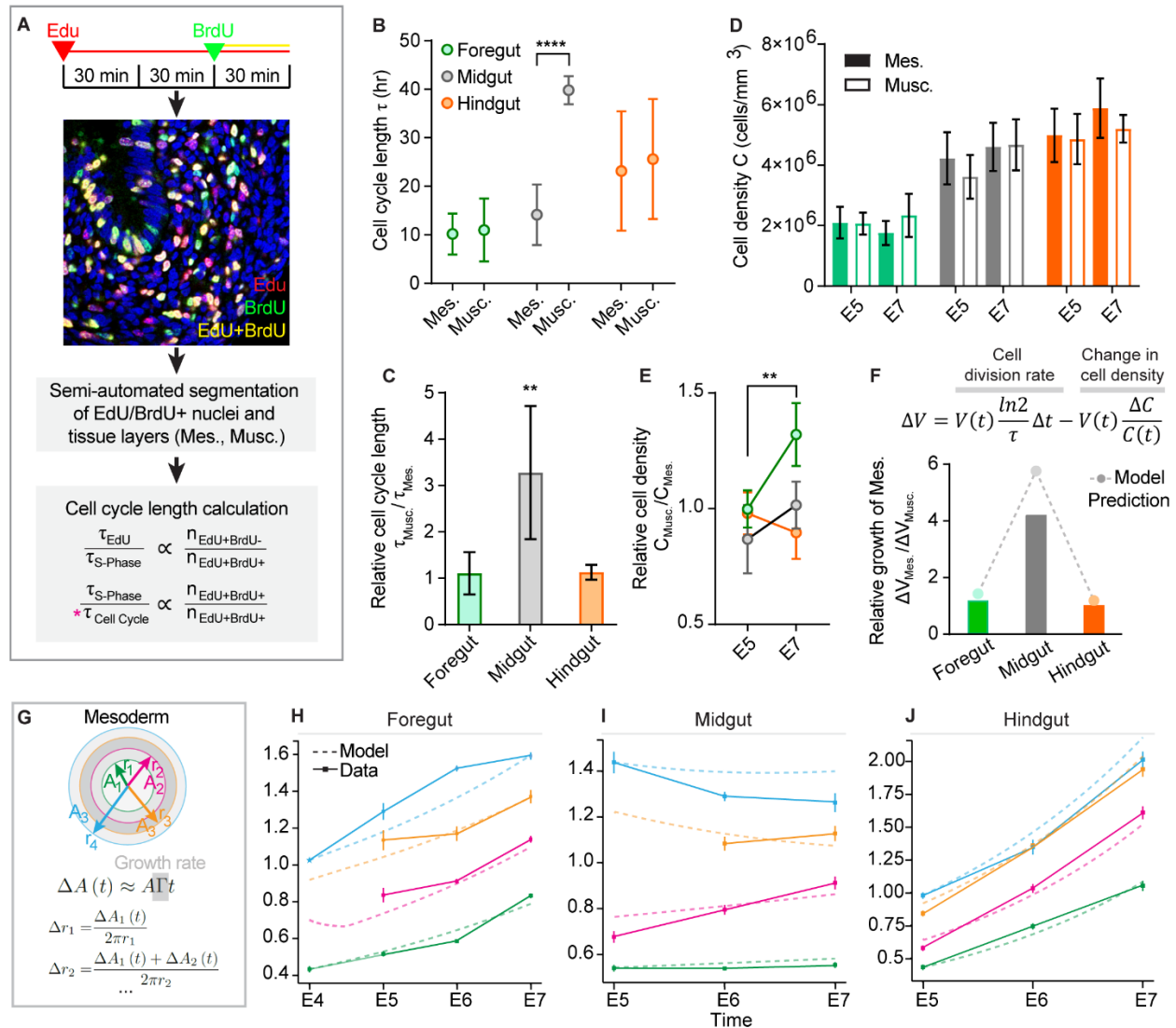


Figure 4. Differential growth via cell division and expansion of intercellular spaces

(A) Illustration of Edu/BrdU pulse labeling method, where an hour-long pulse of Edu is followed by a 30-minute incubation in both Edu and BrdU. After tissue collection and staining, the relative proportions of Edu+ and Edu+/BrdU+ cells are determined using semi-automated image segmentation and analysis and are then used to calculate cell cycle length according to predicated relationships between cell number and time (proportionalities listed at the bottom). (B) Cell cycle length data at E5 across compartments, by tissue layer. Mes. refers to inner mesenchyme between the basement membrane and muscle boundary; Musc. refers to circumferential muscle (****, $p < 0.001$; t-test, $n = 4-5$; error bars, SEM). (C) Expression of the mesenchyme division rate relative to muscle, determined as the ratio of muscle/mesenchyme cell cycle length τ (**, $p < 0.01$; t-test, $n = 4-5$). (D) Cell density as cells/cubic mm, again divided by tissue type, at E5 and E7 in each compartment. $n = 4-5$. (E) Mesenchyme intercellular expansion rate expressed as relative cell density, or muscle/mesenchyme density (**, $p < 0.01$; $n = 4-5$, t-test). (F) Total relative growth of the mesenchyme determined from change in mesenchyme/muscle volume. Bars are calculations from data using the formula shown and dots are predictions from the radial growth model. (G) Schematic defining r_1 - r_4 and corresponding areas A_1 - A_4 , where darker gray is the muscle layer. Formulas indicate method of radius calculation in growth model. (H) r_1 - r_4 radii over time in each compartment (points connected by solid lines) with model predictions overlaid as dotted lines.

rates (Figure 4G, Incorporating growth). Tissue layers were described as shown in Figure 4G, with 4 descriptors of radial growth that evolve with time in the model: r1-r4. R1 is the distance from the center of the lumen to boundary of the mesoderm, r2 is the distance to the inner muscle boundary, r3 is the outer muscle boundary, and r4 is the outer tube boundary.

Mesenchyme and muscle growth rates were manually explored as for morphogen parameters to fit measured values for r1-r4 (Table 3). When we compared model predictions for relative growth rate of the mesenchyme relative to muscle in the foregut, midgut, and hindgut to our $\Delta V_{Mes.} / \Delta V_{Musc.}$ analysis we saw a striking concordance between predicted and measured values (Figure 4F). A low level of differential growth corresponds to a mildly thinning foregut muscle layer (Figure 4H, distance between r2 and r3), while high differential growth leads to extensive muscle thinning in the midgut (Figure 4I). Interestingly, no differential growth between the mesenchyme and muscle in the hindgut predicts its growth well (Figure 4J), while introducing the same relative growth into the model for the foregut, where the mesenchyme grows only slightly faster than the muscle, leads to completely distorted predictions (not shown). Relative growth between tissue layers from intercellular expansion and proliferation therefore predicts distinct growth trajectories along the gut wall.

Table 3. Growth rates for model predicting radial geometry over time

Region	Inner mesenchyme	Muscle	Outer mesenchyme	Extension rate
Foregut	1.28	0.9	1.28	0.88
Midgut	0.57	0.1	0.67	0.50
Hindgut	1.3	1.1	1.2	0.38

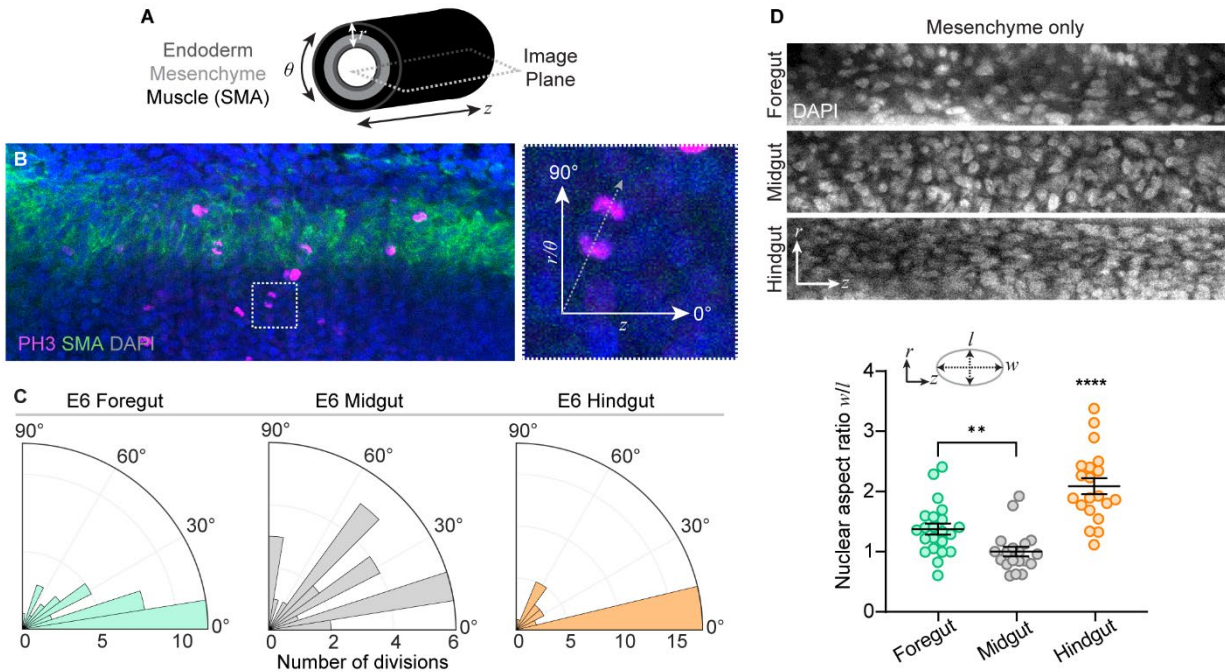


Figure 5. Oriented cells and divisions do not correlate with elongation rates

(A) Schematic showing imaging plane as a dotted line used for division orientation measurements. (B) Example image stained for dividing cells (PH3) and SMA. The horizontal axis is longitudinal (0°) and vertical is collapsed radial and circumferential (90°), as orientations of cells on the circumferential axis are not discernable from images used for measurements. Enlarged inset shows an example division and axes. (C) Polar plots with frequencies of division orientations within the mesenchyme layer only in each compartment at E6. (D) DAPI images of the mesenchyme only from the same images plane shown in A. Single slices are on the radial and longitudinal axes as indicated. Nuclear aspect ratios measured from images like those above, according to the schematic shown, in each region at E6 (****, $p < 0.001$; **, $p < 0.01$; t-test, $n=20$ from 2 biological replicates each).

Oriented mesenchymal cell divisions do not explain differential tube elongation

Importantly, convergent extension was introduced into our model to account for growth that is partitioned axially—area change was adjusted uniformly according to measured length data in Figure 1E (Table 3, Convergent extension). We therefore next want to understand the mechanism behind differential elongation along the gut.

Though we refer to lengthening in our model as convergent extension, it is unclear whether differences in elongation come from oriented cell behaviors in the form of movement along the AP axis, or from oriented cell divisions, both of which are known to contribute to

tissue extension (Keller, 2006). To assess the latter, we imaged whole mount guts from each region stained with PH3 at E6, and measured division orientations in the mesenchyme only (Figure 5A-B). This stage is immediately after muscle differentiation, when we see major differences in elongation rates appear (Figure 1E)—if division orientation is driving differential lengthening between compartments, we may expect to see longitudinally aligned divisions in the foregut and midgut, but not the hindgut. Instead, we found that divisions are the most longitudinally oriented in the hindgut, which lengthens considerably less during this stage (Figure 5C). According to Hertwig’s rule, a cell will divide along its long axis, so we also measured mesenchymal cell aspect ratios in these images, where axially elongated cells are wider and have larger ratios (Scepanovic & Fernandez-Gonzalez, 2018). As a further confirmation of our division angle results, we found that cells are more elongated on the longitudinal axis in the foregut and hindgut, with the strongest difference once again in the hindgut (Figure 5D).

Oriented divisions therefore do not appear to coordinate differential mesenchymal elongation along the gut, so it is possible that oriented collective movements like convergent extension are indeed the main determinants of gut lengthening. Future work using cell lineage tracing and live imaging will be instrumental in uncovering mechanisms of axial growth in the foregut, midgut, and hindgut.

Conclusions

Several studies have reported the importance of Shh and Bmp signaling in patterning small intestinal smooth muscle. However, reported differences in the activation of these

pathways along the AP axis have made translating principles from the midgut directly into the other gut regions, which develop the same muscle layers in a similar concentric pattern, more difficult. Furthermore, it is unclear how radial and axial growth are coordinated to specify the correct tube dimensions along the gut.

Our results indicate that gut regions do indeed show unique muscle differentiation patterns, but regional differences in Shh and Bmp gene expression levels alone cannot explain them. However, differences in sensitivity to morphogen signaling likely affect how those signals are processed into radial patterns—the foregut is more sensitive to Bmp inhibition of muscle, and the hindgut is less sensitive to Hh and Bmp. For subsequent growth and refinement of tube dimensions, substantial differential growth from proliferation between the mesenchyme and muscle determines the temporal evolution of midgut radial growth (namely, thinning of the muscle compartment and thickening of the mesenchyme). By contrast, only mild differential growth in the foregut from decreasing mesenchymal cell density explains its radial growth, while the hindgut grows isotropically.

Finally, while it is still unclear why gut regions elongate to different extents, it is unlikely that positional variation in oriented cell divisions is the driving force. The next possible candidate is therefore positional differences in cell movements such as convergence and extension (Stooke-Vaughan & Campàs, 2018). Such behaviors could result from directional cues that promote different degrees of longitudinal cell migration across compartments—indeed, as discussed above, canonical Wnt signals often involved in convergent extension are important for small intestinal elongation (Cervantes et al., 2009; S. Wang et al., 2018). Regional mechanics

may also affect collective cell movements, as discussed further in Changes in growth and material properties from the foregut to hindgut.

Direct experiments in the next two chapters demonstrate that geometry is a crucial determinant of gut morphogenesis. Our results from this chapter indicate that the influences of both growth and morphogen patterning are combined in unique ways along the early gut to initiate regional specialization of tube dimensions.

Chapter 2: Divergent epithelial bucking across gut regions

Attributions

Hasreet K. Gill devised the project with Tyler R. Huycke, optimized mechanical measurement methods, planned, designed, and performed experiments, wrote codes for and performed all mechanical data analysis. Sifan Yin made and performed simulations for Figures 11-12 and wrote accompanying text, as well as performed simulations and developed all theoretical and numerical method codes/formulations for modeling 2D single- and multi-scale buckling instabilities. Nandan L. Nerurkar developed mechanical measurement methods and assisted with mechanical data analysis. Tyler R. Huycke optimized mechanical measurement methods and designed and performed pilot experiments. John C. Lawlor collected images of foregut development. L. Mahadevan and Clifford J. Tabin supervised the project.

Background

Residual stresses from mismatched strains between growing materials drive the formation of diverse shapes in a variety of natural contexts (Geisel et al., 2022; Nelson, 2016; Trejo et al., 2013; L. Wang et al., 2011). For example, both experimental and theoretical studies have implicated differential growth-induced buckling instabilities in developmental events like the appearance of sulci and gyri in the brain (Tallinen et al., 2014), formation of the chick brain and heart (Garcia et al., 2019; Taber, 2006), tooth germ wrinkling (Takigawa-Imamura et al., 2015) and branching of the lung (Varner et al., 2015; Varner & Nelson, 2014).

In the chick midgut, differential growth is responsible for gut looping, intestinal rotation, and lumen folding (Kurpios et al., 2008; Nerurkar et al., 2017; Savin et al., 2011; Shyer et al., 2013; Sivakumar et al., 2018). As mentioned above, correct shaping of the epithelial surface is critical for intestinal function, and different regions along the gut develop unique morphologies. However, how lumen morphology is tuned along the gut is not understood. In the following chapter, we aimed to understand the mechanical mechanism that leads to diverse buckling patterns along different regions of the chick gut.

Similar morphologies to the fore- and hindguts have been described using material and mathematical models--for example, period-double folds like those of the foregut have been shown to appear in thin, stiff films growing on much softer substrates (high modulus ratio), while creases form in thick materials growing in the context of a low modulus ratio (Budday et al., 2015; Tallinen & Biggins, 2015; Q. Wang & Zhao, 2015). We therefore reasoned that the variation in mucosal shape along the chick gut may be explained by regionally defined physical properties, which, in turn, lead to unique folding modes during constrained growth.

Results

Unique epithelial shapes along the gut anteroposterior axis

To begin understanding how morphologies along the developing gut diverge, we first carefully characterized circumferential and axial buckling in each compartment over time using transverse and sagittal tissue sections. Consistent with previous work and longstanding observations of chick gut development, the midgut lumen first forms circumferential wrinkles, which progressively decrease in wavelength before buckling orthogonally into zigzag folds at

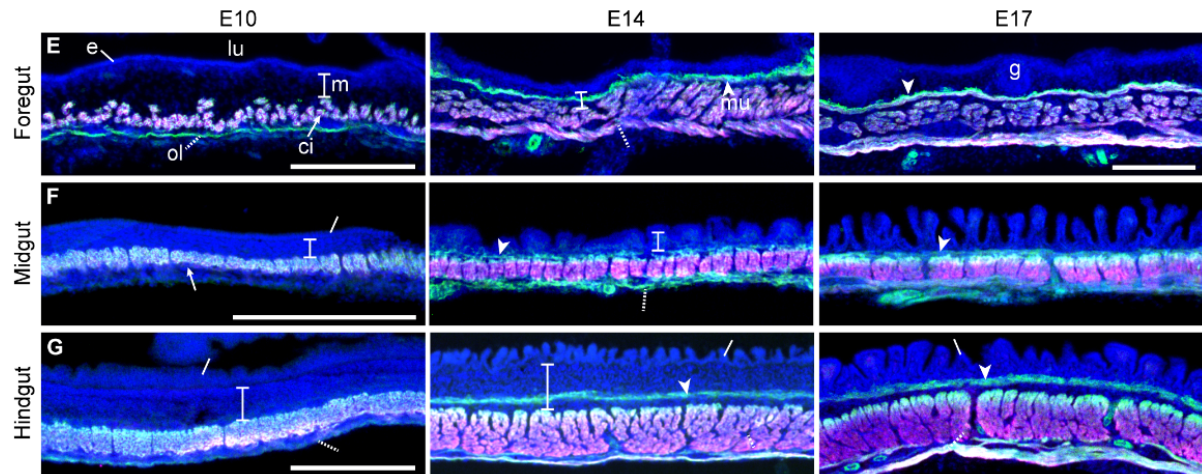
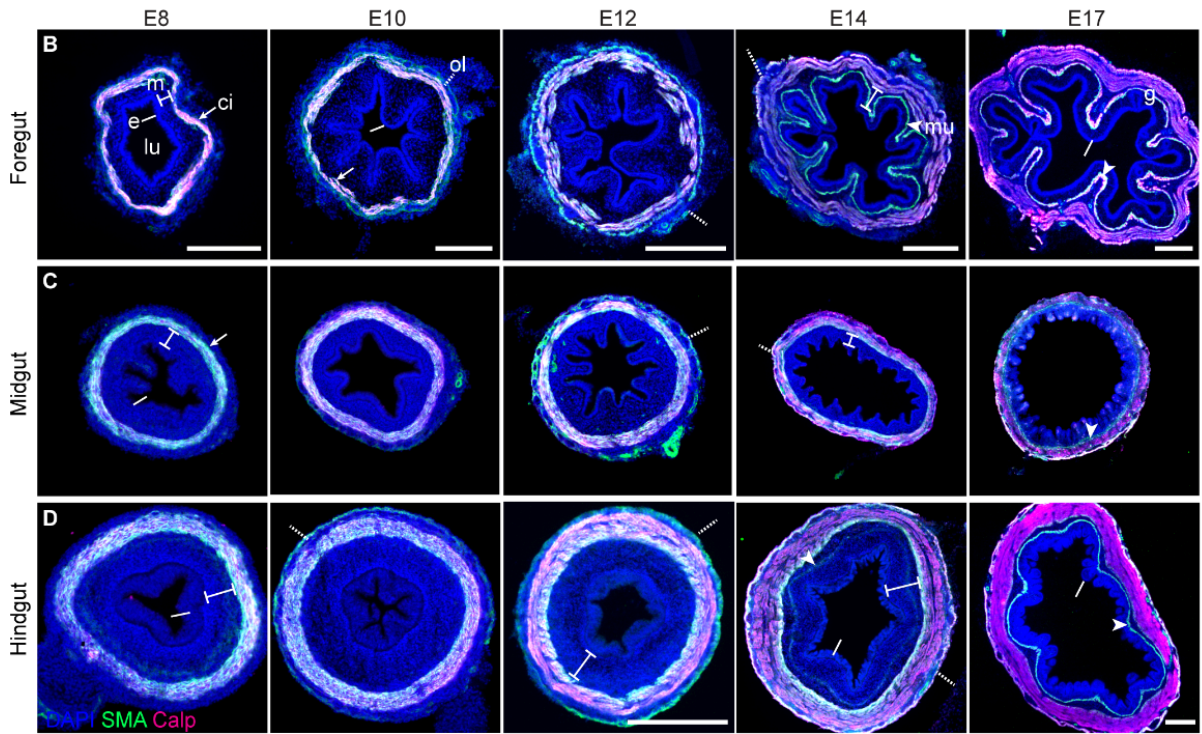
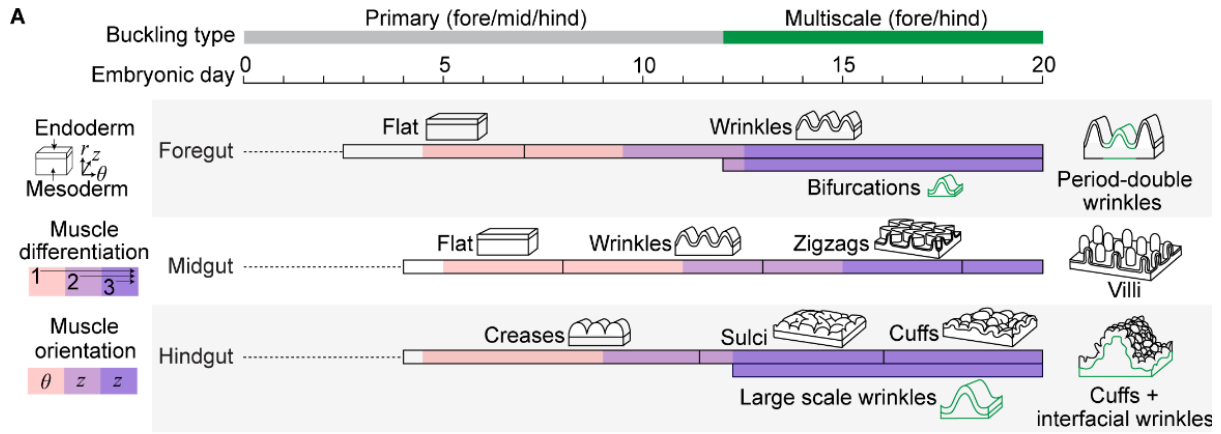
day 14 of development (E14) (Figure 6A, C, F; Extended Figure 4A) (Coulombre & Coulombre, 1958). Zigzags are further compressed and undergo local rotations that pattern the positions of villi (Shyer et al., 2013).

Early morphogenesis of the foregut is like that of the midgut—modest circumferential wrinkles appear in the endoderm-mesenchyme composite around day 8 of development (E8); these progress into laterally self-contacting folds by E10 and wrinkles broader and fewer in number than those of the midgut by E12 (Figure 6A-B; Extended Figure 4A-C). Subsequent elaboration of midgut wrinkles by E17 contrasts with the relatively steady number of consistently wider wrinkles in the foregut (Extended Figure 4B). The pattern wavelengths of the foregut and midgut are initially similar, but as the midgut develops zigzags and protovilli from E14 onward, the foregut progressively expands circumferentially, resulting in significantly greater distances between wrinkle peaks (Extended Figure 4D). Indeed, the most striking distinction from the midgut that we see in the foregut is the persistence of circumferential wrinkles without an additional form of axial buckling (Figure 6A, E; Extended Figure 4A).

While the midgut and foregut form smooth wrinkles comprising both the endoderm and mesenchyme layers, the hindgut forms superficial creases only on the surface of the endoderm, which we quantify as the relative lengths of apical and basal sides of the epithelium (Extended Figure 5A). The relative increase in apical length of the hindgut endoderm at E14 corresponds to the growth and maturation of its creasing pattern; meanwhile, decreasing ratios from the midgut to foregut reflect progressively smoother folding of the endoderm and mesenchyme together (Extended Figure 5B).

Figure 6. Regional gut epithelia develop distinct folding patterns.

(A) Timeline of lumen morphogenesis for each region (Foregut, Midgut, Hindgut). From day 0, dashed lines indicate the periods prior to tubulogenesis. Subsequent boxes correspond to folding states, with accompanying cartoons illustrating 3D patterns of the endoderm-mesenchyme composite (axes are indicated on the left schematic). Colored regions overlaid with morphologies highlight muscle layers present, where pink is just the circumferential muscle, light purple is both the circumferential and outer longitudinal layers, and dark purple is all three layers. Periods of primary folding in all regions and multiscale folding just in the fore- and hindguts are indicated by gray and green boxes on the timeline, and multiscale components of folding pattern cartoons are colored in green. (B-G) Transverse (B-D) and sagittal (E-G) sections immunostained for nuclei (DAPI), early smooth muscle (SMA), and late smooth muscle (calponin) across time for each region (m and brackets, mesenchyme; e and line, endoderm; lu, lumen; ci and arrow, circumferential muscle; ol and dashed line, outer longitudinal layer; mu and arrowhead, muscularis mucosa; g, secretory gland). Scale bar, 200 μ m.



Creases are initially circumferential but eventually form branched sulci between E12 and E14, still just on the surface of the endoderm (Figure 6D, G; Figure 14A). Creased sulci then gradually give way to smooth wrinkling of the endoderm-mesenchyme composite to form cuffs by E17, which are superficially similar in appearance to villi, but distinct in their geometry and topological arrangement on the lumen surface (Figure 6D, G; Figure 14A). Notably, though the hindgut does form intermediate morphologies—circumferential creases and sulci—they do not appear to pre-figure subsequent patterns as in the midgut, where each ridge buckles into a zigzag, and zigzag “arms” specify the locations of villi (Shyer et al., 2013). Thus, though the midgut, hindgut and foregut share some aspects of lumen morphogenesis (orientation of initial folds and timing of folding transitions), they ultimately adopt distinct trajectories to achieve region-specific epithelial structures (Figure 6A).

Foregut and hindgut lumens develop multiscale buckling patterns

In addition to primary differences in lumen architecture, the foregut and hindgut also develop and maintain two-dimensional hierarchical folding behaviors that are ultimately absent in the midgut, where symmetric and uniform villi tile a flat cylindrical surface (Figure 6A, C). In the foregut, following the initial appearance of a symmetrical buckling pattern at E10, some folds spontaneously form bifurcations at their bases, which are maintained and scale with tube growth as it continues to expand from E12 onward (Figure 6B). As a result, foregut wrinkles ultimately display a period-doubling phenomenon, where large and small amplitude waves alternate. Though these folds also appear transiently during early stages of midgut ridge formation and growth, they are eventually lost when the lumen buckles into zigzags.

In the hindgut, we see a distinct and intriguing phenomenon where, coincident with the formation of sulci, broad, radially symmetric circumferential buckles appear at the endoderm-mesenchyme interface (Figure 6D; Figure 14D). While these initially resemble self-contacting folds, they grow to form wrinkles that increase in number with radial growth and are even maintained when surface creases are replaced with smoothly wrinkled/folded cuffs (Figure 6D; Figure 14E). Differences between compartmental forms therefore extend to post-buckling events that contribute to morphological specialization of the hindgut and foregut.

Differences in smooth muscle constraints do not explain morphological differences

Given that stepwise lumen wrinkling in the midgut depends on sequential differentiation of orthogonal muscle layers, we began by asking whether differences in muscle constraints explain deviations from the midgut buckling program elsewhere in the gut. We therefore observed smooth muscle stained with early (Smooth Muscle Actin, SMA) and late (calponin 1) markers in our foregut, midgut, and hindgut sections, as well as muscle orientations using stained whole-mount samples (Figure 6B-G; Figure 7A). We first found that all regions formed three muscle layers in succession, though each layer differentiated slightly earlier in the foregut and hindgut (Figure 6A-D). Focusing on properties of the first circumferential and second longitudinal layers, which drive the critical ridge and zigzag buckling events in the midgut, we concluded that layer orientations, placements, and maturation timelines are essentially identical between regions (Figure 6B-G; Figure 7A-B).

It was not until we considered the third muscle layer, the muscularis mucosa, that we saw differences in muscle properties between regions. While it lies flat and closely adjacent to

the circumferential muscle in the midgut, this layer differentiates deep within all wrinkles in the foregut, and large-scale wrinkles in the hindgut, and therefore achieves a buckled shape (Figure 6D; Figure 14D). Actin fibers within this layer are still clearly oriented along the longitudinal axis in the foregut and hindgut, but some intermixed fibers with random orientations are also present (Figure 7A-B). However, though these differences in the muscularis mucosa may be relevant to later properties of mucosal folds, they arise after the lumens adopt distinctive features (Figure 6A). Therefore, variation in smooth muscle properties along the gut is likely not driving the early (E8-E12) steps of lumen buckling diversification.

Width ratio increases and radius ratio decreases from the foregut to hindgut

If not properties of the muscle constraints themselves, we next considered whether variations in relative geometric and mechanical features of the deforming layers cause regions to assume unique configurations as they alleviate residual stress. To measure radial growth, we used transverse sections to measure endoderm and mesenchyme widths, as well as inner and outer tube radii, and compared between regions (Figure 8A).

Focusing once again on the time frame with wrinkling patterns diverge, from E18-E12, we first observed that the endoderm thins and the mesenchyme thickens in all three regions, resulting in decreasing width ratios over time (Figure 8B, Extended Figure 6A). In the hindgut, radius are consistently larger in the foregut (Figure 8C, Extended Figure 6B). By contrast, the lumen remains small in the hindgut and the outer radius is as large as that of the foregut. In other words, radial growth comes from expansion of the lumen in the foregut and thickening of

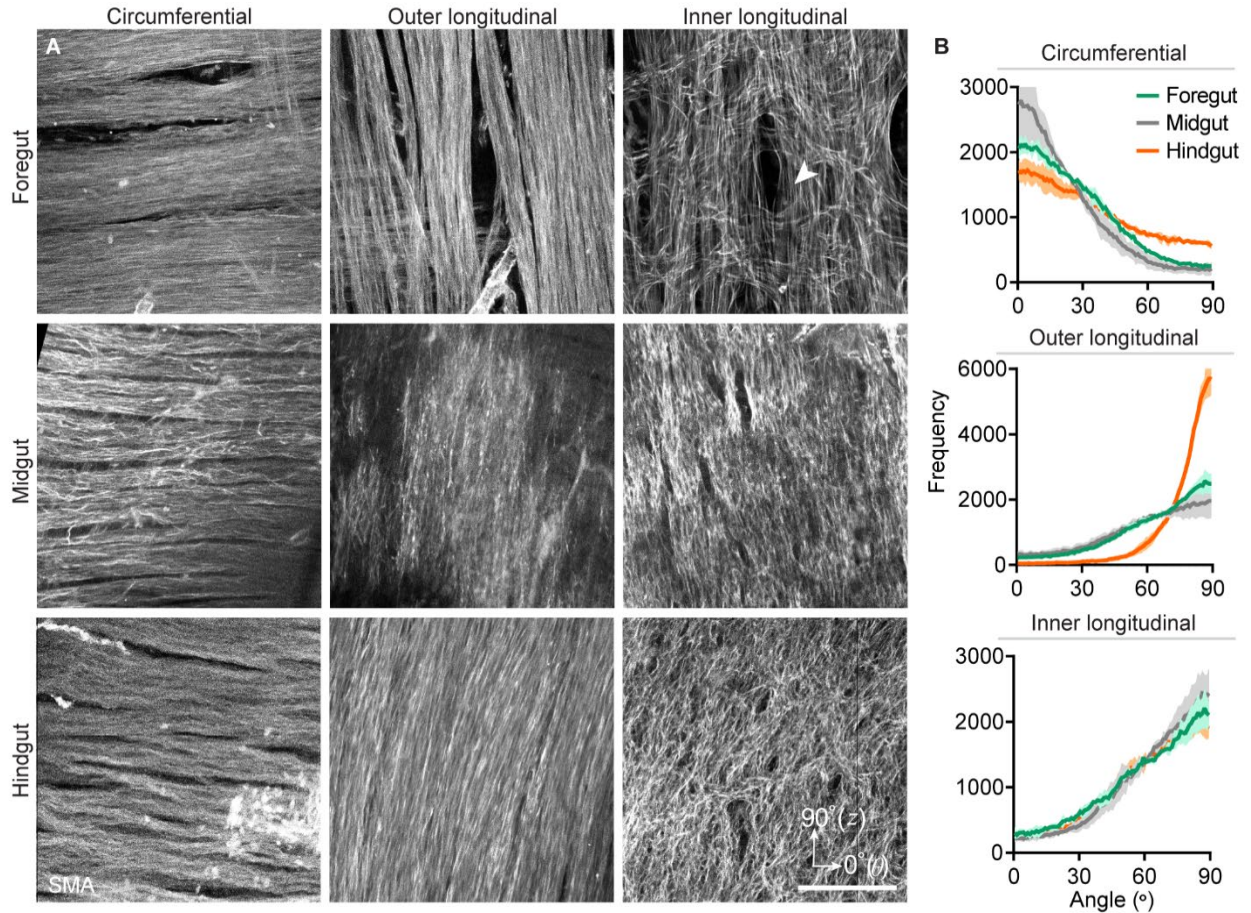


Figure 7. Muscle layer orientations are consistent along the gut.

(A) Whole mount images of muscle fibers stained with SMA at E17 in the foregut, midgut, and hindgut. Each column corresponds to a layer, in order of differentiation in the embryo. Scale bar, 100 μm. (B) Smooth muscle fiber alignment frequencies, where 0° is circumferential and 90° is longitudinal. n=3 images.

the mesenchyme is initially thicker and increases at the same pace as the midgut (Extended Figure 6A). Yet, a substantially thicker endoderm results in a higher width ratio than the midgut and foregut across stages (Figure 8B). By contrast, in the foregut, drastic mesenchymal thickening occurs between E8 and E12, effectively decreasing the relative width of the endoderm (Figure 8B).

For tube radii, the midgut and foregut show proportional increases in inner and outer radii, which maintains a steady radius ratio, but both the inner radius (lumen size) and outer

the tube wall in the hindgut. Notably, the hindgut sees a drop in endoderm width and concomitant increase in inner radius at E12, which lowers the width ratio and increases the radius ratio, when biaxial sulci appear (Figure 8B-C, Extended Figure 6A-B). Together, these simple measurements capture clear differences in radial growth between regions, which we expected reflect and influence how the tissues respond to mechanical constraint.

The inner modulus ratio decreases positionally from the foregut to hindgut

Differences in relative stiffness affect how force is translated into deformation in a material, so to further understand variations in endodermal buckling along the gut, we determined its stiffness relative to that of its substrate, the mesenchyme, in each region. To measure Young's modulus, we used fine dissections to carefully separate the endoderm and endoderm-mesenchyme composite from the outer muscle layer, and then applied a custom uniaxial tensile testing system to stretch the tissue and measure its deformation in response to force (Figure 8D-E) (Modulus measurements). While pinned in agarose, each gut tissue ring was stretched using a cantilever looped through the lumen (Figure 8D)—from the change in distance between Dil dots applied to the tissue and the deflection of the lever, respectively, we generated stress-strain curves, from which we calculated Young's modulus in the small strains regime (Figure 8E). While endoderm modulus was measured directly, modulus of the mesenchyme (a loose collection of cells suspended in extracellular matrix) needed to be calculated from the composite and endoderm moduli and thicknesses (Extended Figure 6C).

Our measurements at E10 revealed an interesting trend in endoderm and mesenchyme moduli along the rostrocaudal axis. The endoderm is stiffest in the foregut and softest in the

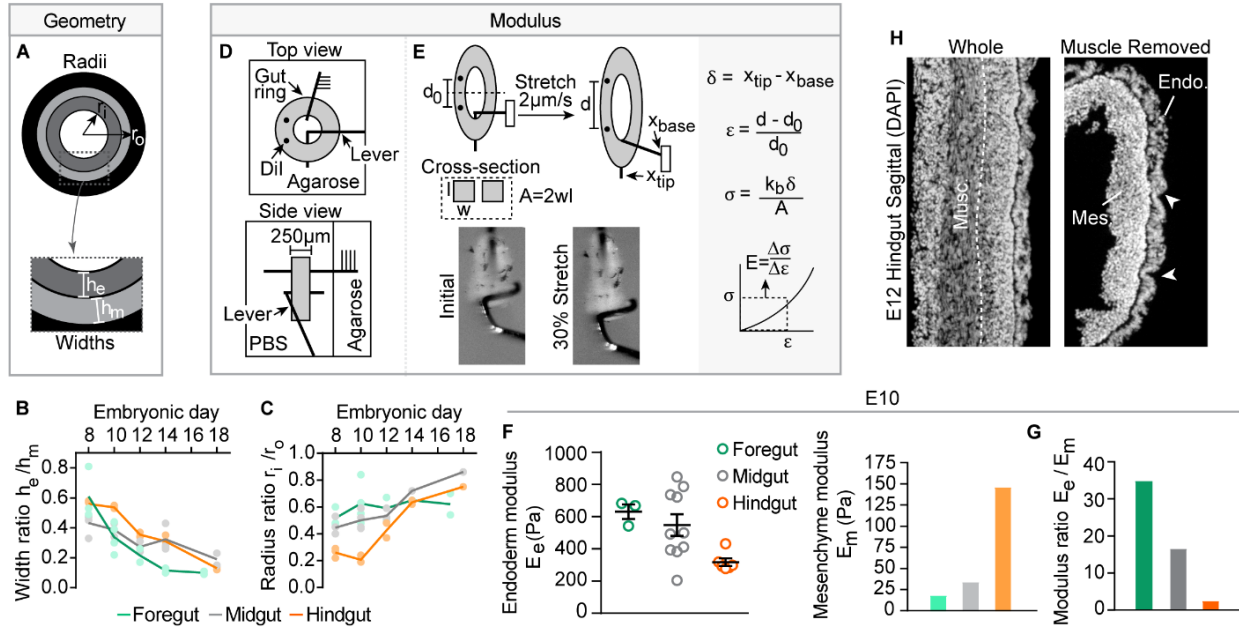


Figure 8. Spatiotemporal evolution of gut inner tissue mechanical properties.

(A) Schematic illustration of radial geometric measurements collected from transverse sections, with tissue layers indicated by color. (B, C) Ratios of inner layer widths (C) and inner to outer radii (E) for each region over time. $n=3$ biological replicates per time point. (D, E) Method of modulus ratio measurement using uniaxial tensile testing. (D) Top and side views of testing set up prior to application of stretch, and (E) measurements during the stretch test at the test start (initial distance between dots d_0 , cross-sectional area, A) and at each time step (current distance between dots, d , position of the lever tip, x_{tip} , position of the lever base, x_{base}). Initial and +30% stretch images from a tensile test show the tissue ring with Dil dots, tungsten pin, and cantilever. Young's modulus, E , is determined from the slope of the strain, ϵ vs. stress, σ curve in the low strains regime (dotted box). (F) Endoderm modulus values at E10, $n=3-10$ measurements, and mesenchyme modulus determined from average endoderm and composite width and modulus values. (G) Ratios of endoderm to mesenchyme modulus. (H) Sagittal, DAPI-stained sections of a whole E12 hindgut, and one with the circumferential and outer longitudinal muscle layers surgically removed. Arrowheads indicate creases on endoderm surface. Dotted line and Musc., muscle boundary; Endo., endoderm; Mes., mesoderm.

hindgut, while the composite modulus and, in turn, mesenchyme modulus is softest in the foregut and stiffest in the hindgut (Figure 8F, Extended Figure 6D, F). The endoderm-to-mesenchyme modulus ratio, therefore, decreases from 35 to 2 from the foregut to hindgut (Figure 8G). Furthermore, previous work on lumen morphogenesis in the midgut assumed the muscle layer to be orders of magnitude stiffer than inner deforming layers, and thus a fixed boundary. However, we found that smooth muscle modulus is similar to that of the endoderm in the foregut and is substantially stiffer than inner layers in the hindgut (Extended Figure 6E).

Consistent with this observation, only smooth muscle in the foregut forms wrinkles at these stages, suggesting that it is more deformable anteriorly (Figure 6B). The increased radial expansion of the foregut may also relate to its softer muscle layer, though this remains to be tested.

In summary, in the foregut, the lumen and outer boundary of the tube expand relatively steeply over time as a stiff endoderm layer grows against a soft mesenchyme and only mildly stiffer muscle layer; thickening of the mesenchyme progressively lowers the relative contribution of the endoderm to composite thickness. In the midgut, the endoderm is still stiffer than the mesenchyme, but layer thicknesses essentially remain constant as the lumen expands modestly. Finally, all tissues are thicker initially in the hindgut, where a uniformly stiff composite thickens the tube wall by growing against a stiffer muscle constraint without expansion of the lumen until E12. Together, these results capture monotonic trends in material properties, relative radii and relative tissue widths along the gut long axis (Extended Figure 6F).

Major ECM components vary in abundance and alignment between regions

To investigate a possible biological basis for differential stiffness along the gut, we performed immunostaining for extracellular matrix components commonly found in the gut—Laminin 1, Elastin, and Collagen (Pompili et al., 2021). While collagen and laminin are typical matrix-stiffening components, the effect of elastin is more variable depending on its macromolecular organization in the extracellular space—it generally allows tissues to accommodate stretch without rupture (Chow et al., 2014; Godwin et al., 2019; He et al., 2013).

Laminin primarily localizes to epithelial basement membranes; accordingly, we first observed strong Lam staining on the basal side of the endoderm in all regions at both E8 and E10 (Extended Figure 8A). However, in the hindgut but less so in the foregut and midgut, we also saw an extension of Lam staining into the mesenchyme, especially at E10. Furthermore, Lam staining and basement membrane qualitatively appears thicker in the foregut, though this must be verified with quantitative measurements. Given that laminin typically stiffens biological materials, these observations suggest that it may be involved in conferring rigidity to the foregut endoderm and hindgut mesenchyme.

Next, elastin is found in all regions at E10 as well, though it appears more abundant throughout the foregut mesodermal wall, including in the muscle (Extended Figure 8C). This muscular localization is even more pronounced at E12, where—unlike in the midgut and hindgut—elastin fibers align with smooth muscle actin fibers (Extended Figure 8B-D). Curiously, elastin in the hindgut, including fibers found within muscle, align radially instead. Finally, collagen is present in the hindgut and foregut at E12, though it appears more uniform and abundant in the hindgut mesenchyme (Extended Figure 8C, D). It is possible, therefore, that collagen and laminin contribute to the increased stiffness of the hindgut mesenchyme, while elastin promotes the extensibility of the mesenchyme and muscle reflected in our modulus measurements. Perturbation experiments will be needed to test these claims.

Development of a computational model to capture buckled morphologies

Our measurements provide a thorough overview of the spatiotemporal mechanical and geometric parameters that are likely regulated by regional genetic identity, but is this

information sufficient to determine the distinct morphologies along the gut? The observed time-dependent evolution of width and radius ratios would suggest a differential growth-induced mechanical instability as the basis for folding, wrinkling, and creasing on compartmental epithelial surfaces. To quantify this, we modeled the gut computationally as a growing two-layer tube composed of endoderm and mesenchyme layers, which are constrained by the outermost muscular layer, as shown in Figure 9A.

In past decades, many studies have implemented a continuum-level differential growth model to explain surface patterns like longitudinal ridges and folds in the esophagus (Balbi et al., 2015), zigzags and villi in the chick midgut (Shyer et al., 2013) and creasing of the brain cortex (Tallinen et al., 2014, 2016). However, aside from the study of chick midgut morphogenesis, these theoretical and numerical works assume mechanical properties and geometries to generate phase diagrams capturing the observed morphological landscape, which are not always consistent with the true developmental processes. Only a handful of studies have begun to incorporate data measured from the developing embryo into mechanical models, such as the investigation of epithelial folding of the *Drosophila* wing disc (Tozluoğlu et al., 2019).

Here, based on physical measurements over time, we have a clear picture of the spatiotemporal anisotropic growth tensor, as well as mechanical properties and geometries. Because different morphologies along the gut initially diverge on the radial and circumferential axes only, we simplified our treatment to the cross-section of a bilayered tube and consider a plain-strain 2D model (Figure 9A). Also, because buckling of the midgut lumen has received considerable attention, we only focus on the foregut and hindgut (Balbi & Ciarletta, 2013;

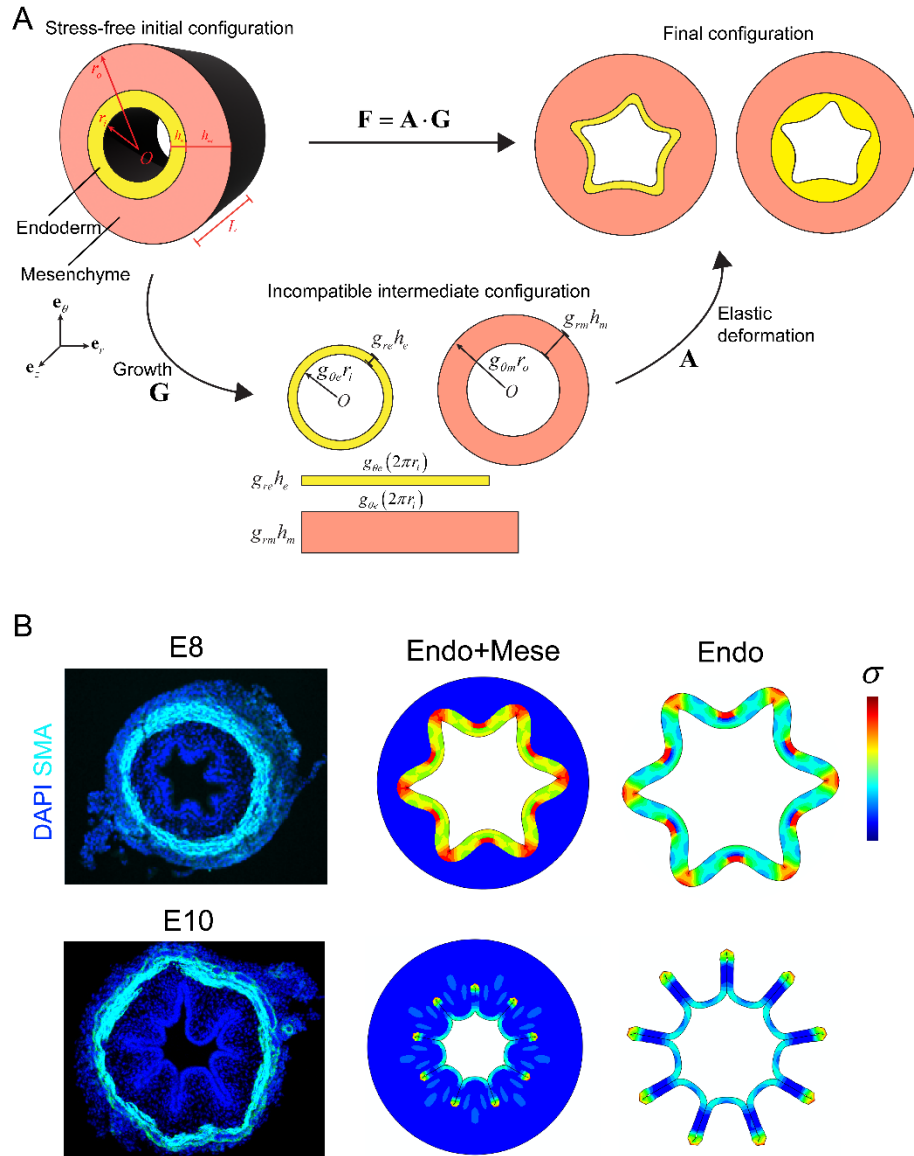


Figure 9. Numerical model of cylindrical bilayer morphogenesis.

(A) Schematic of numerical model and the steps of multiplicative decomposition of the deformation gradient \mathbf{F} to simulate gut lumen buckling. (B) Primary wrinkling (E8, upper row) and folding (E10, lower row) of the foregut in early stages. Initial geometry at E8 is $r_i/r_o = 0.6$, $h_e/h_m = 0.3$, and the endoderm grows isotropically. Initial geometry at E10 is $r_i/r_o = 0.65$, $h_e/h_m = 0.2$, and the endoderm thins over the course of the simulation.

Hannezo et al., 2011). Consistent with established morphoelastic theory, the deformation gradient is multiplicatively decomposed to an elastic part and a growth part as $\mathbf{F} = \mathbf{A} \cdot \mathbf{G}$ (Rodriguez et al., 1994). The elastic tissue is modeled as neo-Hookean material with a

volumetric strain energy density $W_A = \frac{\mu}{2} \left[J_A^{-\frac{2}{3}} \text{Tr}(\mathbf{A} \cdot \mathbf{A}^T) - 3 \right] + \frac{K}{2} (J - 1)^2$ where $J_A = \det \mathbf{A}$,

μ is the elastic shear modulus and the bulk modulus $K = 10^3 \mu$ makes the tissues almost incompressible (Tallinen et al., 2013). The growth tensor $\mathbf{G} = \text{diag}(g_r, g_\theta, g_z)$ captures anisotropic growth for both the endoderm and mesenchyme. For our 2D model, longitudinal growth is assumed to be $g_z = 1$, and the radial and azimuthal growth factors are estimated as $g_r = \bar{h}_\alpha / \bar{h}_{\alpha 0}$ and $g_\theta = \bar{r}_\alpha / \bar{r}_{\alpha 0}$, where $\alpha = 'e'$ and $'m'$ represent endoderm and mesenchyme, respectively; the subscript '0' represents quantities at the initial configuration (Figure 9A). The width and radius are rescaled by the radius of muscle layer as $\bar{h}_\alpha = h_\alpha / r_o$ and $\bar{r}_\alpha = r_\alpha / r_o$.

Relative endodermal thinning drives primary and secondary wrinkling in the foregut

As mentioned above, our observations reveal distinct growth principles for the foregut and hindgut compared to the midgut. From E8 to E12 in the foregut, the endoderm thins modestly while circumferential expansion smoothly increases. Since it is not possible to deduce stress-free states and we only know the current states, we postulate that the initial geometry of E(n) is E(n - 2). For instance, we use the stress-released geometry of E8 as the initial state for E10 (Figure 9A). After E12, though the endoderm does not appreciably change in its absolute width, continued radial expansion lowers the relative thickness of the endoderm further (Figure 8B, Extended Figure 6A).

Implementing our model with the initial geometric and stiffness parameters of the E8 foregut and isotropic growth—equal growth on the radial and circumferential axes—revealed a smooth wrinkling pattern in the endoderm consistent with primary buckling (Figure 6A, Figure

9B), which has been characterized mathematically in the context of midgut morphogenesis (Shyer et al., 2013). However, self-contacting folds of the E10 foregut could not be explained by isotropic growth. We therefore designed and tested two additional growth profiles: (2) endoderm thinning with or without mesenchyme thickening, and (3) endoderm thickening (growth profiles are listed in 2D foregut and hindgut epithelial folding).

Only when the observed feature of endodermal thinning relative to the expansion of tube radius was introduced were we able to recapitulate the surface buckling of foregut at E10 (Figure 9B, Figure 8B; Extended Figure 6A). This folding pattern begins with smooth sinusoidal wrinkles—with radial compression of the mesenchyme, the peaks and valleys of the wrinkles widen and flatten. Eventually, the valleys are compressed until adjacent folds contact one another, forming a symmetry-breaking folding pattern.

From E14 to E17, a novel period-doubling pattern that has not been reported before emerges in the foregut lumen. To systematically investigate the mechanical and geometric drivers behind the emergence and stabilization of the final period-doubling pattern, we first set the initial geometries and modulus ratio as measured (Table 5) and again performed simulations with endoderm isotropic growth, thinning, and thickening. Figure 10A shows three distinct post-buckling patterns due to isotropic and anisotropic growth profiles. We first see that primary buckling into sinusoidal wrinkles is similar between the three models. However, progressive thickening of the endoderm (g_r) relative to mesenchyme radius (g_θ) can sustain symmetric wrinkles (type III) and leads to a folding pattern where the peaks and valleys have almost the same widths (Figure 10A, blue curve). Endoderm isotropic growth, by contrast, can partially inhibit the tendency for neighboring folds to merge, and forms rough period-doubles

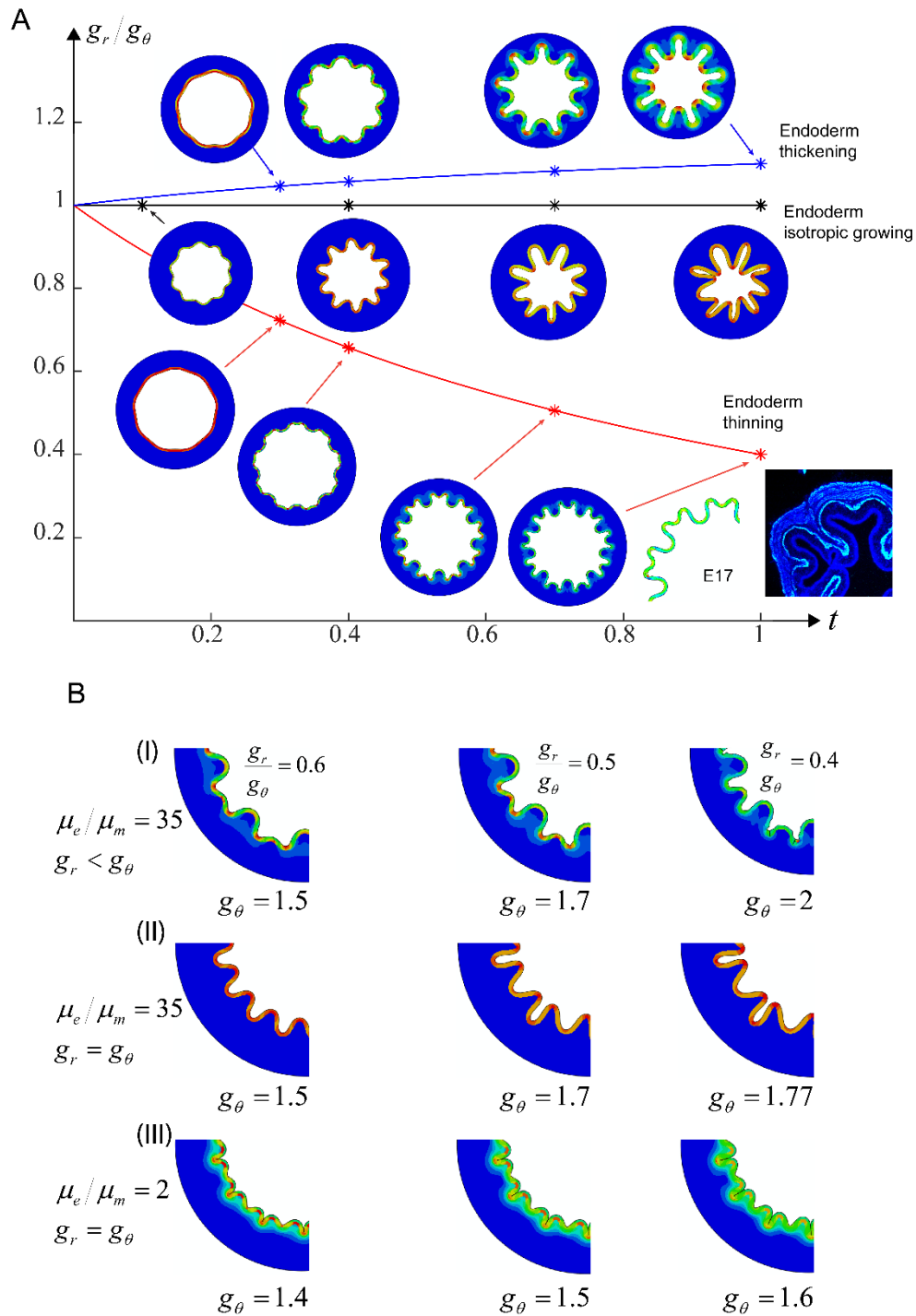


Figure 10. Simulated foregut period-double wrinkles via anisotropic radial growth profiles.

(A) Anisotropic growth models for period-doubling in the foregut. Endoderm thickening, isotropic growth, and thinning are computed. The endoderm thinning model (red line) captures the period-doubling in E17 foregut, shown in the inset. The initial geometry and growth profile at E17 are $r_i/r_o = 0.65$, $h_e/h_m = 0.2$, and endoderm thinning. (B) Three different period-doubling patterns exhibiting endoderm thinning (I) and isotropic growth (II and III), with the results of variations in magnitudes of growth g and modulus ratio μ shown. Color indicates magnitude of stress and deformation.

(type II), as seen in the pre-zigzag midgut (Figure 10A, black curve) (Shyer et al., 2013).

Much like self-contacting folds in the foregut, the remarkable feature of period-doubling (type I) as we see in the E17 foregut, where each valley is split to two halves, can only be captured by the model implementing relative thinning of the endoderm (Figure 10A, B). Finally, to further understand the range of parameters that can generate these patterns, we also simulated type II isotropic growth buckling with varied geometries and modulus ratios. In type II, the sinusoidal wrinkles evolve to period-doubling folds where some valleys widen and the adjacent valleys narrow down and deepen (Figure 10B). With a low modulus ratio, the wrinkles evolve to creases where every pair of adjacent peaks is squeezed and the valleys touch their neighbors to form cusps. This is consistent with a known requirement for a high modulus ratio in smooth instead of cusped wrinkling (Tallinen & Biggins, 2015). Our model results thus indicate that, besides relative stiffness, the primary feature regulating primary and secondary folding patterns in the foregut is decreasing relative thickness of its endoderm layer, which is a consequence of the substantial and rapid mesenchymal thickening in the later stage embryo.

Early hindgut creasing patterns are consistent with geometric and material properties

Consistent with measured features, the final type III wrinkling case in Figure 10B generates a morphology like that of the early hindgut (Figure 8B; Extended Figure 6B). To characterize hindgut morphogenesis further, we next turned our attention to the surface and interfacial patterns that emerge between E8 and E14. Here, we focus solely on the radial and circumferential axes in 2D, though the hindgut develops biaxial sulci from E12 onward—a full computational and biological analysis of these patterns in 3D can be found in

Chapter 3: Genetic and biochemical control of physical forces in hindgut morphogenesis.

Before E12, the hindgut forms a creasing pattern with progressively increasing crease number just on the surface of the endoderm, which thins over time from a much thicker initial state than other compartments (Figure 6D; Extended Figure 5Extended Figure 6B). To simulate this primary instability, we began by applying an isotropic growth model as for the E8 foregut, and incorporated the geometry and low modulus ratio of the early hindgut. As expected from previous work in flat bilayers and curved surfaces (Tallinen et al., 2013; Tallinen & Biggins, 2015), our model recapitulated the cusped surface patterns observed at these stages—the E8 hindgut forms 3 cusps, while the E10 forms 5, as a consequence of their unique tube geometries (Figure 11A).

Multiscale hindgut buckling requires stabilization of inner creases

After E12, however, the morphology of the hindgut becomes more complicated. As the endoderm thins and the wavelength of creases decreases, a multiscale buckling phenomenon emerges, which has not been reported or understood in the past. It is important to note that multiscale wrinkling appears simultaneously with the differentiation of the innermost muscle layer within the subepithelial mesenchyme (Figure 6D, Figure 11B, Figure 14D). As we never observed wrinkling without inner muscle, we are not yet able to conclude whether the instability precedes or follows muscle differentiation. However, given known contributions of smooth muscle to tissue mechanical properties such as stiffness, it is likely that inner muscle contributes to multiscale buckling in some way.

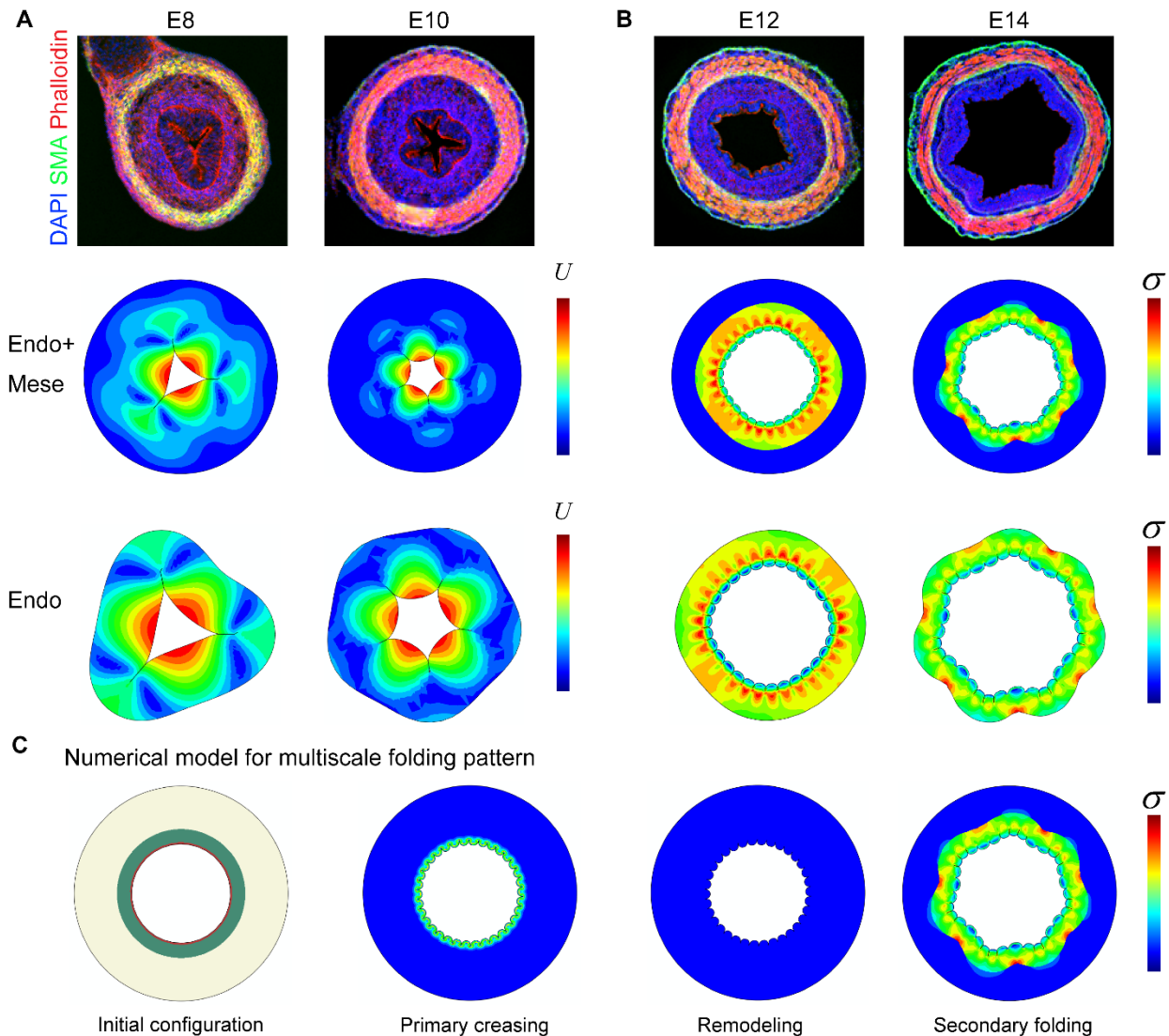


Figure 11. A three-phase model capturing multiscale buckling in the hindgut lumen.

(A-B) Transverse sections stained for muscle (SMA and phalloidin) alongside numerical results of hindgut morphogenesis during (A) primary creasing at E8 and E10, and (B) multiscale creasing and folding at E12 and E14. (C) Numerical model for multiscale pattern showing 3 phases that progress from a bilayer initial configuration: primary creasing as shown in B for E12, followed by stabilization of the pattern via remodeling, and secondary folding of the new endoderm layer with updated thickness and modulus values. Color indicates magnitude of stress and deformation.

We began our investigation by applying our growth model as before with varying geometric and stiffness properties over time; however, it was not possible to capture both creases and large-scale wrinkles simultaneously—creases tended to disappear with the onset of

secondary folding (data not shown). One possible explanation for this finding is that the hindgut relieves its residual stress through a yet-unknown form of tissue remodeling prior to the appearance of interfacial wrinkling. To test this hypothesis, we dissected the outer circumferential muscle boundary away from the inner endoderm-mesenchyme composite to determine whether creases resolve into a flat surface when residual stress is removed (Figure 8H). Remarkably, we found that creases are maintained, indicating that surface epithelial cells stabilize their configuration biologically, or that the endoderm is instead constrained by the mesenchyme layer (as discussed in Chapter 3: Genetic and biochemical control of physical forces in hindgut morphogenesis). In either case, we might expect that the primary creasing pattern would be unaffected by secondary folding due to growth against outer muscle.

To determine whether persistent creases with circumferential muscle removal can explain coincident multiscale morphologies in the hindgut, we developed a three-step growth profile (Figure 11C): first, the innermost endoderm layer experiences isotropic growth with a low modulus ratio, $\mu_e/\mu_m = 2$ (Figure 8G). After this point, residual stress in the endoderm is released and the innermost smooth muscle layer differentiates. For simplicity and because we anticipate a role for this layer in multiscale buckling, in subsequent steps of the simulation, the true endoderm and subepithelial layer are combined and considered to be one “endoderm” layer. Later stage modulus measurements indicate an increase in both endoderm and mesenchyme stiffness, where we expect that the mesenchyme is becoming stiffer from both ECM remodeling and muscle differentiation (Chapter 3).

The result of this simulation is a multiscale wrinkling morphology strikingly like that of the hindgut at E14 (Figure 11B). Along with creases, a mode 5 wrinkling pattern appears at the

base of the “endoderm” as it grows against outer muscle. Accordingly, the prior step at E12, which does not incorporate a change in modulus ratio and the third step of growth after remodeling, produces small wavelength creases only (Figure 11B). Thus, the simultaneous presence of creases and large-scale wrinkles in the hindgut appears to depend on both a change in the deforming layer geometry and stiffness, as well as a critical transition where the superficial creased morphology is stabilized.

Foregut inner layers experience axial pre-stretch

Our theoretical framework can explain the primary differences in morphologies between gut regions based on geometry and stiffness on the circumferential and radial axes, without needing to invoke longitudinal growth (Figure 9A). However, subsequent pattern specialization between regions relies on the appearance of axial differential growth. Axial constraint causes the midgut ridges to buckle into zigzags, and, as described next in Chapter 3: Genetic and biochemical control of physical forces in hindgut morphogenesis, is an important consideration for sulci formation in the hindgut. But, since the foregut develops longitudinal muscle constraints as in the midgut (Figure 7A), why does it maintain ridges instead of forming zigzags?

To address this conundrum, we first considered whether anisotropic stiffness, where the inner composite becomes more resistant to deformation on the longitudinal axis, may prevent buckling. We therefore modified our tensile testing protocol to measure axial stiffness (Extended Figure 7A). However, though we found evidence for material anisotropy in the foregut inner composite, it is still more stiff circumferentially than longitudinally during the

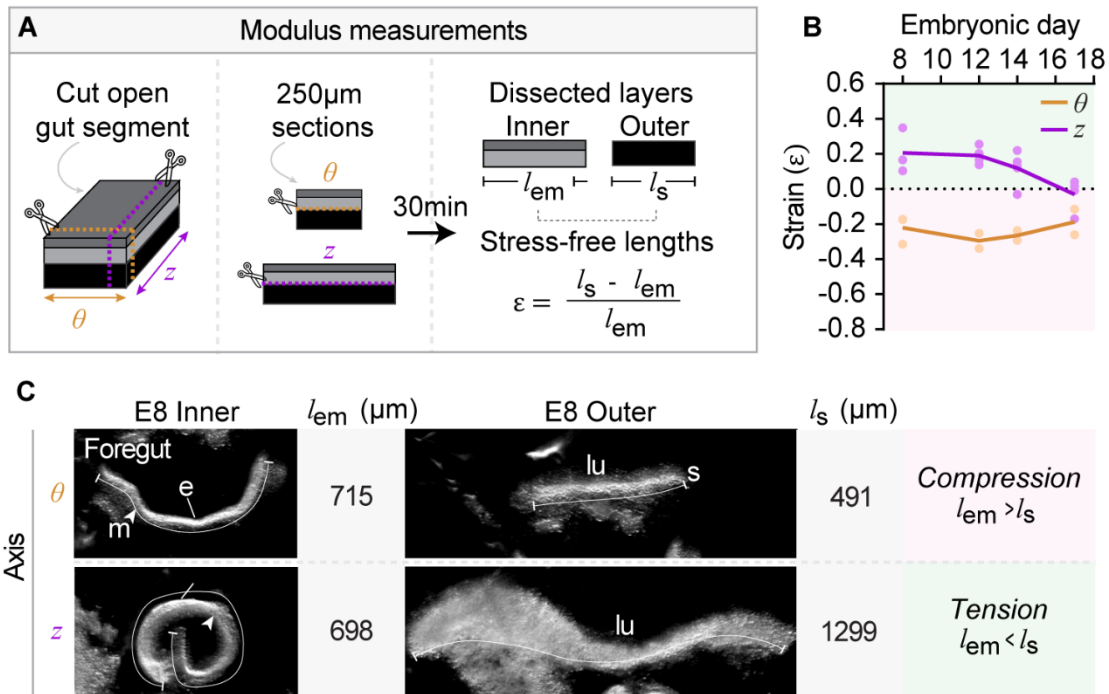


Figure 12. Longitudinal tension from differential growth in the foregut.

(A) Method of differential growth measurement. Strain is determined by first cutting open a segment of the gut and slicing into circumferential (θ) and longitudinal (z) samples (left), separating inner composites from outer muscle (center), and measuring stress-free lengths after allowing tissues to reach their stress-free states (right). Strain, ϵ , is the percent change in length from the unstressed to stressed configuration. (B) θ and z strain measurements over time for the foregut only, where light green indicates the regime where inner layers are tensed, and pink is compressed. $n=3$ measurements per time point. (C) Representative dissecting microscope images and measurements from E8 depicting tissues post-dissection and relaxation on the θ and z axes. Tissue length values in μm , l_{em} and l_s , correspond to bracketed lines in “E8 Inner” and “E8 Outer” images (e, endoderm; m and arrowhead, mesenchyme; s, muscle; lu, lumen side). Relative lengths indicate compression circumferentially, consistent with wrinkling, and tension longitudinally, consistent with axial pre-stretch.

period when we would expect zigzags to appear (E14 onward) (Extended Figure 7B). In fact, both modulus measurement methods—pulling the tissue as a ring and securing it on either end using super glue—confirmed that circumferential stiffness becomes extremely high by E17 (Extended Figure 7C). While it remains possible that the inner composite is particularly stiff longitudinally in the foregut relative to other gut regions, thus preventing axial deformation, we suspect that this parameter alone does not drive the persistence of ridges in the foregut.

We next considered whether the magnitude of axial compression is different between the midgut and foregut. To measure differential growth, we used fine dissections to separate the inner composite from muscle as with tensile testing, on both the circumferential and longitudinal axes (Figure 12A). After allowing tissues to relax to their stress-free states, we measured strain as the percent change in length from the unstressed to stressed configurations.

In the midgut, circumferential compression appears prior to E8 and is maintained throughout morphogenesis, but longitudinal compression does not appear until longitudinal muscle differentiates at E12 (Figure 15B) (Shyer et al., 2013). In the foregut, circumferential compression appears as in the midgut—as shown for E8, the stress-free length of the inner composite is greater than that of the muscle that constrains its growth in the stressed configuration (Figure 12B, C). However, longitudinal strain is in the tensile regime for the entirety of lumen morphogenesis: at E8, the dissected inner composite is shorter than muscle on the longitudinal axis (Figure 12B, C). This means that the inner composite experiences sustained axial pre-stretch, which is consistent with resistance to buckling on that axis (materials buckle under compression, not tension). As a result, despite the presence of longitudinal muscle, this result indicates that zigzags fail to form in the foregut because inner layers are stretched longitudinally and are thus unable to deform.

Sox9 and phospho-Smad staining patterns correlate with post-buckling motifs

In the chick midgut, smooth wrinkling of the endoderm and mesenchyme concentrates morphogens at the tips of protovilli to pattern the nascent crypt-villus axis and its associated

cell types. Bmp is activated at the tips of the wrinkles as a function of their curvature, and Sox9 is localized at their bases.

As discussed above, the organization and repertoire of cell types differs between the mid-, fore-, and hindguts, where the foregut in particular never forms crypts housing ISCs. Yet, at least on the circumferential axis, it wrinkles relatively similarly to the midgut, raising the question of whether it also shows patterned signal activation, and if so, how it evades or responds in a specialized way to the downstream small intestinal cell differentiation landscape. Staining for Sox9 and pSmad1/5/9 at E15, when period-doubling is fully established and the epithelium is beginning to transition to a stratified bilayer (Soliman & Madkour, 2021b), reveals that pSmad2/5/9 does not appear to be patterned according to wrinkle tips as in the midgut (Figure 13A). However, in contrast to the role of Bmp in suppressing epithelial stratification in the mouse esophagus, Bmp is activated in the basal instead of the first suprabasal layer of the epithelium (P. Rodriguez et al., 2010).

Sox9, by contrast, does appear to be highly patterned according to the fold architecture, as it is in the midgut (between villi). Cells in primordial mucosal glands—which are ultimately cuboidal—form as epithelial invaginations from the endoderm and show high Sox9 activation, consistent with its role in specifying cuboidal epithelial identity (Figure 13C). What's even more striking is that these invaginations appear to form preferentially, at least initially, at the sites of period double bifurcations at the bases of folds (72%, average of 2 E17 sections; 71%, Figure 3A image of a similarly staged quail esophagus from Soliman & Madkour, 2021b).

In the hindgut, both pSmad and Sox9 are localized according to lumen buckling, but instead of flanking surface creases, the activation pattern follows the large-scale, interfacial

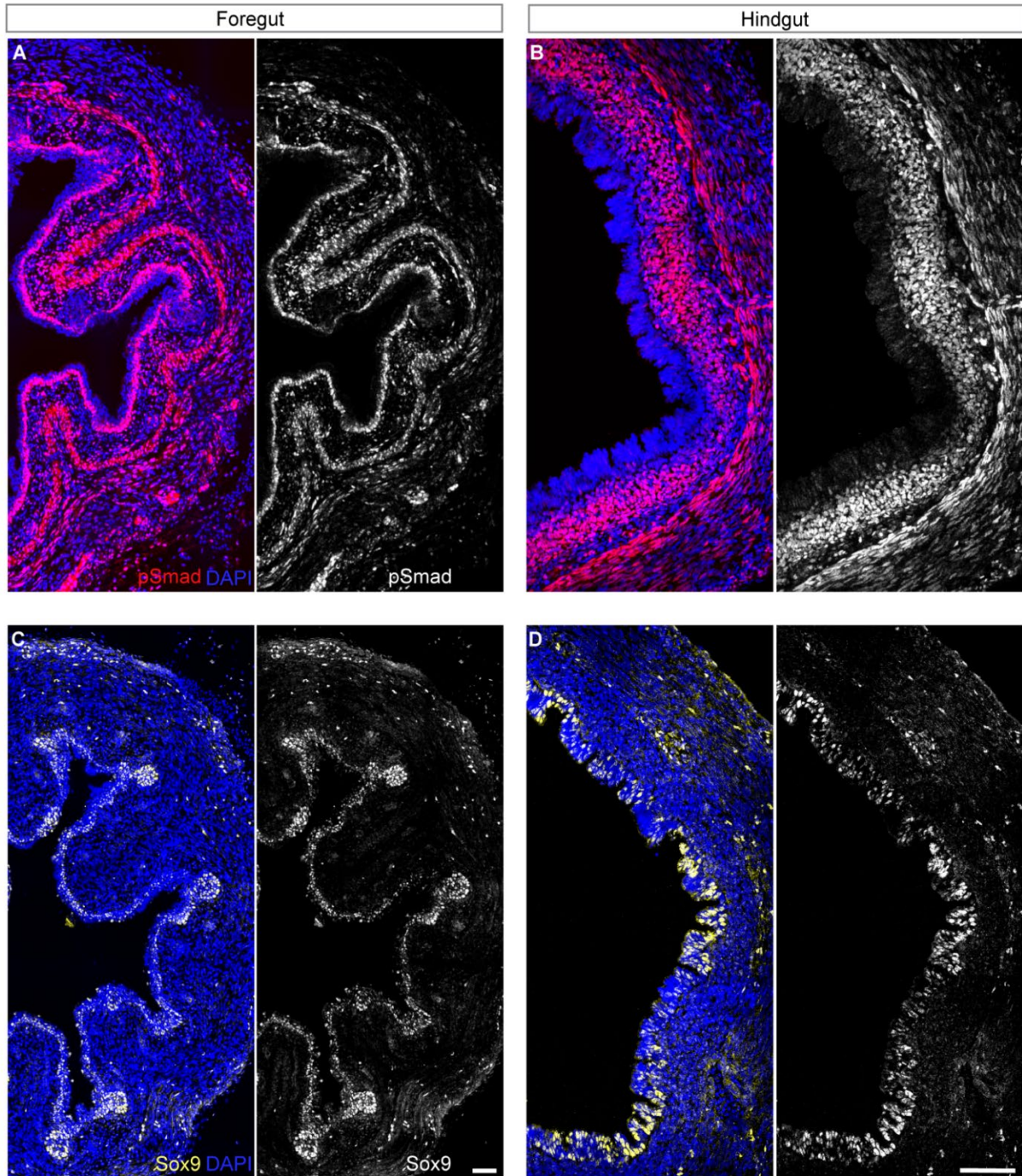


Figure 13. Patterns of Bmp signaling and Sox9 activation correlate with postbuckling motifs. (A-B) phospho-Smad1/5/9 and (C-D) Sox9 immunostaining at E15 in partial views of (A, C) foregut and (B, D) hindgut transverse sections. Nuclear-localized pSmad signal indicates Bmp pathway activation. Scale bar, 50 μ m.

wrinkles (Figure 13B, D). Analogous to the midgut situation, pSmad is high at the apices of wrinkles while Sox9 is high at their vertices. These localizations are unlikely to correlate with

crypt-villus patterns because the hindgut does not form villi, and crypts form much later and evenly tile the large intestinal surface. Given the essential roles for these factors in intestinal development, however, it is likely that interfacial wrinkling plays a role in patterning some aspect of hindgut morphogenesis. Together, our observations point out that, besides a possible mechanical role in digestion, post-buckling evolution of foregut and hindgut morphologies is likely important for their proper development and maturation of the chick gut.

Conclusions

Epithelial folding has long been recognized as a critical feature underlying gut function, and though several studies have focused on morphogenesis of small intestinal villi, other well-known and indispensable parts of the gut have received considerably less attention (Balbi & Ciarletta, 2013; Freddo et al., 2016; Hannezo et al., 2011; Shyer et al., 2013; Walton et al., 2016). Furthermore, many studies have used computational and material models to understand the diverse buckled forms found in nature, but less have incorporated systematically measured data from a developing biological system, let alone one where different patterns appear within the same organ (Cai et al., 2010; Garcia et al., 2019; Li et al., 2012; Taber, 2014; Tozluoğlu et al., 2019; Q. Wang & Zhao, 2015). In this chapter, we combined mechanical measurements from freshly dissected tissues over time and space with mathematical models to explain the emergence of distinct foregut and hindgut mucosal buckling patterns. We further found that complex post-buckling motifs only found in these regions, which most likely influence their proper maturation and function, are also functions of regional mechanical landscapes and modes of growth.

Geometry and stiffness trajectories of inner deforming layers vary positionally in the gut, where their radius ratio decreases, thickness ratio increases, and modulus ratio decreases from anterior to posterior. The foregut expands radially with a thin and stiff endoderm growing against a soft mesenchyme that thickens the most of all compartments over time. This lowers the relative contribution of the endoderm to composite thickness, effectively thinning it. Using a 2D morphoelastic model of gut growth, we found that it is precisely this property of foregut radial development that explains its formation of self-contacting smooth folds and period-double wrinkles.

The hindgut instead develops surface creases in the endoderm, which we recapitulate in our model as a function of its early geometry, where both the endoderm and mesenchyme are thick and the lumen is occluded due to minimal inner radial expansion, and its low modulus ratio. Subsequent simulations of large-scale buckling required invoking a three-phase model, where the lumen forms creases due to growth, which then stabilize before inner layers grow again to develop large wrinkles. Dissecting muscle away from the endoderm-mesenchyme composite did not abolish creasing, confirming the prediction from our model that creases must relieve their residual stress in order to remain when interfacial wrinkles appear.

Our results both establish a mechanical mechanism for morphological regionalization in the gut, as well as demonstrate the remarkably small range and number of physiological parameters that can be tuned to generate distinct forms in structures arising from a common developmental precursor.

Chapter 3: Genetic and biochemical control of physical forces in hindgut morphogenesis

Attributions

Hasreet K. Gill devised the project, designed and performed all experiments, wrote codes for and performed experimental data analysis. Sifan Yin performed simulations and developed all theoretical and numerical method codes/formulations for modeling 3D lumen buckling instabilities. John C. Lawlor analyzed bulk RNA-sequencing data and optimized an ex vivo culture protocol. Emma R. West and Ninning Liu provided reagents for and assistance with Light-seq. Nandan L. Nerurkar and Tyler R. Huycke contributed to mechanical measurement methods as stated in Chapter 2 attributions. Clifford J. Tabin and L. Mahadevan supervised the project.

Background

The Hox genes are transcription factors first discovered in *Drosophila* that play a central role in controlling the development of the body plan. In tetrapods, 39 genes are arranged into 4 clusters, and within each cluster, the chromosomal order of the Hox genes matches the order of their expression domains in the developing embryo. Based on knowledge of Hox gene expression patterns in the mouse, in 1993, Michael Kessel and Peter Gruss proposed that the overlapping pattern of Hox gene activity might serve as a code for establishing differential vertebral morphologies, in analogy to the roles their *Drosophila* counterparts play in determining segment identity (Kessel & Gruss, 1991); this model has since been shown to be essentially correct (reviewed in Wellik, 2007). It is striking, however, that more than 30 years

later, we still have little idea how vertebral Hox genes direct differences in morphology—in other words, the downstream genetic and/or cellular process they act through remains a black box. In fact, though studies in *Drosophila* have uncovered Hox-regulated cellular and mechanical phenomena that drive organogenesis, such mechanistic knowledge is virtually nonexistent for any vertebrate organ system (De Las Heras et al., 2018; Mitchell et al., 2022).

While axial skeletal morphology is the classic example of anterior-posterior Hox patterning in vertebrates, Hox genes contribute to the differential anterior-posterior patterning of a variety of embryonic tissues, from the central nervous system (reviewed in Parker & Krumlauf, 2020), to the reproductive tract (reviewed in Major et al., 2022), to the developing GI tract. Among the most ancient Hox expression domains is that of paralog group 13 in the caudal intestine. Hox 13 homologs are found in the terminal end of the gut in humans, mice, chicks, zebrafish, flies, worms, and sea urchins (Annunziata et al., 2019; Kondo et al., 1996). Loss-of-function destroys the muscular apparatus of the anal sphincter in the mouse, and infection of the chick midgut with RCAS retrovirus carrying a dominant negative form of *Hoxa13* causes hindgut and cloacal atresia (Dan et al. 2010; Warot et al. 1997; Zákány and Duboule 1999; (Barbara and Roberts 2002). Most striking, however, is the finding that *Hoxd13* overexpression in the chick midgut is sufficient to replace villi with an epithelial lining that resembles that of the hindgut and produce the acid mucin-secreting cells typical of the large intestine (Roberts et al., 1998). *Hoxd13* is, thus, both necessary and sufficient to determine critical aspects of hindgut specific morphology—but, how it accomplishes this has, once again, remained a black box.

In this chapter, we identify how distinct mechanical and growth parameters in the midgut and hindgut give rise to their unique morphologies. We further uncover that these regional tissue mechanics are specified by an upstream Hox gene, which patterns the tissue through TGF β signaling.

Results

Distinct biaxial buckling instabilities in mid- and hindgut epithelia

Villi in the midgut display crystalline regularity in their shapes and arrangement (Coulombre & Coulombre, 1958). As we and others have previously described (Shyer et al., 2013), villi arise in a stepwise manner wherein the smooth luminal lining of the midgut at embryonic day (E) 8 transforms into a series of ridges at E12, zigzags at E14 and protovilli—bulges that prefigure final villi locations, born from in-plane rotations of zigzag arms—by E18 (Figure 14A-B). In contrast, the first observable deformation of the luminal surface of the hindgut occurs at E12 when it forms superficial, brain-like sulci, which become extensively branched by E14 and evolve into cuffs by E16 (Figure 14A). Though tightly packed like primordial villi, cuffs are shorter, wider, heterogeneous in size, and appear spatially disordered (Figure 14A, E).

Concomitant with the maturation of sulci in the E14 hindgut, a second order buckling that includes both the endoderm and the inner layer of mesenchyme appears (Figure 6A, D; Figure 11B; Figure 14D). As this is also the time when the innermost layer of longitudinal smooth muscle (muscularis mucosa) differentiates, which forms in a pattern of periodic deformations distanced from the subjacent circumferential smooth muscle—a configuration maintained as

the sulci give way to cuffs (Figure 14E). By comparison, in the midgut, there is no such secondary folding and the circumferential layer of smooth muscle forms as a flat band beneath the epithelial folds, sandwiched between the closely apposed outer and inner longitudinal smooth muscle layers (Figure 14E).

As discussed in Chapter 2: Divergent epithelial bucking across gut regions, it is striking that the same three smooth muscle layers emerge sequentially in the hindgut, in the same order, and with the same fiber orientation as the midgut (Figure 6B-G; Figure 7A-B). Indeed, the fact that muscles are thicker in the hindgut and that each differentiates 1-2 days earlier should only make them more effective in driving such morphological transformations (Figure 6A; Figure 14B, D). We therefore again expected that the mechanical properties of the inner layers themselves must differ between the midgut and hindgut, thus affecting how regional epithelia interpret physical constraints from muscle.

The developing hindgut and midgut are unique in growth and mechanical properties

Clues into the different modes of buckling in the midgut and hindgut come from extensive previous theoretical analyses of the formation of sulci, which superficially resemble the reticulated grooves that first appear on the luminal surface of the hindgut (Hohlfeld & Mahadevan, 2011, 2012; Tallinen et al., 2013). Sulci are unique, nonlinear surface instabilities that have recently been studied in the context of brain, though they appear widely in nature. Previous work would suggest that sulci in the gut may emerge when the endoderm-mesenchyme bilayer is compressed biaxially (through transversely isotropic expansion), where the modulus ratio of the two layers is low (i.e., they are equally stiff, or the endoderm layer is

Figure 14. Hindgut-specific morphological features are replicated with *Hoxd13* misexpression

(A) Notation for gut axes and method of imaging the surface of the endoderm after cutting the tube open longitudinally. Lumen surface morphologies of midgut, hindgut, and RCAS-*Hoxd13* midgut (“Midgut + *Hoxd13*”) at E12 for all conditions, E14 and E16 for the midgut and hindgut, and E16 and E18 for the midgut + *Hoxd13*. Scale bar, 100 μ m. (B) Timeline of lumen morphogenesis in the midgut, hindgut and midgut + *Hoxd13*, with cartoon representation of key morphologies. The shallowness/steepness of each color gradient represents the timescale of the morphological transition. Green lines indicate muscularis mucosa differentiation. (C) Power spectral density profiles corresponding to spatial domain images within the gray box in (A). Color indicates log normalized amplitude. For patterns with peaks corresponding to characteristic pattern wavelengths, wavelength values on the longitudinal axis (z) are indicated on the plot. (D, E) Transverse sections at E14 (E) and E18 (F) depicting one hemisphere of the control midgut, hindgut, and RCAS-*Hoxd13* midgut. SMA, Alpha Smooth Muscle Actin; Calp, Calponin 1; b.m. and straight line, basement membrane; lu., lumen; circ., circumferential muscle layer; muc. and arrowhead, muscularis mucosa; asterisk, secondary large-scale fold. Scale bar, 50 μ m. (F) Method of identifying branch points in lumen patterns by tracing the peaks of folds from raw lumen surface images. Number of branched folds per 500 μ m² at E14 for the midgut and hindgut, and E16 for the RCAS-*Hoxd13* (****, $p < 0.0001$; t-test, $n = 4$ images). (G) Method of measuring fold aspect ratios as height divided by width, where width is measured at the fold half max; tall, thin folds have larger values and short, wide folds have smaller values. Aspect ratios of single folds at E18 only (****, $p < 0.0001$; ns, not significant, t-test, $n = 10$ folds).

softer) (Ciarletta et al., 2014; Holland et al., 2018; Razavi et al., 2016; Tallinen et al., 2014; Tallinen & Biggins, 2015). To test this possibility, we once again measured differential growth, geometric features, and stiffnesses of inner endoderm and mesenchyme layers during late-stage midgut and hindgut lumen morphogenesis.

To measure strain, we used the same method of tissue dissection and relative length measurement described for the foregut in the previous chapter (Figure 15A Figure 12A) (Fung & Liu, 1989; Shyer et al., 2013; Zhao et al., 2007). Measurements from both circumferential and longitudinal dissections yielded differential growth profiles over time. As expected, the midgut initially accrues strain only circumferentially (negative values in Figure 15B), reflecting the circumferential compression that forces the flat lumen to form ridges. Subsequently, between E12 and E14, longitudinal compression appears, concomitant with differentiation of the outer muscle layer, while at this stage the circumferential strain no longer increases (Figure 15B). Therefore, within each growth period (E8-E12, E12-E14, E14-E18), midgut growth is highly anisotropic, as previously reported (Amar & Jia, 2013). By stark contrast, but consistent with the theoretical analyses of sulci formation, the hindgut gradually develops compression on both axes nearly simultaneously, resulting in equibiaxial growth during most of lumen morphogenesis (Figure 15B).

Next, tissue width measurements taken from transverse sections (Figure 15A, Figure 8A) revealed that both the endoderm and mesenchyme layers are thicker in the hindgut (Extended Figure 11B, C). Yet, the ratio of endoderm to mesenchyme width is not different until the appearance of sulci from E12-E14, when the width ratio sharply drops in the hindgut as the mesenchyme thickens (Figure 15C; Extended Figure 11C).

Given that E12-E14 is the key time frame when the midgut and hindgut develop distinct biaxial morphologies, we next measured Young's moduli of the endoderm and mesenchyme layers at E14 using our uniaxial tensile testing system (Figure 8D-E). We first observed that, consistent with measurements during uniaxial buckling at E10, the endoderm is softer in the hindgut at E14 (Extended Figure 11C; Figure 8F). By contrast, mesenchyme modulus, calculated from average endoderm and composite modulus and width measurements as before, is higher in the hindgut at E14; together with a softer endoderm, this lowers the modulus ratio, consistent with E10 data (Figure 15C, Figure 8F; Extended Figure 11B-C). Thus, at the critical time when the midgut forms zigzags, but the hindgut forms sulci, the modulus ratio between the endoderm and mesenchyme is high in the midgut and low in the hindgut (Figure 15D). Notably, the modulus ratio in the hindgut trends upward as the sulci gives way to cuffs (Extended Figure 11D).

Taken together, the elastic, geometric, and growth properties of the hindgut are both distinct from those of the midgut and qualitatively consistent with theoretical work on the emergence of creased sulci patterns.

3D numerical simulations of lumen wrinkling capture mid- and hindgut morphologies

Despite similarities between our observations and theoretical expectations, determining whether measured values sufficiently explain different lumen patterns required turning to computational modeling, as we did for primary and multiscale foregut and hindgut folding (Figure 9A).

To simulate late-stage ridge, zigzag, sulci, and cuff formation, we first adapted our two-

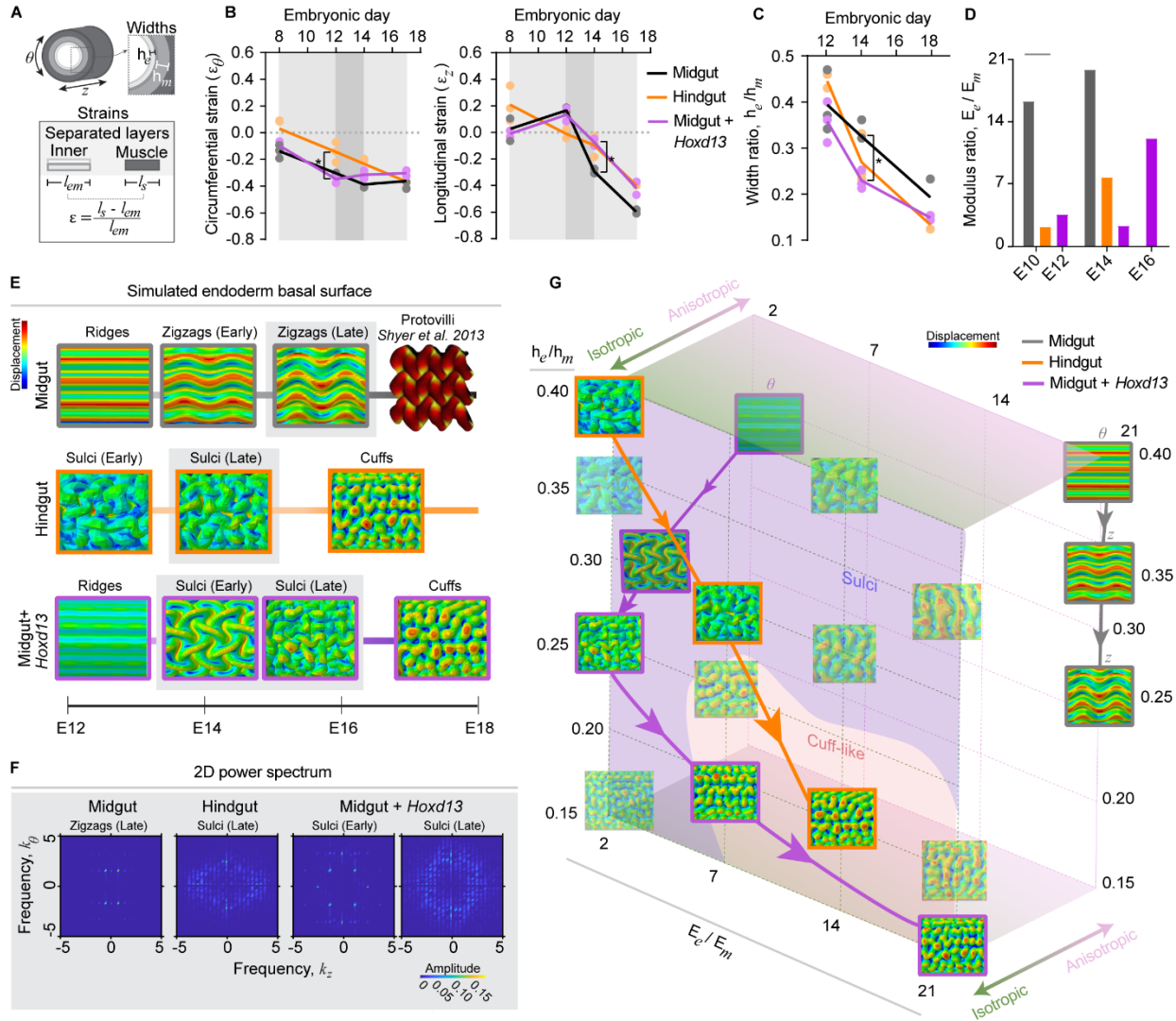


Figure 15. Mechanical properties of the hindgut are regulated by *Hoxd13* activity.

(A) Measurement of widths and strains from cross-sections and dissected, relaxed inner and outer muscle layers (s), respectively. Strain is determined as the percent change in length of inner layers upon constraint by muscle. (B) Differential growth properties of the midgut, hindgut, and RCAS-*Hoxd13* midgut (“Midgut + *Hoxd13*”). Gray boxes in each plot frame time periods of interest, where dark gray corresponds to the biaxial buckling transition. Left, Circumferential (ϑ) and right, longitudinal (z) strains, ε , over time. Dotted gray lines at 0.0 strain in each plot indicate transition between inner composite tensile (>0) and compressive (<0) regimes (*, $p < 0.05$, t-test, $n = 2-3$). (C, D) Ratios of endoderm (e) to mesenchyme (m) (C) width, h (*, $p < 0.05$, $n = 3$), and (D) Young’s modulus, E , over time. Midgut and hindgut modulus ratios at E10 are used here for comparison to the RCAS-*Hoxd13* midgut at E14. (E) Numerical simulation results at successive stages of lumen morphogenesis shown in Figure 1B. In a tube geometry, views correspond to the outer surface of the endoderm layer for ease of visualizing the morphology. Color indicates magnitude of displacement. (F) 2D power spectral densities for major wrinkling modes indicated by gray boxes around simulation results in (D). (G) 3-dimensional parameter space representing experimental lumen folding trajectories (lines and arrows, which indicate progression over time) and simulation results (boxes) used to identify two morphological domains (blue “sulci” and orange “cuff-like” colored regions) as functions of modulus ratio, growth, and thickness ratio. For cases with anisotropic growth, ϑ and z above the boxes represent dominating growth directions.

dimensional growing bilayer model of early buckling initiation to three dimensions (2D model of primary and multiscale buckling in the fore- and hindguts). We therefore applied volumetric growth theory as before, with the deformation gradient decomposed as $\mathbf{F} = \mathbf{A} \cdot \mathbf{G}$. \mathbf{A} is the elastic deformation tensor and $\mathbf{G} = \text{diag}(g_r, g_\theta, g_l)$ is a spatiotemporal growth tensor capturing the addition of material volume and the plastic (irreversible) deformation in three dimensions. Numerical simulations were performed using the finite element method (3D hindgut and midgut lumen wrinkling).

Fitting the spatiotemporal growth tensor to the differential growth behaviors of the midgut and hindgut—stepwise anisotropic growth and transversely isotropic growth, respectively—yielded two representative sets of functions (Table 7). Combined with measured thickness and modulus ratios at each stage of lumen wrinkling (Table 6), these growth tensors predicted the distinct morphological trajectories of the midgut and hindgut. Monotonically increasing and decreasing longitudinal and circumferential growth profiles, respectively, in the context of a relatively high modulus ratio and moderately decreasing thickness ratio yields ridges followed by zigzags (Figure 15E). By contrast, a low modulus ratio with linearly increasing longitudinal and circumferential growth results in sulci at both high and low thickness ratios (Figure 15E, G). Further exploration of the parameter space defined by these three characteristics revealed that, indeed, sulci appearance is driven by transversely isotropic growth, though properties of the folds vary with modulus and thickness ratios—for example, sulci wavelength appears to scale with thickness ratio (Figure 15G).

Most striking from our parameter space, however, was the observation that in the high modulus ratio and low thickness ratio regime, the surface pattern becomes limited to spatially

segmented outgrowths resembling cuffs instead of labyrinthine sulci (Figure 15G). Given the trend of increasing modulus ratio and drastically decreasing width ratio in the hindgut, its morphological trajectory ultimately lands in this predicted “cuff-like” state (Figure 15C-E, G, Extended Figure 11D). Thus, unlike in the midgut where the final stages of villus outgrowth cannot be explained by a continuum-level mechanical model of lumen wrinkling (Shyer et al., 2013), our model captures all major steps of hindgut morphogenesis from biophysical parameters alone, and further indicate that these properties are sufficient to drive luminal morphogenesis in the hindgut.

Cuff formation lacks hallmarks of mesenchymal clustering and requires circular constraint

To confirm the prediction from our model that cuffs in the hindgut form through a purely mechanical process that depends on muscle constraint, and not through a local clustering mechanism as has been reported for mouse villi and similar outgrowths like feather follicles (Ho et al., 2019; Rao-bhatia et al., 2020; Shyer et al., 2017; Walton et al., 2012), we next cultured the hindgut with surgical and pharmacological muscle perturbations and observed effects on cuff formation.

We first optimized a culture strategy and found that when we cultured an E15 hindgut for 2 days, rocking in suspension, the lumen forms cuffs as usual (Figure 16A, top). When cut open longitudinally to relieve circumferential constraint from muscle prior to culture, we found that the hindgut fails to form luminal cuffs and maintains a creasing pattern (Figure 16A, bottom). To determine whether longitudinal compression is needed, we introduced orthogonal “circumferential” cuts partway through the tube prior to culture and found that cuffs form as in

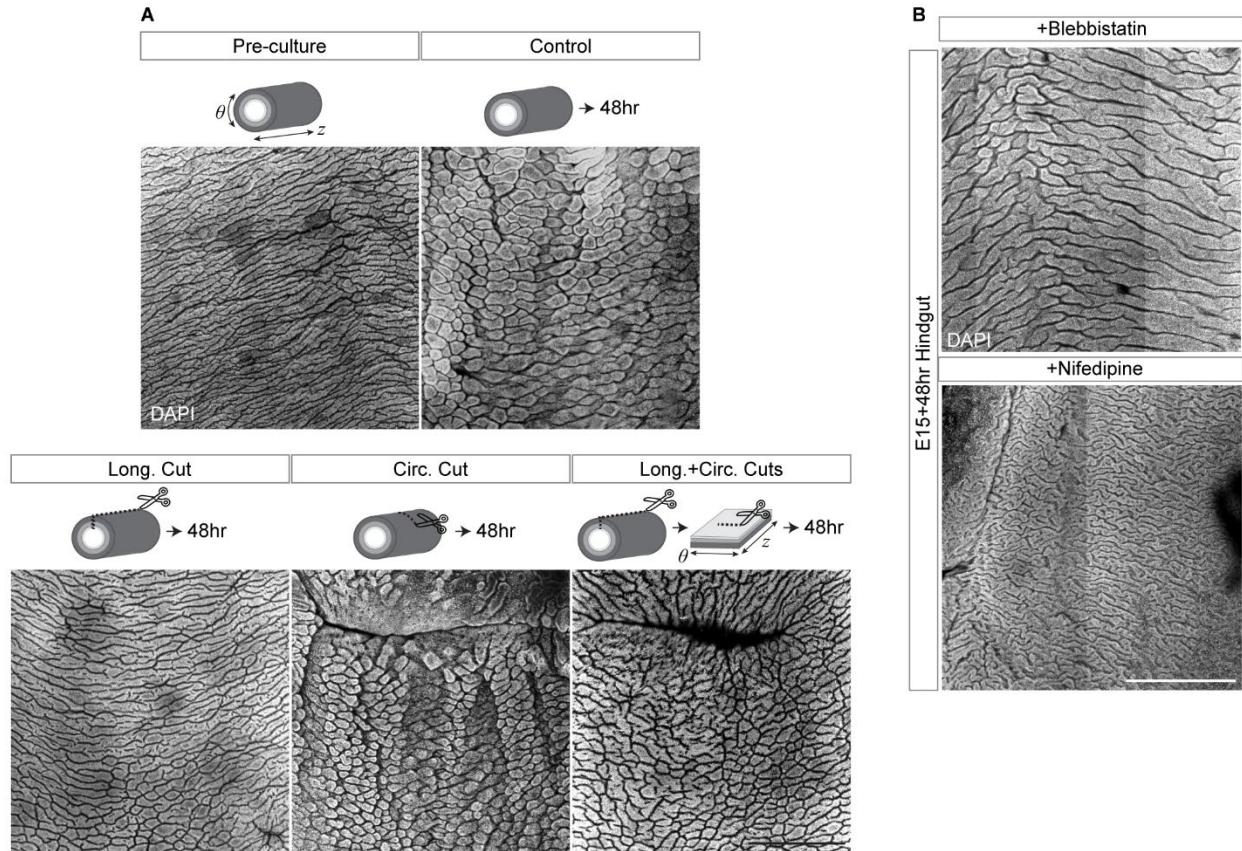


Figure 16. Cuffs require static circumferential compression and cyclic contractions to form

(A) Top-down images of DAPI-stained hindgut lumens after 48 hr culture, starting from E15, in different configurations indicated by schematics. Scissors and dotted lines show different cuts made to the tube prior to culture, where Long.+Circ. Cuts involved two cuts made in succession. Longitudinal axis is indicated by z and is vertical in images; circumferential axis is θ and horizontal. (B) Hindgut lumens after 48 hr culture with 20 μ M blebbistatin and 100 μ M nifedipine. Scale bar, 500 μ m.

the control. Finally, when both defects were introduced, the lumen again failed to form outgrowths, though creases were partitioned into more circular, closed compartments, suggesting that longitudinal constraint is the source of anisotropy in the typical hindgut creasing pattern (Figure 16A). These results support the notion that cuffs are not autonomously forming structures, but rather offshoots of sulci that form in response to residual stress from differential growth.

Next, we cultured the hindgut with nifedipine and blebbistatin, which are inhibitors of muscle contraction and non-muscle myosin contractility, respectively. Midgut villi still form when muscle contraction is blocked (Shyer et al., 2013); however, we found that this is not the case for cuffs, which are replaced by longer-wavelength creases when the hindgut is cultured with nifedipine (Figure 16B). Furthermore, inhibition of non-muscle myosin also generated a creasing pattern, though with a much shorter pattern wavelength (Figure 16B). Therefore, even

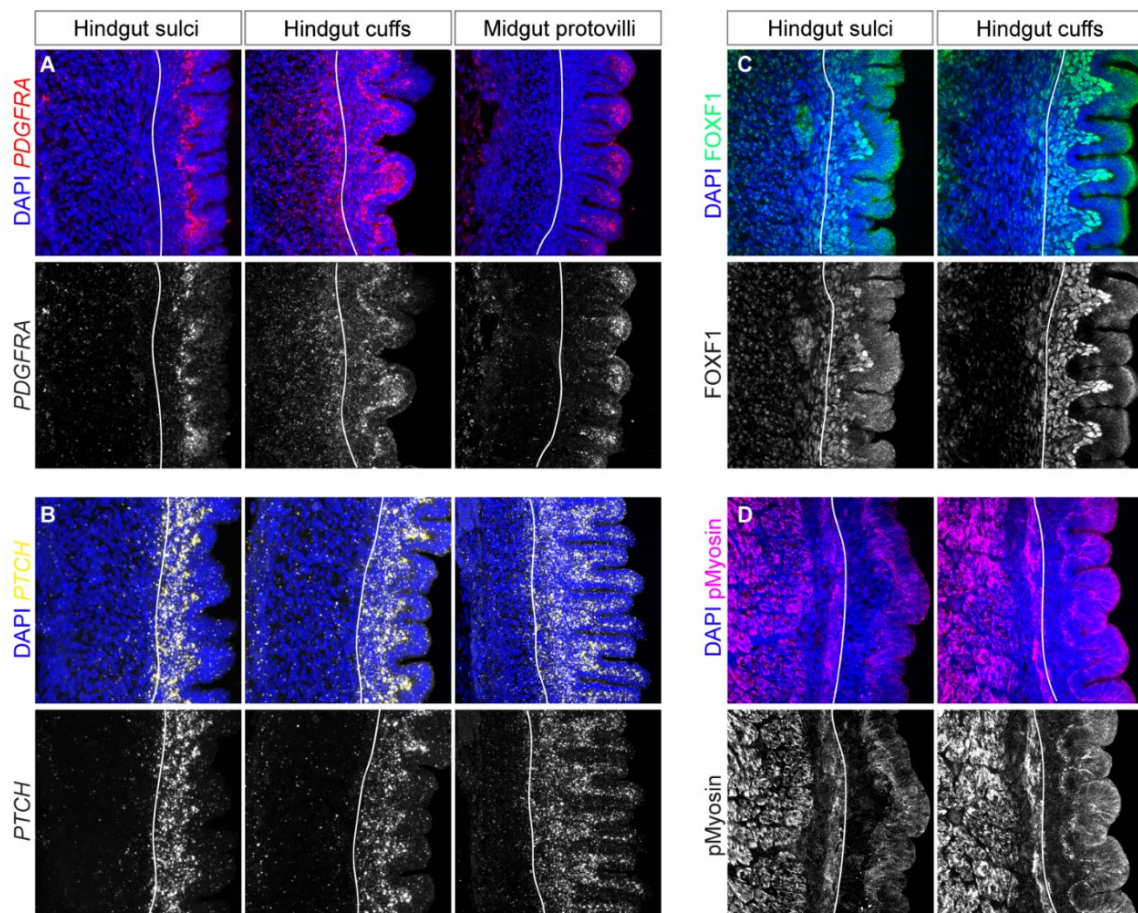


Figure 17. Markers for villi mesenchymal clusters do not prefigure or localize to cuffs
 (A, B) FISH and (C, D) immunostaining of sagittal sections before and after cuff formation in the hindgut (around E15 and E16), and in the E16 midgut after protovilli begin to form. (A) Marker of subepithelial villus clusters *Pdgfra*, (B) Shh receptor and target *Ptch*, (C) mesenchymal marker *Foxf1*, and (D) contractile cell marker phospho-Myosin. White line indicates boundary of the muscularis mucosa, and lumen is on the right side.

though hindgut cuffs require static constraint to form, contractility of the muscle and mesenchyme appear to also be important for proper morphogenesis.

To further ask whether hindgut cuffs show hallmarks of villus clusters, we performed FISH for the cluster marker *Pdgfra* and for *Ptch*, which become enriched in villus tips when the crypt-villus axis is beginning to be specified (Karlsson et al., 2000; McCarthy et al., 2020; Shyer et al., 2015)(Figure 17A, B). Though these show some enrichment in the tips of cuffs after they form, it is much less than in pre-villi; *Pdgfra* in particular lines the subepithelial mesenchyme at the cuff stage, which matches its location prior to the formation of proto-villi in the midgut (Figure 17A). The mesenchymal marker *Foxf1* shows only slight enrichment under nascent cuffs, and despite our finding that cuffs are lost with blebbistatin treatment, phospho-Myosin staining does not indicate evidence of contractile clustering under them either (Figure 17C, D). These results further indicate that cuffs are mechanical instabilities and not structured units like villi.

Hoxd13 misexpression transforms midgut luminal folding a hindgut-like pattern

With a biomechanical understanding of chick large and small intestinal lumen wrinkling in hand, we next turned our focus to the genetic regulation of these patterns. At the time of hindgut morphogenesis, *Hoxd13* is expressed in the developing hindgut in a domain extending more proximally through the hindgut than previously reported at earlier stages (Extended Figure 9A-B Extended Figure 14B). When misexpressed in the developing midgut, *Hoxd13* transforms the luminal folding pattern into a phenocopy of the normal hindgut (Roberts et al., 1998b). To assess this phenotype in more detail, a replication competent retroviral vector transducing *Hoxd13* (RCAS-*Hoxd13*) was electroporated into the midgut lateral plate mesoderm

at E2.5 (Extended Figure 9B). At early stages of gut morphogenesis, the infected midguts look indistinguishable from controls (Figure 14A). However, when the hindgut forms sulci and the midgut adopts a zigzag configuration at E14, the *Hoxd13*-expressing midgut displays an intermediate phenotype between the two (Figure 14A, Extended Figure 10A). By day 16, the *Hoxd13*-expressing midgut ridges have transformed to a sulci pattern like that of the day 14 hindgut, albeit with a two-day delay (Figure 14A). By day 18, instead of an array of thin and long primordial villi, the *Hoxd13*-expressing midguts have formed short, and wide cuffs like those normally seen in the day 16 or 18 hindgut (Figure 14A, G)

Moreover, the E18 *Hoxd13*-expressing midguts display the secondary buckling characteristic of the hindgut at this stage, wherein the innermost layer of smooth muscle forms periodic folds along with the adjacent mesenchyme, as in the hindgut (Figure 14E). Radial quantifications of smooth muscle actin (SMA) stain intensity from the basement membrane to circumferential muscle illustrate the shift in the positions of smooth muscle peaks away from the muscle boundary in these conditions (Extended Figure 10D). Also, as noted above, the smooth muscle layers differentiate earlier in the wild-type hindgut than midgut. In the *Hoxd13*-expressing midgut, the innermost longitudinal layer has already formed at E14, recapitulating earlier muscle differentiation of the hindgut (Figure 14B, D).

Taken together, at least superficially, *Hoxd13* activity appears to be sufficient to posteriorize midgut folding and smooth muscle differentiation. To quantitatively determine if this is the case, we assessed properties of wrinkling patterns in the midgut, hindgut, and *Hoxd13*-expressing midgut; comparing the E16 RCAS-*Hoxd13* midgut (when it appears to form

sulci) to E14 midgut (zigzags) and hindgut (sulci); and the E18 RCAS-*Hoxd13* midgut (when it appears to form cuffs) to the E16 midgut (late zigzags) and hindgut (cuffs) (Figure 14A-B).

First, we used a metric assessing the extent of branching of the epithelial folds (Methods, Figure 1F). While zigzags in the E14 midgut are essentially unbranched, we observe significant branching in both the E14 hindgut and E16 *Hoxd13*-expressing midgut (Figure 14F). At later stages, we used Delaunay triangulation to assess the relative presence of cuff vs. pre-villi outgrowths. In line with our observations, both hindgut cuffs and *Hoxd13*-expressing midgut cuffs show higher variance in their Delaunay triangle edge length distributions compared to primordial villi, consistent with relatively higher spatial disorder in the surface arrangements of outgrowths (Extended Figure 10C). A parallel analysis of Voronoi cell area distributions supported this result.

To further assess the pattern and degree of order in the epithelial folds, we examined 2D Fast Fourier Transformation (FFT) power spectra, again comparing E16 *Hoxd13*-expressing midguts to wild type E14 midguts and hindguts, and E18 *Hoxd13*-expressing midguts and wild type E16 midguts and hindguts. In the normal midgut, the 2D FFT plot at each time point shows a discrete set of peaks at the characteristic pattern wavelengths, where the longitudinal period length decreases as the herringbone pattern is compressed with time (Figure 14C). Complementary autocorrelation profiles separating patterns on the circumferential (θ) and longitudinal (z) axes reveal high-amplitude sinusoidal waves across time points (Extended Figure 10B). Together, these measures capture the stereotyped periodicities of ridge, zigzag and primordial villi patterns.

In contrast, the hindgut has a diffuse spectral density profile at all stages and lower autocorrelation amplitudes, though slight longitudinal bias appears at later stages (Figure 14C, Extended Figure 10B). Accordingly, autocorrelation plots and amplitudes present only moderate evidence of periodic wrinkling on the longitudinal axis, as well as the large-scale circumferential buckling not seen in the midgut (Extended Figure 10B). The E16 and E18 *Hoxd13*-expressing midguts, strikingly, display 2D power spectra and autocorrelation profiles like those of the hindgut two days earlier in each case (Figure 14C; Extended Figure 10B). This analysis therefore supports the contention that ectopic expression of *Hoxd13* drives the midgut towards a hindgut-like morphology by conferring branched wrinkling and diminished pattern periodicity.

Hoxd13 modulates mechanical properties of the developing gut tube

To test whether *Hoxd13* alters luminal gut morphogenesis by modulating the physical parameters we identified as distinguishing the midgut from the hindgut, we again measured differential growth, stiffness, and geometric features of inner endoderm and mesenchyme layers, but now in *Hoxd13*-expressing midguts. Consistent with it initially forming midgut-like ridges, growth of the *Hoxd13*-expressing midgut is indistinguishable from that of the normal midgut until E12 (Figure 15B). However, the dramatic increase in longitudinal compression that normally forces buckling into zigzags between E12 and E14 in the midgut is dampened with *Hox* misexpression, making differential growth less anisotropic during this period. Subsequent differential growth trajectories are closer to that of the hindgut, suggesting, once again, that the biaxial buckling transition is the key time point when the normal and transformed midgut

patterns diverge, and that this deviation in the *Hoxd13*-expressing midgut pattern evolution is marked by loss of anisotropic growth.

We next addressed thickness and modulus ratios between growing layers in the composite endoderm and mesenchyme and found that, like the hindgut, the *Hoxd13*-expressing midgut mesenchyme is notably thicker than that of the normal midgut at the time that their morphological trajectories diverge, which lowers the width ratio (Figure 15C; Extended Figure 11C). The composite modulus of the *Hoxd13*-expressing midgut is significantly higher, corresponding to a stiffer mesenchyme, and consequently a lower modulus ratio relative to the endoderm—in fact, the ratio at E14 is identical to the hindgut modulus ratio just a few days prior (Figure 15D, Figure 8G; Extended Figure 11B-C). Therefore, we conclude that both thickening and stiffening of the mesenchyme, without changes to endoderm properties, is sufficient to imbue the RCAS-*Hoxd13* midgut with hindgut-like physical and geometric characteristics.

To verify that the physical parameters altered by *Hoxd13* misexpression can explain the hindgut-like phenotype we observed, we examined the pattern trajectory predicted by our computational model. We first observed that a transition to isotropic growth with a low modulus ratio, analogous to the transitional E14 morphology in Extended Figure 10A, generated an ordered pattern of sulci from subtle initial ridges (Figure 15E, G). Subsequent models generated sulci like those of hindgut simulations. As in the hindgut, the *Hoxd13*-expressing modulus ratio trends upward afterward, which, in conjunction with a lower width ratio at E18, leads to segmentation of sulci into cuffs (Figure 15D, G; Extended Figure 11D). Key pattern predictions pulled from the path of each condition across parameter space were quantified

using FFT: zigzag patterns show peaks at characteristic wavelengths, while sulci and cuff power spectra are diffuse and circular, all consistent with experimental data (Figure 15F, Figure 14D).

We conclude, therefore, that the breakdown of epithelial ridges into sulci by *Hoxd13* is largely achieved through thickening and stiffening of the developing gut mesenchyme—rendering lower modulus and thickness ratios between the endoderm and mesenchyme—and a shift to isotropic growth; cuffs then resolve through a subsequent increase in modulus ratio and decrease in thickness ratio. However, though this finding advances our understanding of the role of *Hoxd13* in the hindgut, the mechanism by which this transcription factor alters tissue material and geometric properties remained unclear.

***Noggin* misexpression generates sulci and promotes mesenchymal thickening and stiffening**

As another test of our model, we examined the effect of *Noggin* misexpression in the midgut, which was previously shown to disrupt villi and generate a hindgut-like morphology, as well as alter radial geometry through ectopic muscle differentiation (Batts et al., 2006; Huycke, 2018; Nerurkar et al., 2017). Retroviral misexpression of *Noggin* in the midgut with RCAS-*Noggin* leads to the formation of a zigzag/ridge-sulci intermediate at E12, as in RCAS-*Hoxd13* at E14 (Extended Figure 12A, Extended Figure 10A). By E15, the *Noggin*-misexpressing midgut develops extremely disordered sulci folds with interspersed outgrowths resembling cuffs (Extended Figure 12A).

To examine the effect on endoderm surface folding and the mesenchyme, we stained sections for SMA and DAPI, and saw that the subepithelial mesenchyme develops ectopic muscle by E12 in the RCAS-*Noggin* midgut, as expected from previous work (Huycke et al.,

2019). The endodermal surface also forms creases essentially identical to those of the hindgut (Extended Figure 12B). At E15, muscle entirely fills folds, in a similar fashion to the muscularis mucosa in the hindgut, which is positioned closer to the endoderm than in the midgut (Extended Figure 12C).

Finally, mechanical measurements indicate that, while modulus of the endoderm is unaffected by Noggin misexpression, as with *Hoxd13*, the mesenchyme is stiffer and thicker, likely due to the expansion of stiff smooth muscle cells throughout the mesenchyme (Extended Figure 12D-E). Because the endoderm is slightly thicker, however, width ratio is not affected (Extended Figure 12E). Nonetheless, these parameters still place the RCAS-Noggin condition within the sulci-forming regime of our parameter space, further affirming supporting mechanical regulation of lumen morphology in the hindgut.

Mesenchymal TGF β signaling is upregulated in the hindgut and midgut + *Hoxd13*

To begin investigating pathways that might be regulated by *Hoxd13* in the process of establishing gut morphology, we performed bulk RNA sequencing to identify genes commonly differentially expressed in sulci/cuff-forming lumens of both the developing hindgut and *Hoxd13*-expressing midgut. Our pattern analysis and mechanical data suggested that E12 to E14 is the critical time when folding instabilities become distinct, so we collected tissue from the midgut, hindgut, and *Hoxd13*-expressing midgut at these times. Also, because *Hoxd13* misexpression was restricted to the mesoderm and mechanical changes occurred mainly in the mesenchyme layer, we only harvested mesodermal RNA (Extended Figure 11B-C).

Filtering for genes differentially expressed in both the hindgut and *Hoxd13*-expressing midgut relative to the normal midgut yielded a list of 128 genes at E12 and 721 genes at E14, with 62 in common between time points (Extended Figure 13A). Gene function analysis revealed that 16/62 (25%) of these genes are involved at various levels in the TGF β superfamily—including diffusible ligands and antagonists (*Inhba*, *Grem1*, *Chrdl2*), extracellular matrix (ECM) degradation or assembly factors (*Mmp2*, *Thbs2*, *Fmod*), downstream targets (*Ptn*, *Cd44*, *Actn1*), and others (Figure 18A-C; Extended Figure 13B-C) (Godwin et al., 2019; X. Wang et al., 2016). Additional key pathway ligands (*Gdf3*, *Tgfb1*) and ECM factors (*Mfap5*, *Mfap2*, *Col1a2*, *Col1a1*, *Eln*), become newly up- or downregulated at E14, when a phenotypic difference is first apparent in the *Hoxd13*-misexpressing midgut (Figure 18B, C) (Penner et al., 2002; Pompili et al., 2021).

To characterize the expression patterns of the most relevant and significantly upregulated TGF β pathway genes in our dataset, we performed HCR (hybridization chain reaction) smFISH at E14, focusing on factors that span different tiers of pathway regulation: 1) *Inhba*, a subunit for the TGF β ligand activin, 2) *Thbs2*, a thrombospondin that is known to release latent TGF β ligand sequestered in the ECM to promote signaling, and 3) *Cfc1*, a Nodal co-receptor (Figure 18D-E; Extended Figure 13C) (Derynck & Budi, 2019; Gurdziel et al., 2016; Havis et al., 2016; Tzavlaki & Moustakas, 2020; X. Wang et al., 2016). *Inhba* and *Thbs2* were differentially upregulated at both time points, while *Cfc1* was upregulated at E14 only (Figure 18D). HCR-FISH revealed that all three genes show increased expression specifically in the subepithelial mesenchyme (Figure 18E). Plots of radial intensity, from the basement membrane to the circumferential muscle, support higher overall expression levels extending to the

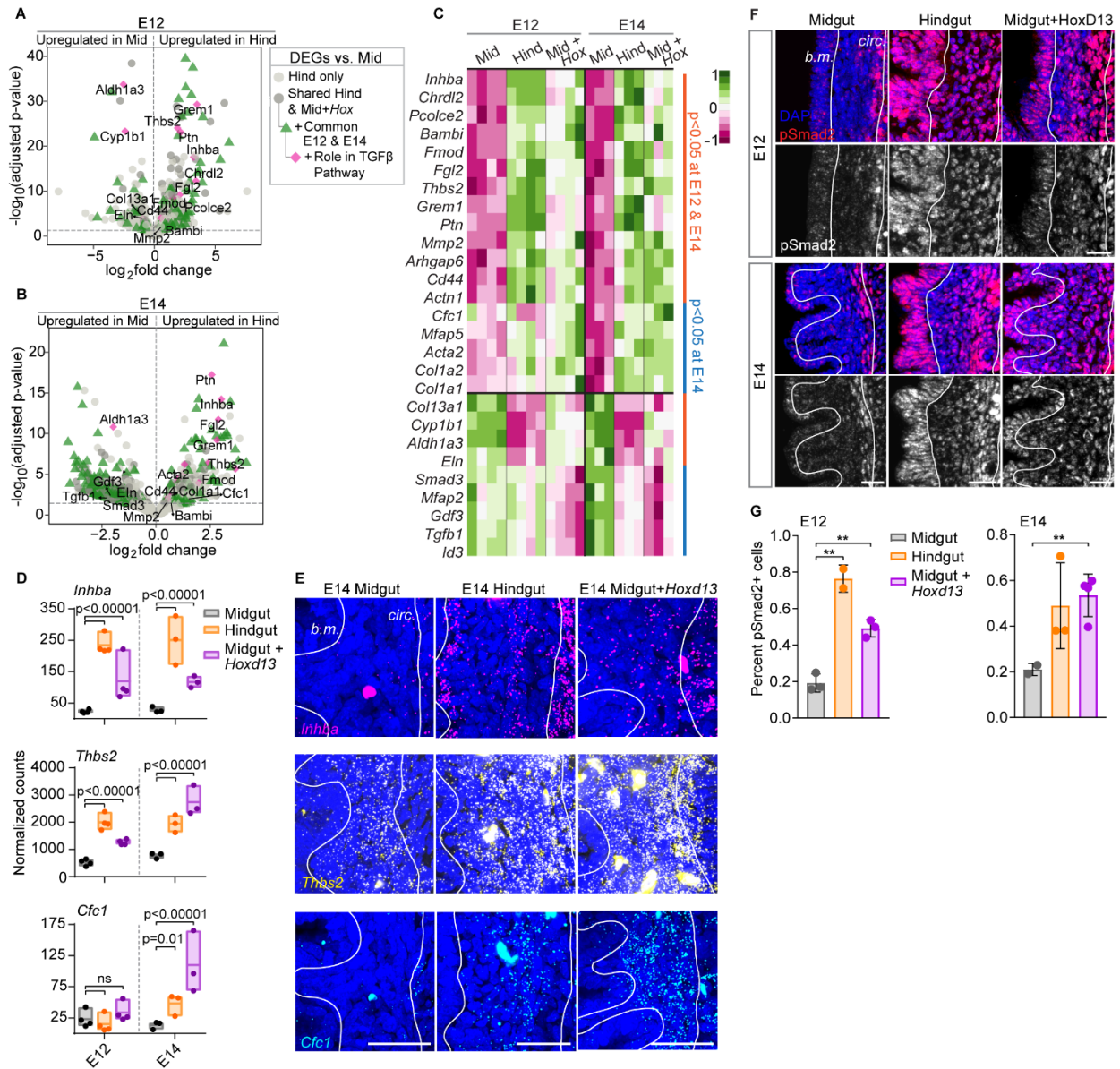


Figure 18. TGFβ signaling is upregulated in the hindgut and RCAS-*Hoxd13* mesenchyme

(A, B) Volcano plots with genes differentially expressed between the hindgut and midgut mesodermal layers at (A) E12 and (B) E14. Dashed gray lines indicate the significance cutoff at adjusted $p=0.05$. Of genes also up- or down-regulated in the RCAS-*Hoxd13* midgut vs. control midgut (darker gray dots), a proportion were commonly differentially expressed at both points (green triangles), and a subset of those were genes known to be involved in the TGFβ pathway (pink diamonds and gene name labels). (C) Heat map of final subset of TGFβ pathway genes, with genes upregulated in the hindgut and midgut + *Hoxd13* in the upper portion and downregulated below. Significantly differentially expressed genes at both E12 and E14 are indicated by orange lines, and only at E14 by blue lines. (D) Normalized counts with indicated p-adjusted values at E12 and E14 for three TGFβ genes of interest (ns, not significant; $n=4$ at 12, $n=3$ at E14) (E) HCR-FISH labeling each gene in the E14 subepithelial mesenchyme bounded by white lines. Note that large, irregular bright spots are auto-fluorescent enteric neural crest cells. Scale bar, 50μm. (F) pSmad2 immunostains in the subepithelial mesenchyme at E12 and E14. b.m., basement membrane; circ., circumferential muscle layer; Scale bar, 20μm. (G) Proportion of pSmad2-positive cells in regions bounded by white lines in (F) for E12 and E14 (**, $p<0.01$; t-test, $n=2-3$).

mesenchyme-epithelium border (Extended Figure 13D). Therefore, key TGF β factors are differentially expressed in the same sub-compartment (mesenchyme) where hindgut and *Hoxd13*-expressing midgut physical properties differ from the normal midgut.

To determine whether enrichment for TGF β genes in our RNA-seq dataset corresponded to differences in pathway activation, we stained for phosphorylated Smad2 (Figure 18F). At both E12 and E14, we observed higher proportions of pSmad2-positive nuclei in mesenchymal cells of the hindgut and *Hoxd13*-expressing midgut and, therefore, concordance between the site of pathway activation and gene upregulation (Figure 18G). Also consistent with HCR results, quantifications of radial pSmad2 signal intensity in this region reveal that, though all three conditions show highest intensities in the innermost longitudinal muscle layers, only segments with posterior identity have pSmad2+ nuclei extending throughout the subepithelial mesenchyme (Extended Figure 13E). As a result, TGF β activity is not only higher, but also decreases to a lesser extent from the circumferential muscle to basement membrane in the hindgut and *Hoxd13*-expressing midgut. Together, these results demonstrate that *Hoxd13* expression in the gut is sufficient to induce mesenchymal expression of TGF β -related genes and to instigate TGF β pathway activation.

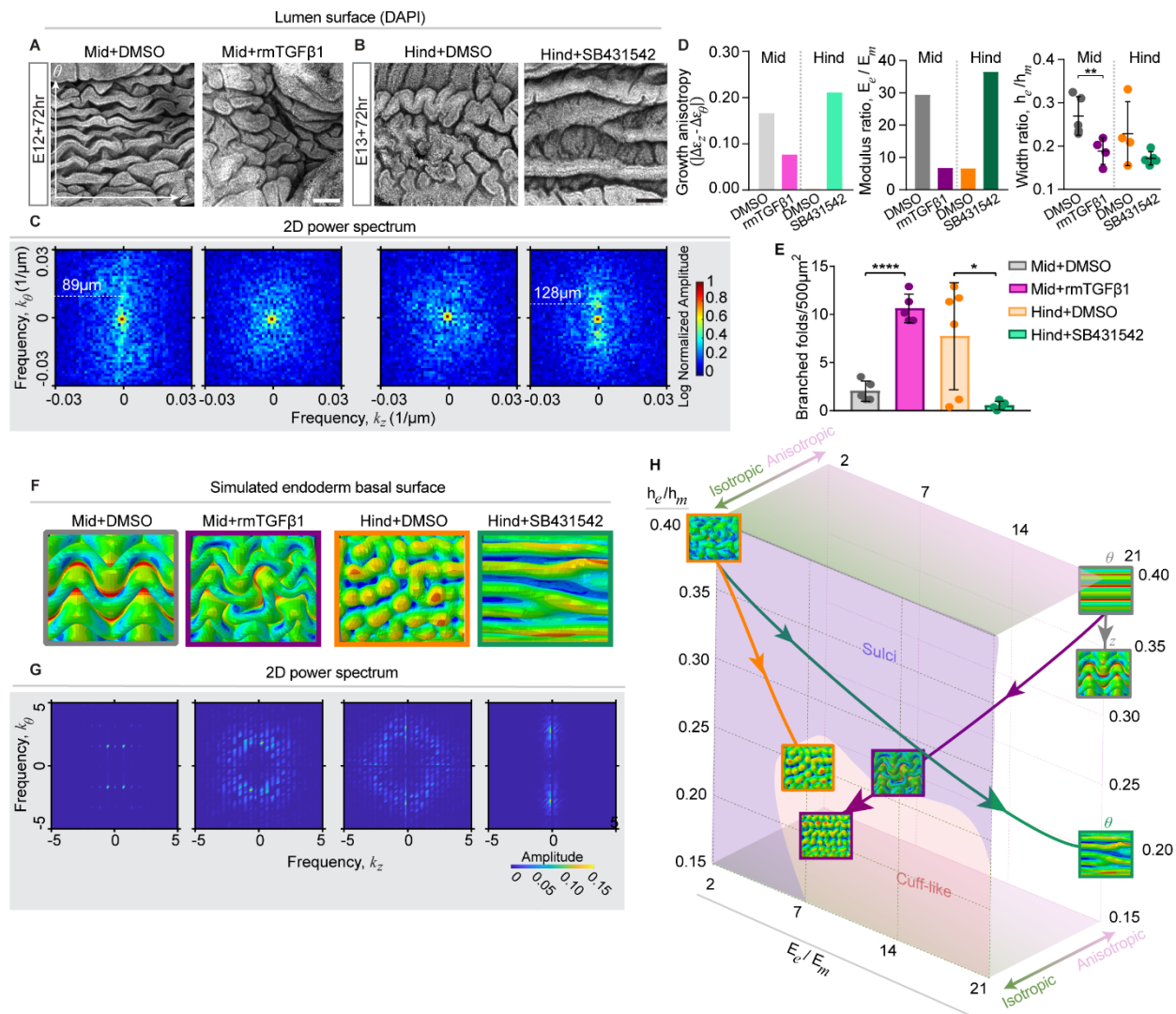
Modulating TGF β signaling toggles the lumen between mid-and hindgut forms

Our data strongly support a role for *Hoxd13* in stimulating spatially patterned TGF β pathway activity. We therefore next modulated TGF β signaling in *ex vivo* culture to ask if this pathway is relevant to specifying lumen morphology. Gut segments developed best when dissected at E12 for midguts and E13 for hindguts, suspended in media, and rocked at 37°C for 3

days, after which they were cut open to observe their lumens. Final morphologies of control midgut and hindgut cultures were close approximations of their *in ovo* counterparts, with midguts forming modest zigzags from initial ridges and hindguts forming sulci from flat surfaces (Figure 19A-B).

When cultured in the presence of recombinant mouse TGF β 1, the midgut developed a labyrinthine surface folding pattern more like the sulci and cuffs of the hindgut than ridges or zigzags of the midgut (Figure 19A). This conclusion was verified through the same quantification methods we used to compare folding patterns of mid- and hindguts that developed *in vivo*: we observed loss of clear pattern periodicity in the FFT and autocorrelation, and a significant increase in branched folds per unit area, consistent with TGF β transforming the midgut to a hindgut-like morphology (Figure 19A, C; Extended Figure 16A-B). Since a component of the Activin A heterodimer, which also activates the canonical TGF β pathway, was upregulated in our RNA-seq dataset, we also cultured the midgut with recombinant Activin and observed similar cuff-like folding as in the midgut with TGF β 1 ligand (Extended Figure 16I).

To then determine whether TGF β signaling is necessary in the hindgut to promote sulci and cuff morphogenesis, we cultured hindgut explants with SB431542, a TGF β inhibitor. Remarkably, instead of branched sulci, sharp and smooth ridges formed—a morphology never seen in the hindgut development trajectory—consistent with a role for TGF β in lumen shaping (Figure 19B, E). Accordingly, FFTs indicated that the lumen showed periodicity and orientation along the circumferential axis (Figure 19C, Extended Figure 16A-B). TGF β signaling downstream of Hoxd13 thus appears to guide the morphological trajectory of the large intestine toward sulci and cuffs.



TGF β activation is necessary and sufficient to promote hindgut mechanical properties.

To ask whether TGF β regulates the same tissue properties as *Hoxd13* to influence lumen shape, we again measured geometry, stiffness, and differential growth of endoderm and mesenchyme layers. We first found that the endoderm was not different in thickness, nor was the endodermal modulus affected by activating or inhibiting TGF β signaling (Extended Figure 16C, E). The composite modulus was also not different between the midgut and TGF β -treated midgut, but given that the mesenchyme thickness drastically increased, much as with *Hoxd13* misexpression, the mesenchyme modulus increased with TGF β activation (Extended Figure 16D, F). The resulting lower modulus and thickness ratios mimic the mechanical landscape of the hindgut (Figure 19D).

The modulus ratio of the hindgut with suppressed TGF β signaling also shifted in the direction expected from its morphology, but its width ratio did not. Instead of thinning of the mesenchyme, the composite modulus decreased with unchanged geometry, thus lowering mesenchyme modulus and increasing the modulus ratio (Figure 19D, Extended Figure 16D, F). Therefore, while TGF β signaling promotes thickening and stiffening of the midgut mesenchyme, it is not needed to thicken the hindgut mesenchyme; instead, suppression of the pathway mimics the midgut by dramatically lowering the mesenchyme modulus.

TGF β signaling promotes equibiaxial inner layer differential growth

To evaluate differential growth, we calculated strain after each culture experiment and compared to initial strains at E12 and E13 to measure relative growth on each axis (Extended Figure 16G-H). We expected that if growth properties are switched between compartments

with pathway perturbations, the change in strain will be roughly equal on both axes (isotropic) for the experimental midgut and more pronounced on one axis than the other for the experimental hindgut (anisotropic). Indeed, the TGF β 1-treated midgut experienced relatively similar changes in compression longitudinally and circumferentially (Extended Figure 16H). The SB431542-treated hindgut, by contrast, experienced no change in compression longitudinally, but a relative increase circumferentially. Thus, in line with genetic perturbations, growth was closer to anisotropic in the cases resulting in ridge/zigzag morphologies, and closer to isotropic when sulci formed (Figure 19D)—TGF β signaling therefore disrupted the anisotropic growth profile characteristic of the midgut, much like *Hoxd13*.

Simulated explant morphologies follow endogenous trajectories in the parameter space.

Like for the midgut, hindgut, and *Hoxd13*-expressing midgut, we next asked whether observed differences in mechanical properties in our explant cultures are sufficient to explain their lumen morphologies. We therefore mapped positions of explant morphological trajectories with and without TGF β perturbations to our 3D parameter space defined in Figure 15 using measured parameters. Our results fall within the domains predicted by folding simulations, with trajectories for midgut and hindgut conditions diverging between isotropic and anisotropic planes (Figure 19H). Simulations corresponding to explant results qualitatively match lumen pattern observations (compare Figure 19A-B to F). These results were once again supported by FFT analyses, where conditions with clear periodic patterns (Mid+DMSO, Hind+SB431542) showed distinct peaks at characteristic wavelengths, and conditions with more randomly arrayed morphologies (Mid+TGF β 1, Hind+DMSO) yielded diffuse, circular profiles

(Figure 19G). Our model results therefore show that we can, in fact, attribute lumen morphology changes upon TGF β perturbation to modified physical and geometric parameters.

Taken together, our data suggest that *Hoxd13* controls mesenchymal width, stiffness, and growth orientation (and, hence, gut lumen morphology) through transcriptional changes to genes in the TGF β pathway. That leaves unexplained, however, how TGF β signaling alters the physical properties of the gut tissues to achieve this effect.

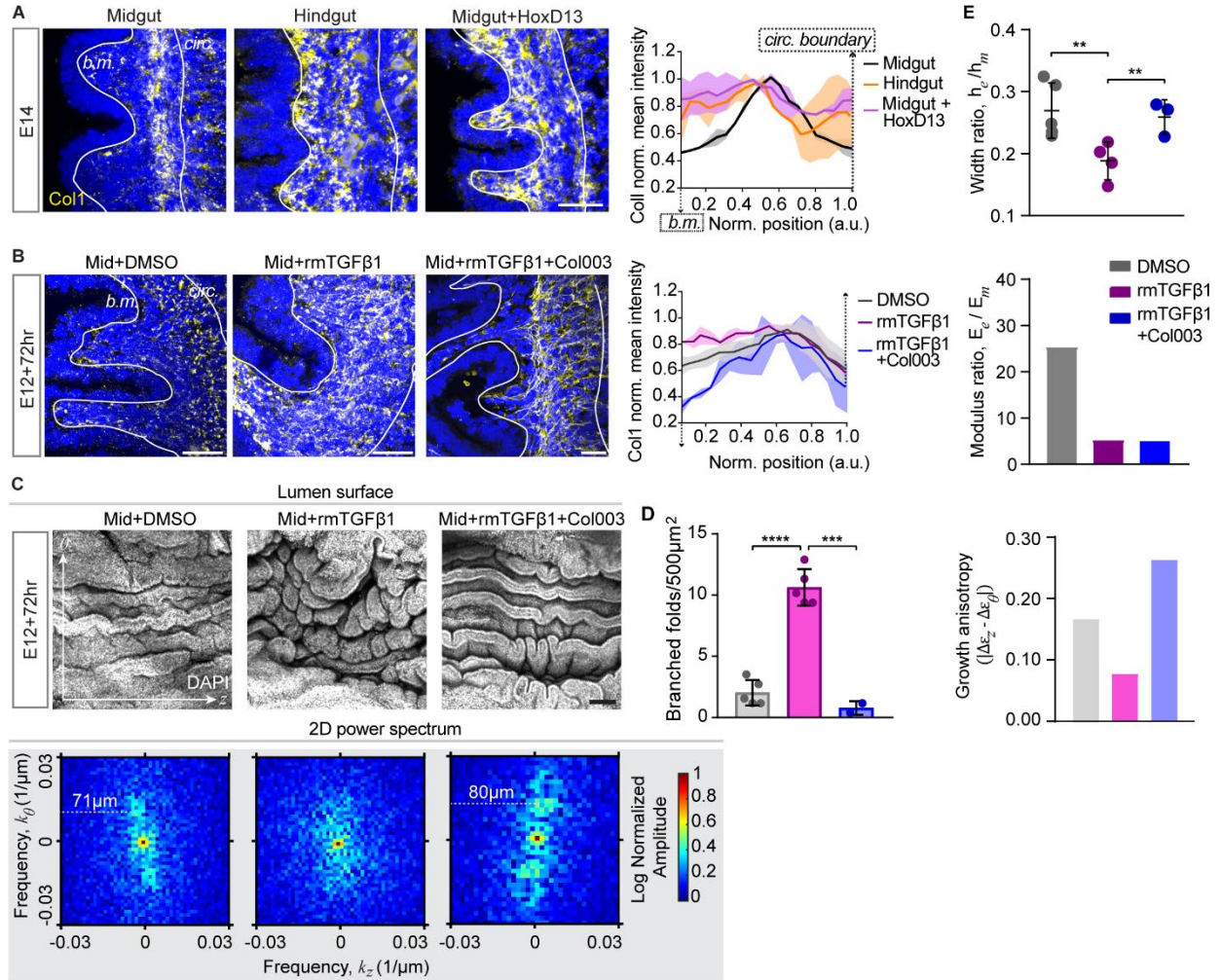
TGF β alters mesenchymal geometry through modulation of the ECM

A clue to at least one way TGF β activity affects the mechanical properties of the gut mesenchyme came from reexamining the list of genes that emerged from our RNA-seq experiment described above. Prominent among the genes differentially expressed in the hindgut and *Hoxd13*-expressing midgut versus the normal midgut at E14 were *Col1a1* and *Col1a2*, encoding the pro-alpha1 and alpha2 chains of collagen 1 (Figure 18B, C). Not only would a change in the ECM be expected to affect the geometric and material properties of tissues, but TGF β signaling is known to regulate collagen 1 production in other settings (reviewed in Verrecchia & Mauviel, 2002). Accordingly, we immunostained for Col1 in the midgut, hindgut and *Hoxd13*-expressing midgut. Analysis of radial Col1 distribution revealed that, while it is limited to a domain immediately adjacent to circumferential muscle in the midgut (roughly co-localizing with smooth muscle, pSmad2, and TGF β gene expression), it extends to the basement membrane in the hindgut and *Hoxd13*-expressing midgut, consistent with a possible role in altering properties of the subepithelial mesenchyme, as it does in other tissues (Figure 20A) (reviewed in Rozario & DeSimone, 2010). We confirmed this observation by

plotting radial mean intensity of the collagen signal from the basement membrane to circumferential muscle boundary (Figure 20A).

To test whether TGF β regulates collagen distribution in the developing gut, we first tried culturing the hindgut in the presence of Col003, an Hsp47 inhibitor that prevents secretion of collagen (S. Wu et al., 2022). However, this condition had no effect on lumen morphology, likely due to pre-existing collagen that is unaffected by halted secretion (Extended Figure 17A). Therefore, as an alternative to test whether TGF β regulates collagen distribution to change the lumen pattern, we instead cultured the midgut—where ectopic TGF β transforms the epithelium to a hindgut-like morphology—with both TGF β 1 and the collagen secretion inhibitor. While TGF β , on its own, is sufficient to change the midgut luminal morphology to resemble that of the hindgut, it is unable to do so when collagen deposition is blocked (Figure 20C). As is the case of *Hoxd13* misexpression in the midgut, TGF β treated midguts display Col1 extending to the basement membrane, but this localization is lost when collagen secretion is inhibited with Col003 (Figure 20B). Moreover, the resulting midgut lumen resembled the control, with a prominent circumferential periodic pattern at a similar wavelength and few branched folds (Figure 20C-D; Extended Figure 16A-B).

In directing hindgut-specific epithelial morphogenesis, TGF β signaling, downstream of *Hoxd13* activity, regulates a number of physical properties of the developing gut, including tissue geometry, growth anisotropy and relative stiffness. The result of exposing the developing midgut to both TGF β and Col003 indicates that one prominent aspect of this regulation is mediated by collagen production. To determine which of the physical properties are dependent on collagen, we examined the material and geometric properties of the midgut treated with



both TGFβ and Col003. Blocking collagen secretion did not affect the increase in mesenchyme modulus and, therefore, decrease in modulus ratio seen in the TGFβ treated midguts (Figure 20E, Extended Figure 16F). However, the TGFβ-induced mesenchyme thickening (which

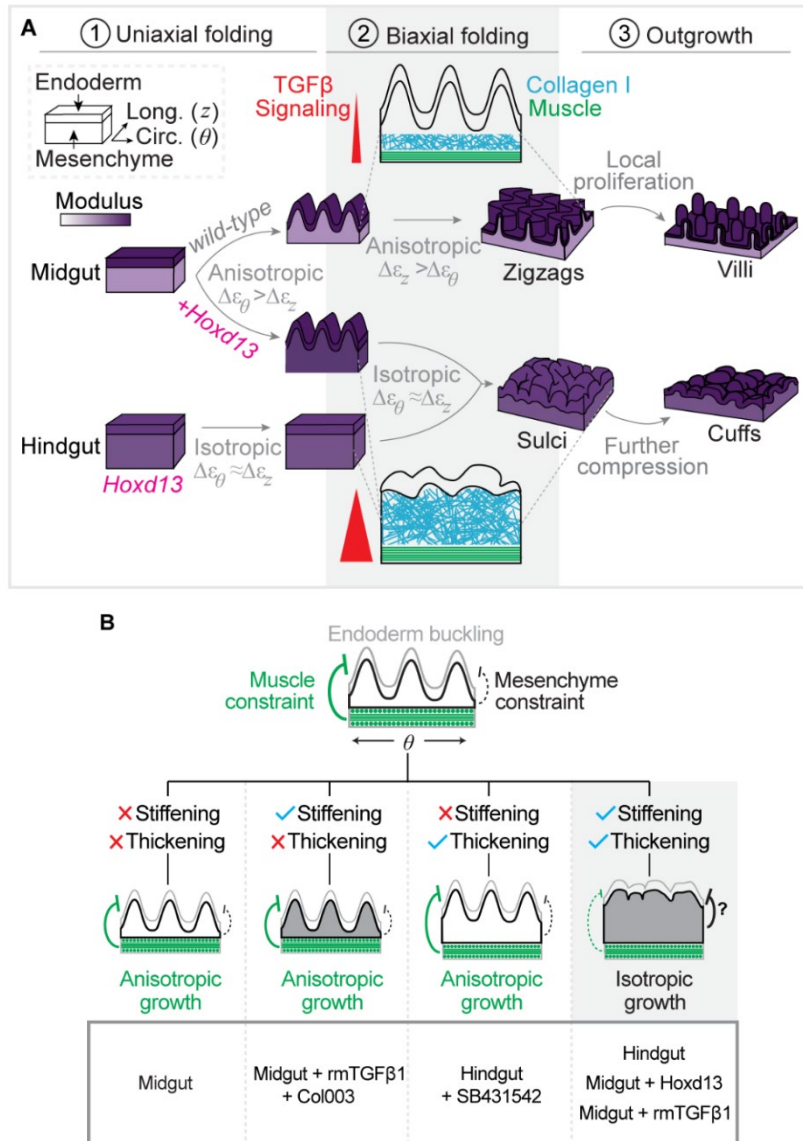


Figure 21. A genetic and mechanical model of differential intestinal morphogenesis

(A) Summary of the integration of gene expression, TGF β pathway activation, and collagen remodeling to define hindgut lumen morphology downstream of *Hoxd13*. The tissue composite is represented as a two-layered rectangular prism, modulus is represented as a purple gradient, and dominant growth directions and categorizations (isotropic vs anisotropic) accompany each arrow. The area in gray highlights the biaxial folding transition (to zigzags or sulci) when the influence of TGF β on tissue properties guides the lumen surface toward a hindgut-like state. Enlarged schematics during stage 2 show a longitudinal view highlighting collagen, muscle and TGF β signaling patterns. (B) Summary of control and perturbed lumen morphology results and effects on tissue geometry, stiffness, and growth. Gray is the endoderm surface, black outlines the mesenchyme, and green indicates smooth muscle layers in a circumferential view. Green and black lines indicate expected constraints imposed on the endoderm from the muscle and mesenchyme, respectively, where a dashed line means little or no constraint, and a thick line means predominant constraint. The four cases below capture results of different combinations of mesenchymal stiffening and thickening, where stiffening is indicated by gray shading and thickening is indicated by a taller mesenchyme layer. Green and black lines again suggest sources of primary constraint/minimal constraint. The gray box at the bottom lists experimental conditions corresponding to each case.

decreased width ratio) was rescued, and growth anisotropy was restored (Figure 20E; Extended Figure 16D, G-H). This result suggests that deposition of new collagen protein contributes to mesenchyme geometry (although not stiffness), and that these geometric changes are required for TGF β signaling to successfully transform the midgut lumen to a hindgut-like morphology (Figure 21B).

Orientation of ECM, but not muscle, correlates with stiffness of the mesenchyme

Another property of both ECM and muscle fibers that affects growth and physical properties is alignment. As fiber alignment can be both a driver and readout of growth anisotropy, we hypothesized that loss of fiber orientation may be related to the observed shift to isotropic growth in sulci-forming lumens (H. Aubin et al., 2010; Prager-Khoutorsky et al., 2011; Sawhney & Howard, 2002). We first examined inner muscle layer orientation in the midgut, hindgut, and midgut + *Hoxd13*, and found that, though hindgut inner muscle loses longitudinal alignment and becomes disordered by E18, the *Hoxd13*-misexpressing midgut retains longitudinal alignment (Figure 22A-B). However, fibrillin-like 2 (*Fbn2*), another fibrous component of the gut mesoderm that is regulated by ECM-related candidates from our RNA-seq dataset, is aligned longitudinally in the midgut but more randomly in the hindgut and RCAS-*Hoxd13* (Figure 22C-D) (Pompili et al., 2021; Sengle & Sakai, 2015; Yin et al., 2019). To see if TGF β also regulates fiber orientation, we characterized *Fbn2* alignment in cultured gut segments, and found that ECM fibers are indeed randomized with TGF β 1 treatment in the midgut (Figure 22E, G). However, Col003 did not rescue this result despite the lumen re-adopting a midgut-like morphology and circumferential anisotropic growth, suggesting that a

disordered ECM in the subepithelial compartment is not sufficient to confer the biaxial sulci morphology.

Additionally, we see a shift from disordered to strongly oriented fibers in the hindgut treated with SB431542, supporting a role for TGF β in disrupting ECM orientation. However, fibers are aligned in the orthogonal direction (longitudinal) from the direction of growth anisotropy (circumferential), suggesting once again that fiber orientation alone does not instruct the direction growth (Figure 22F, G). However, loss of fiber orientation does appear to correlate with modulus, where conditions with high mesenchyme modulus show disordered fibers (Figure 22G; Extended Figure 16F). Because a mesh-like arrangement of fibers is a hallmark of a crosslinked fibrous network, this may be an indication of ECM crosslinking by TGF β , though further investigation and perturbations of collagen crosslinking enzymes will be needed to support this claim (Bastiaansen-Jenniskens et al., 2008; Brereton et al., 2022; X. Chen et al., 2012; Rodriguez-Pascual & Slatter, 2016). Nonetheless, growth orientation does not appear to be controlled by fiber alignment.

Myofibroblast-related genes are upregulated in subepithelial cell layers

Finally, we hoped to begin understanding the cell fate or state induced by Hoxd13 and TGF β upregulation in ECM-secreting mesenchymal cells. To this end, we performed spatial transcriptomics using Light-seq to specifically identify differentially expressed cells within the subepithelial compartment (from the basement membrane to the muscularis mucosa) at E14 (Figure 23A, Light-seq spatial RNA sequencing). Our list of top differentially expressed genes shared between Midgut vs. Hindgut and Midgut vs. Midgut+Hoxd13 included

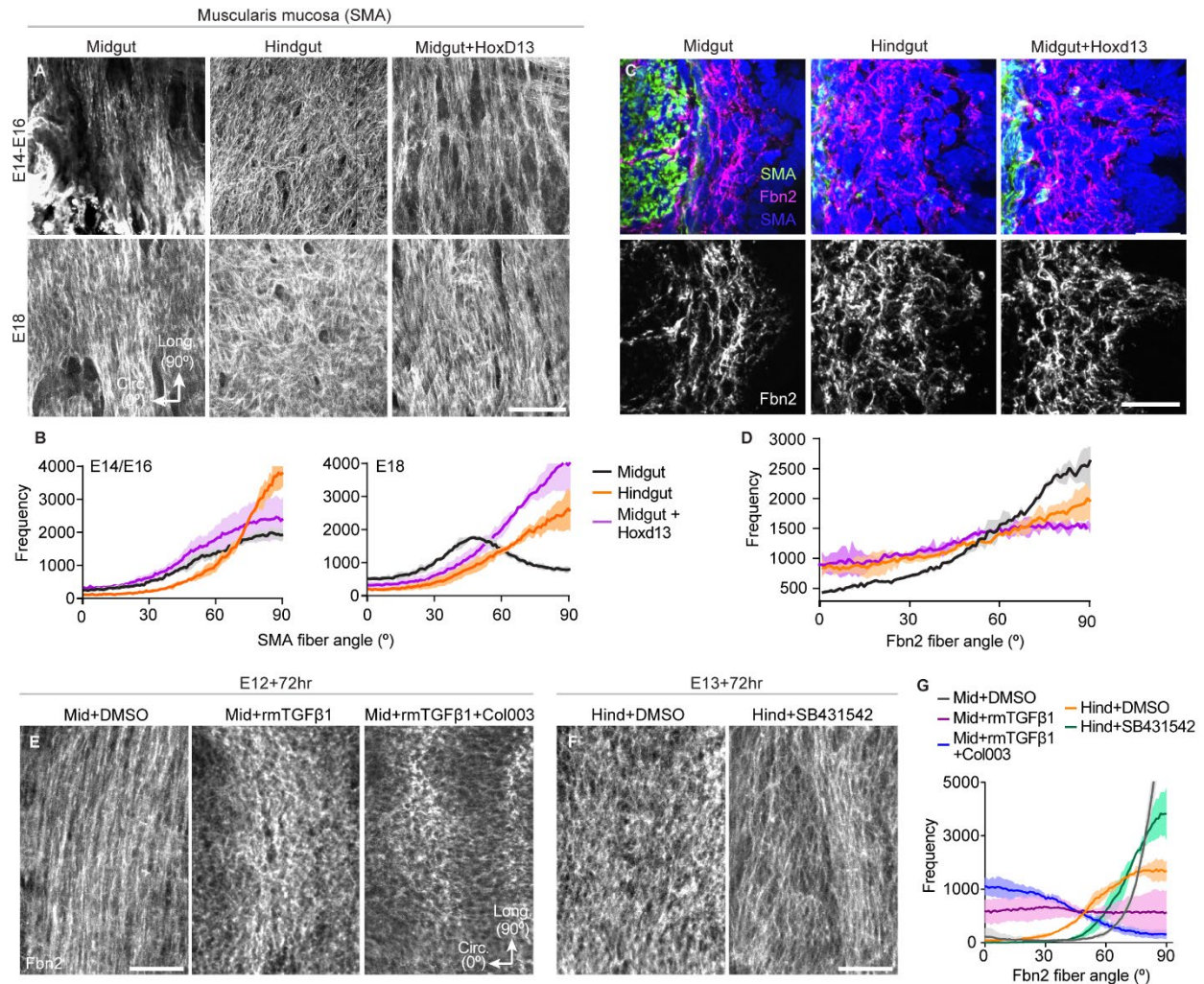


Figure 22. Fibrillin fiber orientation correlates with mesenchyme modulus

(A) Top-down views of SMA-stained midgut, hindgut, and *Hoxd13*-misexpressing midgut inner smooth muscle (muscularis mucosa) layers. Midgut and midgut + *Hoxd13* images are at E14, and hindgut is at E16. Longitudinal axis is vertical and circumferential is horizontal. Scale bar, 100 μ m. (B) Smooth muscle fiber alignment frequencies, where 0 $^{\circ}$ is circumferential and 90 $^{\circ}$ is longitudinal. n=3 images. (C) Fbn2, SMA, and DAPI-stained sagittal sections zoomed into the subepithelial mesenchyme (lumen is on the left). Scale bar, 20 μ m. (D) Fbn2 fiber alignment frequencies determined from images in C, where vertical image axis is longitudinal and 90 $^{\circ}$. n=3 images. (E-F) Fbn2 immunostain top-down views as in A for (E) midgut explants and (F) hindgut explants. Scale bar, 50 μ m. (G) Fbn2 fiber alignment frequencies for explants as in B and D. n=3 images.

several genes known to be involved in myofibroblast function and differentiation, which is most often induced by TGF β signaling (Figure 23B)(Vallée & Lecarpentier, 2019). For example, *Tagln* and *Myh9* are downstream targets of TGF β in the context of myofibroblast differentiation (Figure 23C) (Aldeiri et al., 2017; Guerrero-Juarez et al., 2019; Klingberg et al., 2013). Other

factors like *Smoc1*, *Thbs2*, and *Fbln1* are known regulators of TGF β pathway activation (Awwad et al., 2015; Bornstein, 2001; G. Liu et al., 2019). *Vcan* is another ECM component that regulates and is regulated by TGF β signaling, and *Mtss2* is an I-BAR containing protein involved in Rac activation, which is important for the contractile activity of myofibroblasts (Figure 23B) (Aspenstrom, 2014; D'Urso & Kurniawan, 2020; Hattori et al., 2011; Michalik et al., 2018; Shiwen et al., 2009).

To validate differential gene expression in the subepithelial mesenchyme, we performed HCR-FISH on *Smoc1*, *Mtss2*, *Fbln1*, and *Vcan*, and found that *Smoc1*, which is a TGF β -activating extracellular protein secreted by endothelial cells, is found in the muscularis mucosa, which intersects with the vascular plexus in the hindgut (Figure 23D; Extended Figure 15C) (Delgado Lagos et al., 2021). *Smoc1* expression is expanded in the RCAS-*Hoxd13* midgut compared to the control; *Mtss2* also appears to radiate from the muscularis mucosa/vascular/enteric plexus region in the hindgut and midgut + *Hoxd13* but not the control midgut (Figure 23D). *Fbln1* extends throughout the subepithelial mesenchyme in all conditions but is more heavily expressed, as expected, in the hindgut and RCAS-*Hoxd13* midgut. This is also the case for ECM protein *Vcan*, which appears more lowly expressed in the control midgut mesenchyme than *Fbln1* (Figure 23D). Thus, myofibroblast-related genes are differentially expressed in the subepithelial mesenchyme, where we believe ECM remodeling leads to differences in mechanical properties and, in turn, morphology.

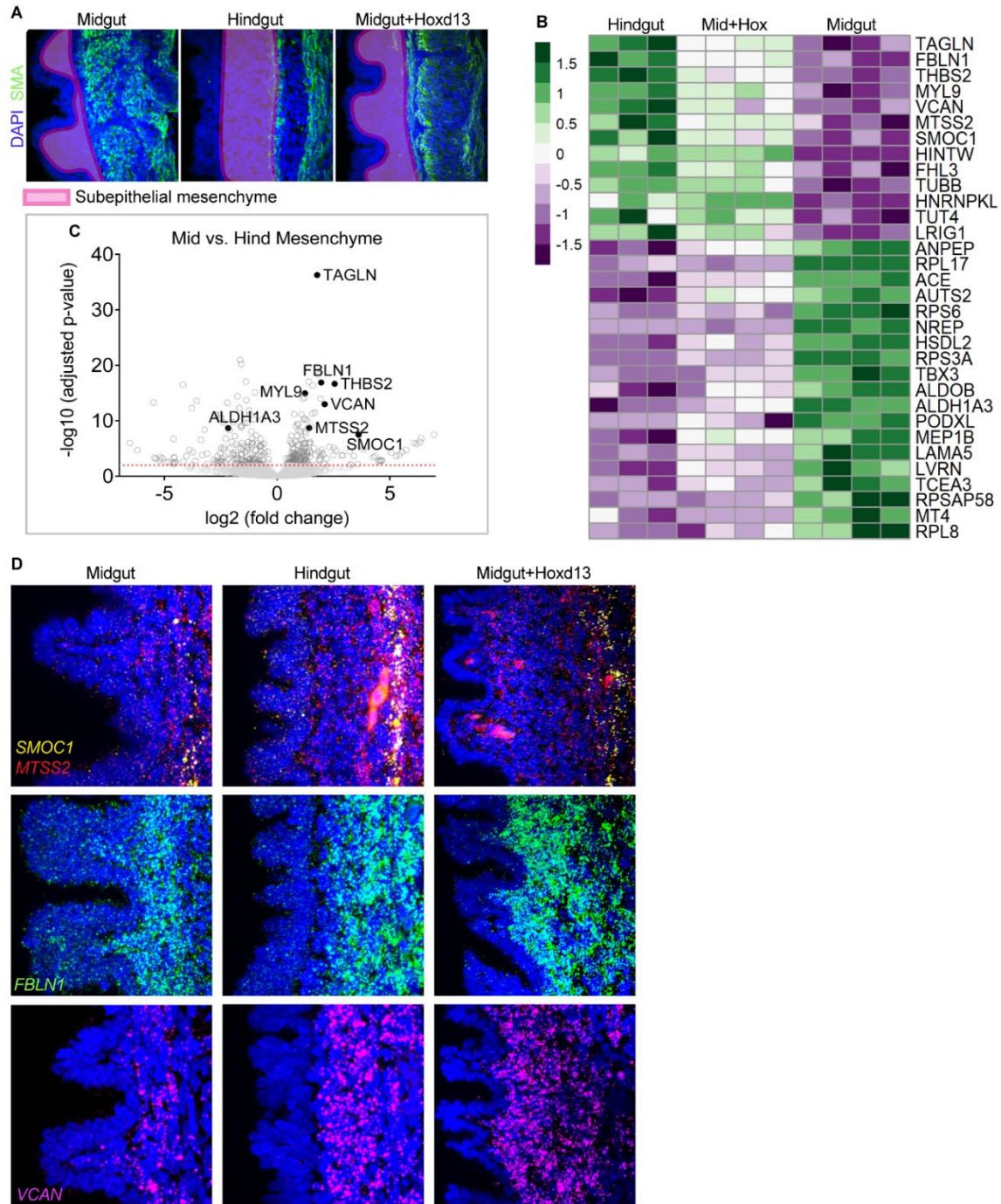


Figure 23. Subepithelial differentially expressed genes include myofibroblast-related factors

(A) Examples of E14 midgut, hindgut, and midgut + *Hoxd13* sections used for Light-seq, where areas chosen for RNA extraction are outlined by a pink shaded box. The subepithelial mesenchyme of each condition was targeted, from the basement membrane to the inner muscularis mucosa. (B) Heatmap of top genes commonly differentially expressed between the midgut and hindgut, and midgut and midgut + *Hoxd13*, at significance cutoff of $p < 0.01$. (C) Volcano plot of DEGs shown in part B, with genes involved in myofibroblast differentiation or function labeled. Red line indicates significance threshold. (D) HCR-FISH for 4 genes performed on sagittal sections for each condition, zoomed into the targeted subepithelial mesenchyme region. Endoderm and lumen are on the left.

Conclusions

For many years, genetic evidence had made it clear that Hox and ParaHox gene activity determines regional differences in the developing gut tube, and that Hoxd13, in particular, plays a key role in specifying hindgut morphology (Kondo et al., 1996; Roberts et al., 1995). However, how this critical Hox gene affected downstream gene expression and cell behavior to alter gut morphogenesis remained unclear. The data presented here allows us to propose the following model (Figure 21A):

The hindgut and the midgut start out as continuous simple tubes of endoderm surrounded by mesenchyme, with a smooth circular lumen in the middle. However, different regions of this tube express different Hox codes, including Hoxd13 in the hindgut. In the midgut, where Hoxd13 is absent, TGF β signaling is high only at the interface of the smooth muscle, and deposition of a complex ECM network is restricted to this region. The mesenchyme therefore remains thin, and its stiffness is significantly lower than that of the endoderm, producing high endoderm-to-mesenchyme width and modulus ratios. Under these conditions, the smooth muscle layers sequentially differentiate and form a barrier to circumferential and then longitudinal expansion of the endoderm. The resultant compressive forces lead to smooth folding into ridges, followed by zigzags.

In contrast, in the hindgut, Hoxd13 drives an expansion of TGF β signaling throughout the subepithelial mesenchyme, thickening it in the process by inducing deposition of new collagen extending to the basement membrane. TGF β also stiffens the mesenchyme, and the inner composite undergoes isotropic growth, which, together with lower width and modulus ratios, leads to creased sulci on the endodermal surface. With further compression and a shift

to a progressively increasing modulus ratio, sulci segment into randomly arrayed outgrowths, or cuffs.

Hoxd13 misexpression in the midgut mesenchyme similarly drives an expansion of TGF β signaling and ECM deposition throughout the subjacent mesenchyme, at the stage when ridges would otherwise be transforming to zigzags. TGF β stiffens and promotes collagen deposition to thicken the mesenchyme, as in the hindgut, resulting in low modulus and thickness ratios, isotropic growth, and consequent formation of sulci and cuffs as morphogenesis progresses.

Our findings also provide insight into why the hindgut lumen fails to undergo stepwise buckling despite stepwise muscle differentiation. In the normal midgut, the endoderm undergoes anisotropic growth because muscle barriers restrict its expansion first circumferentially, then axially; the mesenchyme is simply a thin and soft intermediary in between (Figure 21B). However, bending stiffness of the mesenchyme scales with both its Young's modulus and cross-sectional geometry, so stiffening and thickening of the mesenchyme would increase its resistance to deformation and, hence, decrease the role of muscle in dictating endoderm buckling. We therefore propose that in the hindgut and midgut treated with either *Hoxd13* or TGF β , the endoderm buckles simultaneously on both axes because it is subject to constraint from the stiffer and thicker mesenchyme layer, preempting the constraint from highly oriented muscle (Figure 6B). Noggin misexpression in the midgut has a similar effect on morphology and mechanical properties. Furthermore, as evidenced by the hindgut treated with SB431542 and the midgut treated with TGF β and Col003, neither thickening nor stiffening alone is sufficient to overcome muscle constraint on endoderm growth to confer sulci and cuffs. Interestingly, the formation of secondary folds in the hindgut, according to our model in

Chapter 2, relies on the stabilization of creases--here, we believe that creasing is fixed by presumed constraint from the mesenchyme, thus explaining the formation of large scale wrinkles in these conditions as well.

DISCUSSION

Positional trends in the gut morphogenic landscape

The serial compartments that make up the GI tract have fascinated physicians and philosophers for millennia. From the writings of Herophilus (c. 300 BCE) and Galen (c. 200 CE), to the drawings and writings of Ibn Sina (c. 1000 CE) and Leonardo Da Vinci (c. late 1400s CE), descriptions of intestinal form and function focused on the major morphological features that we still associate with each region—extensive folds in the muscular esophagus permit passage of food into the stomach, and the short, straight, and “dilated” colon uses its muscular wall to expel waste from the body (Bay & Bay, 2010; Galen, 2019; Keele, 1972; Mazenganya & Bhikha, 2018). Yet, how does the embryo differentially sculpt anteroposterior gut domains to generate this morphological complexity?

The three studies presented in this thesis have investigated the biochemical and biomechanical rules that generate unique radial and biaxial lumen morphologies in the chick fore-, mid-, and hindguts. In the process, we have uncovered general principles that govern how each region is shaped as a function of AP position along the gut.

Changes in growth and material properties from the foregut to hindgut

Anterior-posterior gradients of biochemical signals and transcription factors are classic and fundamental tools the embryo uses to pattern the body. As discussed in Patterning positional identity along the early gut, several prominent posterior-to-anterior gradients (with some evidence of cross-talk between them) help determine gut regional identity; for example, Sonic hedgehog signaling induces Bmp4 and Hox gene expression to induce hindgut fate, and a gradient of Wnt signaling similarly induces the master intestinal transcription factor Cdx2, leading to large intestinal fate at high concentrations and small intestinal fate at lower concentrations (Maimets et al., 2022; Roberts et al., 1995; Sherwood et al., 2011; Sprangers et al., 2020). Concurrently, high expression of the transcription factor Sox2 in the anterior gut promotes foregut identity by suppressing Cdx2 activity (Raghoebir et al., 2012).

We have instead noted whole-gut gradients in geometric, growth, and mechanical properties—modulus measurements reveal a linear decrease in stiffness ratio from foregut to hindgut resulting from AP trends in both endoderm and mesenchyme modulus. During early muscle appearance and growth, the thickness of the muscle layer increases from the foregut to hindgut, and the relative contributions of endoderm and mesoderm to tube radius switch from anterior to posterior—while the wall thickness is dominated by mesoderm in all regions, the hindgut shows a larger mesodermal fraction than the foregut. Similarly, at later stages, radius ratio is low posteriorly and high anteriorly, while width ratio is low anteriorly and high posteriorly.

Such large-scale trends in mechanical properties have not received as much attention as molecular gradients, and it is difficult and likely unrealistic to connect these properties to

morphogen gradients (e.g. FGF, Wnt, Bmp) present in the gut at much earlier stages for AP patterning. Nonetheless, several recent studies have discovered gradients of mechanical properties, including stiffness, fluid/solid-like properties, and contractility, that guide morphogenesis on the scale of collective cell behaviors in systems like migrating neural crest, the developing lung, and the elongating zebrafish body axis (Barriga et al., 2018; Goodwin & Nelson, 2021; Gustafson et al., 2022; Nerurkar et al., 2019; Pinheiro et al., 2022). It therefore stands to reason that AP patterns in physical properties may trace upstream to a larger organizational scheme orchestrated by molecular cues. We also found that the distal-most part of the midgut appears hindgut-like by hatch, further pointing to mechanically graded boundaries between regions (Extended Figure 18).

Finally, in the early gut, we have noted positional trends in both lengthening, where the esophagus elongates the most the hindgut the least, and in nuclear density—mesodermal nuclei are less dense in the foregut and more dense in the hindgut. To understand the basis for density differences, we stained for hyaluronic acid (HA), an exclusively extracellular ECM component, and found that it fills intercellular spaces in the foregut but is mostly absent in the hindgut. Furthermore, while cells are tightly packed with clear, aligned cortical F-actin in the hindgut, they are instead suspended in ECM without obvious actin organization in the foregut (Extended Figure 3). Given that directional growth may come from collective cell behaviors in the gut, one possible explanation for differential elongation is that the foregut mesenchyme is more fluid-like and able to flow due to the presence of a viscous ECM component (HA), while the packing and alignment of cells in the hindgut mesenchyme makes it more solid-like (Cowman et al., 2015; Parada et al., 2022; X. Wang et al., 2020). Furthermore, materials that

experience cyclic contractions can undergo plastic, irreversible deformations if they are viscoelastic, depending on the strength of the contractions (Stokkermans et al., 2022). Since the foregut also expresses the contractile marker Myh11 at much higher levels than the other regions (Extended Figure 1), its mesenchyme may elongate more as part of a viscoplastic response to heavy contractile stress, while the hindgut behaves as an elastic solid and grows isotropically instead. Measurements of viscoelasticity using stress-relaxation tests and live imaging will be important next steps in testing this hypothesis.

Tuning regional responses to Shh and Bmp signaling

Our explant experiments and smFISH data suggest that the foregut is more sensitive to Bmp signaling, while the hindgut is less sensitive to muscle signals. There are many ways that differential sensitivity to biochemical signals can be patterned, including modulating the competence of receiving cells, feedback mechanisms, and the through the introduction of adaptation mechanisms (Sagner & Briscoe, 2017). For example, in the neural tube, Shh signal is integrated over time--cells closer to the signal express pathway antagonists, while cells further away become sensitized over time. Furthermore, higher levels of ligand become equivalent to longer durations of signaling due to the intricate signal processing regulatory network (Dessaud et al., 2008). For Bmp signaling, extensive combinatorial interactions of receptors, ligands, and antagonists make a straightforward prediction based on gene or protein levels alone difficult (Antebi et al., 2017). However, given the increased deposition of HA in the foregut, one intriguing form of pathway regulation may come from interactions between Bmp receptors and

CD44, the receptor for HA, which have been shown to augment pathway activation (R.-L. Wu et al., 2018).

Properties shared between the foregut and hindgut

In some cases, among organisms with a regionalized GI tract, the foregut and hindgut share features that are absent from the midgut. For example, the inner linings of the foregut and hindgut in *Drosophila* are ectodermally-derived, while the midgut lining is endodermal (Myat, 2005). This idea extends to mammals as well, where the most anterior and most posterior parts of the alimentary canal are made up of ectodermal skin. Also in mammals, the foregut and hindgut both ultimately incorporate a mix of striated and smooth muscles into their tube walls (Gopalakrishnan et al., 2015; Kondo et al., 1996; Krauss et al., 2016). In our studies, we note three cases where these regions share similar properties: the formation of the inner muscularis mucosa within large scale wrinkles instead of at their bases, equal proliferation rates between the mesenchyme and muscle during early tube development, and the appearance of post-buckling motifs at late stages, after innermost muscle development. While the molecular basis for these observations is unclear, it is intriguing that muscle properties and morphologies would be similar on either end of the gut, given the common presence of striated muscle in other organisms. It is possible that these properties are variations on a more ancient theme of common muscular functionalities on either end of the gut.

From regional gut identity to specialized morphology

One of the most decisive 18th century apologies for epigenesis—the progressive elaboration of embryonic structures from simpler origins—was Caspar Friedrich Wolff’s treatise *De formation intestinorum*, where he described the “foldings, flexions, and fusions” that mold the developing chick gut (Aulie, 1961; Schmitt, 2005; Wolff, Caspar Friedrich, Jean-Claude Dupont, 1769; Wolpert, 2004). Though this idea is now accepted as fact, the opposing view, where the adult body is pre-made in the embryo, gained a new interpretation with the pervasive 20th century focus on genetic determinants of cell fate (Fagan, 2022). It is now clear that both molecular patterning and physical forces cooperate to shape organs, but the phenomena that translate gene expression into forces (and vice versa) have, until recently, remained a mystery (de Belly et al., 2022; Hallou & Brunet, 2020; LeGoff & Lecuit, 2016; Mitchell et al., 2021).

In few cases is this problem more salient than the question of how Hox genes specify appropriate regional forms. In the fly, the *Dfd* homeotic compartment regulates actomyosin to generate tension and, in turn, tissue curvature-induced invagination at the boundary between the head and neck (Villedieu et al., 2023). The homeotic gene *Ultrabithorax* shapes the developing wing pouch via downregulation of *Mmp1*, which degrades extracellular matrix (De Las Heras et al., 2018). Additionally, *Ubx* and *Antp* tune actomyosin contraction to induce convergence-extension movements in the *Drosophila* gut, leading to a reproducible folding pattern (Mitchell et al., 2022). Other forms of downstream gene regulation by Hox genes that likely affect morphogenesis have of course been elucidated, but few have identified physical forces and properties regulated by positional identity during organogenesis (Denans et al., 2015; Hawkins et al., 2021; Imura & Pourquié, 2006; Moreau et al., 2019; Salsi et al., 2008;

Zakany et al., 2017). To understand how embryos are built, it is fundamentally necessary to bridge this gap in our knowledge.

An instructive role for *Hoxd13* in hindgut morphogenesis

We have shown that in the chick hindgut, mechanical properties of the deforming tissues that define lumen morphology, and thus differentiate it from that of the midgut and foregut, are regulated by expression of the highly conserved Hox gene *Hoxd13*. *Hoxd13* activates expression of genes involved in TGF β signaling which, in turn, modulates properties of the ECM to confer hindgut-specific mechanical properties. In this way, we have used the hindgut as a model to bridge the gap between Hox expression and morphogenesis by describing a series of downstream events that physically mold developing tissues.

Formative work on Hox patterning in the mouse intestine pinpointed *Hoxd13* mutant phenotypes to the terminal anorectal region (Kondo et al., 1996; Warot et al., 1997). However, expression of *HFga13* (dominant negative *Hoxa13*) in the chick affects development of the entire hindgut caudal to the ceca (Barbara & Roberts, 2002). Given that *Hoxa13* and *Hoxd13* generally show similar phenotypes, especially for overexpression in the chick, our results suggest that Hox group 13 genes are both necessary and sufficient for hindgut morphogenesis. It is worth noting, however, that *HFga13* was misexpressed in the endoderm—it is possible that mesodermal suppression of these genes would offer an informative variation on the reported phenotype.

Other Hox and ParaHox genes have also been implicated in hindgut development. *Cdx2* is a master regulator of posterior intestinal fate that operates independently of the Hox code.

Upon its ablation, the intestinal epithelium adopts anterior cell fates, and ectopic *Cdx2* expression in the esophagus or stomach causes intestinal metaplasia (Gao et al., 2009; Pinto et al., 2015; Silberg et al., 2002). Though expressed throughout the intestine, *Cdx2* controls regionalization into small and large intestines in a dose dependent manner via Wnt signaling (Sherwood et al., 2011). Notably, *Hoxd12* is the only other *Hoxd* gene exclusively expressed in the hindgut in the chick and mouse; it is needed for both development of the anal sphincter and suppression of cecal budding at the small/large intestinal boundary, where all other *Hoxd* genes are highly expressed (Zacchetti et al., 2007; Zákány & Duboule, 1999). Whether the mechanisms downstream of these genes regulate physical properties to promote posterior identity is not known.

We and others (Kondo et al., 1996; Roberts et al., 1998a) have found that *Hoxd13* regulates multiple aspects of hindgut development, including epithelia folding, smooth muscle differentiation and specification of mucin-producing cells. Here we focused on elucidating the mechanism by which *Hoxd13* controls one of these phenotypes, the morphogenesis of the luminal surface into cuffs, as opposed the villi seen in the midgut. It is striking that *Hoxd13* can recapitulate the hindgut luminal phenotype in the hindgut, despite the presumed continued expression of the midgut specific *Hox* genes in this tissue. This is an example of a widely observed phenomenon called “posterior prevalence”, which refers to a functional dominance often observed when different *Hox* genes are co-expressed, where the more posteriorly expressed *Hox* gene provides the prevailing influence and determines the resultant phenotype (Duboule & Morata, 1994).

TGF β regulation of cells and extracellular matrix in the gut mesenchyme

Hoxd13 interfaces with multiple signaling pathways in the embryo: Shh both activates *Hoxd13* expression the caudal chick intestine and acts synergically with Fgf signaling to activate it in limb progenitors (Roberts et al., 1995; Rodrigues et al., 2017). Hoxd13 also interacts with the Wnt and Bmp pathways during limb and skeletal patterning (Salsi et al., 2008; Yamamoto-Shiraishi & Kuroiwa, 2013). Here, we introduce a role for Hoxd13 in activation of TGF β signaling during late-stage hindgut morphogenesis.

Moving forward, it will be important to resolve whether this is a direct or indirect effect. Preliminary HCR-FISH co-staining from E6 to E10 for *Hoxd13* and the TGF β ligand *Inhba*, which came out of our differential gene expression analysis and may activate the pathway directly, showed strong co-localization over most time points in circumferential muscle (Extended Figure 14B). However, *Inhba* also showed unique localization in the first layer of subepithelial mesenchymal cells. Further work is needed to resolve which TGF β -related candidates are actual downstream targets of Hoxd13.

In later intestinal development, TGF β pathway activation is localized to the tips of the villi in the small intestine, where it maintains the crypt-villus axis by promoting enterocyte differentiation; this is supported by the fact that TGF β downregulation in intestinal cancer accelerates tumor growth via epithelial differentiation (Barnard et al., 1989; Cammareri et al., 2017). However, besides its essential function in regulating the immune system, TGF β has primarily been implicated in intestinal fibrosis (Frangogiannis, 2020; Verrecchia & Mauviel, 2002). Fibrotic diseases like inflammatory bowel disease are marked by excessive tissue thickening and stiffening via changes to cell and extracellular matrix properties, as part of the

chronic wound healing response. TGF β signaling is upregulated in these cases, leading to differentiation or transdifferentiation of mesenchymal cell types into myofibroblasts—stiff, contractile cells that deposit fibrous ECM networks (Stolfi et al., 2021; Vallée & Lecarpentier, 2019).

The work presented in this study suggests a function for TGF β signaling in normal development that relies on downstream ECM remodeling, as in fibrotic conditions. Furthermore, spatial RNA-seq data shows upregulation of several genes involved in myofibroblast cell contractility and ECM deposition in the subepithelial mesenchyme (Figure 23B). Our finding that new secretion of collagen appears to control mesenchymal geometry downstream of TGF β is consistent with other described roles for collagen in tissue expansion (eg. in sclerosis, reviewed in Ayers et al., 2018) . Yet, because collagen generally increases tissue rigidity, it is initially surprising that blocking its secretion does not affect TGF β -mediated mesenchymal stiffening. It is important to note, however, that crosslinking and assembly of collagen into fibril networks, not deposition alone, is often critical to confer tissue stiffness (Brereton et al., 2022). Indeed, the loss of fibrillar collagen organization in the hindgut treated with SB431542 is consistent with the well-known phenomenon of TGF β -driven collagen crosslinking in disease conditions (Bastiaansen-Jenniskens et al., 2008; Semkova & Hsuan, 2021).

Though subepithelial myofibroblasts (SEMFs, also known as telocytes) appear during later states of crypt-villus patterning, earlier roles for these cells in gut morphogenesis have not been directly described (McCarthy et al., 2020). However, loss of mesenchymal Fgf9 shortens the developing mouse midgut by promoting premature, TGF β -mediated differentiation of

myofibroblasts, suggesting that proper regulation of this pathway is indeed needed for regional gut shaping (Geske et al., 2008). Recent work also revealed a role for TGF β signaling in defining differential tissue mechanics along the left-right axis of the dorsal mesentery during gut tube rotation, further implicating the pathway in gut morphogenesis via modulation of material properties (Sanketi et al., 2022).

Finally, given that *Hoxd13* patterns the muscular anal sphincter, it is not surprising that it is most highly expressed in muscle (Extended Figure 9Extended Figure 14). Formation of musculature in the posterior gut naturally requires extensive enteric innervation and vascularization as well (Hatch & Mukoyama, 2015; Kondo et al., 1996; Lake & Heuckeroth, 2013). As we noted several genes involved in both vascular and enteric nervous system development, we stained for enteric neurons and endothelial cells, and observed an expansion of these cells in the midgut misexpressing *Hoxd13* (Extended Figure 15). Because these cell types interface strongly with TGF β signaling and are important regulators of the intestinal extracellular matrix environment, another possibility is that *Hoxd13* may regulates the TGF β pathway indirectly through cells that migrate into the subepithelial environment (Boezio et al., 2020; Chevalier et al., 2016; Conway & Kaartinen, 2011; Fu et al., 2004; Nagy et al., 2018).

Molecular and functional consequences of gut morphogenesis

Specializing tube dimensions or the surface topography in different gut regions affects the organization of cells and signals in space, which can then feed back on shape, or determine cell and tissue gene expression and function. The connection between shape and epithelial differentiation has been addressed to some extent in the small intestine, where curvature both

concentrates signals to pattern the crypt villus axis via Bmp, Shh, and Wnt signaling and is sufficient to pattern the arrangement of ISCs and Paneth cells within the crypt, but is less clear for the esophagus and large intestine (Gjorevski et al., 2022; Shyer et al., 2015). Mucosal shape also has mechanical consequences for the passage of materials through the gut tube, where some submucosal properties and buckling patterns may facilitate or restrict distensibility. Here, we describe both primary and secondary buckling events that may allow and refine proper regional function along gut segments.

Axial buckling and pre-stretch in the foregut

In the vertebrate esophagus, bifurcated wrinkles are a highly conserved morphological feature—as opposed to arrays of adjacent villi in the small intestine with roughly equal heights and widths, the esophagi of snakes, chickens, humans, and mice show doubled or “secondary” folds (Gogone et al., 2017; Khamas & Reeves, 2011; Martyniuk et al., 2023; Weinstein et al., 1975). Mathematically, period double wrinkling has primarily been investigated in films or curved substrates (Budday et al., 2015; Q. Wang & Zhao, 2015). Our simulations and data indicate that period doubling is driven by progressive endodermal thinning, which is a hallmark of esophageal epithelial transformation from a pseudostratified layer to stratified squamous layer (Y. Zhang et al., 2021). While the functional relevance of these events is unclear, it is worth noting that the progressive doubling of circumferential folds eventually coincides with the formation of secretory gland invaginations, suggesting that perhaps bifurcations are relevant for patterning gland positions along the mucosal surface (Long & Orlando, 1999; Nie et al., 2017; Soliman & Madkour, 2021b).

Our differential growth measurements revealed longitudinal pre-stretch in the esophageal inner endoderm-mesenchyme composite relative to the outer muscle. Since we know that the proliferation rate of the composite is comparable to the muscle, this property could arise from cell-autonomous differences in growth anisotropy, i.e. from a directional cue (Gros et al., 2009; Keller, 2006). Another possibility, however, is that the entire tube grows under tension, and differential growth between the inner mucosa and muscle arises from their differences in stiffness and distensibility, where inner layers stretch less (Ramachandran et al., 2021). For example, since static pre-stretch aligns fibers and cells parallel to the direction of the stretch, and since anisotropic materials are stiffest in the direction of fiber orientation, it stands to reason that the longitudinal cell and ECM alignment in the foregut mesenchyme would cause strain-stiffening, thus limiting inner layer deformation (C. Liu et al., 2014; Tondon & Kaunas, 2014; Vader et al., 2009). Circumferential muscle fibers, by contrast, could distend in the direction of the stretch, thus causing longitudinal compression in muscle and tension in the mucosa. Stabilization of this elastic phenomenon through growth could lead to the observed growth ratio results.

Consistent with this idea, several studies have reported the presence of longitudinal stretch in the esophagus at embryonic and postnatal stages, which may arise from a mismatch between the elongation rates of the foregut and other axially growing structures (Fausett & Klingensmith, 2012). In the mouse, axial tension contributes both to the helical orientation of smooth muscle and the transition of basal epithelial progenitors from a developmental to homeostatic phenotype after birth (Huycke et al., 2019; McGinn et al., 2021). Longitudinal stretch is also a well-established feature of arteries that prevents axial deformation (Chuong &

Fung, 1986; Horný et al., 2014; W. Zhang et al., 2005). This effect is mediated by deposition of elastin, and the loss or dampening of tension with age leads to detrimental axial buckling, such as in the femoral artery (Cardamone et al., 2009; Kamenskiy et al., 2013). We expect that the inner longitudinal pre-stretch described here, and that is consistent with previous work, prevents buckling of the foregut lumen into zigzags upon differentiation of longitudinal smooth muscle layers. Thus, the fundamental phenomenon of axial stretch in foregut development may underlie the conserved morphological feature of circumferential, but not axial, buckling in the lumen, which ultimately facilitates proper esophageal function.

Hindgut isotropic growth, creasing, and large-scale wrinkling

A common feature of hindgut growth throughout development, which impacts its cross-sectional geometry, initial formation of cusped creases, and formation of sulci, is isotropic growth of inner deforming layers. In other words, proper hindgut morphogenesis relies on relatively equal expansion of the endoderm and mesenchyme layers, which is likely a consequence of basic cell and extracellular matrix properties unique to this compartment.

In the previous study of midgut epithelial morphogenesis from our lab, the authors found that numerical simulations based on physical constraints alone were not sufficient to explain the transition from zigzags to villi. This finding pushed them to look for additional factors at play and led to an elucidation of the role of constrained Shh and Bmp signaling in altering proliferation and stem cell localization during villus morphogenesis in the midgut (Shyer et al., 2015). Importantly, the curvature of the nascent villus itself induced a downstream molecular cascade that patterned the crypt-villus axis, thus directly linking geometry to gene

expression and intestinal function. In the hindgut, we have demonstrated using mathematical modeling that, in fact, the macroscale geometric and physical properties of hindgut tissues are sufficient to explain its lumen pattern trajectory, including the formation of large-scale wrinkles. Importantly, our simulations indicate that large scale wrinkles also appear to depend on stiffening of the mesenchyme, which we see as an effect of TGF pathway activation. These findings beg the question of what role, if any, luminal folding plays in large intestinal function and evolution. For example, secondary wrinkles in the hindgut are at least superficially reminiscent of rectal columns, or columns of Morgagni, which are broad wrinkles found in the most terminal portion of the human rectum, raising the possibility that this feature has a conserved role in proper rectal function.

In our observations of developing embryos and in *in silico* analyses, we have identified a morphological intermediate—sulci—that precedes hindgut cuffs. The colon forms crypts without villi, lacks Paneth cells, and accrues a greater proportion of secretory goblet cells. While descriptions of the hindgut epithelial surface have largely focused on these features (especially the absence of villi), the appearance of superficial, branched, and striated folds is a common feature across birds and mammals, including humans (Chang & Leblond, 1971; Rubio, 2020). As mentioned above, high epithelial curvature concentrates mesenchymal morphogen signals in the chick to pattern the crypt-villus axis. Therefore, the mechanical landscape that maintains a flat hindgut epithelial-mesenchymal interface for most of development necessarily precludes the morphogen distributions that define villi and differentiated cells found in the small intestine. Indeed, the pattern of pSmad1/5/9 and Sox9 localization found in nascent villi is absent in hindgut cuffs (Figure 13). Along with the previous finding that *Hoxd13* misexpression

induces differentiation of cell types found in the hindgut (Roberts et al., 1998a), our results suggest that the topographical consequence of regional mechanics may contribute to regionalization of epithelial cell types, and, thus functional differences between intestinal compartments.

Perspectives and future work

It is remarkable that transcription factors such as Hox genes can confer specialized mechanical properties to tissues such that they reproducibly generate the correct forms. This is particularly impressive considering our finding that these material and growth properties are not drastically different between gut regions. It is likely that compensation by other factors and feedback from gene expression to mechanical properties are important for ensuring the robustness of gene regulatory networks that define physical forces in morphogenesis.

Along these lines, for early specification of tube dimensions along the gut, it will be important to discern both how morphogens affect cell growth through division and ECM deposition, and how growth and morphology affects the muscle patterning landscape across regions. For example, what is the consequence of changing cell density on the interpretation of morphogens in space, and downstream differentiation? For hindgut lumen morphogenesis, the connection between Hox expression and ECM remodeling appears to be surprisingly linear in our treatment thus far, but there are most likely highly complex feedback loops that ensure correct pathway activation in time and space. For example, ECM remodeling can release latent TGF β ligand, which can then induce ECM breakdown and deposition. Broadly speaking, it would

be interesting for the field to move toward mechanical “regulatory networks” that work in constant communication with molecular networks to shape the embryo.

For further studies of lumen morphogenesis in the foregut, it will be interesting to see whether misexpression of Sox2, the regulator of esophageal fate that can induce esophageal epithelial differentiation in the posterior gut, in the midgut or hindgut can alter mechanical properties of the endoderm and mesenchyme, as with Hoxd13 for the hindgut. *In ovo* or *ex vivo* growth perturbations may also lend insight into the source of longitudinal tension in the inner composite. In the hindgut, it will be important to figure out how Hoxd13 regulates TGF β signaling--does it directly bind to TGF β -regulating genes? Does it induce changes in the migration or infiltration of vascular or enteric neural plexus cells, which then influence signaling? One method to address this question is to induce cell autonomous misexpression of Hoxd13, followed by ATAC- and RNA-seq to identify genes potentially regulated by Hoxd13 directly.

Complex models of morphogenesis that consider events on different spatial scales also require consideration of variable time scales. To assess whether a two-phase model of muscle differentiation followed by growth is appropriate for our work on initial tube morphogenesis along the gut, the temporal dynamics of muscle differentiation must be assessed experimentally. In other words, when do cells stop differentiating into muscle, and is growth coincident with ongoing patterning? Additionally, understanding the mechanism of directional growth will likely require further tests of tissue mechanical properties and cell behaviors via timelapse imaging and/or lineage tracing. The development of the early gut tube may be a useful and relatively simple model for bridging mechanics and growth on the continuum level

to discrete cell behaviors, which is still largely a challenge in computational modeling of development.

Finally, functional implications of lumen morphology in the gut will be important for understanding both disease and intestinal evolution. How do buckling patterns formed during development relate to organismal life history, eg. diet and behavior? Furthermore, how does disrupting mucosal form relate to disease, particularly cancer of the colon and esophagus? Mechanical insights into proper morphogenesis in the gut may lend new interpretations to pathologies and offer novel therapeutic avenues in the future.

MATERIALS & METHODS

Experimental

Use of chicken embryos

All animal studies were performed in compliance with NIH guidelines and standard operating protocols approved by the Institutional Animal Care and Use Committee at Harvard Medical School. Chickens Fertilized Specific Pathogen Free (SPF) White Leghorn Chicken eggs (Charles River) were incubated in a 38°C humidified chamber, and embryos and guts were staged according to the Hamburger and Hamilton and Southwell staging guides (Hamburger and Hamilton, 1992; Southwell, 2006).

Chick intestinal electroporation

Expression constructs were electroporated into the midgut splanchnic lateral plate at HH17, as described in detail previously (Huycke et al., 2019). Because RCAS viral particles do not cross the basement membrane, this method ensured tissue-specific misexpression in the mesoderm (Abzhanov et al., 2004; Grapin-Botton et al., 2001; Huycke et al., 2019; Nerurkar et al., 2017). Hindgut and midgut controls were electroporated with RCAS-*mGFP* or obtained from stage-matched non-electroporated embryos. RCAS-*Hoxd13* (Roberts et al., 1998b), RCAS-*mGFP* (Kan et al., 2013), and RCAS-*Noggin* (Huycke et al., 2019) were electroporated concentrations of 2.5µg/µL. Successful viral spread was confirmed using whole-mount AMV-3C2 immunostaining.

Lumen surface imaging

Surface relief structures of intestinal segments were imaged by first dissecting and longitudinally slicing gut tubes in 1X PBS. Opened guts were then pinned flat (without stretching) to 3% agarose using 0.002-inch or 0.004-inch diameter tungsten rods, and submerged in 4% PFA for fixation at 4°C overnight, or at room temperature for 1-2 hours. Fixed guts were stained with DAPI in 1X PBS overnight at 4°C and imaged on a Zeiss LSM 710 point-scanning inverted confocal microscope. Maximum projections of, depending on stage and region, approximately 20-60µm Z stacks at 2-5µm step size were generated using Fiji. Depth coding of z-stacks was performed using the Temporal Color Code function in Fiji.

Section immunostaining

Tissues fixed for 2 hours at room temperature or overnight in 4% paraformaldehyde in 1X PBS (PFA) were washed, dehydrated in 30% sucrose in 1X PBS and embedded in OCT blocks. Samples were kept as tubes for transverse section images and cut open and pinned flat in a 3% agarose dish using tungsten rods prior to fixation for sagittal sections. Using a cryostat, guts were sectioned onto Superfrost slides as 16 μ m thick slices and allowed to dry completely. Tissues were permeabilized with PBSTT (1X PBS + 0.1% Tween-20 + 0.05% Triton-X100) prior to application of primary antibodies at 4°C overnight. The following primary antibodies were used: α SMA-FITC (1:1000, F3777 Sigma-Aldrich), calponin 1 (1:100, Cell Signaling), phospho-Smad1/5/9 (1:300, 13820S Cell Signaling Technology), phospho-Smad2 (1:300, Cell Signaling), collagen I (1:300, Abcam), fibrillin-like 2 (1:100, DSHB), hyaluronic acid binding protein (1:100, Sigma-Aldrich), laminin-1 (1:50, L9393 Sigma-Aldrich), Tuj1 (1:1000, ab18207 Abcam), Sox9 (1:100, AB5535 Sigma-Aldrich), elastin (1:100, ab21610 Abcam), Foxf1 (1:300, 8F6G3 ThermoFisher), phospho-Myosin Light Chain 2 (1:100, 3671 Cell Signaling), AMV-3C2 (1:100, DSHB). All secondary antibodies were added 1:300 in PBSTT at room temperature for 2 hours. Secondary antibodies conjugated to fluorescent dyes were chosen with regard to primary antibody species (Jackson Immuno, 1:300). The following dyes were used and applied in the same way as primary antibodies: A488-phalloidin (1:40 of a 200u/mL stock, A12379 ThermoFisher), Sambucus Nigra Agglutinin-Cy3 (10 μ g/mL, CL-1313 Vector Laboratories).

For phospho-Smad2 and 1/5/9 stains, antigen retrieval was performed by boiling slides for 5 min in pH 6.0 citrate buffer using a veggie steamer prior to antibody application. TSA signal amplification was then performed according to kit recommendations (Perkin Elmer) following a biotinylated anti-rabbit secondary incubation (1:300) and a streptavidin-HRP

incubation (1:300). Transverse section images were taken using a compound epifluorescence microscope or a Nikon Ti2 inverted W1 Yokogawa Spinning disk microscope (50 μ m pinhole disk). 10 μ m Z stacks at 0.5-1 μ m step size were also analyzed as maximum projections.

Whole mount immunostaining and tissue clearing

Tissue clearing was performed for fixed whole guts older than E12. Samples to be immunostained were dehydrated through a methanol series (1 hour incubations in 20%, 40%, 60%, 80%, 100%, 100% methanol in distilled water), followed by rehydration the same way in methanol + 1X PBS. Guts were then permeabilized in 1X PBS containing 0.1% Triton-X100 and 1% BSA for 4-6 hours and incubated in α SMA-FITC (1:300, F3777 Sigma) or fibrillin-like 2 (1:50, DSHB) at 4°C for 3-5 days. Following 2 days of washes in the permeabilization solution, secondary antibodies were added at 1:100 concentration and samples were again incubated at 4°C for 3-5 days. Dye-conjugated secondary antibodies were used at 1:100 dilutions (Jackson Immuno). Guts were then post-fixed for 2 hours at room temperature in 4% PFA, followed by washes and dehydration through a methanol series as before. 2 1 hour incubations with dichloromethane were performed after transferring tissues to 5mL glass vials, followed by a 1 hour incubations in ethyl cinnamate. Stained, cleared tissues were imaged in ethyl cinnamate, in the same fashion as lumen surface imaging described above. PH3, SMA, and DAPI-stained guts in Figure 5 were imaged without clearing on a two-photon microscope; phospho-histone H3 (06-570 Millipore) was used at 1:300 (Huycke, 2018).

EdU/BrdU labeling

Eggs were windowed at E2.5 and incubated until E5, E6, or E7. At a given time point, 500 μ l of 1mM EdU in 1X PBS was pipetted on top of the embryo, after which eggs were incubated for 1hr. The same procedure was then performed with a 10mM solution of BrdU in PBS. After an additional 30 minutes, guts were dissected, fixed and sectioned as described in Section immunostaining. Transverse sections were stained for EdU according to manufacturer instructions using a Click-iT Edu kit; tissues were then immunostained for BrdU (1:100, MoBU-1, Invitrogen) using heat-mediated antigen retrieval in citrate buffer as described for phospho-Smad2. Stained sections were imaged on a Spinning disk microscope.

Differential growth measurements

To measure circumferential compression, whole guts were dissected and cut into 250 μ m thick rings using a vibratome. Rings were transferred to a 3% agarose dish with 1X PBS and pre-dissection images were taken using a Leica stereoscope camera. Inner layers were carefully dissected from outer muscle using electrolytically-sharped, 0.002in-diameter tungsten needles. For longitudinal compression, 1-2mm gut segments were cut open longitudinally and inner layers were separated the same way. Dissected tissues were allowed to relax for 30 minutes before post-dissection images were taken.

Modulus measurements

Gut layers of interest were first isolated via fine dissections as described for circumferential compression measurements. Tissue rings were then immobilized using a tungsten rod pierced through the lumen (without puncturing the tissue) and into a 3% agarose

dish filled with PBS. A tungsten cantilever connected to a motorized actuator was hooked into the lumen, which was then programmed to stretch the tissue at a constant velocity of 0.002mm/sec using custom software. Timelapse movies were made from images captured every 10 seconds using Leica imaging software.

Fluorescence in situ hybridization (FISH)

After 2 5 minute washes with PBST (1X PBS and 0.1% Tween-20), sections were treated with 1µg/mL Proteinase K for 10 minutes, followed by additional PBST washes and post-fixation with 4% formaldehyde/PBS for 5 minutes. After washing off fixative with PBST, probes were added in hybridization buffer to the slides and plastic cover slips were placed on the slides for hybridization overnight at 65°C in a humidified chamber. Stringency washes were then performed as follows at 65°C: 1X SSC/ 50% formamide for 30 minutes, 2X SSC for 20 minutes, 2 0.2X SSC washes for 20 minutes each. Sections were washed with TNT (0.1 M Tris-HCl pH 7.5; 0.15 M NaCl; 0.05% Tween-20), after which peroxidase activity was quenched with 3% H₂O₂ for 15 minutes. Subsequent TNT rinses were followed by a blocking step in TNTB blocking solution (Perkin Elmer) for 1 hour. 1:300 Anti-DIG-POD (Roche) was applied overnight at 4°C.

Several 5 minute TNT washes were then performed, and TSA amplification was completed by adding Tyr-Cy3 or Tyr-Cy5 1:50 in amplification diluent to the slides for 7 minutes. After final TNT washes, sections were stained with DAPI in 1X PBS and mounted for imaging using Prolong Gold Antifade reagent.

Single molecule FISH

SABER-FISH was performed using in-house reagents and hairpin oligos. Custom unextended probe sets for chick *Acta2*, *Ptch*, *Myocd*, *Bmp2*, *Bmp4*, and *Bmp7* were designed and ordered from IDT, and kept as 100uM stocks. Full probes were synthesized with hairpins using BST polymerase and verified on a gel before being purified. Sectioned tissues on Superfrost slides were washed before applying probes with the Hybridization solution I (2X SSC + 1% Tween-20 + 40% Formamide + 12.5% Dextran sulfate) and incubating for 16 hours at 43°C. Small circular chambers were applied over tissues and probe hybridization solutions were pipetted in for incubations. Tissues were then washed with SSCT (5X SSC buffer + 0.1% Tween-20) and placed at 37°C for a 10 minute fluorescence oligo incubation in Hybridization solution II (1X PBS + 0.2% Tween-20). Samples were stained with DAPI after several 1X PBST and 1X PBS washes and mounted for imaging.

FISH using HCR was performed using reagents and an adapted protocol from Molecular Instruments. Sections on slides were washed with 1X PBS and permeabilized for 2 hours in 70% ethanol. After a short pre-incubation in Hybridization Buffer at 37°C, custom probes from 1µM stocks were mixed with pre-warmed Hybridization Buffer to a final concentration of 6nM. Probe solutions were added to slides and coverslips cut from polypropylene bags were applied before placing slides in a humidified chamber at 37°C for 18 hours. The following probe sets were manufactured by Molecular Instruments from the associated sequence IDs: INHBA (NM_001396543.1), CFC1 (NM_204700.3), THBS2 (NM_001397325.1), HOXD13 (NM_205434.1), SMOC1 (XM_015287582.4), MTSS1L (XM_015279207), FBLN1 (NM_204165.1), VCAN (NM_204787.1). Excess probes were washed at 37°C using 30 minute washes in 4 graded concentrations of Probe Wash Buffer/5X SSCT followed by 2 washes in 5X

SSCT at room temperature. H1 and H2 hairpins from 3 μ M stocks were separately heated to 95°C in a heat block and allowed to reanneal at room temperature for 30 minutes in the dark. Hairpins were then mixed with Amplification Buffer at a final concentration of 50nM, and incubated in the dark for 5 minutes. The hairpin solutions were added to slides, which were covered with polypropylene coverslips and incubated at room temperature for 20 hours. Samples were then washed with 5X SSCT to remove excess hairpins, stained with DAPI in 1X PBS, and mounted for imaging.

Quantitative PCR

For E5-E7, gut regions were isolated via dissection and whole guts were used. For Hox gene qPCR at late stages, the endoderm was peeled away after a short incubation in dispase before harvesting RNA. RNA was extracted using the QIAGEN RNeasy Micro Kit, and cDNA was synthesized using a First Strand cDNA Synthesis Kit (Sigma-Aldrich). For QPCR, AzuraQuant mixes were used and cycle parameters were set according to kit instructions. Fold change expression was calculated using the $\Delta\Delta$ Ct method, and *GAPDH* was used as the housekeeping gene for normalization. Primers for early muscle patterning genes can be found in (Huycke et al., 2019), and primers for Hoxd11-13 amplification are listed in Table 4.

Table 4. Primers for qPCR amplification of *Hox* genes

Target	Primers
<i>Hoxd11</i>	5'-CGGCCAGGAGAAGAAAGTGACA-3' 5'-TCGATCGCTGAGGAACTGC-3'

<i>Hoxd12</i>	5'-GTGAATTCCTGCACTTCCAGCC-3'
	5'-GCAAACCATCCTGCACTGAAGG-3'
<i>Hoxd13</i>	5'-CTCTGGCTAATGGCTGGAACG-3'
	5'-GGCTGGTTTAGTGCAACGTCC-3'

RNA sequencing library preparation

Whole guts were dissected from electroporated embryos in fresh, ice-cold 1X PBS. 4 replicates of RCAS-*mGFP* midguts, RCAS-*mGFP* hindguts, and RCAS-*Hoxd13* midguts were collected for each of 2 time points – E12 and E14. RCAS-*mGFP* midguts and hindguts were obtained from the same individuals (4 total at each time point). To harvest tissue samples of roughly equivalent mass, 2-3mm hindgut segments and 3-4mm midgut segments were isolated and immediately cut open longitudinally. Samples were then placed in Eppendorf tubes containing 1mL of 2Units/ μ L dispase in 1X PBS and incubated on a rocker at 37°C for 10 minutes. Segments were transferred to a new dish of 1X PBS and the inner epithelium was carefully peeled away using fine forceps. Remaining mesodermal tissue was kept on ice until all tissues were collected. RNA was extracted using the QIAGEN RNeasy Micro Kit. All E12 samples were collected simultaneously, and E14 samples were collected in 4 batches with 1 replicate of each condition collected per batch. RNA quality was assessed using an Agilent 2100 Bioanalyzer. Libraries were prepared from 500ng input RNA using the Illumina TruSeq Stranded mRNA kit and pooled separately for E12 and E14 prior to sequencing.

Chick intestinal explant culture

For Shh and Bmp perturbations, E4 guts were pinned taut using tungsten rods to 2mm-thick pads of 4% Noble Agar in 6-well dishes. Enough media was added to barely cover the samples, about 200 μ L, and dishes were placed in a 37°C incubator with 5% CO₂ and 19% O₂. Media was changed every 24 hours for 2 days. For TGF β perturbations, 2-3mm segments of E12 midguts and E13 hindguts were dissected in pre-warmed 1X DMEM containing 1% Pen/Strep and transferred to 6-well dishes with 2 segments per dish. All explants were cultured in 1X DMEM containing 1% Pen/Strep and 10% chick embryo extract. Enough media was added to each dish such that guts were at the air-liquid interface, which ranged from 800 μ L to 1mL depending on the size of the tissue. Dishes were then placed on a rocker at approximately 12 rocks per minute, within a 37°C incubator with 5% CO₂ and 19% O₂. Media was changed every 24 hours for 72 hours of culture. Finally, for cuff perturbations, guts were cultured as tubes, slabs cut open longitudinally using forceps, tubes with partial circumferential “notches” introduced using forceps, or “notched” tubes that were then cut open longitudinally. E15 hindguts were cultured in the same fashion as TGF β explants: rocking for 2 days with 24hr media changes.

The following stock solutions of pharmacological compounds were made, stored at -20°C, and diluted before adding to media at 0.1% to achieve final concentrations indicated here or in figure legends: recombinant mouse TGF β 1 (50 μ g/mL in 1X PBS + 4mM HCL + 0.1% BSA, R&D Systems; final concentration 10ng/mL), Activin A (10 μ g/mL in 1X PBS + 4mM HCL + 0.1% BSA, R&D Systems; final concentration 10ng/mL), SB431542 (20mM in DMSO, Selleck; final concentration 20 μ M), Col003 (100mM in DMSO, MedChemExpress; final concentration 50 μ M),

Recombinant mouse N-Shh (500 μ M in PBS +0.1% BSA, R&D Systems), mouse Bmp4 (100 μ g/mL in 4mM HCl and 0.1% BSA, R&D Systems), mouse Noggin (100 μ g/mL in PBS + 0.1% BSA, R&D Systems), cyclopamine (2.5mM in ethanol, Millipore), nifedipine (200mM in DMSO, Sigma), blebbistatin (100mM in DMSO, Selleck). An equivalent volume of vehicle was added to each control (for experiments employing compounds dissolved in different solvents, an equivalent volume of each solvent was added to a single set of controls).

Light-seq spatial RNA sequencing

Light-seq was performed according to the methodology described in Kishi et al., 2022 on 4 sections each of the E14 midgut, hindgut, and RCAS-*Hoxd13* midgut. Tissues were collected and fixed for 1hr at room temperature in 4% PFA with 0.1% Tween, followed by washes, a 1hr incubation in 30% sucrose, and 1hr in 100% OCT. Guts were embedded in OCT blocks and sectioned onto Superfrost slides. Square plastic chambers were then superglued on top of sections for subsequent reactions. Sections were washed with PBS followed by PBS-Tween, before completing *in situ* reverse transcription of RNA using a 12-cycle ramp program, which added 5N3G sequences onto cDNA strands for eventual crosslinking to barcodes. A-tailing was performed for 45 minutes at 37°C.

Samples were barcoded using a DMD on a Nikon confocal microscope. Sections were incubated in barcoding solution for 30 minutes at room temperature before outlining regions in Nikon software and using DMD illumination to cross-link barcodes onto cDNAs in tissues. A FITC-labeled barcode was used for the subepithelial mesenchyme. Successful barcoding was confirmed using a fluorescence widefield microscope. Barcoded cDNAs were displaced from

samples, and HopPER reactions were performed to stitch barcoded cDNAs into single strands. DNA was then amplified using qPCR, purified using Ampure XP beads, and concentrations were quantified using a Qubit assay. Library prep was performed using a Nextera kit.

Data analysis

Radial and axial geometry measurements

Radial geometry was measured from 3x replicates of DAPI, SMA and laminin-stained sections imaged on an epifluorescence compound microscope. For Figure 1, a custom semi-automated code determined SMA and laminin intensity as a function of position from the lumen surface using geodesics projected from user-drawn inner and outer boundaries. Each sample was divided into 4 quadrants and results were averaged. Position and FWHM of the SMA peak, along with the position of the basement membrane, were used to calculate endoderm, mesenchyme, and muscle thicknesses. For Figure 4, r1-r4 were measured by hand from the same 3x replicates. 6 evenly spaced measurements were taken and averaged for each radius per sample.

Lengths over time were measured from 3x replicates of freshly dissected whole guts imaged on a dissecting microscope. Anatomical landmarks were used to determine regional boundaries: the esophagus was measured from the base of the pharynx to anterior boundary of the proventriculus, the small intestine from the base of the stomach to the ceca, and the hindgut from the ceca to the anterior boundary of the cloaca.

EdU/BrdU quantification

Z-stacks were first analyzed in 3D using Imaris, and the positions of all DAPI+ nuclei, EdU+ nuclei, and BrdU+ nuclei in the red (EdU), green (BrdU), and blue (DAPI) channels were extracted and imported into a custom MATLAB script. When positions from the red and green channels were overlaid, nuclei that were within a specified distance in pixels from one another were assumed to be EdU+ BrdU+ nuclei, whereas those in the EdU channel without a BrdU counterpart were labeled as EdU+ only. The inner surface, basement membrane, and muscle boundaries were then segmented by hand, and the number of EdU+ and EdU+BrdU+ nuclei, as well as the total number of cells, were counted in each layer.

Following image analysis, S-phase length in each layer was calculated under the assumption that it is proportional to the number of cells in S-phase at the end of the experiment (Huycke et al., 2019; Martynoga et al., 2005). Since EdU is incorporated by dividing cells during almost the entire 1.5 hours, but BrdU is only incorporated during the last 30 minutes, the number of EdU+/BrdU+ cells is considered to be the number of cells in S-phase. This is proportional to the number of cells harboring EdU only, which, by the same token, is proportional to the time spent incorporating EdU (1 hr, since it takes 30 minutes for EdU to be incorporated). Cell cycle length is thus calculated by the equation

$$T_{S\text{-phase}} = T_{\text{EdU}} / (N_{\text{EdU}} / N_{\text{EdU+BrdU}}),$$

where T_{EdU} is the time cells can incorporate EdU but not BrdU, N_{EdU} is the fraction of cells that are labeled with EdU only, and $N_{\text{EdU+BrdU}}$ is the fraction that is labeled with both EdU and BrdU. Total cell cycle length was then estimated using a second proportionality with the assumption that all cells are dividing:

$$T_{\text{Cell cycle}} = T_{S\text{-phase}} / (N_{\text{EdU+BrdU}} / N_{\text{Total}}),$$

where N_{Total} is the total number of cells in the region of interest. We used N_{Total} to measure cell density as well, by dividing it by layer volume (area of mesenchyme or muscle layer x section thickness).

FISH and immunostain quantification

Radial signal intensity measurements were performed as described in Huycke et al., 2019. Briefly, z-stacks or maximum projections were imported into a MATLAB script, and the basement membrane and outer tube or circumferential muscle boundaries were outlined manually. This space was then divided into 10-20 concentric rings and mean intensity was calculated within each ring to yield an intensity profile as a function of position. For SABER-FISH quantification, the user-defined region is instead overlaid with a geodesic, which calculates mean intensity per pixel instead of within binned rings.

Nucleus and division orientation measurements

Whole-mount z-stacks of gut tubes were first reoriented, and the view was adjusted to a plane at the dorsoventral midline. An SMA co-stain and the basement membrane, which is visible in the DAPI channel, were used to isolate the mesenchyme. The line segment tool in Fiji was then used to calculate division angle by drawing a line connecting both ends of a dividing cell marked by PH3. To measure aspect ratio, the line segment tool was used to draw a line parallel to the horizontal axis from one end of a nucleus to the other; the same procedure was repeated with a line perpendicular to the horizontal axis. The first measurement (width) was divided by the second (height) to determine nucleus aspect ratio,.

Surface wrinkling quantification

Pattern analysis of lumen surface images was performed using a combination of custom and adapted pipelines in MATLAB. For Fast Fourier Transforms (FFTs), we first applied a series of pre-processing operations to DAPI channel maximum projections using MATLAB. These generally involved a Gaussian filter followed by adaptive thresholding before binarization of the image. Power spectra in the frequency domain were obtained from the log of the absolute value of the 2D FFT (fft2) performed on binary images. To count branched folds, binary images were skeletonized, and branch points were scored manually using the point selection tool in Fiji. Autocorrelation profiles were obtained by first cropping raw midgut images in x and y to isolate a representative segment of the periodic pattern. The dimensions of this segment varied between stages but not between conditions (midgut, hindgut, *RCAS-Hoxd13* midgut). Autocorrelation was calculated using the MATLAB autocorr function applied to a vector containing the 1D signal intensity pattern of the cropped image (Jacko et al., 2018). For each sinusoidal pattern, amplitude was measured as the average amplitude of the first 2 waves of the autocorrelation plot. For Delaunay triangulation and Voronoi cell analysis, center points of primordial villi and cuffs were manually extracted in MATLAB, and the delaunay and voronoi functions were used to generate tessellations. Variances were calculated from distributions of triangle edge lengths and Voronoi cell areas from 4 images per condition.

Muscle and ECM orientation analysis

SMA- and Fbn2-stained whole guts were imaged in the same way as DAPI-stained lumen surfaces described above. Guts were imaged lumen side down to capture the muscularis mucosa and circumferential muscle, and imaged outer edge down to capture the outer longitudinal layer. Maximum projections encompassing each muscle layer or the subepithelial mesenchyme were divided into $100\mu\text{m} \times 100\mu\text{m}$ sample images, and the OrientationJ plugin in Fiji was used to determine the distribution of fiber angles present in each image. For the innermost muscle layer, z-stacks were pre-processed using Arivis software to manually segment muscle alone, as its folded morphology in the fore- and hindguts prevented capturing only muscle in a given series of z-slices. Results returned in 180° were limited to a $0\text{-}90^\circ$ axis by adding $-90\text{-}0$ and $0\text{-}90$ distributions.

Fold morphology measurements

Geometric properties of foregut, hindgut, and midgut wrinkles were measured in Fiji from transverse DAPI-stained sections, or from depth-coded projections of lumen surfaces (Lumen surface imaging). For wrinkle number and aspect ratio, sections were imaged on a compound epifluorescence microscope. For apical-to-basal path length, sections were imaged on a Spinning disk microscope (Section immunostaining), and maximum projections created in Fiji were used for measurements.

Number of wrinkles per cross section was counted for each full section, and wrinkle aspect ratios and wavelengths were measured using the line segment tool. Aspect ratios were measured from randomly sampled wrinkles taken from 3 transverse sections per region and time points. The bottom of a fold was defined as the average radial position of the valleys on

either side of a protrusion, and the top of a fold was the radial position located closest to the lumen center; width was measured orthogonally across the fold at the radial position halfway between these points (Figure 14G). Wrinkle wavelengths were measured from the center points of adjacent longitudinal folds on the circumferential axis. Apical-to-basal path length was measured using the freehand line tool from distinct quadrants of 1-2 transverse sections per condition.

Differential growth calculations

Strain was calculated as the percent change in inner composite length upon compression into the stressed configuration $[(\text{pre-dissection length} - \text{post-dissection length}) / \text{pre-dissection length}]$ (Figure 4A). Radii and tissue layer widths over time were measured using DAPI and SMA-stained transverse sections.

Modulus calculations

Movies were analyzed using a custom analysis pipeline in MATLAB by implementing the Computer Vision Toolbox to track 1) Dil dots applied to tissue and 2) the cantilever tip over time. Strain was calculated from the percent change in distance between dots over time, and stress was calculated as

$$\sigma = \frac{k_b \delta}{2wl},$$

where δ is the deflection of the tungsten cantilever, measured from the difference between the cantilever tip and base positions at each time step, and $2wl$ is the cross-sectional area of the tissue ring. k_b is the bending stiffness the cantilever, defined as

$$k_b = \frac{3EI}{L^3}.$$

E is the Young's modulus of tungsten, L is the length of the lever, and I is the area moment of inertia of a circle, or

$$I = \frac{\pi r^4}{4},$$

where r is the radius of the lever. Stress was plotted as a function of strain, and Young's modulus was determined from the slope of the resulting curve in the small strains regime, corresponding to actual measured strains. For muscle samples, the earliest linear parts of the curves were used to determine moduli. Mesenchyme modulus was determined from endoderm and composite moduli and thicknesses, as shown in Extended Figure 6. Anteroposterior trends in mechanical properties along the gutC. For guts older than 14 days for the midgut and hindgut, and 16 days for the *Hoxd13*-misexpressing midgut, tissue layers were too thin to dissect for modulus measurements and had to be inferred by fitting a curve to data from several earlier stages. Widths were measured from fixed 16 μ m transverse sections stained with DAPI.

For longitudinal modulus measurements, whole foreguts were dissected and the outer muscle layers were peeled away to leave the inner endoderm-mesenchyme composite (and muscularis mucosa from E14 onward). One end of the foregut was then attached to a Superfrost glass slide, and other to a 0.004in cantilever, using small amounts of superglue. Stretch tests then performed in 1X PBS as described above, and strain measurements were taken from Dil dots applied approximately halfway between the slide and lever attachment sites. Stress was calculated as

$$\sigma = \frac{k_b \delta}{\pi r_1^2 - \pi r_2^2}$$

where r_1 is outer radius and r_2 is inner radius, to consider the cross-sectional area of the composite tube.

RNA sequencing and data analysis

For whole-mesoderm bulk RNA-seq, Single end 75bp reads were sequenced on a NextSeq 500 flowcell. For RCAS-GFP midgut, RCAS-GFP hindgut, and RCAS-*Hoxd13* midgut, respectively, average reads per replicate generated by E12 libraries were 13.3, 14.0, and 14.0 million, and by E14 libraries were 14.2, 14.5, and 13.4 million. Reads were quasi-mapped to the reference chick transcriptome using Salmon, and the Salmon pseudocount matrix was used for differential gene expression analysis in R using DESeq2 (Love et al., 2014; Patro et al., 2017). Hierarchical clustering was performed to identify differentially expressed genes commonly shared between control vs. RCAS-*Hoxd13* midgut and control vs. hindgut. To identify differentially regulated pathways, we analyzed lists of commonly differentially expressed genes between comparisons using the free online suite of gene set enrichment tools, EnrichR (Figure S4B) (E. Y. Chen et al., 2013; Kuleshov et al., 2016; Xie et al., 2021). After identifying TGF β as a pathway of interest, the KEGG 2021 and BioPlanet 2019 lists of TGF β signaling pathway genes were used to sub-classify genes as they are represented in Figure 3.

Light-seq data analysis employed a bulk RNA-seq analysis pipeline to extract a count matrix from raw data, after which analysis was performed in R using DESeq2 as described above. Raw reads were first processed to extract barcode sequences, which resulted in parsed

and trimmed reads. Reads were then mapped to a STAR index constructed from the galgal6 chicken genome assembly, and UMI deduplication was performed. Featurecounts and PCA were used to assess sequencing quality.

Simulations

Radial muscle patterning and growth

Full model formulations are provided in APPENDIX 1: Supplementary materials for *Radial and axial geometry in early gut tube development*. Because growth is predicted to be slow compared with morphogen diffusion and degradation, we assumed that Shh and Bmp pathway component concentrations are in steady-state at all times. We also assumed that muscle differentiation ceases after the first day of its appearance. Simulations were therefore designed to have two phases. In phase one, Hh and Bmp signals interact according to reaction-diffusion equations, and the area where the SMA level is higher than a given threshold would differentiate into muscle, setting the initial inner and outer muscle radii r_2, r_3 . The inputs to this portion were initial (measured) whole tube inner and outer radii, and signaling parameters were fitted to the E4 foregut, as it differentiates muscle first. Hh concentration (η_{Hh}) and the degree of Bmp4 activation by Shh (β_{max}) were adjusted to fit their E5 radial geometries. In phase 2, the tissue was set to grow, with area change in each compartment determined by relative tissue growth rates and the rate of convergent extension (CE), which is applied uniformly across tissue types. CE rates were determined from the data in Figure 1B (average percent change in total length), and were kept constant while inner mesenchyme, muscle, and

outer mesenchyme growth rates were manually fitted to radii over time. Endoderm growth was not considered in this model.

2D foregut and hindgut epithelial folding

Model details can be found in APPENDIX 2: Supplementary materials for *Divergent epithelial buckling across gut regions*. 2D simulations were performed using a user-defined material (UMAT/VUMAT) subroutine in the commercial finite program ABAQUS/Standard (version 6.14). Geometric models for the foregut and hindgut are listed in Table 5. Three qualitatively different growth profiles are adopted as follows, where the accurate coefficients C_i are fitted from experimental data. The axial growth is set as $g_z = 1$.

1. Endoderm isotropic growth

$$g_r = 1 + C t$$

$$g_\theta = 1 + C t$$

2. Endoderm thinning

$$g_r = 1 - C_r t$$

$$g_\theta = 1 + C_\theta t$$

3. Endoderm thickening

$$g_r = 1 + C_r t$$

$$g_\theta = 1 + C_\theta t^2$$

Table 5. Geometries and mechanical properties of 2D numerical models.

Model	Thickness ratio h_e/h_m	Radius ratio R_i/R_o	Modulus ratio μ_e/μ_m	Growth
Foregut (E8)	0.3	0.6	35	Endoderm isotropic growth
Foregut (E10)	0.3	0.6	35	Endoderm thinning + Mesenchyme thickening
Foregut (E14, E17)	0.3	0.6	35	Endoderm thinning
Hindgut (E8)	0.5	0.33	2	Endoderm isotropic growth
Hindgut (E10)	0.4	0.42	2	Endoderm isotropic growth
Hindgut (E12)	0.5	0.4	2 – 7	Stepwise endoderm growth
Hindgut (E14)	0.35	0.46	2 – 7	Stepwise endoderm growth

3D hindgut and midgut lumen wrinkling

To perform 3D simulations, we again implemented a UMAT/VUMAT subroutines in the ABAQUS, reapplying the same theoretical framework used for 2D models. Three biophysical parameters are defined in the initial stress-free state in ABAQUS: the thickness ratio and modulus ratio of the endodermal and mesenchymal layers, and the radius ratio of the innermost and outermost layers. While thickness and modulus ratios were fitted to the data, the radius ratio was kept as 0.65 for all simulations. To simplify the process of phase diagram construction, experimental data were binned such that simulation parameters do not perfectly match, but closely approximate, actual, or predicted values (Table 6). 27 simulations were performed in total to create the diagram in Figure 15F.

The stepwise anisotropic growth profile of the midgut and the transversely isotropic growth profile of hindgut were also based on experimental results. The following sets of growth functions were developed to be qualitatively consistent with the data and were applied to simulation conditions as specified in Table 7.

4. Stepwise anisotropic

$$g_r = 1$$

$$g_\theta = 1 - t^2 + 2t$$

$$g_x = 1 + 2t^2$$

5. Stepwise anisotropic with endoderm thinning

$$g_r = 1 - 0.5t$$

$$g_\theta = 1 - 2t^2 + 4t$$

$$g_x = 1 + 4t^2$$

6. Transversely isotropic

$$g_r = 1$$

$$g_\theta = g_x = 1 + t$$

7. Transversely isotropic with endoderm thinning

$$g_r = 1 - 0.5t$$

$$g_\theta = g_x = 1 + t$$

8. Circumferential anisotropic

$$g_r = 1$$

$$g_\theta = 1 + 2t^2$$

$$g_x = 1$$

In contrast to our previous computational model for the wild-type midgut (Shyer et al., 2013), here we used UMAT and the implicit method to ensure the slow formation of ridge and zigzag patterns (occurring over the course of several days in the embryo) reaches mechanical equilibrium at every time step; for the hindgut, we used VUMAT and the explicit method to mimic the process of sulci (creasing) and cuff formation, which occurs embryonically in the span of hours, and thus relatively quickly (Table 6, Table 7). Evolution of the RCAS-*Hoxd13* midgut morphology was initially simulated using the implicit method to reflect its deviation from the ridge-to-zigzag to a ridge-to-sulci transition. Simulations of later stage wrinkling, which mimics that of the hindgut, employed the explicit method for comparison to the hindgut. The same principle was applied to the choice of implicit vs. explicit models for explant experiment simulations (Table 7).

Table 6. Measured values used to determine lumen wrinkling model parameters.

Condition	Width ratio	Growth anisotropy*	Modulus ratio
E12-E16 midgut	0.40→0.27	Anisotropic Circ.→Long.	12.3→20
E12 hindgut	0.45	Isotropic	4.2 [§]
E14 hindgut	0.27	Isotropic	7.9
E16 hindgut	0.20	Isotropic	15.5 [§]
E12-E14 midgut + <i>Hoxd13</i>	0.36→0.23	Circ.→Isotropic	3.7→2.3
E14 midgut + <i>Hoxd13</i>	0.23	Isotropic	2.3
E16 midgut + <i>Hoxd13</i>	0.19	Isotropic	12.2 [§]
E18 midgut + <i>Hoxd13</i>	0.15	Isotropic	18.5 [§]
E12 midgut + DMSO	0.40→0.27	Anisotropic Long.	12.3→29.4
E12 midgut + rmTGFβ1	0.35→0.19	Isotropic	12.3→6.5
E12 midgut + rmTGFβ1 (final)	0.19	Isotropic	6.5
E13 hindgut + DMSO	0.23	Isotropic	6.5
E13 hindgut + SB431542	0.16	Anisotropic Circ.	36.6

*Qualitatively determined from strain data over time (Figure 15A)

[§] Value predicted from polynomial fit of measured data for the hindgut and midgut + *Hoxd13* (Extended Figure 11D)

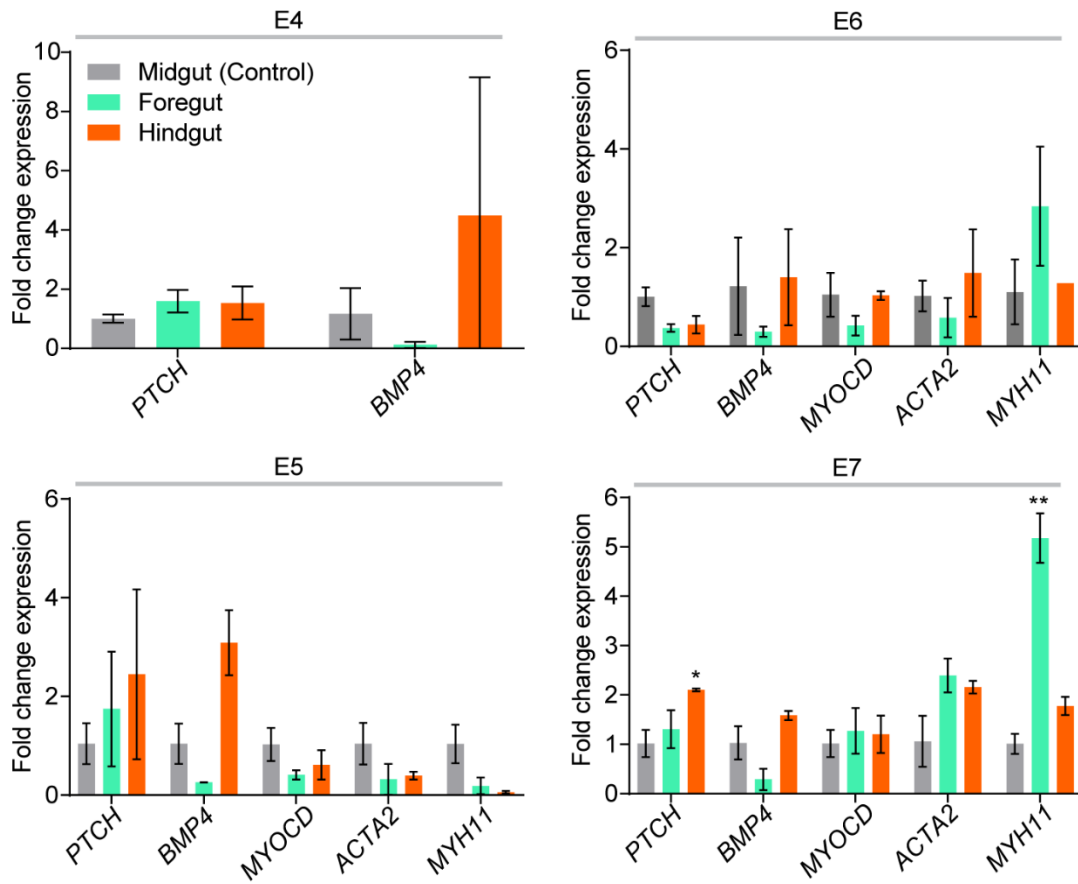
Table 7. 3D midgut, midgut + *Hoxd13*, and hindgut simulation parameters.

Condition	Model type	Initial width ratio	Growth functions
E12-E16 midgut	Implicit	0.40	Stepwise anisotropic with endoderm thinning
E12 hindgut	Explicit	0.40	Transversely isotropic
E14 hindgut	Explicit	0.30	Transversely isotropic
E16 hindgut	Explicit	0.20	Transversely isotropic
E12-E14 midgut + <i>Hoxd13</i>	Implicit	0.35	Transversely isotropic with endoderm thinning ^{††}
E14 midgut + <i>Hoxd13</i>	Explicit	0.25	Transversely isotropic
E16 midgut + <i>Hoxd13</i>	Explicit	0.20	Transversely isotropic
E18 midgut + <i>Hoxd13</i>	Explicit	0.15	Transversely isotropic
E12 midgut + DMSO	Implicit	0.35	Stepwise anisotropic
E12 midgut + rmTGFβ1	Implicit	0.35	Transversely isotropic with endoderm thinning
E12 midgut + rmTGFβ1 (final)	Explicit	0.20	Transversely isotropic
E13 hindgut + DMSO	Explicit	0.25	Transversely isotropic
E13 hindgut + SB431542	Explicit	0.20	Circumferential anisotropic

^{††} Initial imperfection - circumferential ridges

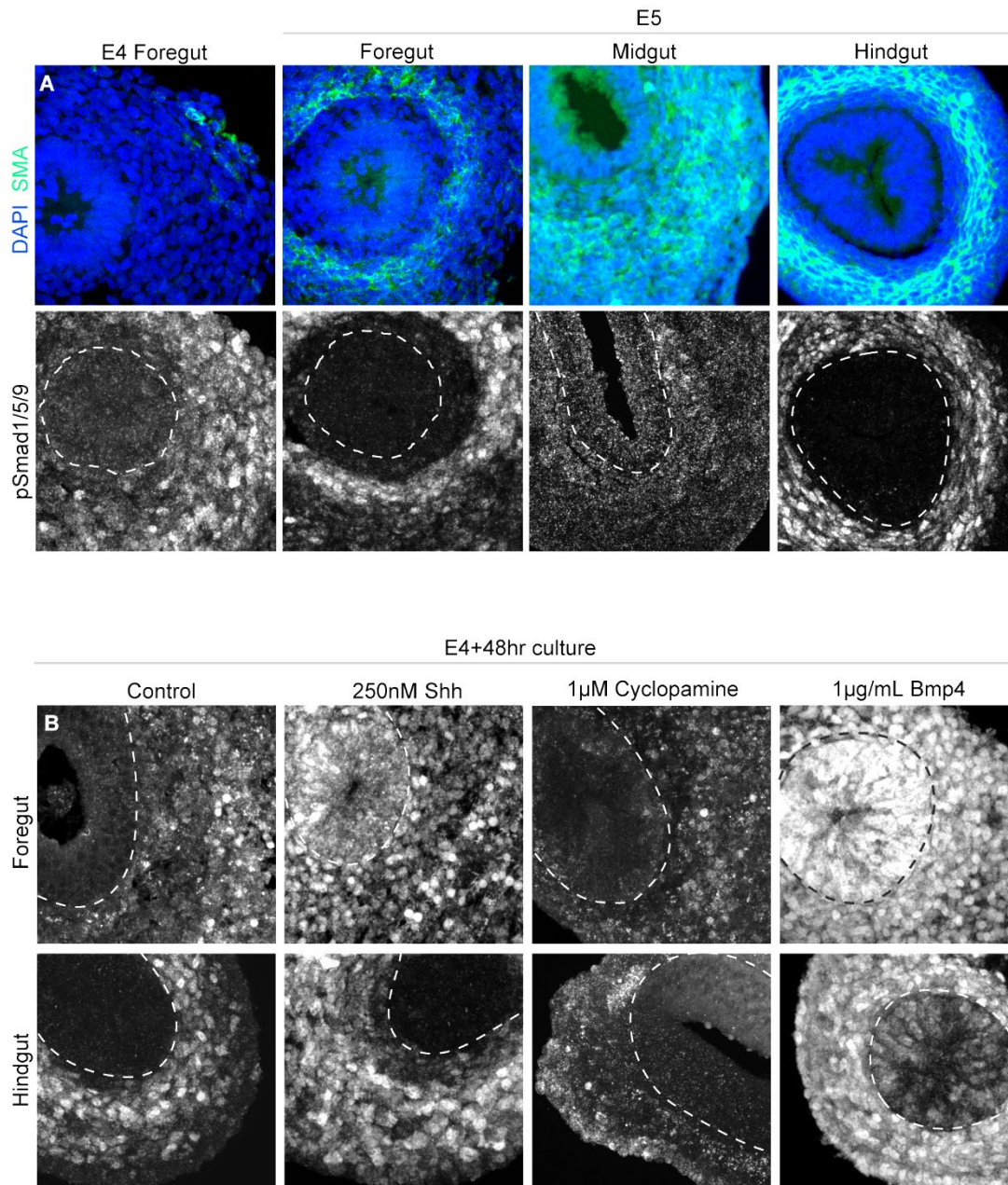
APPENDIX 1: Supplementary materials for *Radial and axial geometry* in early gut tube development

Extended Figures 1-3



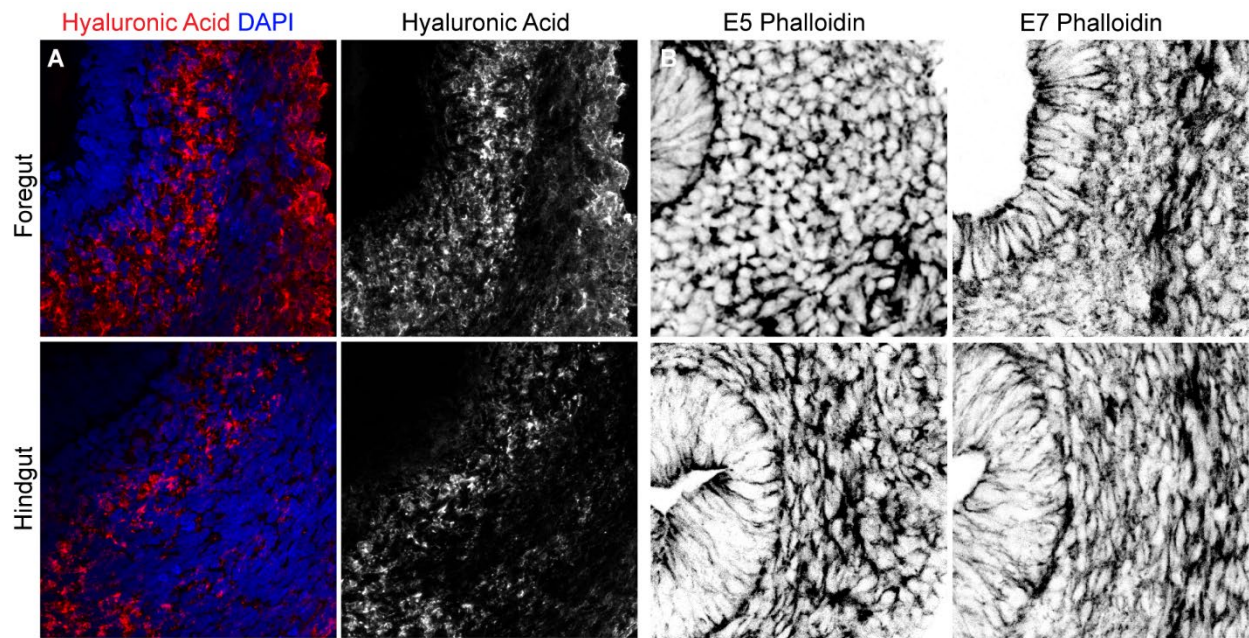
Extended Figure 1. qPCR results for muscle patterning and differentiation genes

qPCR targeting muscle genes, performed on fore-, mid-, and hindgut samples with all tissue layers included at E4, E5, E6, and E7. Fold change expression and statistical significance is calculated relative to the midgut (**, $p < 0.01$; *, $p < 0.05$; t-test, $n = 3$ biological replicates).



Extended Figure 2. Endogenous and explant Bmp activation during muscle patterning

(A) Endogenous Bmp pathway activation in transverse sections of the early foregut, midgut, and hindgut assessed by pSmad1/5/9 nuclear localization, shown alone in the panels on the bottom row. Dotted line outlines the basement membrane, where the endoderm is in the center. Top panels show muscle (SMA) patterns at corresponding time points, in separate samples. E5 is shown for all regions, and E4 is shown for the foregut because it appears to pattern muscle slightly earlier. (B) pSmad stains in the foregut and hindgut after various perturbations of Hh and Bmp signaling in 48hr culture starting from E4.



Extended Figure 3. Unique cell shapes and ECM properties in the early fore- and hindguts

(A) Immunostain for hyaluronic acid binding protein (Habbp) in transverse sections at E7 in the foregut and hindgut. Endoderm is in the top left corner. (B) Phalloidin stain for F-actin in transverse sections at E5 and E7 in the foregut and hindgut. Endoderm is on the left.

Calculating contributions of cell density and proliferation to volumetric growth

Written by David Sprinzak and Hasreet Gill.

We begin by asking how V , volume, changes with proliferation and ECM secretion.

If we consider only cell division:

$$V = V_0 2^{\frac{t}{\tau}} = V_0 e^{\frac{t \ln 2}{\tau}}$$

Where τ is the cell cycle length. For cell density, $C = \frac{N}{V}$, or the number of cells N per unit

volume. Thus, when ECM is secreted, the number of cells per unit volume decreases:

$$V = \frac{N}{C(t)}$$

If N doesn't change and C decreases, volume will increase. More generally, if we incorporate both density change and change in cell number via proliferation, where N_0 is the initial number of cells:

$$V = \frac{N(t)}{C(t)} = \frac{N_0 e^{\frac{t \ln 2}{\tau}}}{C(t)}$$

$$dV = \frac{dN(t)}{C(t)} + \frac{N(t)}{C(t)^2} dC$$

Relative change in volume is:

$$\frac{dV}{V} = \frac{dN(t)}{N(t)} + \frac{dC}{C(t)}$$

Or, the partial derivative:

$$\frac{\partial V}{\partial t} = \frac{\partial V}{\partial N} \frac{\partial N}{\partial t} + \frac{\partial V}{\partial C} \frac{\partial C}{\partial t}$$

$$\frac{\partial V}{\partial t} = \frac{1}{C} \frac{\partial N}{\partial t} + \frac{N(t)}{C(t)^2} \frac{\partial C}{\partial t}$$

$$\frac{\partial N}{\partial t} = kN, k = \frac{\ln 2}{\tau}$$

The total change in volume is equal to the change in volume due to cell division and due to ECM secretion:

$$\frac{\Delta V}{\Delta t} = \frac{1}{C} \frac{\ln 2}{\tau} N - \frac{N(t)}{C(t)^2} \frac{\Delta C}{\Delta t}$$

$$\frac{\Delta V}{\Delta t} = V(t) \frac{\ln 2}{\tau} - \frac{V(t)}{C(t)} \frac{\Delta C}{\Delta t}$$

$$\Delta V = V(t) \frac{\ln 2}{\tau} \Delta t - \frac{V(t)}{C(t)} \Delta C$$

$$\Delta V = V(t) \frac{\ln 2}{\tau} \Delta t - V(t) \frac{\Delta C}{C(t)}$$

$$\frac{\Delta V}{V} = \frac{\ln 2}{\tau} \Delta t - \frac{\Delta C}{C(t)}$$

The relative contribution of each can be defined:

$$\text{Contribution due to cell division} = \frac{\frac{\ln 2}{\tau} \Delta t}{\Delta V/V}$$

$$\text{Contribution due to cell density (ECM secretion)} = \frac{\frac{\Delta C}{C(t)}}{\Delta V/V(t)}$$

Reaction-diffusion model of muscle patterning with differential growth

Model formulations are provided here for reference. All equations, codes, and descriptions were developed and written by Shahar Kasirer. Descriptions edited by Hasreet Gill.

Simple model without growth

Simulation assumptions:

1. Hh is secreted from the endoderm and diffuses into the mesenchyme.
2. BMP4 is activated by HH in mesenchymal cells and diffuses.
3. BMP2/7 (assumed to be only one ligand) is secreted from outer mesothelial cells and diffuses into the mesenchyme.
4. We initially assume no cell growth (clearly wrong).
5. We initially perform simulation in 1D (radial symmetry).

Equations:

$$\begin{aligned}\frac{\partial[hh]}{\partial t} &= D_{hh}\nabla^2[hh] - \gamma_{hh}[hh] \\ \frac{\partial[B2]}{\partial t} &= D_{B2}\nabla^2[B2] - \gamma_{B2}[B2] \\ \frac{\partial[B4]}{\partial t} &= \beta_{B4}[hh] + D_{B4}\nabla^2[B4] - \gamma_{B4}[B4], \beta_{B4}[hh] \equiv \beta_{\max} \frac{[hh]^n}{k_d^n + [hh]^n} \\ \frac{\partial[SMA]}{\partial t} &= \beta_{SMA}[hh, B2, B4] - \gamma_{SMA}[SMA], \\ \beta_{SMA}[hh, B2, B4] &\equiv \beta_{SMA-\max} \frac{[hh]^{n_1}}{k_{d_1}^{n_1} + [hh]^{n_1}} \cdot \frac{k_{d_2}^{n_2}}{k_{d_2}^{n_2} + [B4]^{n_2}} \cdot \frac{k_{d_3}^{n_3}}{k_{d_3}^{n_3} + [B2]^{n_3}}\end{aligned}$$

Boundary conditions:

$$\begin{aligned} \left. \frac{\partial [hh]}{\partial r} \right|_{r=0} &= -\eta_{hh}, & \left. \frac{\partial [hh]}{\partial r} \right|_{r=R} &= 0 \\ \left. \frac{\partial [B2]}{\partial r} \right|_{r=0} &= 0, & \left. \frac{\partial [B2]}{\partial r} \right|_{r=R} &= \eta_{B2} \end{aligned}$$

Change to dimensionless variables

We would like to work with dimensionless variables. To do that, we normalize our distance unit by R , our time unit by $1/\gamma_{hh}$ and our concentration unit by k_d . We define new, dimensionless variables:

$$\begin{aligned} \tilde{r} &= r \sqrt{\frac{\gamma_{hh}}{D_{hh}}}, \tilde{R} = R \sqrt{\frac{\gamma_{hh}}{D_{hh}}}, \tilde{t} = \gamma_{hh} t, ; a = \frac{[hh]}{k_d}, b = \frac{[B2]}{k_d}, D_b = \frac{D_{B2}}{D_{hh}}, \gamma_b = \frac{\gamma_{B2}}{\gamma_{hh}} \\ c &= \frac{[B4]}{k_d}, D_c = \frac{D_{B4}}{D_{hh}}, \gamma_c = \frac{\gamma_{B4}}{\gamma_{hh}}, \beta_{\max-c} = \frac{\beta_{\max}}{\gamma_{hh}}, s = \frac{[SMA]}{k_d} \\ \gamma_s &= \frac{\gamma_{SMA}}{\gamma_{hh}}, \beta_{\max-s} = \frac{\beta_{SMA-\max}}{\gamma_{hh}}, k_1 = \frac{k_{d1}}{k_d}, k_2 = \frac{k_{d2}}{k_d}, k_3 = \frac{k_{d3}}{k_d} \\ \eta_a &= \frac{\eta_{hh}}{k_d} \sqrt{\frac{D_{hh}}{\gamma_{hh}}}, \eta_b = \frac{\eta_{B2}}{k_d} \sqrt{\frac{D_{hh}}{\gamma_{hh}}} \end{aligned}$$

We then get:

$$\begin{aligned} \frac{\partial a}{\partial \tilde{t}} &= \tilde{\nabla}^2 a - a \\ \frac{\partial b}{\partial \tilde{t}} &= D_b \tilde{\nabla}^2 b - \gamma_b b \\ \frac{\partial c}{\partial \tilde{t}} &= \beta_c [a] + D_c \tilde{\nabla}^2 c - \gamma_c c, \beta_c [a] \equiv \beta_{\max-c} \frac{a^n}{1 + a^n} \\ \frac{\partial s}{\partial \tilde{t}} &= \beta_s [a, b, c] - \gamma_s s, \beta_s [a, b, c] \equiv \beta_{\max-s} \frac{a^{n_1}}{k_1^{n_1} + a^{n_1}} \cdot \frac{k_2^{n_2}}{k_2^{n_2} + b^{n_2}} \cdot \frac{k_3^{n_3}}{k_3^{n_3} + c^{n_3}} \end{aligned}$$

With the boundary conditions:

$$\begin{aligned} \left. \frac{\partial a}{\partial \tilde{r}} \right|_{\tilde{r}=0} &= -\eta_a, & \left. \frac{\partial a}{\partial \tilde{r}} \right|_{\tilde{r}=\tilde{R}} &= 0 \\ \left. \frac{\partial b}{\partial \tilde{r}} \right|_{\tilde{r}=0} &= 0, & \left. \frac{\partial b}{\partial \tilde{r}} \right|_{\tilde{r}=\tilde{R}} &= \eta_b \end{aligned}$$

Steady state solution in 1D

The simplest case is in 1D where $\nabla^2 \rightarrow \frac{\partial^2}{\partial \tilde{x}^2}$, in which we can assume a solution from the form $Ae^{-k\tilde{x}} + Be^{k\tilde{x}}$. For steady state, all time derivatives vanish, and we can solve the first two equations explicitly. Inserting the assumed solutions we get:

$$\begin{aligned} a(k_a^2 - 1) &= 0 \\ b(D_b k_b^2 - \gamma_b) &= 0 \end{aligned}$$

To satisfy the boundary conditions we need non-trivial (non-zero) solution for a, b . Therefore, we get $k_a = 1$ and $k_b = \sqrt{\frac{\gamma_b}{D_b}}$. Using the boundary conditions to find the constants A, B we get

$$\begin{aligned} a(\tilde{x}) &= \frac{\eta_a \cosh(\tilde{R} - \tilde{x})}{\sinh(\tilde{R})} \\ b(\tilde{x}) &= \frac{\eta_b \cosh(k_b \tilde{x})}{k_b \sinh(k_b \tilde{R})} \end{aligned}$$

Now we get the following equation for c in a steady state

$$D_c \tilde{\nabla}^2 c - \gamma_c c = -\beta_c [a]$$

First we can solve the homogeneous part, $D_c \frac{\partial^2 c}{\partial \tilde{x}^2} - \gamma_c c = 0$ easily. The solution is

$$c_{\text{homogenous}} = Ae^{k_c \tilde{x}} + Be^{-k_c \tilde{x}}, k_c \equiv \sqrt{\frac{\gamma_c}{D_c}}$$

For the un-homogeneous part we define $f(\tilde{x}) \equiv -\beta_c [a(\tilde{x})]/D_c$ to get the equation

$$\tilde{\nabla}^2 c - k_c^2 c = f(\tilde{x})$$

One can verify that a this equation is solved by

$$c_{\text{private}} = \frac{1}{2k_c} \left(e^{k_c \tilde{x}} \int_0^{\tilde{x}} e^{-k_c y_1} f(y_1) dy_1 - e^{-k_c \tilde{x}} \int_0^{\tilde{x}} e^{k_c y_2} f(y_2) dy_2 \right)$$

And the general solution is

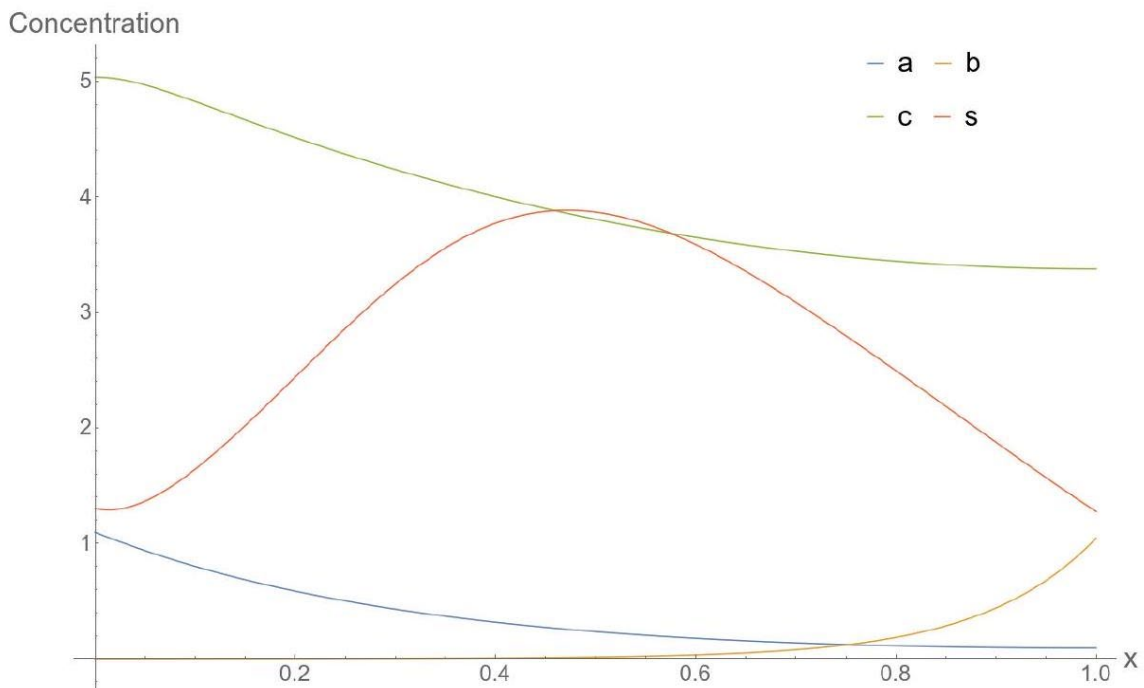
$$c_{\text{general}} = \frac{1}{2\sqrt{\gamma_c D_c}} \left(e^{-k_c \tilde{x}} \int_0^{\tilde{x}} e^{k_c y_2} \beta_c[a(y_2)] dy_2 - e^{k_c \tilde{x}} \int_0^{\tilde{x}} e^{-k_c y_1} \beta_c[a(y_1)] dy_1 \right) + A e^{k_c \tilde{x}} + B e^{-k_c \tilde{x}}$$

Using the boundary conditions we can find the constants A, B . The solution is

$$c = \frac{1}{2\sqrt{\gamma_c D_c}} \left(e^{-k_c \tilde{x}} \int_0^{\tilde{x}} e^{k_c y_2} \beta_c[a(y_2)] dy_2 - e^{k_c \tilde{x}} \int_0^{\tilde{x}} e^{-k_c y_1} \beta_c[a(y_1)] dy_1 \right) + \frac{1}{2\sqrt{\gamma_c D_c}} \frac{\cosh(k_c \tilde{x})}{\sinh(k_c \tilde{R})} \left(e^{-k_c} \int_0^{\tilde{R}} e^{k_c y_2} \beta_c[a(y_2)] dy_2 + e^{k_c} \int_0^{\tilde{R}} e^{-k_c y_1} \beta_c[a(y_1)] dy_1 \right)$$

Having a steady state solution for a, b, c gives us immediately a solution for s :

$$s = \frac{\beta_s[a(\tilde{x}), b(\tilde{x}), c(\tilde{x})]}{\gamma_s}$$



Steady state results of the 1D model. Parameters: $\eta_a = 3.45, D_a = 0.1, \eta_b = 9.06, \gamma_b = 7.52, D_b = 0.1, \gamma_c = 0.1, D_c = 0.1, \beta_{\max-c} = 10, n = 10, \gamma_s = 0.1, \beta_{\max-s} = 3.9, n_1 = 1, n_2 = 1, n_3 = 10, k_1 = 1, k_2 = 1, k_3 = 3.85$

Steady state solution in 2D with radial symmetry

A more realistic case is the 2D one, with radial symmetry. In that case we get $\nabla^2 \rightarrow \frac{\partial^2}{\partial r^2} + \frac{1}{r} \frac{\partial}{\partial r}$. In that case the equations for a, b take, in a steady state, the form

$$\begin{aligned} \frac{\partial^2 a}{\partial \tilde{r}^2} + \frac{1}{\tilde{r}} \frac{\partial a}{\partial \tilde{r}} - a &= 0 \\ D_b \frac{\partial^2 b}{\partial \tilde{r}^2} + D_b \frac{1}{\tilde{r}} \frac{\partial b}{\partial \tilde{r}} - \gamma_b b &= 0 \end{aligned}$$

Those are Bessel equations, with the solutions

$$\begin{aligned} a &= A I_0(\tilde{r} - r_0) \\ b &= B I_0(k_a(\tilde{r} - r_1)), k_b = \sqrt{\frac{\gamma_b}{D_b}} \end{aligned}$$

where J_0 is the Bessel function from the first kind. To find the constants A, B, r_0, r_1 we use

boundary conditions. Since $\frac{dI_0(x)}{dx} = I_1(x)$, which is an odd function, we get $A = \frac{\eta_a}{I_1(\tilde{R})}, B =$

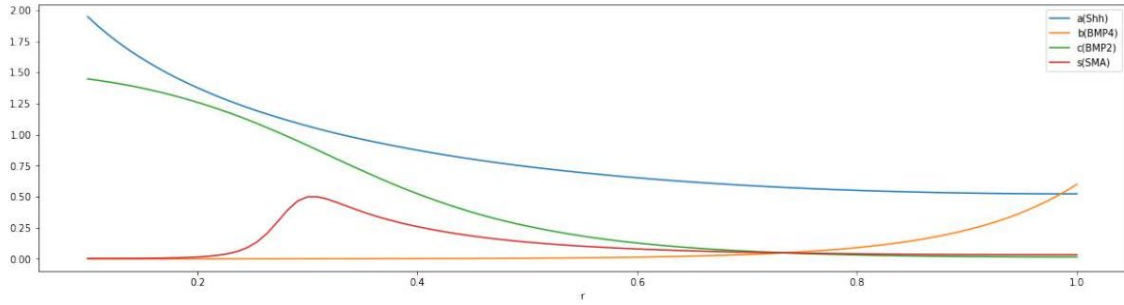
$\frac{\eta_b}{k_b I_1(\tilde{R})}, r_0 = \tilde{R}$ and $r_1 = 0$. The solutions for a, b are

$$\begin{aligned} a &= \frac{\eta_a}{k_b I_1(\tilde{R})} I_0((\tilde{r} - \tilde{R})) \\ b &= \frac{\eta_a}{k_b I_1(\tilde{R})} I_0(\tilde{r}) \end{aligned}$$

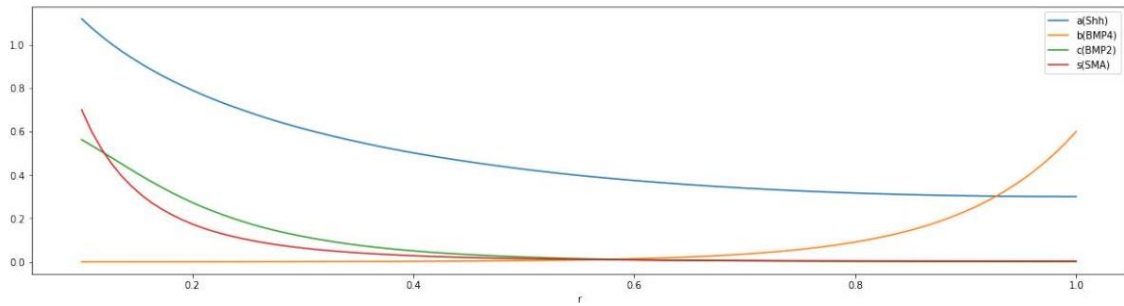
The steady state equation for c takes the form

$$D_c \frac{\partial^2 c}{\partial \tilde{r}^2} c + \frac{D_c}{\tilde{r}} \frac{\partial c}{\partial r} - \gamma_c c + \beta_b [a(\tilde{r})] = 0$$

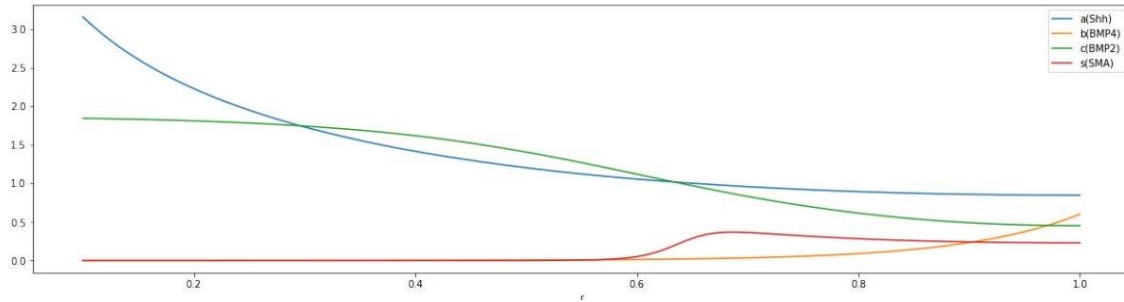
This equation can be solved numerically and then used to calculate s using equation (14).



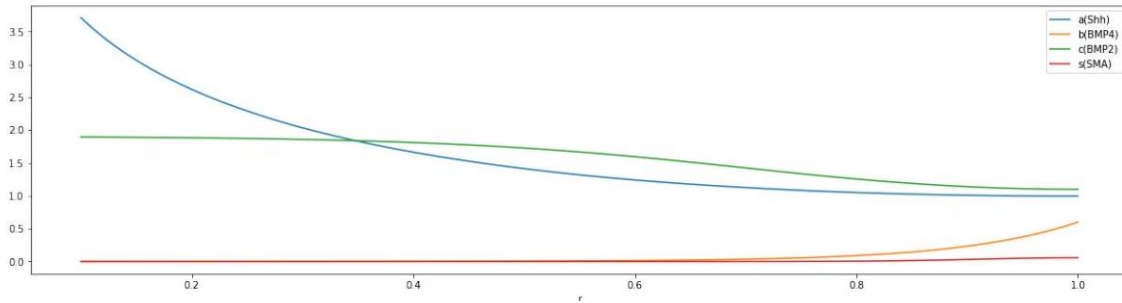
Steady state results of the 2D model - Control. Parameters: $\eta_a = 8305, D_a = 0.4, \eta_b = 5.7, \gamma_b = 10, D_b = 0.1, \gamma_c = 5.2, D_c = 0.1, \beta_{\max-c} = 10, n = 10, \gamma_s = 2.9, \beta_{\max-s} = 806, n_1 = 4, n_2 = 5, n_3 = 20, k_1 = 5, k_2 = 4, k_3 = 1$



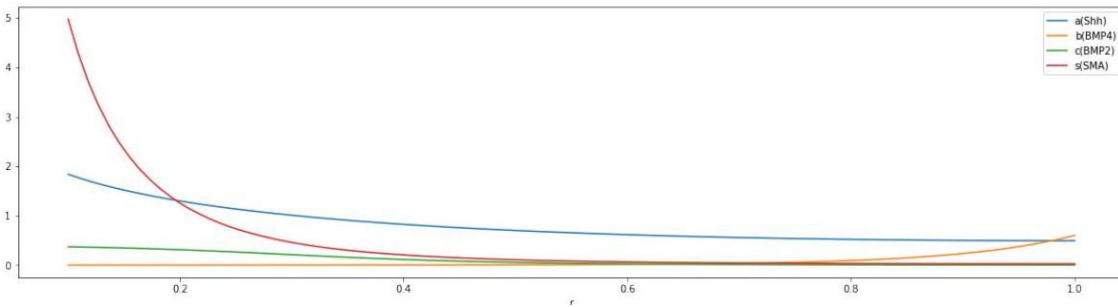
Steady state results of the 2D model - inhibiting Shh. Parameters: $\eta_a = 5068, D_a = 0.4, \eta_b = 5.7, \gamma_b = 10, D_b = 0.1, \gamma_c = 5.2, D_c = 0.1, \beta_{\max-c} = 10, n = 10, \gamma_s = 2.9, \beta_{\max-s} = 806, n_1 = 4, n_2 = 5, n_3 = 20, k_1 = 5, k_2 = 4, k_3 = 1$



Steady state results of the 2D model - intermediate Shh. Parameters: $\eta_a = 14272, D_a = 0.4, \eta_b = 5.7, \gamma_b = 10, D_b = 0.1, \gamma_c = 5.2, D_c = 0.1, \beta_{\max-c} = 10, n = 10, \gamma_s = 2.9, \beta_{\max-s} = 806, n_1 = 4, n_2 = 5, n_3 = 20, k_1 = 5, k_2 = 4, k_3 = 1$



Steady state results of the 2D model - high Shh. Parameters: $\eta_a = 14272, D_a = 0.4, \eta_b = 5.7, \gamma_b = 10, D_b = 0.1, \gamma_c = 5.2, D_c = 0.1, \beta_{\max-c} = 10, n = 10, \gamma_s = 2.9, \beta_{\max-s} = 806, n_1 = 4, n_2 = 5, n_3 = 20, k_1 = 5, k_2 = 4, k_3 = 1$



Steady state results of the 2D model - inhibiting BMP4. Parameters: $\eta_a = 8305, D_a = 0.4, \eta_b = 5.7, \gamma_b = 10, D_b = 0.1, \gamma_c = 5.2, D_c = 0.1, \beta_{\max-c} = 2.7, n = 10, \gamma_s = 2.9, \beta_{\max-s} = 806, n_1 = 4, n_2 = 5, n_3 = 20, k_1 = 5, k_2 = 4, k_3 = 1$

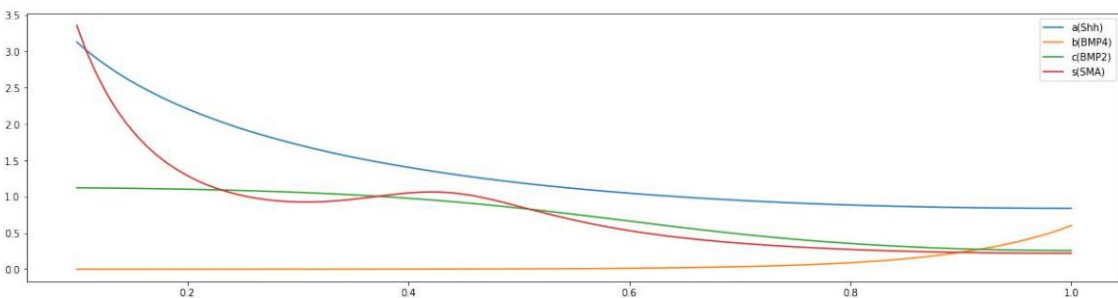


Figure 7: Steady state results of the 2D model - high Shh. Parameters: $\eta_a = 14272$, $D_a = 0.4$, $\eta_b = 5.7$, $\gamma_b = 10$, $D_b = 0.1$, $\gamma_c = 5.2$, $D_c = 0.1$, $\beta_{\max-c} = 6.1$, $n = 10$, $\gamma_s = 2.9$, $\beta_{\max-s} = 806$, $n_1 = 4$, $n_2 = 5$, $n_3 = 20$, $k_1 = 5$, $k_2 = 4$, $k_3 = 1$

Incorporating growth

To incorporate growth, we assume that each cell has a certain division rate such that the probability that it will divide at the exact time t is $p = e^{-\Gamma t}/\Gamma$, meaning that this is a Poisson-like process. This only includes divisions in the radial direction (which change the cross-section area of the gut). With this assumption we get the probability of dividing at the next t seconds to be:

$$\int_0^t \frac{e^{-\Gamma t'}}{\Gamma} dt' = 1 - e^{-\Gamma t}$$

And so the average change in area do to cell division is

$$\Delta A(t) = A(1 - e^{-\Gamma t})$$

and for short times ($t \ll 1/\Gamma$) we get

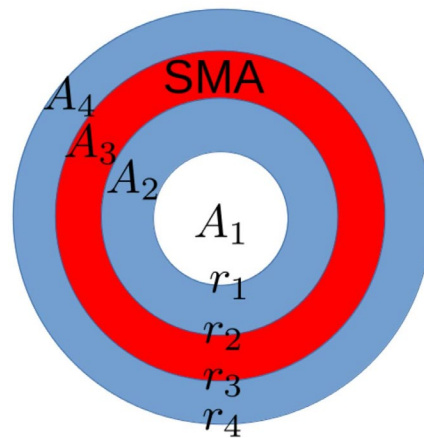
$$\Delta A(t) \approx A\Gamma t$$

In our simulation we want to follow the change of the different radii in the gut: r_1 is the inner radius of the gut, r_2, r_3 are the inner and outer radii of the SMA, respectively, and r_4 is the outer radius of the gut. We assume 3 different growth rates: 1 for the region inside the gut, one for the undifferentiated gut and one for the differentiated SMA tissue. The change in each radius is calculated according to

$$\Delta r(t) = \frac{\Delta A(t)}{dA/dr} = \frac{\Delta A(t)}{2\pi r}$$

where r is the initial radius and ΔA is the total change the area inside radius r . For the different radii we get

$$\begin{aligned}\Delta r_1 &= \frac{\Delta A_1(t)}{2\pi r_1} \\ \Delta r_2 &= \frac{\Delta A_1(t) + \Delta A_2(t)}{2\pi r_2} \\ \Delta r_3 &= \frac{\Delta A_1(t) + \Delta A_2(t) + \Delta A_3(t)}{2\pi r_3} \\ \Delta r_4 &= \frac{\Delta A_1(t) + \Delta A_2(t) + \Delta A_3(t) + \Delta A_4(t)}{2\pi r_4}\end{aligned}$$



Schematic drawing of the model cross-section

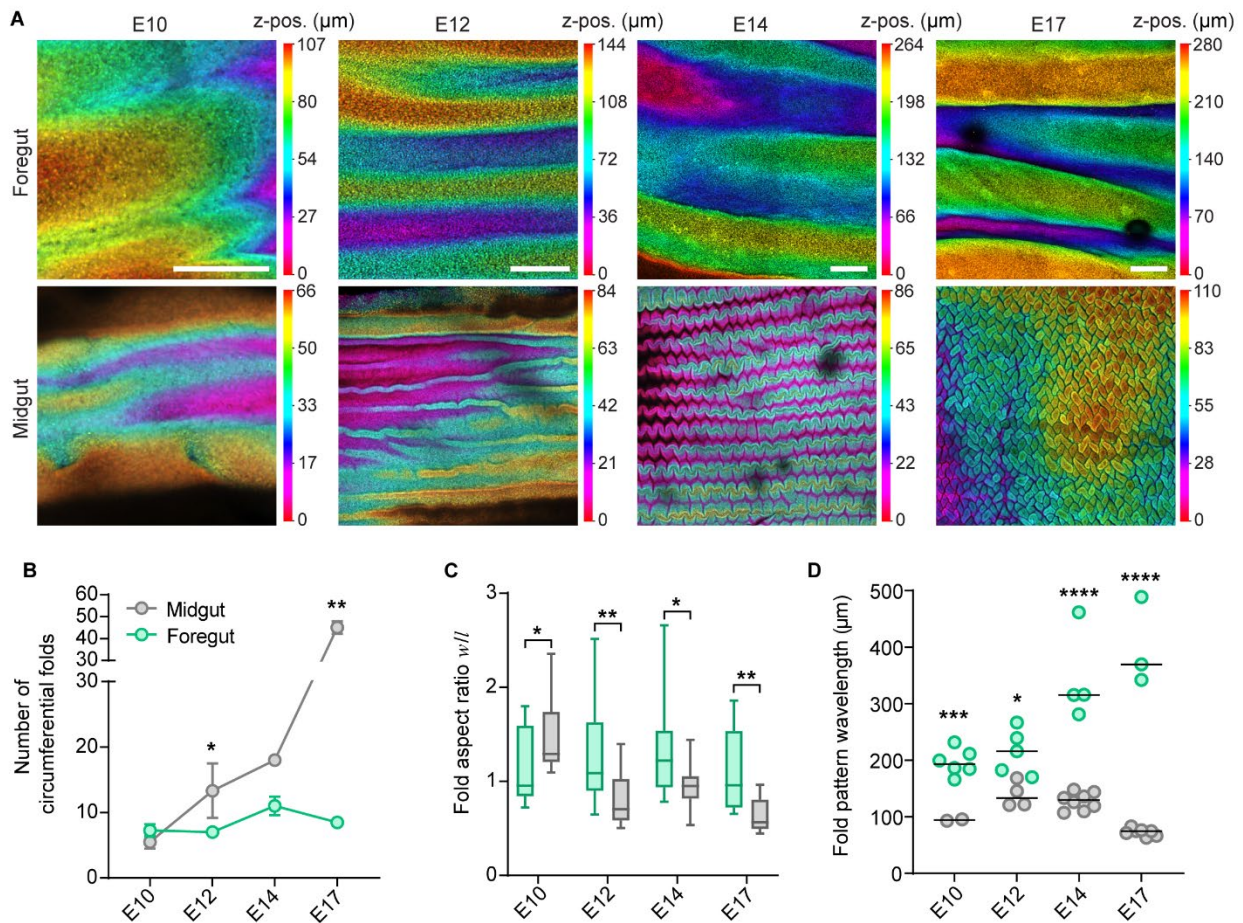
Convergent extension

We incorporate gut lengthening as convergent extension, where cells are assumed to converge towards the middle of the gut, without changing their volume. In that case volume is conserved and we get that the relative change in cross-section area equals the relative change in the length of the gut

$$\frac{\Delta A}{A} = \frac{\Delta h}{h}$$

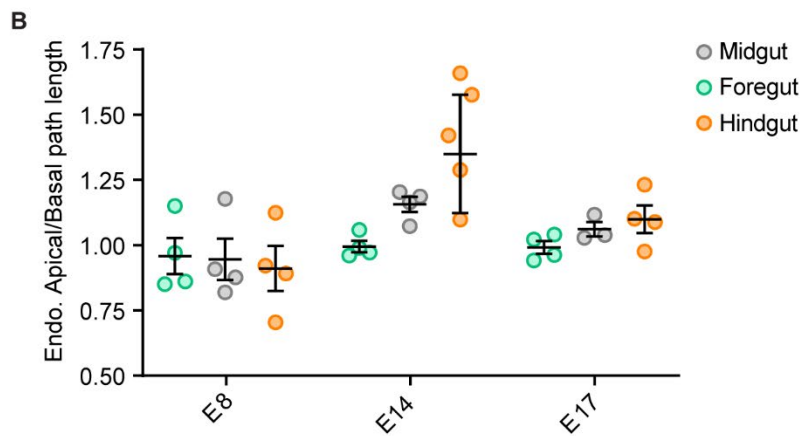
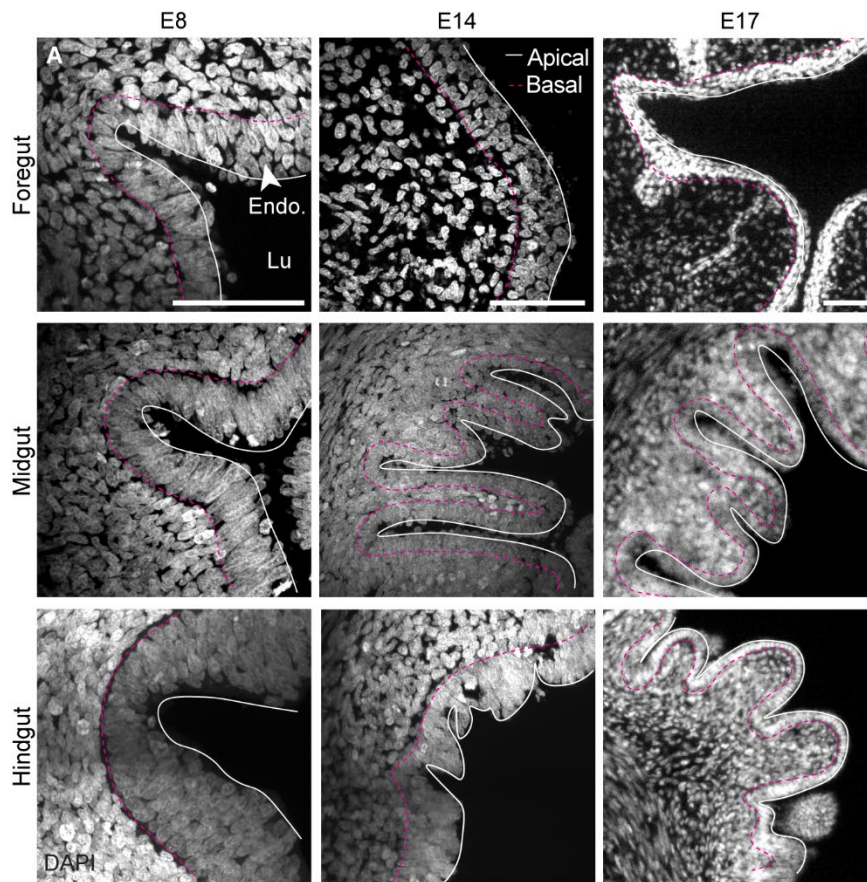
APPENDIX 2: Supplementary materials for *Divergent epithelial buckling across gut regions*

Extended Figures 4-8



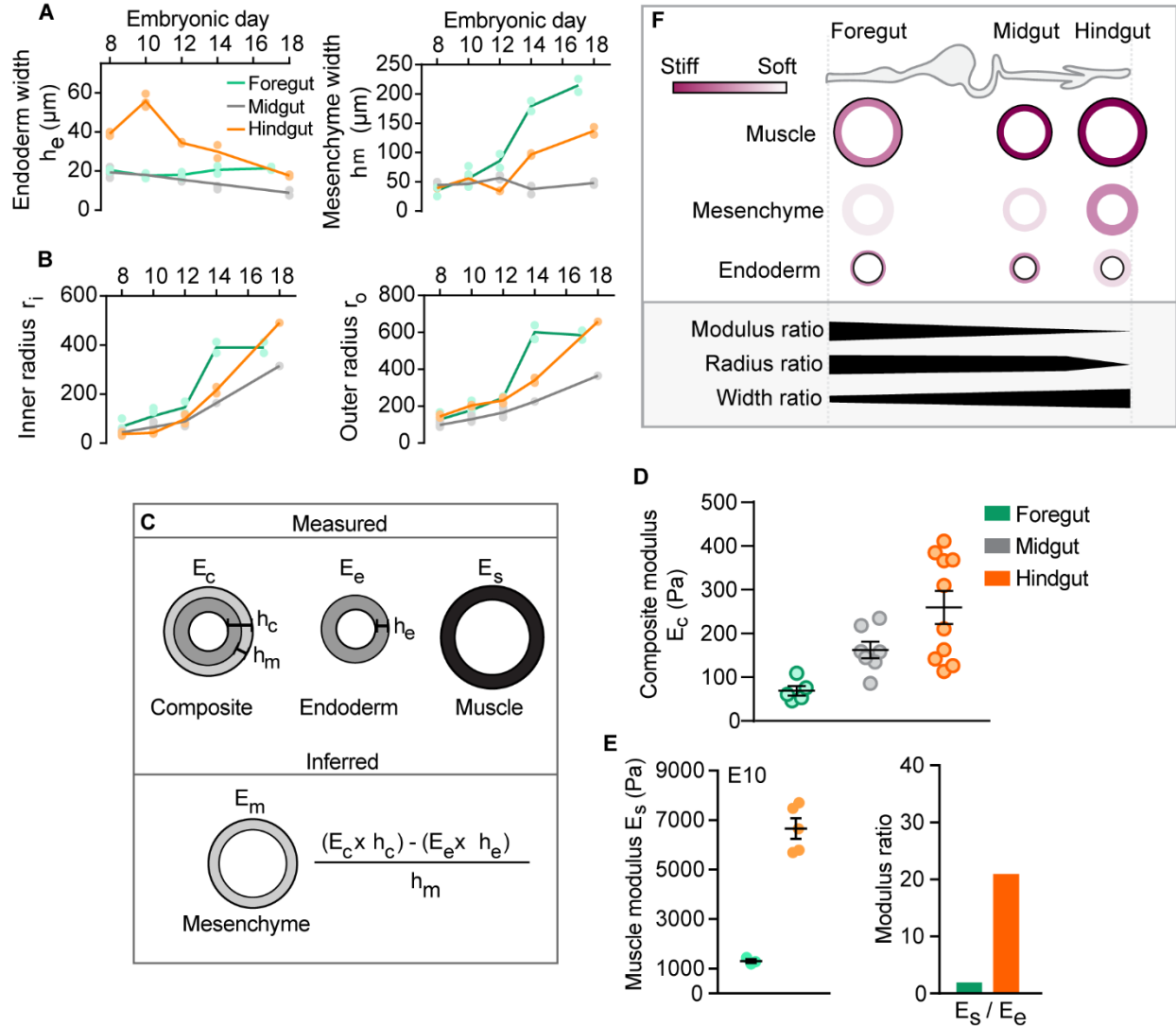
Extended Figure 4. Wrinkle morphology and lack of stepwise buckling in the foregut.

(A) Lumen surfaces in the foregut and midgut over time stained with DAPI and imaged on a confocal microscope (Methods). Color indicates depth according to associated scales in μm . Scale bar, 200 μm . (B) Number of wrinkles per cross-sectional area over time, measured from DAPI-stained transverse sections. $n=3-4$ biological replicates per time point. (C) Fold aspect ratios over time, where large values correspond to broad wrinkles and small values are tall and thin wrinkles. $n=10-15$ folds. (D) Distances between the apices of adjacent wrinkles on the circumferential axis, measured from lumen surface images. $n=3-8$ pairs of folds (****, $p<0.0001$; ***, $p<0.001$; **, $p<0.01$; *, $p<0.05$; t-test).



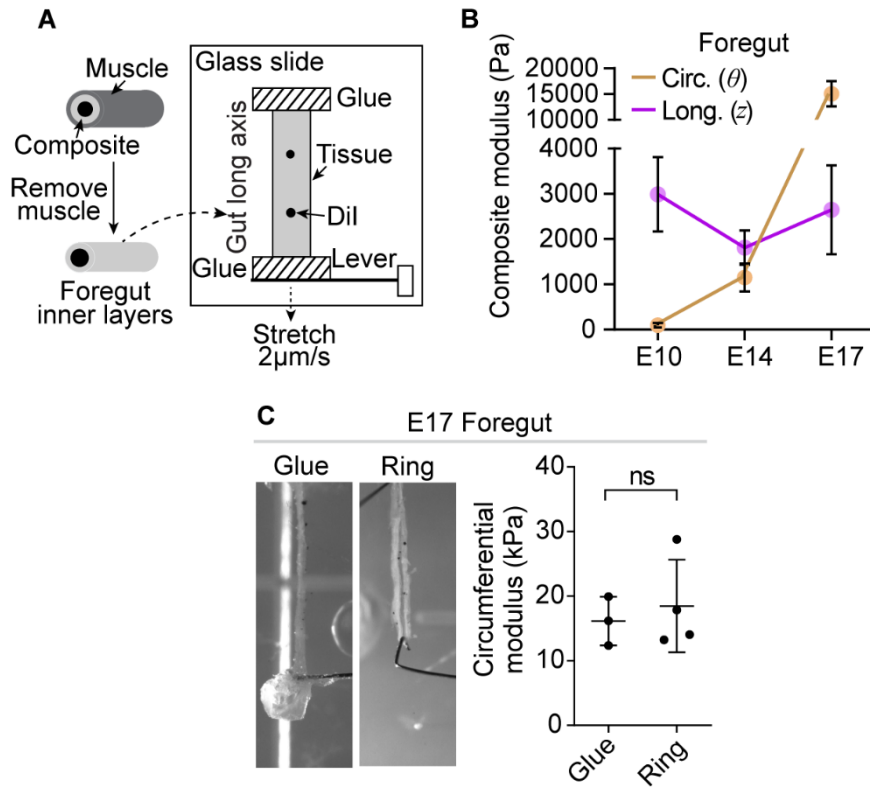
Extended Figure 5. Endodermal surface creasing in the hindgut.

(A) Partial views of DAPI-stained transverse sections through gut segments over time (dashed magenta line, basal endoderm-mesenchyme interface; white line, apical endoderm surface; arrowhead and Endo., endoderm; Lu, lumen). Scale bar, 100 μ m. (B) Ratio of apical (white line in part A) to basal (dashed pink line in part A) path length in each compartment over time, where higher ratios correspond to creased epithelial morphologies and lower to smooth folding. n=3-5 images.



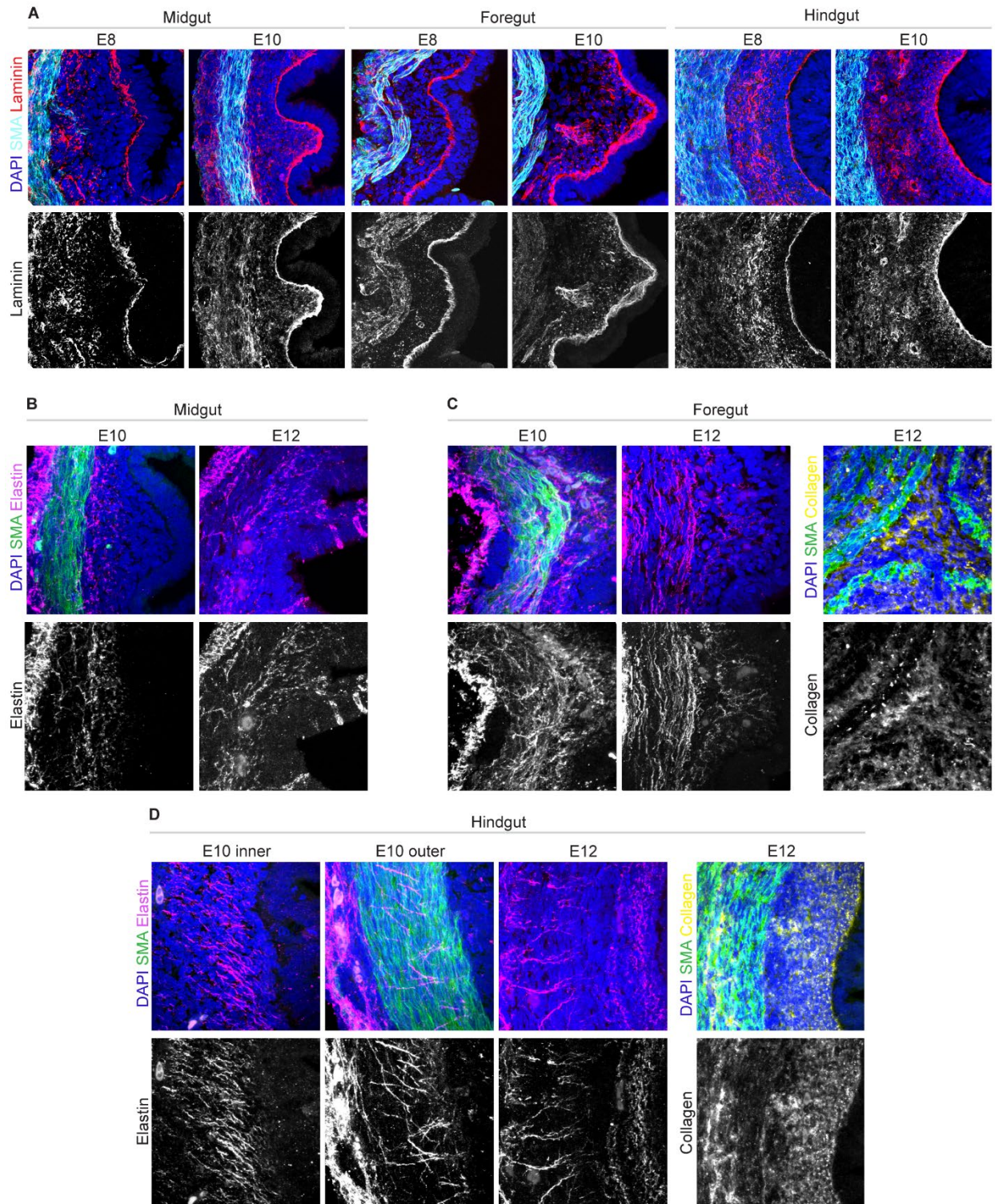
Extended Figure 6. Anteroposterior trends in mechanical properties along the gut

(A) Endoderm and mesenchyme widths and (B) inner and outer radii from foregut, midgut, and hindgut sections from E8-E18. (C) Method of mesenchyme (m) modulus calculation from endoderm and composite measurements. (D) Composite modulus values at E10. $n=3-10$ measurements. (E) Muscle (s) modulus in the foregut and hindgut at E10 and modulus ratio of muscle to endoderm (e). (F) Schematic summary of geometric and modulus data at E10 (purple gradient represents modulus magnitude and geometries of ring illustrations reflect qualitative differences between regions). Modulus, radius, and width ratios show anterior-to-posterior trends during primary buckling along the gut lumen.



Extended Figure 7. Anisotropic stiffness in the foregut inner composite

(A) Method of longitudinal modulus measurement. Muscle was first removed, and the inner layer composite was fixed to a glass slide on one end, and the cantilever on the other. The tissue sample was labeled with Dil dots as with circumferential ring measurements to trace deformation over time. (B) Composite modulus values from E10-E17 on both circumferential and longitudinal axes, where longitudinal measurements were performed as shown in part A, and circumferential measurements were performed as shown in Figure 8E. (C) Circumferential modulus measurements and corresponding frames from movies of the foregut inner composite at E17 using two different methods—the typical ring method for other circumferential samples, and the glue method used for longitudinal modulus measurements (ns, not significant; t-test, $n=3-4$)



Extended Figure 8. ECM organization across compartments.

(A-D) Partial views of SMA- and DAPI-stained transverse sections co-immunostained at (A) E8 and E10 for laminin in all compartments, and (B-D) E10 and E12 for elastin and collagen in the (B) midgut, (C) foregut, and (D) hindgut, where “inner” refers to the subepithelial mesenchyme and “outer” refers to the circumferential muscle.

2D model of primary and multiscale buckling in the fore- and hindguts

Model formulations are provided here for reference. All equations, codes, and descriptions were developed and written by Sifan Yin. Descriptions edited by Hasreet Gill.

Basic model and growth description

We consider a typical three-layer ring consisting of the inner endodermal and mesenchymal layers, and the outermost muscular layer. The muscular layer is assumed to provide a fixed boundary condition for the two inner layers. An incompressible hyperelastic material is used to model the endodermal and mesenchymal layers. The position of any material point in the initial (stress-free) and the current configurations are described as \mathbf{X} and \mathbf{x} , respectively (Figure 9A). According to the theory of volumetric growth, the deformation gradient tensor $\mathbf{F} = \partial\mathbf{x}/\partial\mathbf{X}$ can be decomposed as (Rodriguez et al., 1994).

$$\mathbf{F} = \mathbf{A} \cdot \mathbf{G}$$

where \mathbf{A} is the elastic deformation tensor and \mathbf{G} is the growth tensor describing the addition of material/volume. Elastic incompressibility requires $\det \mathbf{A} = 1$ and thus $J = \det \mathbf{G}$ stands for the volume change due to growth. In general, the growth tensor depends on the stress state, position, spatiotemporal biological signaling concentrations, etc. Here, we obtain the spatiotemporal growth tensor by measuring the radius, thickness, and length of each layer at different time points. The growth tensor is generally anisotropic during chick intestinal morphogenesis which can be expressed as

$$\mathbf{G} = g_r \mathbf{E}_r \otimes \bar{\mathbf{E}}_r + g_\theta \mathbf{E}_\theta \otimes \bar{\mathbf{E}}_\theta + g_z \mathbf{E}_z \otimes \bar{\mathbf{E}}_z$$

where \mathbf{E}_i and $\bar{\mathbf{E}}_i$ are the normalized basic vectors in the reference and intermediate configuration, respectively. Growth only changes the lengths of basic vectors but maintains their directions. Thus, the normalized basic vectors in the intermediate and reference configurations are identical, i.e., $\bar{\mathbf{E}}_i = \mathbf{E}_i$. For the cylindrical configuration, the stress-free intermediate states of the endoderm and mesenchyme are measured by $g_r = \bar{h}_\alpha / \bar{h}_{\alpha 0}$ and $g_\theta = \bar{r}_\alpha / \bar{r}_{\alpha 0}$ with $\alpha = e$ and m . The width and radius are rescaled by the radius of muscle layer as $\bar{h}_\alpha = h_\alpha / r_o$ and $\bar{r}_\alpha = r_\alpha / r_o$. h, w, l are the thickness, width, and length of the endoderm or mesenchyme layer, respectively; R is the radius of the clamped muscular layer. The growth tensor varies with time. In our simulations, for simplicity, we consider the muscular layer to be fixed and the growth rates of endodermal and mesenchymal layers are expressed as relative growth ratios with respect to muscular layer.

Constitutive relations and stresses

The endodermal and mesenchymal layers are modeled as hyperelastic materials described by a strain energy function $W_e(\mathbf{A})$. The first Piola-Kirchhoff stress \mathbf{P} is related to \mathbf{A} as

$$\mathbf{P} = J_G \frac{\partial W_e}{\partial \mathbf{A}} \mathbf{G}^{-T}$$

The Cauchy stress is given by

$$\boldsymbol{\sigma} = J^{-1} \mathbf{P} \cdot \mathbf{F}^T = J_A^{-1} \frac{\partial W_e}{\partial \mathbf{A}} \mathbf{A}^T$$

The strain energy function of a Neo-Hookean material is (Shyer et al., 2013; Tallinen et al., 2013):

$$W_e = \frac{\mu}{2} [J_A^{-2/3} \text{Tr}(\mathbf{A} \cdot \mathbf{A}^T) - 3] + K(J_A - \ln J_A - 1)$$

where μ is the initial shear modulus and K is the bulk modulus of the material; $K \rightarrow \infty$ represents incompressibility. There are also alternative neo-Hookean strain energy functions, such as the logarithmic neo-Hookean free energy function (Holland et al., 2018; Lee et al., 2021):

$$W_e = \frac{\mu}{2} [\text{Tr}(\mathbf{A}) - 3 - 2 \ln J_A] + \frac{\lambda}{2} \ln^2 J_A$$

and (Tallinen et al., 2016):

$$W_e = \frac{\mu}{2} [J_A^{-2/3} \text{Tr}(\mathbf{A} \cdot \mathbf{A}^T) - 3] + \frac{K}{2} (J_A - 1)^2$$

with $K = 10^3 \mu$ representing an almost incompressible material.

In our simulations, we choose the first strain energy function above for modeling a nearly incompressible Neo-Hookean material. Substituting this equation into the previous, we obtain

$$\sigma = \mu J_A^{-5/3} \left[\mathbf{A} \cdot \mathbf{A}^T - \frac{1}{3} \text{tr}(\mathbf{A} \cdot \mathbf{A}^T) \mathbf{I} \right] + K \left(1 - \frac{1}{J_A} \right) \mathbf{I}$$

Governing equations and boundary conditions.

In the absence of body forces, the mechanical equilibrium reads

$$\text{Div} \mathbf{S} = \mathbf{0} \text{ or } \text{div } \sigma = \mathbf{0}$$

where 'Div' and 'div' stand for the divergence operators in the initial and current configurations, respectively. The boundary conditions include: (1) the traction-free condition at the inner surface of the endodermal layer,

$$\mathbf{P} \cdot \mathbf{N} = \mathbf{0} \text{ or } \sigma \cdot \mathbf{n} = \mathbf{0}$$

(2) the fixed boundary condition at the outer surface of the mesenchymal layer (i.e. the interface between the mesenchymal and muscular layers)

$$\mathbf{x} - \mathbf{X} = \mathbf{0}$$

(3) the continuity condition at the interface between the endodermal and mesenchymal layers

$$\begin{aligned} [\mathbf{x}] &= \mathbf{0}, \\ [\mathbf{P}] \cdot \mathbf{N} &= \mathbf{0} \text{ or } [\sigma] \cdot \mathbf{n} = \mathbf{0}, \end{aligned}$$

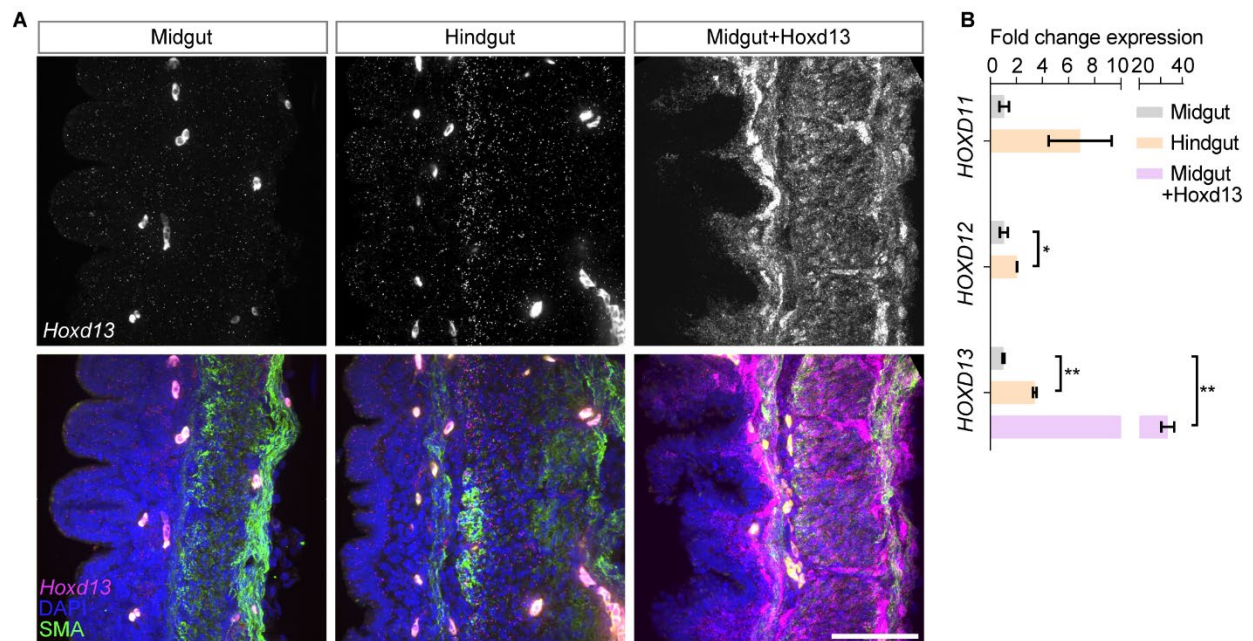
where the left Cauchy-Green strain tensor is defined as $\mathbf{B}_A = \mathbf{A} \cdot \mathbf{A}^T$, and the modified left Cauchy-Green strain tensor $\bar{\mathbf{B}}_A = J_A^{-2/3} \mathbf{B}_A$; the deviatoric deformation gradient is defined as $\bar{\mathbf{F}} = J^{-1/3} \mathbf{F}$, and the deviatoric growth tensor is $\bar{\mathbf{G}} = J_G^{-1/3} \mathbf{G}$. For our anisotropic growth model, the main orientations of the material are set parallel to the initial cylindrical coordinates. In Abaqus UMAT, this local coordinate frame is invoked by the keyword "orientation". In such scheme, the basis vectors in the current configuration co-rotate with the material. The deformation gradient passed into UMAT is $\mathbf{F}^{al} = \mathbf{R}^T \cdot \mathbf{F} \cdot \mathbf{R}$, and the Cauchy stress and consistent tangent modulus matrix in the UMAT are denoted as σ^{al} and \mathbf{C}^{al} , which are related to the global Cauchy stress σ and global tangent matrix \mathbf{C} as

$$\begin{aligned} \sigma_{ij}^{al} &= R_{mi} R_{nj} \sigma_{mn}, \\ C_{ijkl}^{al} &= R_{mi} R_{jn} R_{pk} R_{ql} C_{mnpq}. \end{aligned}$$

Here, the superscript "al" stands for "Abaqus local", and the orthogonal rotation matrix \mathbf{R} is calculated by right polar decomposition of the deformation gradient $\mathbf{F} = \mathbf{R} \cdot \mathbf{U}$ with \mathbf{U} being the right stretch tensor. We import a small stress-free geometric imperfection ($|\delta u| < 0.0001R$), obtained from buckling analysis into the initial state to initiate bifurcation. In explicit models, Cauchy stress is calculated from the deformation gradient and transformed to the co-rotational coordinate system.

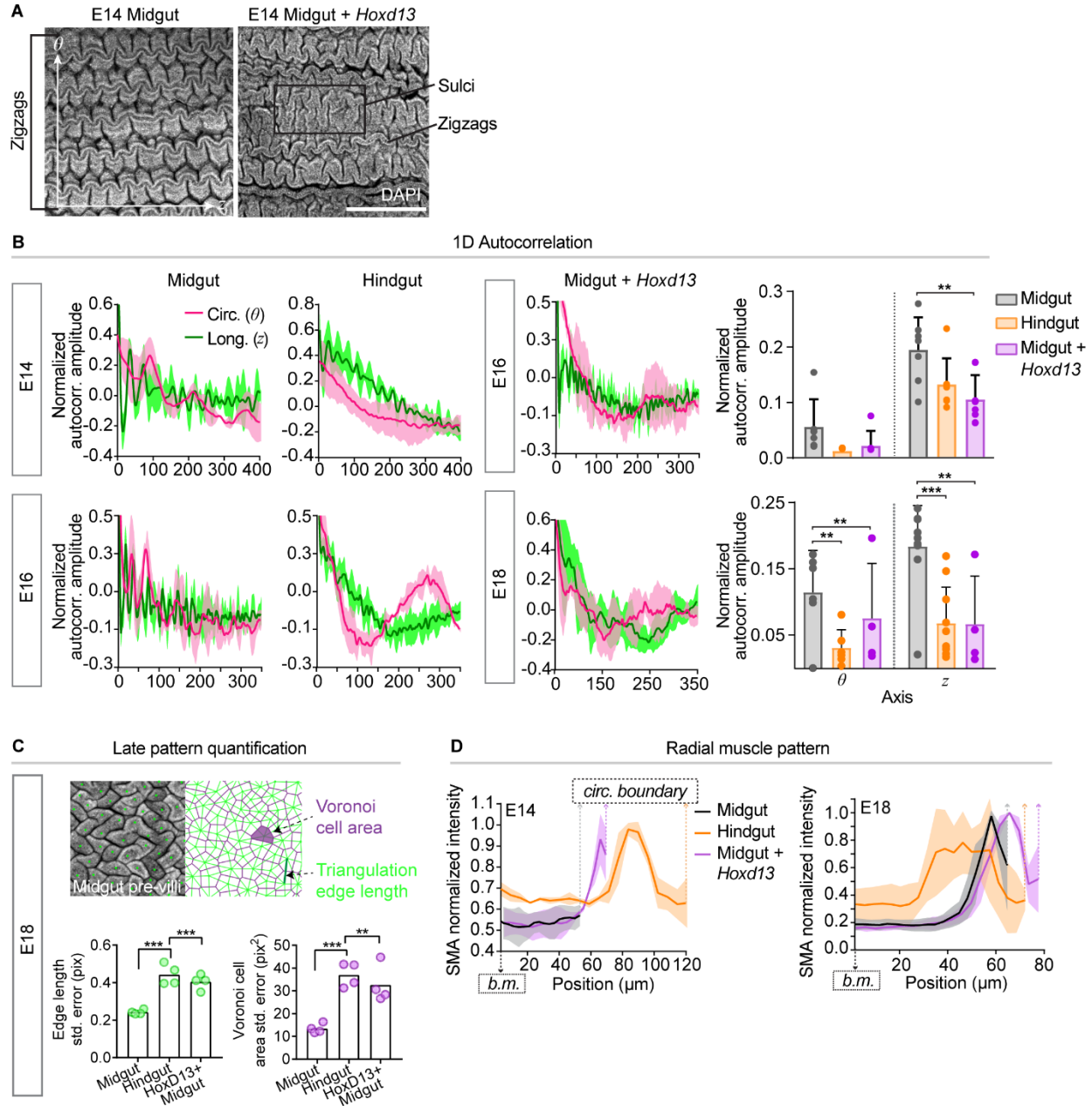
APPENDIX 3: Supplementary materials for *Genetic and biochemical control of physical forces in hindgut morphogenesis*

Extended Figures 9-18



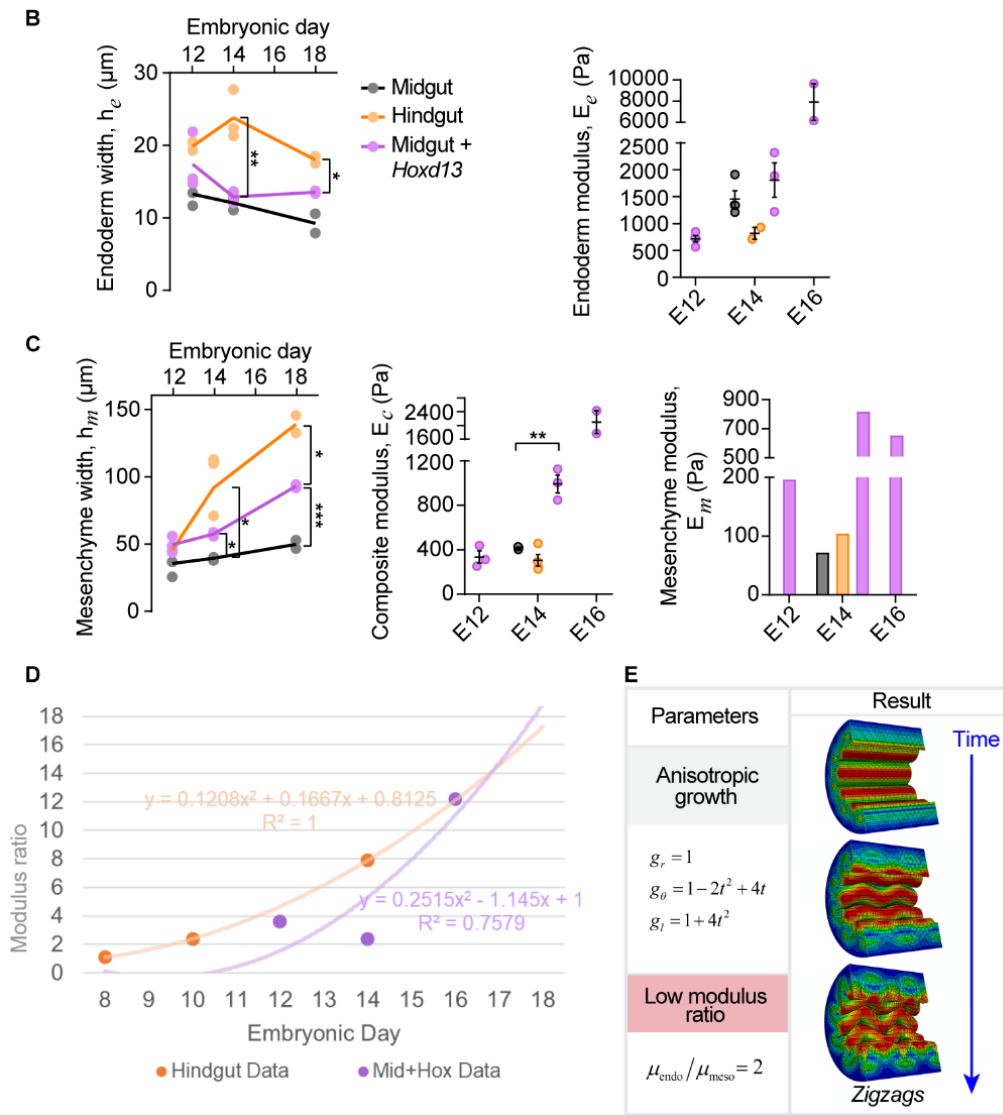
Extended Figure 9. *Hoxd13* endogenous and ectopic expression levels

(A) HCR-FISH for *Hoxd13* co-stained with SMA and DAPI at E14 in midgut, hindgut, and *Hoxd13*-misexpressing midgut sagittal sections. Scale bar, 50 μ m. (B) Mesoderm-only qPCR at E14 targeting posterior *Hox* genes expressed in the hindgut, *Hoxd11*, *Hoxd12*, and *Hoxd13*. Expression levels are calculated relative to the midgut (**, $p < 0.01$; *, $p < 0.05$; t-test, $n = 3$).



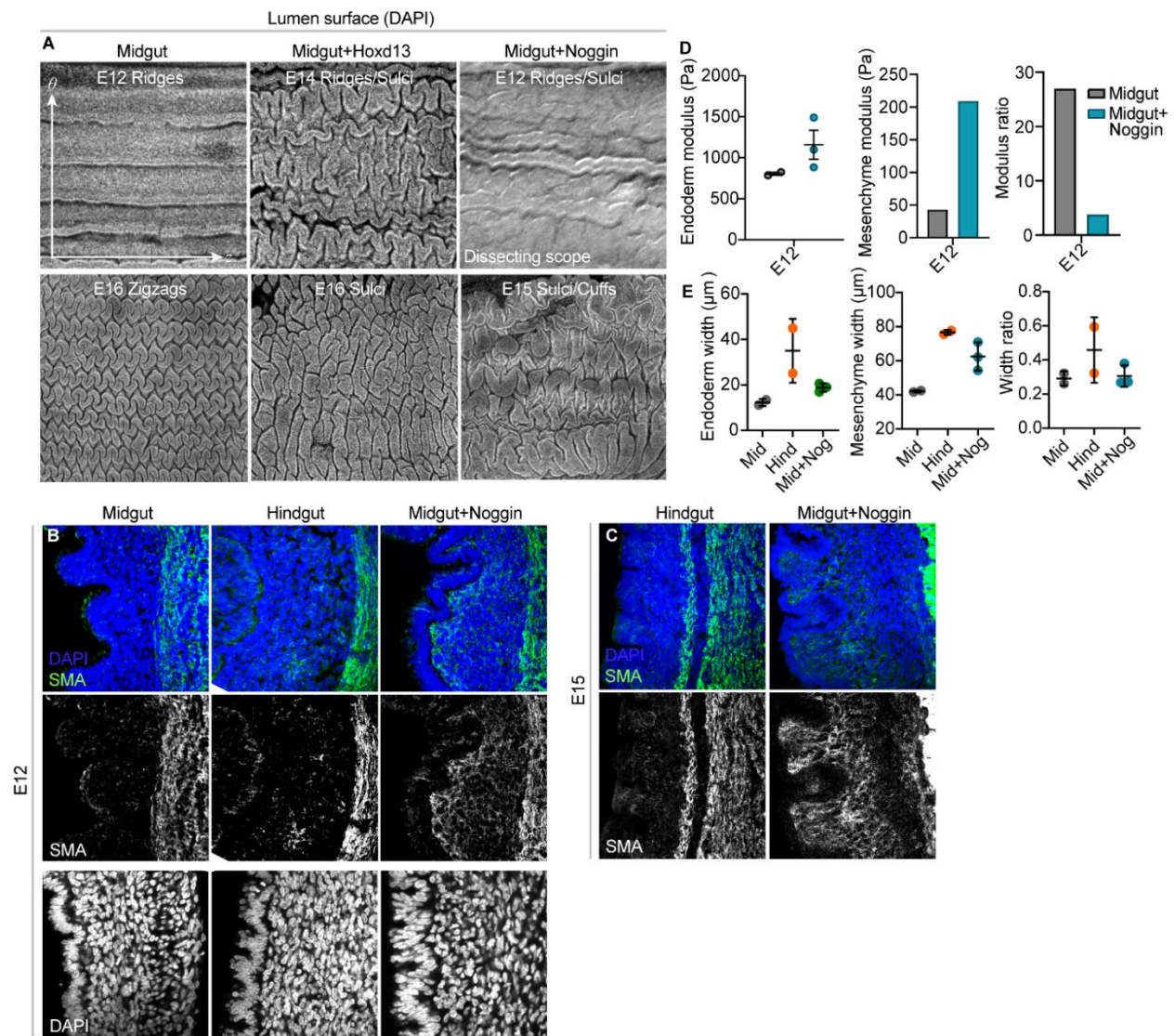
Extended Figure 10. Additional quantifications of mid/hindgut and midgut+*Hoxd13* lumens

(A) E14 lumen patterns in the control and RCAS-*Hoxd13* midguts, illustrating zigzags and sulci appearing simultaneously in the latter. Scale bar, 500 μm . (B) Normalized mean 1D autocorrelation profiles for $n=6-7$ cropped pattern segments per axis and condition (Methods) at E14, E16, and E18. Shaded areas, SD. Right column plots contain characteristic amplitude values extracted from each profile replicate (***, $p<0.001$; **, $p<0.01$; ns, not significant, t-test). (C) Standard errors of edge lengths (green) and cell areas (purple) obtained from Delaunay triangulation and Voronoi tessellation at E18 (***, $p<0.001$; **, $p<0.01$, t-test, $n=4$ images). The schematic illustrates an example of a tessellation result using E18 midgut pre-villi. (D) Normalized mean SMA intensity profiles from the basement membrane, *b.m.*, to the circumferential muscle boundaries, colored dashed lines, at E14 and E18. Shaded areas, SD; $n=4$.



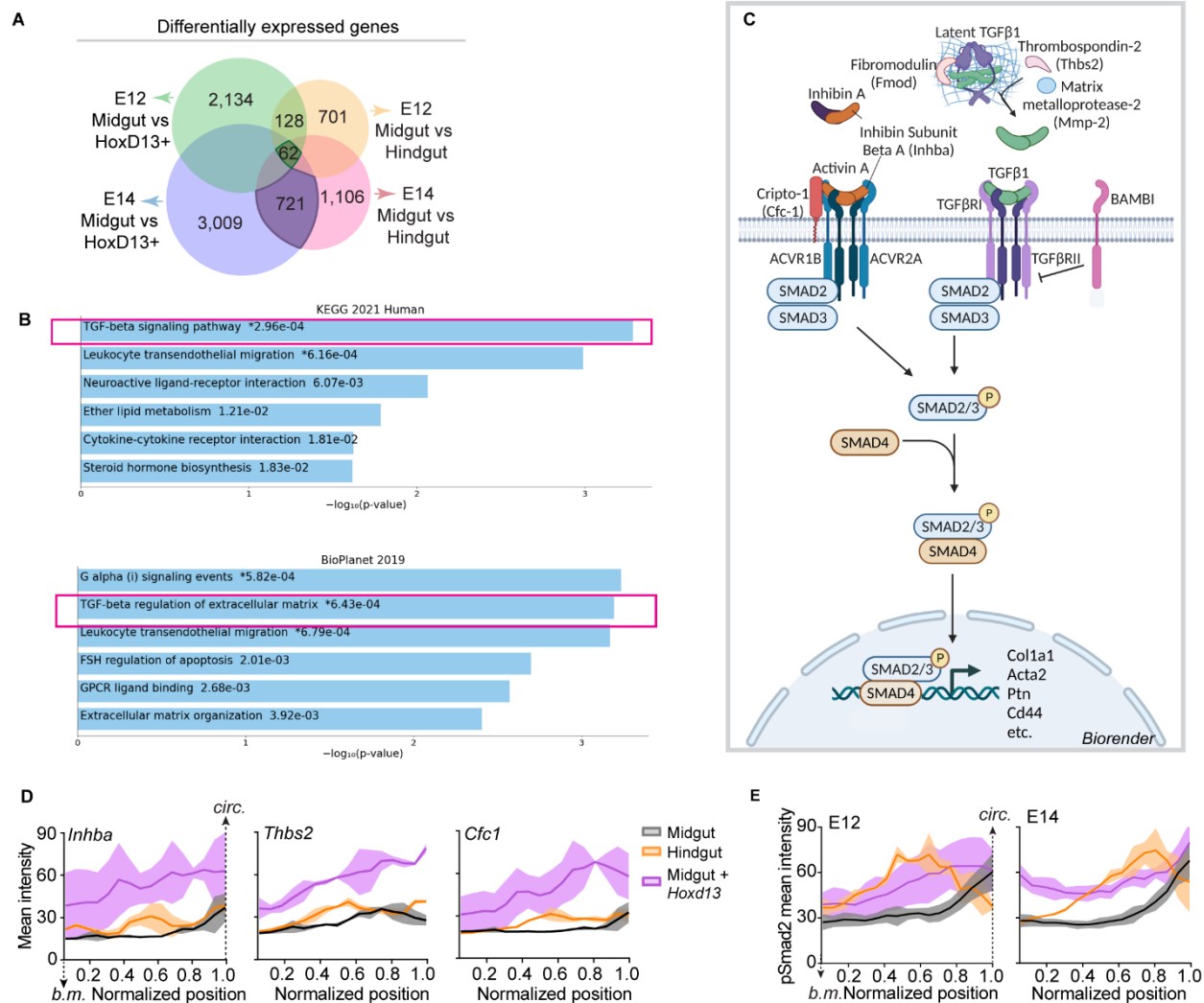
Extended Figure 11. Modulus and width parameters in the intestine and midgut+*Hoxd13*

B) Endoderm widths over time for all conditions, and endoderm modulus values over time for the RCAS-*Hoxd13* midgut and midgut and hindgut at E14. (C) Corresponding mesenchyme widths and raw composite measurements. Mesenchyme modulus values determined from average widths and modulus measurements, as shown in (A) (***, $p < 0.001$; **, $p < 0.01$; *, $p < 0.05$; t-test, $n=3$). (D) Modulus ratio predictions at late stages using polynomial curves fitted to three data points each for the hindgut and midgut + *Hoxd13*. (E) Simulation parameters and result of zigzags, shown in three simulation time steps, for anisotropic growth (specified via the growth functions listed on the left) in the context of a low endoderm-to-mesenchyme modulus ratio (2, bottom left).



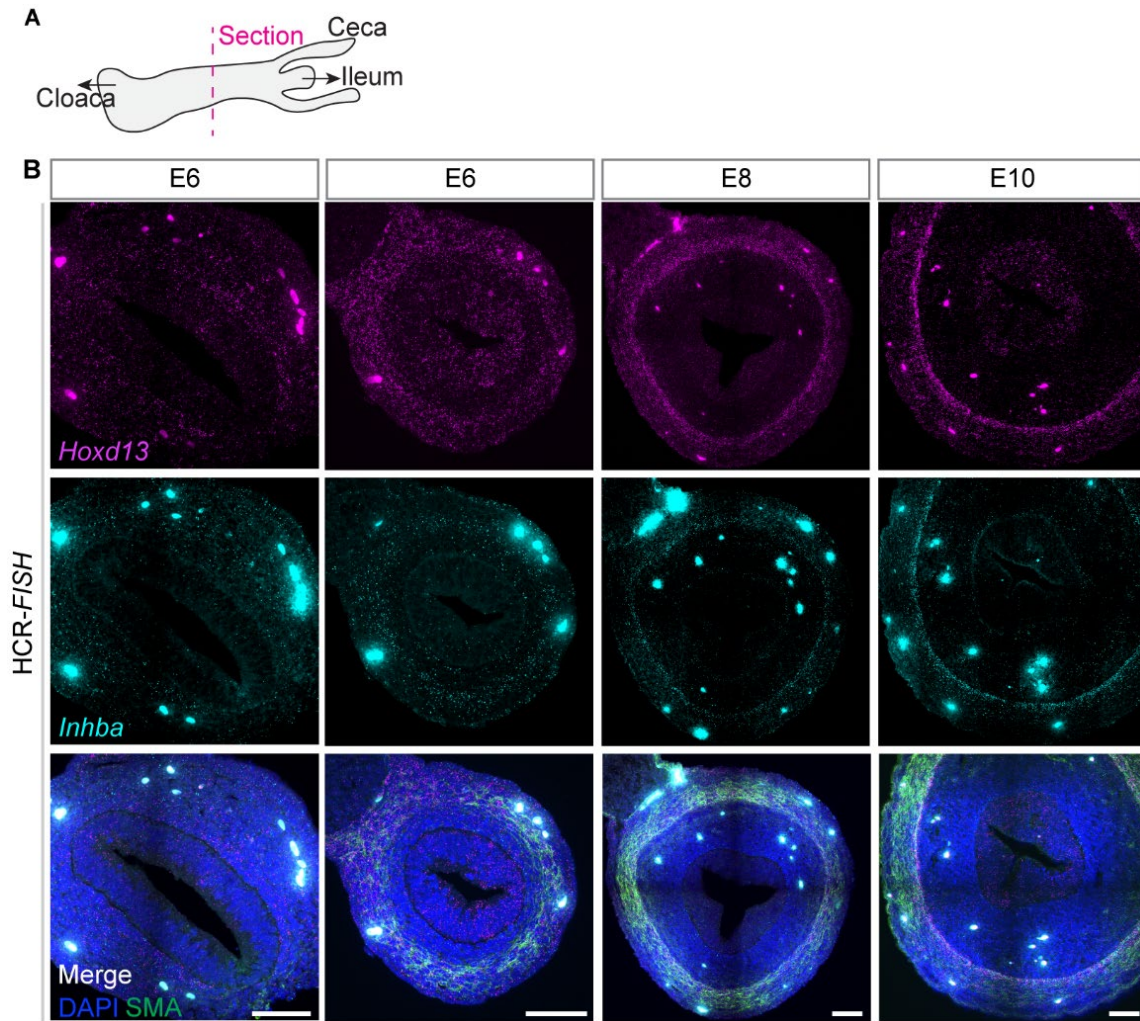
Extended Figure 12. *Noggin* misexpression in the midgut phenocopies RCAS-*Hoxd13*

(A) DAPI-stained confocal z-stack projections (aside from E12 *Noggin*, which is a dissecting scope image) of midgut, RCAS-*Hoxd13* midgut, and RCAS-*Noggin* midgut lumen surfaces, where the horizontal direction is longitudinal and vertical is circumferential. (B, C) Transverse sections stained with SMA at (B) E12 and (C) E15 showing expansion of muscle into subepithelial mesenchyme. Bottom row at E12 shows sagittal sections stained with DAPI alone to highlight the endodermal creasing pattern seen in RCAS-*Noggin*. (D,E) Mechanical properties of RCAS-*Noggin* midguts. (D) Endoderm modulus values, mesenchyme modulus calculated from composite measurements (Extended Figure 6C), and modulus ratio of the midgut and *Noggin*-misexpressing midgut at E12. (E) Endoderm and mesenchyme widths and width ratios of the midgut, hindgut, and RCAS-*Noggin* midgut.



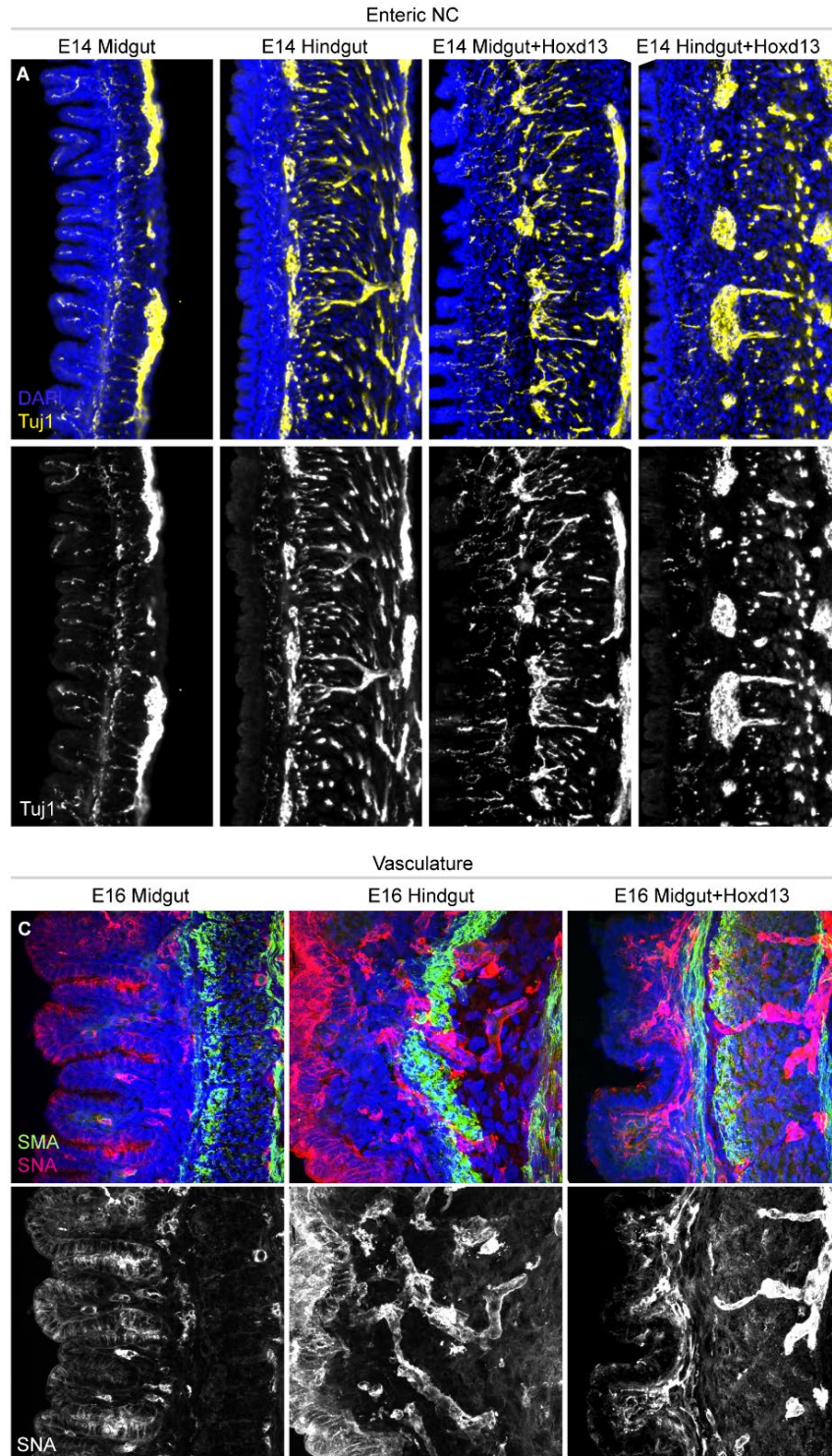
Extended Figure 13. Enrichment of TGFβ genes in the hindgut and with *Hoxd13* expression

(A) Venn diagram highlighting gene set of interest—genes commonly differentially expressed in the hindgut and RCAS-*Hoxd13* midgut at both E12 and E14. (B) Pathway enrichment analysis using two databases via Enrichr. Red boxes illustrate the prominent appearance of the TGFβ pathway in the core set of 62 genes. (C) TGFβ pathway schematic made using Biorender.com specifically highlighting the roles of factors differentially expressed in the dataset. (D, E) Average radial mean intensities of (D) FISH and (E) pSmad2 signals for three TGFβ genes in the subepithelial mesenchyme. Position on the x-axis is normalized to circumferential muscle position. basement membrane, *b.m.*, circumferential muscle inner boundary, *circ.* Shaded area=SD, n=3.



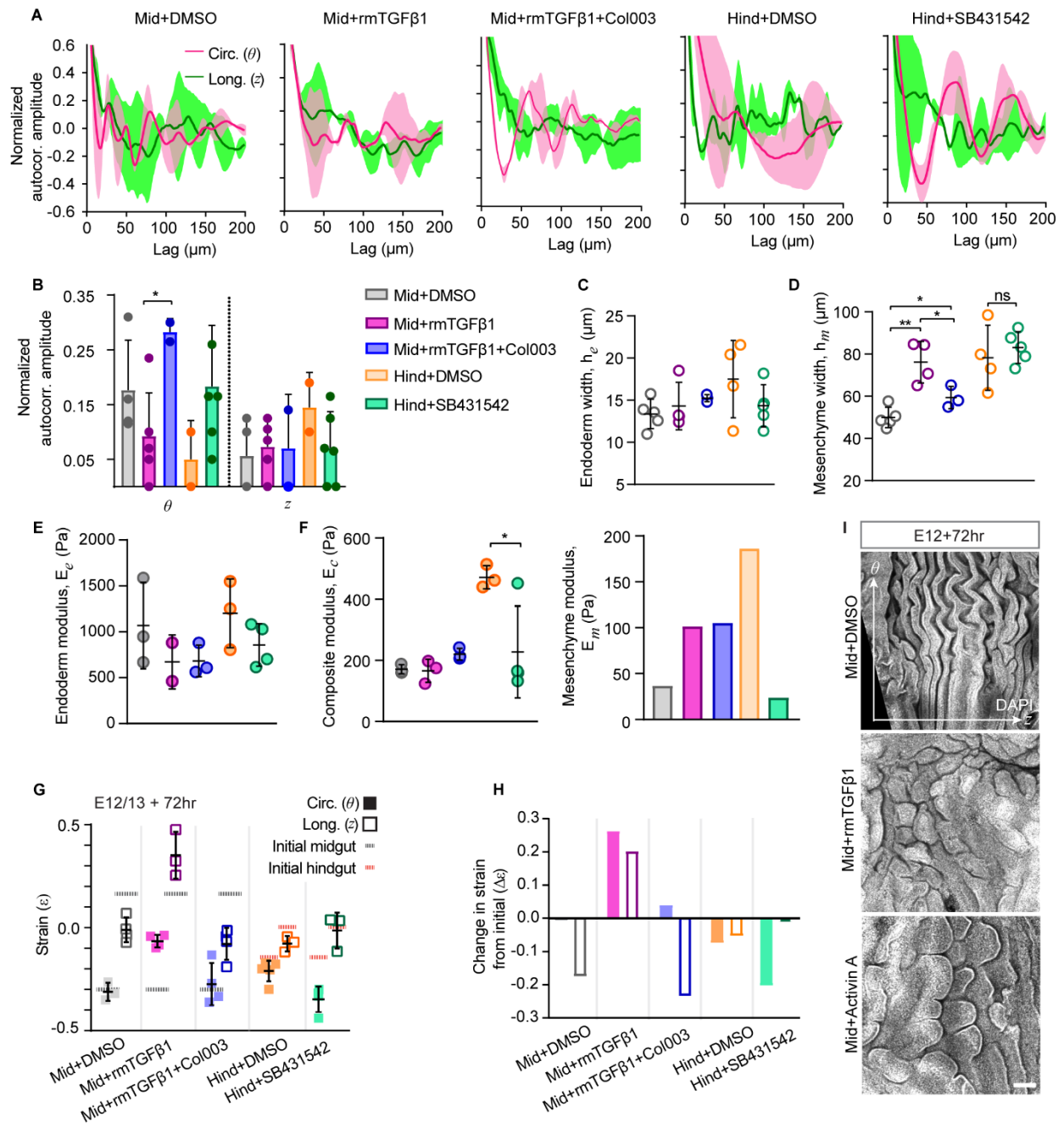
Extended Figure 14. Hindgut expression of *Hoxd13* and putative downstream gene *Inhba*.

(A) Schematic illustrating locations of hindgut sections used for HCR-FISH. (B) *Hoxd13* and *Inhba* FISH patterns alone and overlaid with DAPI and SMA. Images are of whole transverse sections with the endoderm layer in the center. Scale bar, 20 μ m.



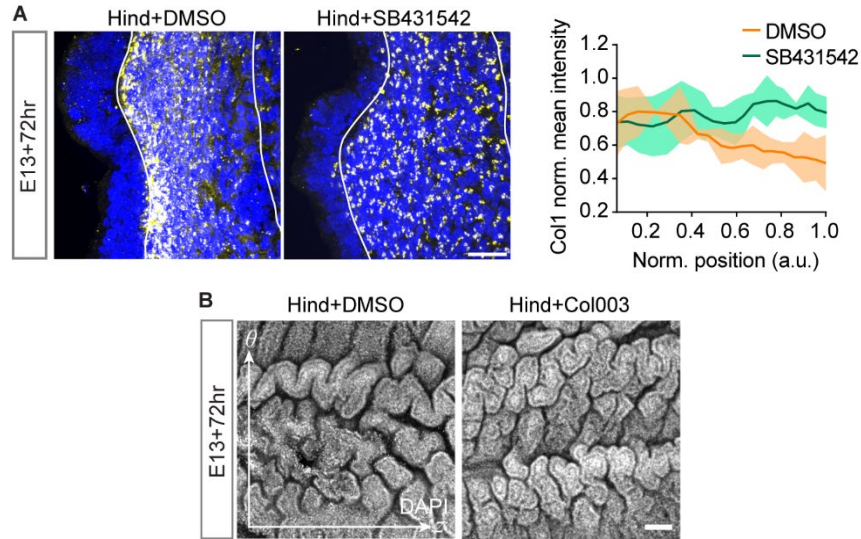
Extended Figure 15. NCC aggregation and endothelial expansion with *Hoxd13* expression

(A) Immunostain for enteric neural crest cell (NCC) marker Tuj1 in sagittal sections at E14 in the midgut, hindgut, RCAS-*Hoxd13* midgut and RCAS-*Hoxd13* hindgut. Lumen is on the left. (C) Sambucus nigra lectin (SNA) stain for endothelial cells, co-stained with SMA, at E16.



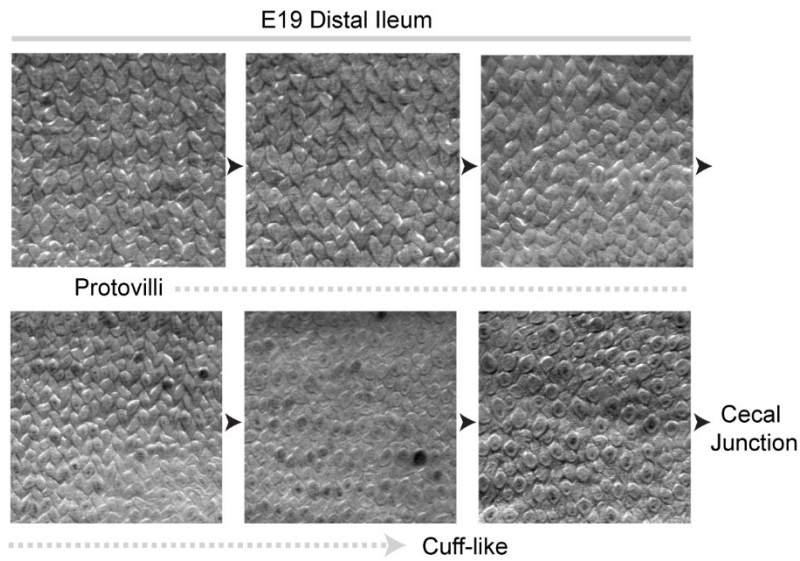
Extended Figure 16. TGFβ modulation effect on gut morphology, growth and mechanics

(A) 1D normalized autocorrelation profiles for $n=3-6$ cropped representative pattern segments for all explant perturbation results; Shaded areas, SD. (B) Normalized amplitudes corresponding to sinusoidal autocorrelation profiles in (A) (*, $p<0.05$; t-test). (C) Endoderm widths and (E) moduli, and (D) mesenchyme widths and (F) moduli, calculated from composite moduli as described in Figure S2A. (**, $p<0.01$; *, $p<0.05$; t-test, $n=3-5$). (G, H) Differential growth measurements for TGFβ explants. (G) Strain values in each axis (θ , circumferential; z , longitudinal) at the end of each experiment, with initial strain values for the midgut and hindgut indicated at dashed lines. (H) Change in strain for each condition, in each axis, compared to initial values for the midgut and hindgut from Figure 2A. (I) Lumen surface images of midgut explants treated with DMSO (top), rmTGFβ1 (middle), and Activin A (bottom). Scale bar, 100 μm .



Extended Figure 17. Collagen dysregulation in the hindgut

(A) Collagen distribution in the hindgut subepithelial mesenchyme with suppression of TGF β signaling, and radial profiles of collagen intensity. Shaded area, SD; n=3. Scale bar, 20 μ m. (B) Hindgut lumen morphology with and without blocked collagen secretion (Col003) in 72hr explant culture. Scale bar, 100 μ m.



Extended Figure 18. Lumen morphology becomes hindgut-like in the distal small intestine

Approximately 1.5mm x 1.5mm lumen surface images taken on a dissecting scope at E19. Arrows indicate anterior-posterior direction, where each successive image is about 3mm closer to the midgut-hindgut junction than the previous image. Dashed gray arrow and labels indicate qualitative characterization of the surface morphology based on spatial arrangement, size, and shape of outgrowths, where the bottom row begins to appear more cuff-like.

3D model of biaxial buckling instabilities in the midgut and hindgut

All equations, codes, and descriptions for 3D models were developed and written by Sifan Yin. Descriptions edited by Hasreet Gill.

Lumen wrinkling models in 3D used the same theory as 2D models, outlined in “2D model of primary and multiscale buckling in the fore- and hindguts”. A cylindrical tube model was employed instead, with growth ratios defined from experimental measurements as

$$g_{ri} = h_i/R, g_{\theta i} = w_i/(2\pi R), g_{zi} = l_i/L (i = \text{endo, mese}),$$

with h, w, l being the thickness, width and length of the endodermal or mesenchymal layer, respectively; R being the radius of the clamped muscular layer, and L being length of the three-layer tube.

For simulations, the mesenchymal layer does not grow for simplicity, and the relative growth factors of endodermal layer are g_r, g_θ , and g_z . Eight-node 3D hybrid elements (C3D8RH) were used for both endoderm and mesenchyme.

Our 3D treatment partially required the use of implicit models, where the current Cauchy stress σ and consistent tangent matrix \mathbf{C} are calculated in UMAT via

$$\begin{aligned} \sigma_{ij} &= \mu J_A^{-1} \left[\bar{B}_{Aij} - \frac{1}{3} \bar{B}_{Amm} \delta_{ij} \right] + K \left(1 - \frac{1}{J_A} \right) \delta_{ij}. \\ C_{ijkl} &= \mu J_A^{-1} \left[\frac{1}{2} (\bar{B}_{Ajl} \delta_{ik} + \bar{B}_{Aik} \delta_{jl} + \bar{B}_{Ail} \delta_{jk} + \bar{B}_{Ajk} \delta_{il}) \right. \\ &\quad \left. - \frac{2}{3} (\bar{B}_{Aij} \delta_{kl} + \bar{B}_{Akl} \delta_{ij}) + \frac{2}{9} \delta_{ij} \delta_{kl} \bar{B}_{Amm} \right] + K \delta_{ij} \delta_{kl}, \end{aligned}$$

where the left Cauchy-Green strain tensor is defined as $\mathbf{B}_A = \mathbf{A} \cdot \mathbf{A}^T$, and the modified left Cauchy Green strain tensor $\bar{\mathbf{B}}_A = J_A^{-2/3} \mathbf{B}_A$; the deviatoric deformation gradient is defined as $\bar{\mathbf{F}} = J^{-1/3} \mathbf{F}$, and the deviatoric growth tensor is $\bar{\mathbf{G}} = J_G^{-1/3} \mathbf{G}$, as in the 2D case.

REFERENCES

- Abzhanov, A., Protas, M., Grant, B. R., Grant, P. R., & Tabin, C. J. (2004). Bmp4 and morphological variation of beaks in Darwin's finches. *Science*, *305*(5689), 1462–1465. <https://doi.org/10.1126/science.1098095>
- Aldeiri, B., Roostalu, U., Albertini, A., Wong, J., Morabito, A., & Cossu, G. (2017). Transgelin-expressing myofibroblasts orchestrate ventral midline closure through TGF β signalling. *Development (Cambridge)*, *144*(18), 3336–3348. <https://doi.org/10.1242/dev.152843>
- Amar, M. Ben, & Jia, F. (2013). Anisotropic growth shapes intestinal tissues during embryogenesis. *Proceedings of the National Academy of Sciences of the United States of America*, *110*(26), 10525–10530. <https://doi.org/10.1073/pnas.1217391110>
- Annunziata, R., Andrikou, C., Perillo, M., Cuomo, C., & Arnone, M. I. (2019). Development and evolution of gut structures: from molecules to function. *Cell and Tissue Research*, *377*(3), 445–458. <https://doi.org/10.1007/s00441-019-03093-9>
- Annunziata, R., & Arnone, M. I. (2014). A dynamic regulatory network explains ParaHox gene control of gut patterning in the sea urchin. *Development (Cambridge)*, *141*(12), 2462–2472. <https://doi.org/10.1242/dev.105775>
- Antebi, Y. E., Linton, J. M., Klumpe, H., Bintu, B., Gong, M., Su, C., McCardell, R., & Elowitz, M. B. (2017). Combinatorial Signal Perception in the BMP Pathway. *Cell*, *170*(6), 1184-1196.e24. <https://doi.org/10.1016/j.cell.2017.08.015>
- Aspenstrom, P. (2014). BAR domain proteins regulate Rho GTPase signaling. *Small GTPases*, *5*(2). <https://doi.org/10.4161/SGTP.28580>

- Aubin, H., Nichol, J. W., Hutson, C. B., Bae, H., Sieminski, A. L., Cropek, D. M., Akhyari, P., & Khademhosseini, A. (2010). Directed 3D cell alignment and elongation in microengineered hydrogels. *Biomaterials*, *31*(27), 6941–6951.
<https://doi.org/10.1016/j.biomaterials.2010.05.056>
- Aubin, J., Déry, U., Lemieux, M., Chailier, P., & Jeannotte, L. (2002). Stomach regional specification requires Hoxa5-driven mesenchymal-epithelial signaling. *Development*, *129*(17), 4075–4087.
- Aulie, R. P. (1961). Caspar friedrich wolff and his “theoria generationis”, 1759. *Journal of the History of Medicine and Allied Sciences*, *16*(2), 124–144.
<https://doi.org/10.1093/jhmas/XVI.2.124>
- Awwad, K., Hu, J., Shi, L., Mangels, N., Abdel Malik, R., Zippel, N., Fisslthaler, B., Eble, J. A., Pfeilschifter, J., Popp, R., & Fleming, I. (2015). Role of secreted modular calcium-binding protein 1 (SMOC1) in transforming growth factor β signalling and angiogenesis. *Cardiovascular Research*, *106*(2), 284–294. <https://doi.org/10.1093/CVR/CVV098>
- Ayers, N. B., Sun, C., & Chen, S. Y. (2018). Transforming growth factor- β signaling in systemic sclerosis. In *Journal of Biomedical Research* (Vol. 32, Issue 1, pp. 3–12). Nanjing Medical University. <https://doi.org/10.7555/JBR.31.20170034>
- Balbi, V., & Ciarletta, P. (2013). Morpho-elasticity of intestinal villi. *Journal of the Royal Society Interface*, *10*(82). <https://doi.org/10.1098/rsif.2013.0109>
- Balbi, V., Kuhl, E., & Ciarletta, P. (2015). Morphoelastic control of gastro-intestinal organogenesis: Theoretical predictions and numerical insights. *Journal of the Mechanics and Physics of Solids*, *78*, 493–510. <https://doi.org/10.1016/J.JMPS.2015.02.016>

- Barbara, P. D. S., & Roberts, D. J. (2002). *Tail gut endoderm and gut / genitourinary / tail development : a new tissue- specific role for Hoxa13*. 561, 551–561.
- Bardot, E. S., & Hadjantonakis, A. K. (2020). Mouse gastrulation: coordination of tissue patterning, specification and diversification of cell fate. *Mechanisms of Development*, 163, 103617. <https://doi.org/10.1016/J.MOD.2020.103617>
- Barnard, J. A., Beauchamp, R. D., Coffey, R. J., & Moses, H. L. (1989). Regulation of intestinal epithelial cell growth by transforming growth factor type β . *Proceedings of the National Academy of Sciences of the United States of America*, 86(5), 1578–1582. <https://doi.org/10.1073/pnas.86.5.1578>
- Barriga, E. H., Franze, K., Charras, G., & Mayor, R. (2018). Tissue stiffening coordinates morphogenesis by triggering collective cell migration in vivo. *Nature*, 554(7693), 523–527. <https://doi.org/10.1038/nature25742>
- Bastiaansen-Jenniskens, Y. M., Koevoet, W., De Bart, A. C. W., Zuurmond, A. M., Bank, R. A., Verhaar, J. A. N., DeGroot, J., & Van Osch, G. J. V. M. (2008). TGF β affects collagen cross-linking independent of chondrocyte phenotype but strongly depending on physical environment. *Tissue Engineering - Part A*, 14(6), 1059–1066. <https://doi.org/10.1089/ten.tea.2007.0345>
- Batts, L. E., Brent Polk, D., Dubois, R. N., Kulesa, H., & Hogan, B. (2006). Bmp signaling is required for intestinal growth and morphogenesis. *Developmental Dynamics*, 235(6), 1563–1570. <https://doi.org/10.1002/dvdy.20741>
- Bay, N. S.-Y., & Bay, B.-H. (2010). Greek anatomist herophilus: the father of anatomy. *Anatomy & Cell Biology*, 43(4), 280. <https://doi.org/10.5115/acb.2010.43.4.280>

- Beck, F. (2002). Homeobox genes in gut development. *Gut*, *51*(3), 450–454.
<https://doi.org/10.1136/gut.51.3.450>
- Bell, L., & Williams, L. (1982). A scanning and transmission electron microscopical study of the morphogenesis of human colonic villi. *Anatomy and Embryology*, *165*(3), 437–455.
<https://doi.org/10.1007/BF00305579>
- Berking, S. (2007). Generation of bilateral symmetry in Anthozoa: A model. *Journal of Theoretical Biology*, *246*(3), 477–490. <https://doi.org/10.1016/J.JTBI.2007.01.008>
- Birchough, G. M. H., Nystrom, E. E. L., Johansson, M. E. V., & Hansson, G. C. (2016). A sentinel goblet cell guards the colonic crypt by triggering Nlrp6-dependent Muc2 secretion. *Science*, *352*(6293), 1535–1542.
https://doi.org/10.1126/SCIENCE.AAF7419/SUPPL_FILE/BIRCHENOUGH.SM.PDF
- Blum, M., Feistel, K., Thumberger, T., & Schweickert, A. (2014). The evolution and conservation of left-right patterning mechanisms. *Development*, *141*(8), 1603–1613.
<https://doi.org/10.1242/DEV.100560>
- Boezio, G. L. M., Bensimon-Brito, A., Piesker, J., Guenther, S., Helker, C. S. M., & Stainier, D. Y. R. (2020). Endothelial tgfb signaling instructs smooth muscle cell development in the cardiac outflow tract. *ELife*, *9*(September), 1–32. <https://doi.org/10.7554/ELIFE.57603>
- Bonis, V., Rossell, C., & Gehart, H. (2021). The Intestinal Epithelium – Fluid Fate and Rigid Structure From Crypt Bottom to Villus Tip. *Frontiers in Cell and Developmental Biology*, *9*, 1222. <https://doi.org/10.3389/FCELL.2021.661931/BIBTEX>
- Bornstein, P. (2001). Thrombospondins as matricellular modulators of cell function. *The Journal of Clinical Investigation*, *107*(8), 929–934. <https://doi.org/10.1172/JCI12749>

- Boulet, A. M., & Capecchi, M. R. (1996). Targeted disruption of *hoxc-4* causes esophageal defects and vertebral transformations. *Developmental Biology*, *177*(1), 232–249.
<https://doi.org/10.1006/dbio.1996.0159>
- Boyle, M. J., & Seaver, E. C. (2010). Expression of FoxA and GATA transcription factors correlates with regionalized gut development in two lophotrochozoan marine worms: *Chaetopterus* (Annelida) and *Themiste lageniformis* (Sipuncula). *EvoDevo*, *1*(1).
<https://doi.org/10.1186/2041-9139-1-2>
- Brereton, C. J., Yao, L., Davies, E. R., Zhou, Y., Vukmirovic, M., Bell, J. A., Wang, S., Ridley, R. A., Dean, L. S. N., Andriotis, O. G., Conforti, F., Brewitz, L., Mohammed, S., Wallis, T., Tavassoli, A., Ewing, R. M., Alzetani, A., Marshall, B. G., Fletcher, S. V., ... Jones, M. G. (2022). Pseudohypoxic HIF pathway activation dysregulates collagen structure-function in human lung fibrosis. *ELife*, *11*. <https://doi.org/10.7554/ELIFE.69348>
- Budday, S., Kuhl, E., & Hutchinson, J. W. (2015). Period-doubling and period-tripling in growing bilayered systems. *Philosophical Magazine (Abingdon, England)*, *95*(28–30), 3208.
<https://doi.org/10.1080/14786435.2015.1014443>
- Cai, S., Bertoldi, K., Wang, H., & Suo, Z. (2010). Osmotic collapse of a void in an elastomer: Breathing, buckling and creasing. *Soft Matter*, *6*(22), 5770–5777.
<https://doi.org/10.1039/c0sm00451k>
- Cammareri, P., Vincent, D. F., Hodder, M. C., Ridgway, R. A., Murgia, C., Nobis, M., Campbell, A. D., Varga, J., Huels, D. J., Subramani, C., Prescott, K. L., Nixon, C., Hedley, A., Barry, S. T., Greten, F. R., Inman, G. J., & Sansom, O. J. (2017). TGF β pathway limits dedifferentiation

- following WNT and MAPK pathway activation to suppress intestinal tumourigenesis. *Cell Death and Differentiation*, 24(10), 1681–1693. <https://doi.org/10.1038/cdd.2017.92>
- Cardamone, L., Valentín, A., Eberth, J. F., & Humphrey, J. D. (2009). Origin of Axial Prestretch and Residual Stress in Arteries. *Biomechanics and Modeling in Mechanobiology*, 8(6), 431. <https://doi.org/10.1007/S10237-008-0146-X>
- Cervantes, S., Yamaguchi, T. P., & Hebrok, M. (2009). Wnt5a is essential for intestinal elongation in mice. *Developmental Biology*, 326(2), 285. <https://doi.org/10.1016/J.YDBIO.2008.11.020>
- Chang, W. W. L., & Leblond, C. P. (1971). Renewal of the epithelium in the descending colon of the mouse. II. Renewal of argentaffin cells. *American Journal of Anatomy*, 131(1), 101–109. <https://doi.org/10.1002/aja.1001310106>
- Chen, E. Y., Tan, C. M., Kou, Y., Duan, Q., Wang, Z., Meirelles, G. V., Clark, N. R., & Ma'ayan, A. (2013). Enrichr: Interactive and collaborative HTML5 gene list enrichment analysis tool. *BMC Bioinformatics*, 14. <https://doi.org/10.1186/1471-2105-14-128>
- Chen, X., Nadiarynkh, O., Plotnikov, S., & Campagnola, P. J. (2012). Second harmonic generation microscopy for quantitative analysis of collagen fibrillar structure. *Nature Protocols*, 7, 654. <https://doi.org/10.1038/nprot.2012.009>
- Chevalier, N. R., De Witte, T. M., Cornelissen, A. J. M., Dufour, S., Proux-Gillardeaux, V., & Asnacios, A. (2018). Mechanical Tension Drives Elongational Growth of the Embryonic Gut. *Scientific Reports*, 8(1), 1–10. <https://doi.org/10.1038/s41598-018-24368-1>
- Chevalier, N. R., Gazquez, E., Bidault, L., Guilbert, T., Vias, C., Vian, E., Watanabe, Y., Muller, L., Germain, S., Bondurand, N., Dufour, S., & Fleury, V. (2016). How Tissue Mechanical

- Properties Affect Enteric Neural Crest Cell Migration. *Scientific Reports*, 6(January), 1–17.
<https://doi.org/10.1038/srep20927>
- Chow, M. J., Turcotte, R., Lin, C. P., & Zhang, Y. (2014). Arterial extracellular matrix: A mechanobiological study of the contributions and interactions of elastin and collagen. *Biophysical Journal*, 106(12), 2684–2692. <https://doi.org/10.1016/j.bpj.2014.05.014>
- Chuong, C. J., & Fung, Y. C. (1986). Residual Stress in Arteries. *Frontiers in Biomechanics*, 117–129. https://doi.org/10.1007/978-1-4612-4866-8_9
- Ciarletta, P., Balbi, V., & Kuhl, E. (2014). Pattern selection in growing tubular tissues. *Physical Review Letters*, 113(24), 1–5. <https://doi.org/10.1103/PhysRevLett.113.248101>
- Conway, S. J., & Kaartinen, V. (2011). TGF β superfamily signaling in the neural crest lineage. *Cell Adhesion & Migration*, 5(3), 232. <https://doi.org/10.4161/CAM.5.3.15498>
- Coulombre, A. J., & Coulombre, J. L. (1958). Intestinal development. I. Morphogenesis of the villi and musculature. *J Embryol Exp Morphol*, 6(3), 403–411.
- Cowman, M. K., Schmidt, T. A., Raghavan, P., & Stecco, A. (2015). Viscoelastic Properties of Hyaluronan in Physiological Conditions. *F1000Research*, 4.
<https://doi.org/10.12688/F1000RESEARCH.6885.1>
- Crampin, E. J., Gaffney, E. A., & Maini, P. K. (1999). Reaction and diffusion on growing domains: Scenarios for robust pattern formation. *Bulletin of Mathematical Biology*, 61(6), 1093–1120. <https://doi.org/10.1006/BULM.1999.0131/METRICS>
- de Belly, H., Paluch, E. K., & Chalut, K. J. (2022). Interplay between mechanics and signalling in regulating cell fate. *Nature Reviews Molecular Cell Biology*, 23(7), 465–480.
<https://doi.org/10.1038/s41580-022-00472-z>

- De Las Heras, J. M., García-Cortés, C., Foronda, D., Pastor-Pareja, J. C., Shashidhara, L. S., & Sánchez-Herrero, E. (2018). The *Drosophila* Hox gene Ultrabithorax controls appendage shape by regulating extracellular matrix dynamics. *Development (Cambridge)*, *145*(13), 1–10. <https://doi.org/10.1242/dev.161844>
- De Santa Barbara, P., Van Den Brink, G. R., & Roberts, D. J. (2003). Development and differentiation of the intestinal epithelium. *Cellular and Molecular Life Sciences*, *60*(7), 1322–1332. <https://doi.org/10.1007/S00018-003-2289-3/METRICS>
- De Santa Barbara, P., Williams, J., Goldstein, A. M., Doyle, A. M., Nielsen, C., Winfield, S., Faure, S., & Roberts, D. J. (2005). Bone morphogenetic protein signaling pathway plays multiple roles during gastrointestinal tract development. *Developmental Dynamics*, *234*(2), 312–322. <https://doi.org/10.1002/dvdy.20554>
- Delgado Lagos, F., Elgheznawy, A., Kyselova, A., Meyer zu Heringdorf, D., Ratiu, C., Randriamboavonjy, V., Mann, A. W., Fisslthaler, B., Siragusa, M., & Fleming, I. (2021). Secreted modular calcium-binding protein 1 binds and activates thrombin to account for platelet hyperreactivity in diabetes. *Blood*, *137*(12), 1641–1651. <https://doi.org/10.1182/BLOOD.2020009405>
- Denans, N., Imura, T., & Pourquié, O. (2015). Hox genes control vertebrate body elongation by collinear Wnt repression. *eLife*, *2015*(4), 1–33. <https://doi.org/10.7554/eLife.04379>
- Derynck, R., & Budi, E. H. (2019). Specificity, versatility, and control of TGF- β family signaling. *Science Signaling*, *12*(570). <https://doi.org/10.1126/scisignal.aav5183>

- Dessaud, E., McMahon, A. P., & Briscoe, J. (2008). Pattern formation in the vertebrate neural tube: A sonic hedgehog morphogen-regulated transcriptional network. *Development*, *135*(15), 2489–2503. <https://doi.org/10.1242/dev.009324>
- Domyan, E. T., Ferretti, E., Throckmorton, K., Mishina, Y., Nicolis, S. K., & Sun, X. (2011). Signaling through BMP receptors promotes respiratory identity in the foregut via repression of Sox2. *Development*, *138*(5), 971–981. <https://doi.org/10.1242/DEV.053694>
- Douarin, N. M. (1975). An experimental analysis of liver development. *Medical Biology*, *53*(6), 427–455. <http://europepmc.org/abstract/MED/765644>
- Duboule, D., & Morata, G. (1994). Colinearity and functional hierarchy among genes of the homeotic complexes. *Trends in Genetics*, *10*(10), 358–364. [https://doi.org/10.1016/0168-9525\(94\)90132-5](https://doi.org/10.1016/0168-9525(94)90132-5)
- D’Urso, M., & Kurniawan, N. A. (2020). Mechanical and Physical Regulation of Fibroblast–Myofibroblast Transition: From Cellular Mechanoresponse to Tissue Pathology. *Frontiers in Bioengineering and Biotechnology*, *8*, 1459. <https://doi.org/10.3389/FBIOE.2020.609653/BIBTEX>
- Engert, S., Bartscher, I., Liao, W. P., Dulev, S., Schotta, G., & Lickert, H. (2013). Wnt/ β -catenin signalling regulates Sox17 expression and is essential for organizer and endoderm formation in the mouse. *Development (Cambridge)*, *140*(15), 3128–3138. <https://doi.org/10.1242/dev.088765>
- Fagan, M. B. and J. M. (2022). Theories of Biological Development. *The Stanford Encyclopedia of Philosophy*, Summer 202.

- Fausett, S. R., & Klingensmith, J. (2012). Compartmentalization of the foregut tube: Developmental origins of the trachea and esophagus. *Wiley Interdisciplinary Reviews: Developmental Biology*, *1*(2), 184–202. <https://doi.org/10.1002/wdev.12>
- Fleming, B. M., Yelin, R., James, R. G., & Schultheiss, T. M. (2013). A role for Vg1/Nodal signaling in specification of the intermediate mesoderm. *Development (Cambridge, England)*, *140*(8), 1819. <https://doi.org/10.1242/DEV.093740>
- Frangiannis, N. G. (2020). Transforming growth factor- β in tissue fibrosis. *Journal of Experimental Medicine*, *217*(3), 1–16. <https://doi.org/10.1084/jem.20190103>
- Freddo, A. M., Shoffner, S. K., Shao, Y., Taniguchi, K., Grosse, A. S., Guysinger, M. N., Wang, S., Rudraraju, S., Margolis, B., Garikipati, K., Schnell, S., & Gumucio, D. L. (2016). Coordination of signaling and tissue mechanics during morphogenesis of murine intestinal villi: A role for mitotic cell rounding. *Integrative Biology (United Kingdom)*, *8*(9), 918–928. <https://doi.org/10.1039/c6ib00046k>
- Fu, M., Lui, V. C. H., Sham, M. H., Pachnis, V., & Tam, P. K. H. (2004). Sonic hedgehog regulates the proliferation, differentiation, and migration of enteric neural crest cells in gut. *Journal of Cell Biology*, *166*(5), 673–684. <https://doi.org/10.1083/jcb.200401077>
- Fung, Y. C., & Liu, S. Q. (1989). Change of residual strains in arteries due to hypertrophy caused by aortic constriction. *Circulation Research*, *65*(5), 1340–1349. <https://doi.org/10.1161/01.RES.65.5.1340>
- Galen, C. (2019). *On the natural faculties*. Dalcassian Publishing Company.

- Gao, N., White, P., & Kaestner, K. H. (2009). Establishment of Intestinal Identity and Epithelial-Mesenchymal Signaling by Cdx2. *Developmental Cell*, 16(4), 588–599.
<https://doi.org/10.1016/j.devcel.2009.02.010>
- Garcia, K. E., Stewart, W. G., Espinosa, M. G., Gleghorn, J. P., & Taber, L. A. (2019). *Molecular and mechanical signals determine morphogenesis of the cerebral hemispheres in the chicken embryo*. <https://doi.org/10.1242/dev.174318>
- Garman, K. S. (2017). Origin of Barrett’s Epithelium: Esophageal Submucosal Glands. *Cellular and Molecular Gastroenterology and Hepatology*, 4(1), 153.
<https://doi.org/10.1016/J.JCMGH.2017.01.016>
- Gehart, H., & Clevers, H. (2018). Tales from the crypt: new insights into intestinal stem cells. *Nature Reviews Gastroenterology & Hepatology* 2018 16:1, 16(1), 19–34.
<https://doi.org/10.1038/S41575-018-0081-Y>
- Geisel, S., Secchi, E., & Vermant, J. (2022). The role of surface adhesion on the macroscopic wrinkling of biofilms. *ELife*, 11. <https://doi.org/10.7554/eLife.76027>
- Geske, M. J., Zhang, X., Patel, K. K., Ornitz, D. M., & Stappenbeck, T. S. (2008). Fgf9 signaling regulates small intestinal elongation and mesenchymal development. *Development*, 135(17), 2959–2968. <https://doi.org/10.1242/dev.020453>
- Ginzl, M., Huber, N., Bauer, L., Kluth, D., & Metzger, R. (2023). Development of the foregut and the formation of the trachea and esophagus in rat embryos. A symphony of confusion. *Frontiers in Cell and Developmental Biology*, 11.
<https://doi.org/10.3389/fcell.2023.1092753>

- Gjorevski, N., Nikolaev, M., Brown, T. E., Mitrofanova, O., Brandenburg, N., DelRio, F. W., Yavitt, F. M., Liberali, P., Anseth, K. S., & Lutolf, M. P. (2022). Tissue geometry drives deterministic organoid patterning. *Science*, *375*(6576). <https://doi.org/10.1126/science.aaw9021>
- Godwin, A. R. F., Singh, M., Lockhart-Cairns, M. P., Alanazi, Y. F., Cain, S. A., & Baldock, C. (2019). The role of fibrillin and microfibril binding proteins in elastin and elastic fibre assembly. *Matrix Biology*, *84*, 17–30. <https://doi.org/10.1016/j.matbio.2019.06.006>
- Gogone, I. C. V. P., de Carvalho, M. P. N., Grego, K. F., Sant'Anna, S. S., Hernandez-Blazquez, F. J., & Catão-Dias, J. L. (2017). Aspectos histológicos do trato gastrointestinal de *Bothrops jararaca* e *Crotalus durissus*. *Brazilian Journal of Veterinary Research and Animal Science*, *54*(3), 253–263. <https://doi.org/10.11606/issn.1678-4456.bjvras.2017.133256>
- Gohel, V. K., Edell, S. L., Laufer, I., & Rhodes, W. H. (1978). Transverse folds in the human esophagus. *Radiology*, *128*(2), 303–308. <https://doi.org/10.1148/128.2.303>
- Goodwin, K., & Nelson, C. M. (2021). Mechanics of Development. *Developmental Cell*, *56*(2), 240–250. <https://doi.org/10.1016/J.DEVCEL.2020.11.025>
- Gopalakrishnan, S., Comai, G., Sambasivan, R., Francou, A., Kelly, R. G., & Tajbakhsh, S. (2015). A Cranial Mesoderm Origin for Esophagus Striated Muscles. *Developmental Cell*, *34*(6), 694–704. <https://doi.org/10.1016/J.DEVCEL.2015.07.003>
- Graham, V., Khudyakov, J., Ellis, P., & Pevny, L. (2003). SOX2 functions to maintain neural progenitor identity. *Neuron*, *39*(5), 749–765. [https://doi.org/10.1016/S0896-6273\(03\)00497-5](https://doi.org/10.1016/S0896-6273(03)00497-5)

- Grapin-Botton, A. (2005). Antero-posterior patterning of the vertebrate digestive tract: 40 Years after Nicole Le Douarin's PhD thesis. *International Journal of Developmental Biology*, 49(2-3 SPEC. ISS.), 335–347. <https://doi.org/10.1387/ijdb.041946ag>
- Grapin-Botton, A., Majithia, A. R., & Melton, D. A. (2001). Key events of pancreas formation are triggered in gut endoderm by ectopic expression of pancreatic regulatory genes. *Genes and Development*, 15(4), 444–454. <https://doi.org/10.1101/gad.846001>
- Gros, J., Serralbo, O., & Marcelle, C. (2009). WNT11 acts as a directional cue to organize the elongation of early muscle fibres. *Nature*, 457(7229), 589–593. <https://doi.org/10.1038/nature07564>
- Guerrero-Juarez, C. F., Dedhia, P. H., Jin, S., Ruiz-Vega, R., Ma, D., Liu, Y., Yamaga, K., Shestova, O., Gay, D. L., Yang, Z., Kessenbrock, K., Nie, Q., Pear, W. S., Cotsarelis, G., & Plikus, M. V. (2019). Single-cell analysis reveals fibroblast heterogeneity and myeloid-derived adipocyte progenitors in murine skin wounds. *Nature Communications* 2019 10:1, 10(1), 1–17. <https://doi.org/10.1038/s41467-018-08247-x>
- Gurdziel, K., Vogt, K. R., Walton, K. D., Schneider, G. K., & Gumucio, D. L. (2016). Transcriptome of the inner circular smooth muscle of the developing mouse intestine: Evidence for regulation of visceral smooth muscle genes by the hedgehog target gene, cJun. *Developmental Dynamics*, 245(5), 614–626. <https://doi.org/10.1002/dvdy.24399>
- Gustafson, H. J., Claussen, N., De Renzis, S., & Streichan, S. J. (2022). Patterned mechanical feedback establishes a global myosin gradient. *Nature Communications* 2022 13:1, 13(1), 1–12. <https://doi.org/10.1038/s41467-022-34518-9>

- Hallou, A., & Brunet, T. (2020). On growth and force: Mechanical forces in development. *Development (Cambridge)*, 147(4). <https://doi.org/10.1242/dev.187302>
- Hannezo, E., Prost, J., & Joanny, J. F. (2011). Instabilities of monolayered epithelia: Shape and structure of villi and crypts. *Physical Review Letters*, 107(7), 1–5. <https://doi.org/10.1103/PhysRevLett.107.078104>
- Hartenstein, V., & Martinez, P. (2019a). Structure, Development and Evolution of the Digestive System. *Cell and Tissue Research*, 377(3), 289. <https://doi.org/10.1007/S00441-019-03102-X>
- Hartenstein, V., & Martinez, P. (2019b). Phagocytosis in cellular defense and nutrition: a food-centered approach to the evolution of macrophages. *Cell and Tissue Research* 2019 377:3, 377(3), 527–547. <https://doi.org/10.1007/S00441-019-03096-6>
- Hatch, J., & Mukoyama, Y.-S. (2015). Spatiotemporal Mapping of Vascularization and Innervation in the Fetal Murine Intestine. *Developmental Dynamics*, 244, 56–68. <https://doi.org/10.1002/dvdy>
- Hattori, N., Carrino, D. A., Lauer, M. E., Vasanji, A., Wylie, J. D., Nelson, C. M., & Apte, S. S. (2011). Pericellular Versican Regulates the Fibroblast-Myofibroblast Transition: A ROLE FOR ADAMTS5 PROTEASE-MEDIATED PROTEOLYSIS*. *The Journal of Biological Chemistry*, 286(39), 34298. <https://doi.org/10.1074/JBC.M111.254938>
- Havis, E., Bonnin, M. A., De Lima, J. E., Charvet, B., Milet, C., & Duprez, D. (2016). TGF β and FGF promote tendon progenitor fate and act downstream of muscle contraction to regulate tendon differentiation during chick limb development. *Development (Cambridge)*, 143(20), 3839–3851. <https://doi.org/10.1242/dev.136242>

- Hawkins, M. B., Henke, K., & Harris, M. P. (2021). Latent developmental potential to form limb-like skeletal structures in zebrafish. *Cell*, *184*(4), 899-911.e13.
<https://doi.org/10.1016/j.cell.2021.01.003>
- He, B., Wu, J. P., Chen, H. H., Kirk, T. B., & Xu, J. (2013). Elastin fibers display a versatile microfibril network in articular cartilage depending on the mechanical microenvironments. *Journal of Orthopaedic Research*, *31*(9), 1345–1353. <https://doi.org/10.1002/jor.22384>
- Hejnol, A., & Martindale, M. Q. (2008). Acoel development indicates the independent evolution of the bilaterian mouth and anus. *Nature* *2008* 456:7220, *456*(7220), 382–386.
<https://doi.org/10.1038/NATURE07309>
- Hejnol, A., & Martín-Durán, J. M. (2015). Getting to the bottom of anal evolution. *Zoologischer Anzeiger*, *256*, 61–74. <https://doi.org/10.1016/J.JCZ.2015.02.006>
- Ho, W. K. W., Freem, L., Zhao, D., Painter, K. J., Woolley, T. E., Gaffney, E. A., McGrew, M. J., Tzika, A., Milinkovitch, M. C., Schneider, P., Drusko, A., Matthäus, F., Glover, J. D., Wells, K. L., Johansson, J. A., Davey, M. G., Sang, H. M., Clinton, M., & Headon, D. J. (2019). Feather arrays are patterned by interacting signalling and cell density waves. In *PLoS Biology* (Vol. 17, Issue 2). <https://doi.org/10.1371/journal.pbio.3000132>
- Hohlfeld, E., & Mahadevan, L. (2011). Unfolding the sulcus. *Physical Review Letters*, *106*(10).
<https://doi.org/10.1103/PhysRevLett.106.105702>
- Hohlfeld, E., & Mahadevan, L. (2012). Scale and nature of sulcification patterns. *Physical Review Letters*, *109*(2). <https://doi.org/10.1103/PhysRevLett.109.025701>

- Holland, M., Budday, S., Goriely, A., & Kuhl, E. (2018). Symmetry Breaking in Wrinkling Patterns: Gyri Are Universally Thicker than Sulci. *Physical Review Letters*, *121*(22).
<https://doi.org/10.1103/PhysRevLett.121.228002>
- Horný, L., Netušil, M., & Voňavková, T. (2014). Axial prestretch and circumferential distensibility in biomechanics of abdominal aorta. *Biomechanics and Modeling in Mechanobiology*, *13*(4), 783–799. <https://doi.org/10.1007/S10237-013-0534-8/FIGURES/11>
- Houtekamer, R. M., van der Net, M. C., Maurice, M. M., & Gloerich, M. (2022). Mechanical forces directing intestinal form and function. *Current Biology*, *32*(14), R791–R805.
<https://doi.org/10.1016/j.cub.2022.05.041>
- Hughes, A. J., Miyazaki, H., Coyle, M. C., Zhang, J., Laurie, M. T., Chu, D., Vavrušová, Z., Schneider, R. A., Klein, O. D., & Gartner, Z. J. (2018). Engineered Tissue Folding by Mechanical Compaction of the Mesenchyme. *Developmental Cell*, *44*(2), 165-178.e6.
<https://doi.org/10.1016/j.devcel.2017.12.004>
- Huycke, T. R. (2018). *On the Developmental Patterning and Alignment of Intestinal Smooth Muscle*.
- Huycke, T. R., Miller, B. M., Gill, H. K., Nerurkar, N. L., Sprinzak, D., Mahadevan, L., Tabin, C. J., Huycke, T. R., Miller, B. M., Gill, H. K., Nerurkar, N. L., Sprinzak, D., & Mahadevan, L. (2019). Genetic and Mechanical Regulation of Intestinal Smooth Muscle Development. *Cell*, *179*(1), 90-105.e21. <https://doi.org/10.1016/j.cell.2019.08.041>
- Imura, T., & Pourquié, O. (2006). Collinear activation of Hoxb genes during gastrulation is linked to mesoderm cell ingression. *Nature*, *442*(7102), 568–571.
<https://doi.org/10.1038/nature04838>

Jacko, M., Weyn-Vanhentenryck, S. M., Smerdon, J. W., Yan, R., Feng, H., Williams, D. J., Pai, J.,

Xu, K., Wichterle, H., & Zhang, C. (2018). Rbfox Splicing Factors Promote Neuronal Maturation and Axon Initial Segment Assembly. *Neuron*, 97(4), 853-868.e6.

<https://doi.org/10.1016/j.neuron.2018.01.020>

Jeffery, T. K., Upton, P. D., Trembath, R. C., & Morrell, N. W. (2005). BMP4 inhibits proliferation and promotes myocyte differentiation of lung fibroblasts via Smad1 and JNK pathways.

American Journal of Physiology - Lung Cellular and Molecular Physiology, 288(2 32-2), 370–378. <https://doi.org/10.1152/ajplung.00242.2004>

Jones, C., & Chen, P. (2007). Planar cell polarity signaling in vertebrates. *BioEssays : News and Reviews in Molecular, Cellular and Developmental Biology*, 29(2), 120.

<https://doi.org/10.1002/BIES.20526>

Kamenskiy, A. V., Pipinos, I. I., Dzenis, Y. A., Lomneth, C. S., Kazmi, S. A. J., Phillips, N. Y., &

MacTaggart, J. N. (2013). Passive biaxial mechanical properties and in vivo axial pre-stretch of the diseased human femoropopliteal and tibial arteries. *Acta Biomaterialia*, 10(3),

1301–1313. <https://doi.org/10.1016/J.ACTBIO.2013.12.027>

Kan, A., Ikeda, T., Fukai, A., Nakagawa, T., Nakamura, K., Chung, U. Il, Kawaguchi, H., & Tabin, C.

J. (2013). SOX11 contributes to the regulation of GDF5 in joint maintenance. *BMC Developmental Biology*, 13(1). <https://doi.org/10.1186/1471-213X-13-4>

Karlsson, L., Lindahl, P., Heath, J. K., & Betsholtz, C. (2000). Abnormal gastrointestinal

development in PDGF-A and PDGFR-?? deficient mice implicates a novel mesenchymal structure with putative instructive properties in villus morphogenesis. *Development*, 127(16), 3457–3466.

- Keele, K. D. (1972). Leonardo da Vinci's Studies of the Alimentary Tract. *Journal of the History of Medicine and Allied Sciences*, XXVII(2), 133–144.
<https://doi.org/10.1093/JHMAS/XXVII.2.133>
- Keller, R. (2006). Mechanisms of elongation in embryogenesis. *Development*, 133(12), 2291–2302. <https://doi.org/10.1242/dev.02406>
- Kessel, M., & Gruss, P. (1991). Homeotic Transformations of Murine Vertebrae and Concomitant Alteration of Hox Codes Induced by Retinoic Acid. In *Cell* (Vol. 67, Issue 104).
- Khalipina, D., Kaga, Y., Dacher, N., Chevalier, N. R., & Chevalier, N. R. (2019). *Smooth muscle contractility causes the gut to grow anisotropically*.
- Khamas, W., & Reeves, R. (2011). Morphological study of the oesophagus and stomach of the Gopher snake *Pituophis catenifer*. *Anatomia, Histologia, Embryologia*, 40(4), 307–313.
<https://doi.org/10.1111/J.1439-0264.2011.01072.X>
- Kicheva, A., Bollenbach, T., Ribeiro, A., Pérez Valle, H., Lovell-Badge, R., Episkopou, V., & Briscoe, J. (2014). Coordination of progenitor specification and growth in mouse and chick spinal cord. *Science*, 345(6204).
https://doi.org/10.1126/SCIENCE.1254927/SUPPL_FILE/KICHEVA_SM.PDF
- Kishi, J. Y., Lapan, S. W., Beliveau, B. J., West, E. R., Zhu, A., Sasaki, H. M., Saka, S. K., Wang, Y., Cepko, C. L., & Yin, P. (2019). SABER amplifies FISH: enhanced multiplexed imaging of RNA and DNA in cells and tissues. *Nature Methods*, 16(6), 533–544.
<https://doi.org/10.1038/s41592-019-0404-0>
- Kishi, J. Y., Liu, N., West, E. R., Sheng, K., Jordanides, J. J., Serrata, M., Cepko, C. L., Saka, S. K., & Yin, P. (2022). Light-Seq: light-directed in situ barcoding of biomolecules in fixed cells and

tissues for spatially indexed sequencing. *Nature Methods*, 19(11), 1393–1402.

<https://doi.org/10.1038/s41592-022-01604-1>

Kishimoto, K., Tamura, M., Nishita, M., Minami, Y., Yamaoka, A., Abe, T., Shigeta, M., & Morimoto, M. (2018). Synchronized mesenchymal cell polarization and differentiation shape the formation of the murine trachea and esophagus. *Nature Communications*, 9(1).

<https://doi.org/10.1038/s41467-018-05189-2>

Klingberg, F., Hinz, B., & White, E. S. (2013). The myofibroblast matrix: implications for tissue repair and fibrosis. *The Journal of Pathology*, 229(2), 298.

<https://doi.org/10.1002/PATH.4104>

Kondo, T., Dollé, P., Zákány, J., & Duboule, D. (1996). Function of posterior HoxD genes in the morphogenesis of the anal sphincter. *Development*, 122(9), 2651–2659.

<https://doi.org/10.1242/dev.122.9.2651>

Kostouros, A., Koliarakis, I., Natsis, K., Spandidos, D. A., Tsatsakis, A., & Tsiaoussis, J. (2020).

Large intestine embryogenesis: Molecular pathways and related disorders (Review).

International Journal of Molecular Medicine, 46(1), 27.

<https://doi.org/10.3892/IJMM.2020.4583>

Krauss, R. S., Chihara, D., & Romer, A. I. (2016). Embracing change: Striated-for-smooth muscle replacement in esophagus development. *Skeletal Muscle*, 6(1), 1–8.

<https://doi.org/10.1186/s13395-016-0099-1>

Kuleshov, M. V., Jones, M. R., Rouillard, A. D., Fernandez, N. F., Duan, Q., Wang, Z., Koplev, S., Jenkins, S. L., Jagodnik, K. M., Lachmann, A., McDermott, M. G., Monteiro, C. D., Gundersen, G. W., & Maayan, A. (2016). Enrichr: a comprehensive gene set enrichment

analysis web server 2016 update. *Nucleic Acids Research*, 44(1), W90–W97.

<https://doi.org/10.1093/nar/gkw377>

Kurpios, N. A., Ibañes, M., Davis, N. M., Lui, W., Katz, T., Martin, J. F., Belmonte, J. C. I., & Tabin, C. J. (2008). The direction of gut looping is established by changes in the extracellular matrix and in cell: Cell adhesion. *Proceedings of the National Academy of Sciences of the United States of America*, 105(25), 8499–8506. <https://doi.org/10.1073/pnas.0803578105>

Lake, J. I., & Heuckeroth, R. O. (2013). Enteric nervous system development: migration, differentiation, and disease. *Am J Physiol Gastrointest Liver Physiol*, 305, 1–24.

<https://doi.org/10.1152/ajpgi.00452.2012.-The>

Lee, T., Holland, M. A., Weickenmeier, J., Gosain, A. K., & Tepole, A. B. (2021). The geometry of incompatibility in growing soft tissues: Theory and numerical characterization. *Journal of the Mechanics and Physics of Solids*, 146, 104177.

<https://doi.org/10.1016/J.JMPS.2020.104177>

LeGoff, L., & Lecuit, T. (2016). Mechanical forces and growth in animal tissues. *Cold Spring Harbor Perspectives in Biology*, 8(3), 1–18. <https://doi.org/10.1101/cshperspect.a019232>

Levine, M. S., & Rubesin, S. E. (2005). Diseases of the esophagus: Diagnosis with esophagography. In *Radiology* (Vol. 237, Issue 2, pp. 414–427).

<https://doi.org/10.1148/radiol.2372050199>

Levit, G. S., Hoßfeld, U., Naumann, B., Lukas, P., & Olsson, L. (2022). The biogenetic law and the Gastraea theory: From Ernst Haeckel’s discoveries to contemporary views. In *Journal of Experimental Zoology Part B: Molecular and Developmental Evolution* (Vol. 338, Issues 1–2, pp. 13–27). John Wiley and Sons Inc. <https://doi.org/10.1002/jez.b.23039>

- Lewis, S. L., & Tam, P. P. L. (2006). Definitive endoderm of the mouse embryo: Formation, cell fates, and morphogenetic function. *Developmental Dynamics*, 235(9), 2315–2329.
<https://doi.org/10.1002/dvdy.20846>
- Li, B., Cao, Y. P., Feng, X. Q., & Gao, H. (2012). Mechanics of morphological instabilities and surface wrinkling in soft materials: A review. *Soft Matter*, 8(21), 5728–5745.
<https://doi.org/10.1039/c2sm00011c>
- Liao, D., Zhao, J., Yang, J., & Gregersen, H. (2007). The oesophageal zero-stress state and mucosal folding from a GIOME perspective. *World Journal of Gastroenterology : WJG*, 13(9), 1347. <https://doi.org/10.3748/WJG.V13.I9.1347>
- Liu, C., Baek, S., Kim, J., Vasko, E., Pyne, R., & Chan, C. (2014). Effect of static pre-stretch induced surface anisotropy on orientation of mesenchymal stem cells. *Cellular and Molecular Bioengineering*, 7(1), 106–121. <https://doi.org/10.1007/s12195-013-0300-0>
- Liu, G., Cooley, M. A., Jarnicki, A. G., Borghuis, T., Nair, P. M., Tjin, G., Hsu, A. C., Haw, T. J., Fricker, M., Harrison, C. L., Jones, B., Hansbro, N. G., Wark, P. A., Horvat, J. C., Scott Argraves, W., Oliver, B. G., Knight, D. A., Burgess, J. K., & Hansbro, P. M. (2019). Fibulin-1c regulates transforming growth factor- β activation in pulmonary tissue fibrosis. *JCI Insight*, 4(16). <https://doi.org/10.1172/JCI.INSIGHT.124529>
- Long, J. D., & Orlando, R. C. (1999). *Esophageal Submucosal Glands: Structure and Function*.
- Love, M. I., Huber, W., & Anders, S. (2014). Moderated estimation of fold change and dispersion for RNA-seq data with DESeq2. *Genome Biology*, 15(12), 1–21.
<https://doi.org/10.1186/s13059-014-0550-8>

- Mahoney, Z. X., Stappenbeck, T. S., & Miner, J. H. (2008). Laminin α 5 influences the architecture of the mouse small intestine mucosa. *Journal of Cell Science*, *121*(15), 2493–2502.
<https://doi.org/10.1242/jcs.025528>
- Maimets, M., Pedersen, M. T., Guiu, J., Dreier, J., Thodberg, M., Antoku, Y., Schweiger, P. J., Rib, L., Bressan, R. B., Miao, Y., Garcia, K. C., Sandelin, A., Serup, P., & Jensen, K. B. (2022). Mesenchymal-epithelial crosstalk shapes intestinal regionalisation via Wnt and Shh signalling. *Nature Communications*, *13*(1). <https://doi.org/10.1038/s41467-022-28369-7>
- Major, A. T., Estermann, M. A., Roly, Z. Y., & Smith, C. A. (2022). An evo-devo perspective of the female reproductive tract. *Biology of Reproduction*, *106*(1), 9–23.
<https://doi.org/10.1093/BIOLRE/IOAB166>
- Mamo, T. M., Wittern, A. B., Kleppa, M. J., Bohnenpoll, T., Weiss, A. C., & Kispert, A. (2017). BMP4 uses several different effector pathways to regulate proliferation and differentiation in the epithelial and mesenchymal tissue compartments of the developing mouse ureter. *Human Molecular Genetics*, *26*(18), 3553–3563. <https://doi.org/10.1093/HMG/DDX242>
- Mao, J., Kim, B. M., Rajurkar, M., Shivdasani, R. A., & McMahon, A. P. (2010). Hedgehog signaling controls mesenchymal growth in the developing mammalian digestive tract. *Development*, *137*(10), 1721–1729. <https://doi.org/10.1242/dev.044586>
- Martyniuk, K., Ziółkowska, N., Hanuszewska-Dominiak, M., Szyryńska, N., & Lewczuk, B. (2023). Histology and Ultrastructure of the Esophagus in European Beaver (*Castor fiber*) Displays Features Adapted to Seasonal Changes in Diet. *Animals* 2023, Vol. 13, Page 635, *13*(4), 635. <https://doi.org/10.3390/ANI13040635>

- Martynoga, B., Morrison, H., Price, D. J., & Mason, J. O. (2005). Foxg1 is required for specification of ventral telencephalon and region-specific regulation of dorsal telencephalic precursor proliferation and apoptosis. *Developmental Biology*, 283(1), 113–127. <https://doi.org/10.1016/j.ydbio.2005.04.005>
- Mazengenya, P., & Bhikha, R. (2018). Revisiting Avicenna's (980–1037 AD) anatomy of the abdominal viscera from the Canon of Medicine. *Morphologie*, 102(338), 225–230. <https://doi.org/10.1016/j.morpho.2018.05.002>
- McCarthy, N., Kraiczy, J., & Shivdasani, R. A. (2020). Cellular and molecular architecture of the intestinal stem cell niche. *Nature Cell Biology*, 22(9), 1033–1041. <https://doi.org/10.1038/s41556-020-0567-z>
- McGinn, J., Hallou, A., Han, S., Krizic, K., Ulyanchenko, S., Iglesias-Bartolome, R., England, F. J., Verstreken, C., Chalut, K. J., Jensen, K. B., Simons, B. D., & Alcolea, M. P. (2021). A biomechanical switch regulates the transition towards homeostasis in oesophageal epithelium. *Nature Cell Biology* 2021 23:5, 23(5), 511–525. <https://doi.org/10.1038/s41556-021-00679-w>
- Ménard, D. (1995). Morphological studies of the developing human esophageal epithelium. *Microscopy Research and Technique*, 31(3), 215–225. <https://doi.org/10.1002/jemt.1070310305>
- Michalik, M., Wójcik-Pszczoła, K., Paw, M., Wnuk, D., Koczurkiewicz, P., Sanak, M., Pękala, E., & Madeja, Z. (2018). Fibroblast-to-myofibroblast transition in bronchial asthma. *Cellular and Molecular Life Sciences : CMLS*, 75(21), 3943–3961. <https://doi.org/10.1007/S00018-018-2899-4>

- Mitchell, N. P., Cislo, D. J., Shankar, S., Lin, Y., Shraiman, B. I., & Streichan, S. J. (2021). Visceral organ morphogenesis via calcium-patterned muscle constrictions. *BiorXiv*, 1–20.
- Mitchell, N. P., Cislo, D. J., Shankar, S., Lin, Y., Shraiman, B. I., & Streichan, S. J. (2022). Visceral organ morphogenesis via calcium-patterned muscle constrictions. *ELife*, *11*.
<https://doi.org/10.7554/eLife.77355>
- Moreau, C., Caldarelli, P., Rocancourt, D., Roussel, J., Denans, N., Pourquie, O., & Gros, J. (2019). Timed Collinear Activation of Hox Genes during Gastrulation Controls the Avian Forelimb Position. *Current Biology*, *29*(1), 35-50.e4. <https://doi.org/10.1016/j.cub.2018.11.009>
- Múnera, J. O., Sundaram, N., Rankin, S. A., Hill, D., Watson, C., Mahe, M., Vallance, J. E., Shroyer, N. F., Sinagoga, K. L., Zarzoso-Lacoste, A., Hudson, J. R., Howell, J. C., Chatuvedi, P., Spence, J. R., Shannon, J. M., Zorn, A. M., Helmrich, M. A., & Wells, J. M. (2017). Differentiation of human pluripotent stem cells into colonic organoids via transient activation of BMP signaling. *Cell Stem Cell*, *21*(1), 51.
<https://doi.org/10.1016/J.STEM.2017.05.020>
- Myat, M. M. (2005). Making tubes in the Drosophila embryo. *Developmental Dynamics*, *232*(3), 617–632. <https://doi.org/10.1002/DVDY.20293>
- Nagy, N., Barad, C., Hotta, R., Bhave, S., Arciero, E., Dora, D., & Goldstein, A. M. (2018). Collagen 18 and agrin are secreted by neural crest cells to remodel their microenvironment and regulate their migration during enteric nervous system development. *Development (Cambridge)*, *145*(9). <https://doi.org/10.1242/dev.160317>

- Nakayama, S., Sekiguchi, T., & Ogasawara, M. (2019). Molecular and evolutionary aspects of the protochordate digestive system. *Cell and Tissue Research*, 377(3), 309–320.
<https://doi.org/10.1007/S00441-019-03035-5/FIGURES/3>
- Nelson, C. M. (2016). On buckling morphogenesis. *Journal of Biomechanical Engineering*, 138(2), 1–6. <https://doi.org/10.1115/1.4032128>
- Nerurkar, N. L., Lee, C. H., Mahadevan, L., & Tabin, C. J. (2019). Molecular control of macroscopic forces drives formation of the vertebrate hindgut. *Nature*, 565(7740), 480–484. <https://doi.org/10.1038/s41586-018-0865-9>
- Nerurkar, N. L., Mahadevan, L., & Tabin, C. J. (2017). BMP signaling controls buckling forces to modulate looping morphogenesis of the gut. *Proceedings of the National Academy of Sciences of the United States of America*, 114(9), 2277–2282.
<https://doi.org/10.1073/pnas.1700307114>
- Nie, L., Wu, H. Y., Shen, Y. H., Fan, X. S., Sun, Q., Huang, Q., & Chen, J. (2017). Esophageal submucosal gland duct adenoma: a clinicopathological and immunohistochemical study with a review of the literature. *Diseases of the Esophagus*, 30(6), 1–6.
<https://doi.org/10.1111/DOTE.12442>
- Nowotschin, S., Setty, M., Kuo, Y. Y., Liu, V., Garg, V., Sharma, R., Simon, C. S., Saiz, N., Gardner, R., Boutet, S. C., Church, D. M., Hoodless, P. A., Hadjantonakis, A. K., & Pe'er, D. (2019). The emergent landscape of the mouse gut endoderm at single-cell resolution. *Nature*, 569(7756), 361–367. <https://doi.org/10.1038/s41586-019-1127-1>
- Pandit, K., Dhote, B. S., Mahanta, D., Sathapathy, S., Tamilselvan, S., Mrigesh, M., & Mishra, S. (2018). Histological, Histomorphometrical and Histochemical Studies on the Large Intestine

- of Uttara Fowl. *International Journal of Current Microbiology and Applied Sciences*, 7(03), 1477–1491. <https://doi.org/10.20546/ijcmas.2018.703.176>
- Parada, C., Banavar, S. P., Khalilian, P., Rigaud, S., Michaut, A., Liu, Y., Joshy, D. M., Campàs, O., & Gros, J. (2022). Mechanical feedback defines organizing centers to drive digit emergence. *Developmental Cell*, 57(7), 854–866.e6. <https://doi.org/10.1016/j.devcel.2022.03.004>
- Parikh, K., Antanaviciute, A., Fawkner-Corbett, D., Jagielowicz, M., Aulicino, A., Lagerholm, C., Davis, S., Kinchen, J., Chen, H. H., Alham, N. K., Ashley, N., Johnson, E., Hublitz, P., Bao, L., Lukomska, J., Andev, R. S., Björklund, E., Kessler, B. M., Fischer, R., ... Simmons, A. (2019). Colonic epithelial cell diversity in health and inflammatory bowel disease. *Nature* 2019 567:7746, 567(7746), 49–55. <https://doi.org/10.1038/S41586-019-0992-Y>
- Parker, H. J., & Krumlauf, R. (2020). A Hox gene regulatory network for hindbrain segmentation. In *Current Topics in Developmental Biology* (Vol. 139, pp. 169–203). Academic Press Inc. <https://doi.org/10.1016/bs.ctdb.2020.03.001>
- Patro, R., Duggal, G., Love, M. I., Irizarry, R. A., & Kingsford, C. (2017). Salmon provides fast and bias-aware quantification of transcript expression. *Nature Methods*, 14(4), 417–419. <https://doi.org/10.1038/nmeth.4197>
- Penner, A. S., Rock, M. J., Kielty, C. M., & Michael Shipley, J. (2002). Microfibril-associated glycoprotein-2 interacts with fibrillin-1 and fibrillin-2 suggesting a role for MAGP-2 in elastic fiber assembly. *Journal of Biological Chemistry*, 277(38), 35044–35049. <https://doi.org/10.1074/jbc.M206363200>

- Pérez-González, C., Ceada, G., Greco, F., Matejčić, M., Gómez-González, M., Castro, N., Menendez, A., Kale, S., Krndija, D., Clark, A. G., Gannavarapu, V. R., Álvarez-Varela, A., Roca-Cusachs, P., Batlle, E., Vignjevic, D. M., Arroyo, M., & Trepát, X. (2021). Mechanical compartmentalization of the intestinal organoid enables crypt folding and collective cell migration. In *Nature Cell Biology* (Vol. 23, Issue 7). Springer US.
<https://doi.org/10.1038/s41556-021-00699-6>
- Peterson, L. W., & Artis, D. (2014). Intestinal epithelial cells: regulators of barrier function and immune homeostasis. *Nature Reviews Immunology* 2014 14:3, 14(3), 141–153.
<https://doi.org/10.1038/NRI3608>
- Pinheiro, D., Kardos, R., Hannezo, É., & Heisenberg, C. P. (2022). Morphogen gradient orchestrates pattern-preserving tissue morphogenesis via motility-driven unjamming. *Nature Physics* 2022 18:12, 18(12), 1482–1493. <https://doi.org/10.1038/s41567-022-01787-6>
- Pinto, R., Barros, R., Pereira-Castro, I., Mesquita, P., da Costa, L. T., Bennett, E. P., Almeida, R., & David, L. (2015). CDX2 homeoprotein is involved in the regulation of ST6GalNAc-I gene in intestinal metaplasia. *Laboratory Investigation*, 95(7), 718–727.
<https://doi.org/10.1038/labinvest.2015.52>
- Pompili, S., Latella, G., Gaudio, E., Sferra, R., & Vetuschi, A. (2021). The Charming World of the Extracellular Matrix: A Dynamic and Protective Network of the Intestinal Wall. *Frontiers in Medicine*, 8. <https://doi.org/10.3389/fmed.2021.610189>
- Prager-Khoutorsky, M., Lichtenstein, A., Krishnan, R., Rajendran, K., Mayo, A., Kam, Z., Geiger, B., & Bershadsky, A. D. (2011). Fibroblast polarization is a matrix-rigidity-dependent

process controlled by focal adhesion mechanosensing. *Nature Cell Biology*, 13(12), 1457–1465. <https://doi.org/10.1038/ncb2370>

Probst, S., Sagar, T., Tomic, J., Schwan, C., Grün, D., & Arnold, S. J. (2021). Spatiotemporal sequence of mesoderm and endoderm lineage segregation during mouse gastrulation. *Development (Cambridge)*, 148(1). <https://doi.org/10.1242/DEV.193789>/VIDEO-4

Que, J., Choi, M., Ziel, J. W., Klingensmith, J., & Hogan, B. L. M. (2006). Morphogenesis of the trachea and esophagus: Current players and new roles for noggin and Bmps. *Differentiation*, 74(7), 422–437. <https://doi.org/10.1111/j.1432-0436.2006.00096.x>

Que, J., Okubo, T., Goldenring, J. R., Nam, K. T., Kurotani, R., Morrisey, E. E., Taranova, O., Pevny, L. H., & Hogan, B. L. M. (2007). Multiple dose-dependent roles for Sox2 in the patterning and differentiation of anterior foregut endoderm. *Development*, 134(13), 2521–2531. <https://doi.org/10.1242/dev.003855>

Raghoebir, L., Bakker, E. R. M., Mills, J. C., Swagemakers, S., Kempen, M. B. Van, Munck, A. B. De, Driegen, S., Meijer, D., Grosveld, F., Tibboel, D., Smits, R., & Rottier, R. J. (2012). SOX2 redirects the developmental fate of the intestinal epithelium toward a premature gastric phenotype. *Journal of Molecular Cell Biology*, 4(6), 377–385.

<https://doi.org/10.1093/jmcb/mjs030>

Ramachandran, R. G., de Cortie, J., Maiti, S., Deseri, L., & Velankar, S. S. (2021). Uniaxial stretch-release of rubber-plastic bilayers: Strain-dependent transition to stable helices, rolls, saddles, and tubes. *Extreme Mechanics Letters*, 48, 101384.

<https://doi.org/10.1016/J.EML.2021.101384>

- Ramalho-Santos, M., Melton, D. A., & McMahon, A. P. (2000). Hedgehog signals regulate multiple aspects of gastrointestinal development. *Development*, *127*(12), 2763–2772.
- Rao-bhatia, A., Zhu, M., Yin, W., Mcneill, H., Hopyan, S., Kim, T., Ko, P. C. P., Rao-bhatia, A., Zhu, M., Yin, W., Coquenlorge, S., Zhang, X., Woo, J., & Sun, Y. (2020). Mediate Mesenchymal Cell Clustering and Villus Formation in Gut Development Hedgehog-Activated Fat4 and PCP Pathways Mediate Mesenchymal Cell Clustering and Villus Formation in Gut Development. *Developmental Cell*, *52*(5), 647-658.e6. <https://doi.org/10.1016/j.devcel.2020.02.003>
- Rasolonjanahary, M., & Vasiev, B. (2016). Scaling of morphogenetic patterns in reaction-diffusion systems. *Journal of Theoretical Biology*, *404*, 109. <https://doi.org/10.1016/J.JTBI.2016.05.035>
- Razavi, M. J., Pidaparti, R., & Wang, X. (2016). Surface and interfacial creases in a bilayer tubular soft tissue. *Physical Review E*, *94*(2). <https://doi.org/10.1103/PhysRevE.94.022405>
- Roberts, D. J., Johnson, R. L., Burke, A. C., Nelson, C. E., Morgan, B. A., & Tabin, C. (1995). Sonic hedgehog is an endodermal signal inducing Bmp-4 and Hox genes during induction and regionalization of the chick hindgut. *Development*, *121*(10), 3163–3174.
- Roberts, D. J., Smith, D. M., Goff, D. J., & Tabin, C. J. (1998a). Epithelial-mesenchymal signaling during the regionalization of the chick gut. *Development*, *125*(15), 2791–2801.
- Roberts, D. J., Smith, D. M., Goff, D. J., & Tabin, C. J. (1998b). *Epithelial-mesenchymal signaling during the regionalization of the chick gut. 2801*, 2791–2801.
- Rodrigues, A. R., Yakushiji-Kaminatsui, N., Atsuta, Y., Andrey, G., Schorderet, P., Duboule, D., & Tabin, C. J. (2017). Integration of Shh and Fgf signaling in controlling Hox gene expression

- in cultured limb cells. *Proceedings of the National Academy of Sciences of the United States of America*, 114(12), 3139–3144. <https://doi.org/10.1073/pnas.1620767114>
- Rodriguez, E. K., Hoger, A., & McCulloch, A. D. (1994). Stress-dependent finite growth in soft elastic tissues. *Journal of Biomechanics*, 27(4), 455–467. [https://doi.org/10.1016/0021-9290\(94\)90021-3](https://doi.org/10.1016/0021-9290(94)90021-3)
- Rodriguez, P., Da Silva, S., Oxburgh, L., Wang, F., Hogan, B. L. M., & Que, J. (2010). BMP signaling in the development of the mouse esophagus and forestomach. *Development*, 137(24), 4171–4176. <https://doi.org/10.1242/dev.056077>
- Rodriguez-Pascual, F., & Slatter, D. A. (2016). Collagen cross-linking: insights on the evolution of metazoan extracellular matrix. *Scientific Reports 2016 6:1*, 6(1), 1–7. <https://doi.org/10.1038/srep37374>
- Rosekrans, S. L., Baan, B., Muncan, V., & Van Den Brink, G. R. (2015). Esophageal development and epithelial homeostasis. *American Journal of Physiology - Gastrointestinal and Liver Physiology*, 309(4), G216–G228. <https://doi.org/10.1152/AJPGI.00088.2015/ASSET/IMAGES/LARGE/ZH30171569410004.JPG>
- EG
- Rozario, T., & DeSimone, D. W. (2010). The extracellular matrix in development and morphogenesis: A dynamic view. *Developmental Biology*, 341(1), 126–140. <https://doi.org/10.1016/j.ydbio.2009.10.026>
- Rubio, C. A. (2020). Innominate grooves of the colon: Histological reappraisal. *Anticancer Research*, 40(12), 7031–7035. <https://doi.org/10.21873/anticanres.14729>

- Sagner, A., & Briscoe, J. (2017). Morphogen interpretation: concentration, time, competence, and signaling dynamics. In *Wiley Interdisciplinary Reviews: Developmental Biology* (Vol. 6, Issue 4). John Wiley and Sons Inc. <https://doi.org/10.1002/wdev.271>
- Salsi, V., Vigano, M. A., Cocchiarella, F., Mantovani, R., & Zappavigna, V. (2008). Hoxd13 binds in vivo and regulates the expression of genes acting in key pathways for early limb and skeletal patterning. *Developmental Biology*, *317*(2), 497–507.
<https://doi.org/10.1016/j.ydbio.2008.02.048>
- Sanketi, B. D., Zuela-Sopilniak, N., Bundschuh, E., Gopal, S., Hu, S., Long, J., Lammerding, J., Hopyan, S., & Kurpios, N. A. (2022). Pitx2 patterns an accelerator-brake mechanical feedback through latent TGF β to rotate the gut. *Science*, *377*(6613).
<https://doi.org/10.1126/science.abl3921>
- Savin, T., Kurpios, N. A., Shyer, A. E., Florescu, P., Liang, H., Mahadevan, L., & Tabin, C. J. (2011). On the growth and form of the gut. *Nature*, *476*(7358), 57–62.
<https://doi.org/10.1038/nature10277>
- Sawhney, R. K., & Howard, J. (2002). Slow local movements of collagen fibers by fibroblasts drive the rapid global self-organization of collagen gels. *Journal of Cell Biology*, *157*(6), 1083–1091. <https://doi.org/10.1083/jcb.200203069>
- Scepanovic, G., & Fernandez-Gonzalez, R. (2018). Oriented Cell Division: The Pull of the Pole. In *Developmental Cell* (Vol. 47, Issue 6, pp. 686–687). Cell Press.
<https://doi.org/10.1016/j.devcel.2018.11.040>

- Schmitt, S. (2005). From eggs to fossils: Epigenesis and transformation of species in Pander's biology. *International Journal of Developmental Biology*, 49(1), 1–8.
<https://doi.org/10.1387/ijdb.041908ss>
- Semkova, M. E., & Hsuan, J. J. (2021). TGFβ-1 induced cross-linking of the extracellular matrix of primary human dermal fibroblasts. *International Journal of Molecular Sciences*, 22(3), 1–26. <https://doi.org/10.3390/ijms22030984>
- Sengle, G., & Sakai, L. Y. (2015). The fibrillin microfibril scaffold: A niche for growth factors and mechanosensation? *Matrix Biology*, 47, 3–12.
<https://doi.org/https://doi.org/10.1016/j.matbio.2015.05.002>
- Sherwood, R. I., Chen, T. Y. A., & Melton, D. A. (2009). Transcriptional dynamics of endodermal organ formation. *Developmental Dynamics*, 238(1), 29–42.
<https://doi.org/10.1002/dvdy.21810>
- Sherwood, R. I., Maehr, R., Mazzoni, E. O., & Melton, D. A. (2011). Wnt signaling specifies and patterns intestinal endoderm. *Mechanisms of Development*, 128(7–10), 387–400.
<https://doi.org/10.1016/j.mod.2011.07.005>
- Shibata, T., Takita, K., & Inomata, M. (2019). Observation of the cytoarchitecture of the human esophageal mucosa with special attention to the lamina muscularis mucosae and the distribution of lymphatic vessels. *Esophagus*, 16(1), 44–51.
<https://doi.org/10.1007/s10388-018-0632-x>
- Shi-wen, X., Liu, S., Eastwood, M., Sonnylal, S., Denton, C. P., Abraham, D. J., & Leask, A. (2009). Rac Inhibition Reverses the Phenotype of Fibrotic Fibroblasts. *PLoS ONE*, 4(10).
<https://doi.org/10.1371/JOURNAL.PONE.0007438>

- Shyer, A. E., Huycke, T. R., Lee, C., Mahadevan, L., & Tabin, C. J. (2015). Bending Gradients: How the intestinal stem cell gets its home. *Cell*, *161*(3), 569–580.
<https://doi.org/10.1016/j.cell.2015.03.041>
- Shyer, A. E., Rodrigues, A. R., Schroeder, G. G., Kassianidou, E., Kumar, S., & Harland, R. M. (2017). Emergent cellular self-organization and mechanosensation initiate follicle pattern in the avian skin. *Science*, *357*(6353), 811–815. <https://doi.org/10.1126/science.aai7868>
- Shyer, A. E., Tallinen, T., Nerurkar, N. L., Wei, Z., Gil, E. S., Kaplan, D. L., Tabin, C. J., & Mahadevan, L. (2013). Villification: How the gut gets its villi. *Science*, *342*(6155), 212–218.
<https://doi.org/10.1126/science.1238842>
- Silberg, D. G., Sullivan, J., Kang, E., Swain, G. P., Moffett, J., Sund, N. J., Sackett, S. D., & Kaestner, K. H. (2002). Cdx2 ectopic expression induces gastric intestinal metaplasia in transgenic mice. *Gastroenterology*, *122*(3), 689–696.
<https://doi.org/10.1053/gast.2002.31902>
- Sivakumar, A., Mahadevan, A., Lauer, M. E., Narvaez, R. J., Ramesh, S., Demler, C. M., Souchet, N. R., Hascall, V. C., Midura, R. J., Garantziotis, S., Frank, D. B., Kimata, K., & Kurpios, N. A. (2018). Midgut Laterality Is Driven by Hyaluronan on the Right. *Developmental Cell*, *46*(5), 533–551.e5. <https://doi.org/10.1016/j.devcel.2018.08.002>
- Smith, C. L., & Mayorova, T. D. (2019). Insights into the evolution of digestive systems from studies of *Trichoplax adhaerens*. *Cell and Tissue Research* *2019 377:3*, *377*(3), 353–367.
<https://doi.org/10.1007/S00441-019-03057-Z>

- Smith, C. L., Pivovarova, N., & Reese, T. S. (2015). Coordinated Feeding Behavior in Trichoplax, an Animal without Synapses. *PLOS ONE*, *10*(9), e0136098.
<https://doi.org/10.1371/JOURNAL.PONE.0136098>
- Smith, D. M., Nielsen, C., Tabin, C. J., & Roberts, D. J. (2000). Roles of BMP signaling and Nkx2.5 in patterning at the chick midgut-foregut boundary. *Development*, *127*(17), 3671–3681.
- Soliman, S. A., & Madkour, F. A. (2021a). Developmental events and cellular changes occurred during esophageal development of quail embryos. *Scientific Reports 2021 11:1*, *11*(1), 1–21. <https://doi.org/10.1038/s41598-021-86503-9>
- Soliman, S. A., & Madkour, F. A. (2021b). Developmental events and cellular changes occurred during esophageal development of quail embryos. *Scientific Reports 2021 11:1*, *11*(1), 1–21. <https://doi.org/10.1038/s41598-021-86503-9>
- Southwell, B. R. (2006). Staging of intestinal development in the chick embryo. *Anatomical Record - Part A Discoveries in Molecular, Cellular, and Evolutionary Biology*, *288*(8), 909–920. <https://doi.org/10.1002/ar.a.20349>
- Spence, J. R., Lauf, R., & Shroyer, N. F. (2011). Vertebrate intestinal endoderm development. *Developmental Dynamics*, *240*(3), 501–520. <https://doi.org/10.1002/dvdy.22540>
- Sprangers, J., Zaalberg, I. C., & Maurice, M. M. (2020). Organoid-based modeling of intestinal development, regeneration, and repair. *Cell Death & Differentiation 2020 28:1*, *28*(1), 95–107. <https://doi.org/10.1038/s41418-020-00665-z>
- Steinmetz, P. R. H. (2019). A non-bilaterian perspective on the development and evolution of animal digestive systems. *Cell and Tissue Research*, *377*(3), 321.
<https://doi.org/10.1007/S00441-019-03075-X>

- Steinmetz, P. R. H., Aman, A., Kraus, J. E. M., & Technau, U. (2017). Gut-like ectodermal tissue in a sea anemone challenges germ layer homology. *Nature Ecology & Evolution* 2017 1:10, 1(10), 1535–1542. <https://doi.org/10.1038/s41559-017-0285-5>
- Stokkermans, A., Chakrabarti, A., Subramanian, K., Wang, L., Yin, S., Moghe, P., Steenbergen, P., Mönke, G., Hiiragi, T., Prevedel, R., Mahadevan, L., & Ikmi, A. (2022). Muscular hydraulics drive larva-polyp morphogenesis. *Current Biology*, 32(21), 4707-4718.e8. <https://doi.org/10.1016/j.cub.2022.08.065>
- Stolfi, C., Troncone, E., Marafini, I., & Monteleone, G. (2021). Role of tgf-beta and smad7 in gut inflammation, fibrosis and cancer. *Biomolecules*, 11(1), 1–15. <https://doi.org/10.3390/biom11010017>
- Stooke-Vaughan, G. A., & Campàs, O. (2018). Physical control of tissue morphogenesis across scales. *Current Opinion in Genetics and Development*, 51, 111–119. <https://doi.org/10.1016/j.gde.2018.09.002>
- Sugimoto, S., Kobayashi, E., Fujii, M., Ohta, Y., Arai, K., Matano, M., Ishikawa, K., Miyamoto, K., Toshimitsu, K., Takahashi, S., Nanki, K., Hakamata, Y., Kanai, T., & Sato, T. (2021). An organoid-based organ-repurposing approach to treat short bowel syndrome. *Nature*. <https://doi.org/10.1038/s41586-021-03247-2>
- Sukegawa, A., Narita, T., Kameda, T., Saitoh, K., Nohno, T., Hideo, I., Yasugi, S., & Fukuda, K. (2000). The concentric structure of the developing gut is regulated by Sonic hedgehog derived from endodermal epithelium. *Development*, 127(9), 1971–1980.
- Taber, L. A. (2006). Biophysical mechanisms of cardiac looping. *International Journal of Developmental Biology*, 50(2–3), 323–332. <https://doi.org/10.1387/ijdb.052045lt>

- Taber, L. A. (2014). Morphomechanics: Transforming tubes into organs. *Current Opinion in Genetics and Development*, 27(1c), 7–13. <https://doi.org/10.1016/j.gde.2014.03.004>
- Takigawa-Imamura, H., Morita, R., Iwaki, T., Tsuji, T., & Yoshikawa, K. (2015). Tooth germ invagination from cell-cell interaction: Working hypothesis on mechanical instability. *Journal of Theoretical Biology*, 382, 284–291. <https://doi.org/10.1016/j.jtbi.2015.07.006>
- Tallapragada, N. P., Cambra, H. M., Wald, T., Keough Jalbert, S., Abraham, D. M., Klein, O. D., & Klein, A. M. (2021). Inflation-collapse dynamics drive patterning and morphogenesis in intestinal organoids. *Cell Stem Cell*, 28(9), 1516-1532.e14. <https://doi.org/10.1016/j.stem.2021.04.002>
- Tallinen, T., & Biggins, J. S. (2015). Mechanics of invagination and folding: Hybridized instabilities when one soft tissue grows on another. *Physical Review E - Statistical, Nonlinear, and Soft Matter Physics*, 92(2), 1–8. <https://doi.org/10.1103/PhysRevE.92.022720>
- Tallinen, T., Biggins, J. S., & Mahadevan, L. (2013). Surface sulci in squeezed soft solids. *Physical Review Letters*, 110(2). <https://doi.org/10.1103/PhysRevLett.110.024302>
- Tallinen, T., Chung, J. Y., Biggins, J. S., & Mahadevan, L. (2014). Gyrification from constrained cortical expansion. *Proceedings of the National Academy of Sciences of the United States of America*, 111(35), 12667–12672. <https://doi.org/10.1073/pnas.1406015111>
- Tallinen, T., Chung, J. Y., Rousseau, F., Girard, N., Lefèvre, J., & Mahadevan, L. (2016). On the growth and form of cortical convolutions. *Nature Physics* 2016 12:6, 12(6), 588–593. <https://doi.org/10.1038/nphys3632>

- Thompson, C. A., DeLaForest, A., & Battle, M. A. (2018). Patterning the gastrointestinal epithelium to confer regional-specific functions. *Developmental Biology*, *435*(2), 97–108. <https://doi.org/10.1016/J.YDBIO.2018.01.006>
- Tondon, A., & Kaunas, R. (2014). The direction of stretch-induced cell and stress fiber orientation depends on collagen matrix stress. *PLoS ONE*, *9*(2). <https://doi.org/10.1371/journal.pone.0089592>
- Tozluoğlu, M., Duda, M., Kirkland, N. J., Barrientos, R., Burden, J. J., Muñoz, J. J., & Mao, Y. (2019). Planar Differential Growth Rates Initiate Precise Fold Positions in Complex Epithelia. *Developmental Cell*, *51*(3), 299–312.e4. <https://doi.org/10.1016/j.devcel.2019.09.009>
- Trejo, M., Douarache, C., Bailleux, V., Poulard, C., Mariot, S., Regeard, C., & Raspaud, E. (2013). Elasticity and wrinkled morphology of *Bacillus subtilis* pellicles. *Proc. Natl Acad. Sci. USA*, *110*(6), 2011–2016. <https://doi.org/10.1073/pnas.1217178110>
- Tzavlaki, K., & Moustakas, A. (2020). TGF- β Signaling. *Biomolecules*, *10*(3), 487. <https://doi.org/10.3390/biom10030487>
- Uygur, A., Young, J., Huycke, T. R., Koska, M., Briscoe, J., & Tabin, C. J. (2016). Scaling Pattern to Variations in Size during Development of the Vertebrate Neural Tube. *Developmental Cell*, *37*(2), 127–135. <https://doi.org/10.1016/J.DEVCEL.2016.03.024>
- Vader, D., Kabla, A., Weitz, D., & Mahadevan, L. (2009). Strain-induced alignment in collagen gels. *PLoS ONE*, *4*(6). <https://doi.org/10.1371/journal.pone.0005902>

- Vallée, A., & Lecarpentier, Y. (2019). TGF- β in fibrosis by acting as a conductor for contractile properties of myofibroblasts. *Cell and Bioscience*, 9(1), 1–15.
<https://doi.org/10.1186/s13578-019-0362-3>
- Varner, V. D., Gleghorn, J. P., Miller, E., Radisky, D. C., & Nelson, C. M. (2015). Mechanically patterning the embryonic airway epithelium. *Proceedings of the National Academy of Sciences of the United States of America*, 112(30), 9230–9235.
<https://doi.org/10.1073/pnas.1504102112>
- Varner, V. D., & Nelson, C. M. (2014). Cellular and physical mechanisms of branching morphogenesis. *Development (Cambridge)*, 141(14), 2750–2759.
<https://doi.org/10.1242/dev.104794>
- Verrecchia, F., & Mauviel, A. (2002). Transforming growth factor- β signaling through the Smad pathway: Role in extracellular matrix gene expression and regulation. *Journal of Investigative Dermatology*, 118(2), 211–215. <https://doi.org/10.1046/j.1523-1747.2002.01641.x>
- Villedieu, A., Alpar, L., Gaugué, I., Joudat, A., Graner, F., Bosveld, F., & Bellaïche, Y. (2023). Homeotic compartment curvature and tension control spatiotemporal folding dynamics. *Nature Communications*, 14(1). <https://doi.org/10.1038/s41467-023-36305-6>
- Viotti, M., Nowotschin, S., & Hadjantonakis, A. K. (2014). SOX17 links gut endoderm morphogenesis and germ layer segregation. *Nature Cell Biology*, 16(12), 1146–1156.
<https://doi.org/10.1038/ncb3070>
- Wake, D. B. (1978). Biology of the Reptilia. Volume 6: Morphology E. Carl Gans. *The Quarterly Review of Biology*, 53(4), 470. <https://doi.org/10.1086/410893>

- Walton, K. D., Kolterud, Å., Czerwinski, M. J., Bell, M. J., Prakash, A., Kushwaha, J., Grosse, A. S., Schnell, S., & Gumucio, D. L. (2012). Hedgehog-responsive mesenchymal clusters direct patterning and emergence of intestinal villi. *Proceedings of the National Academy of Sciences of the United States of America*, *109*(39), 15817–15822.
<https://doi.org/10.1073/pnas.1205669109>
- Walton, K. D., Whidden, M., Kolterud, Å., Shoffner, S. K., Czerwinski, M. J., Kushwaha, J., Parmar, N., Chandrasekhar, D., Freddo, A. M., Schnell, S., & Gumucio, D. L. (2016). Villification in the mouse: Bmp signals control intestinal villus patterning. *Development (Cambridge)*, *143*(3), 427–436. <https://doi.org/10.1242/dev.130112>
- Wang, L., Castro, C. E., & Boyce, M. C. (2011). Growth strain-induced wrinkled membrane morphology of white blood cells. *Soft Matter*, *7*(24), 11319–11324.
<https://doi.org/10.1039/c1sm06637d>
- Wang, Q., & Zhao, X. (2015). A three-dimensional phase diagram of growth-induced surface instabilities. *Scientific Reports*, *5*. <https://doi.org/10.1038/srep08887>
- Wang, S., Cebrian, C., Schnell, S., & Gumucio, D. L. (2018). Radial WNT5A-Guided Post-mitotic Filopodial Pathfinding Is Critical for Midgut Tube Elongation. *Developmental Cell*, *46*(2), 173-188.e3. <https://doi.org/10.1016/j.devcel.2018.06.011>
- Wang, X., Merkel, M., Sutter, L. B., Erdemci-Tandogan, G., Manning, M. L., & Kasza, K. E. (2020). Anisotropy links cell shapes to tissue flow during convergent extension. *Proceedings of the National Academy of Sciences of the United States of America*, *117*(24), 13541–13551.
<https://doi.org/10.1073/pnas.1916418117>

- Wang, X., Zhang, L., Li, H., Sun, W., Zhang, H., & Lai, M. (2016). THBS2 is a Potential Prognostic Biomarker in Colorectal Cancer. *Scientific Reports*, 6. <https://doi.org/10.1038/srep33366>
- Warot, X., Fromental-Ramain, C., Fraulob, V., Chambon, P., & Dollé, P. (1997). Gene dosage-dependent effects of the Hoxa-13 and Hoxd-13 mutations on morphogenesis of the terminal parts of the digestive and urogenital tracts. *Development*, 124(23), 4781–4791.
- Weinstein, W. M., Bogoch, E. R., & Bowes, K. L. (1975). The Normal Human Esophageal Mucosa: A Histological Reappraisal. *Gastroenterology*, 68(1), 40–44. [https://doi.org/10.1016/S0016-5085\(75\)80046-1](https://doi.org/10.1016/S0016-5085(75)80046-1)
- Wellik, D. M. (2007). Hox patterning of the vertebrate axial skeleton. In *Developmental Dynamics* (Vol. 236, Issue 9, pp. 2454–2463). <https://doi.org/10.1002/dvdy.21286>
- Wells, J. M., & Melton, D. A. (2000). Early mouse endoderm is patterned by soluble factors from adjacent germ layers. *Development*, 127(8), 1563–1572.
<https://doi.org/10.1242/DEV.127.8.1563>
- Wolff, Caspar Friedrich, Jean-Claude Dupont, and M. P. (1769). *De Formatione Intestinorum/La Formation des Intestins (1768–1769)*. Translated by Michel Jean Louis Perrin. Introduction and Notes by Jean-Claude Dupont. Vol. 68(Brepols).
- Wolpert, L. (2004). Much more from the chicken's egg than breakfast - A wonderful model system. *Mechanisms of Development*, 121(9), 1015–1017.
<https://doi.org/10.1016/j.mod.2004.04.021>
- Wu, R.-L., Sedlmeier, G., Kyjacova, L., Schmaus, A., Philipp, J., Thiele, W., Garvalov, B. K., & Sleeman, J. P. (2018). Hyaluronic acid-CD44 interactions promote BMP4/7-dependent

Id1/3 expression in melanoma cells. *Scientific Reports*, 8(1).

<https://doi.org/10.1038/s41598-018-33337-7>

Wu, S., Liang, C., Xie, X., Huang, H., Fu, J., Wang, C., Su, Z., Wang, Y., Qu, X., Li, J., & Liu, J.

(2022). Hsp47 Inhibitor Col003 Attenuates Collagen-Induced Platelet Activation and Cerebral Ischemic–Reperfusion Injury in Rats. *Frontiers in Pharmacology*, 12(January), 1–12. <https://doi.org/10.3389/fphar.2021.792263>

Xie, Z., Bailey, A., Kuleshov, M. V., Clarke, D. J. B., Evangelista, J. E., Jenkins, S. L., Lachmann, A.,

Wojciechowicz, M. L., Kropiwnicki, E., Jagodnik, K. M., Jeon, M., & Ma'ayan, A. (2021).

Gene Set Knowledge Discovery with Enrichr. *Current Protocols*, 1(3), 1–51.

<https://doi.org/10.1002/cpz1.90>

Yamada, M., Udagawa, J., Matsumoto, A., Hashimoto, R., Hatta, T., Nishita, M., Minami, Y., &

Otani, H. (2010). Ror2 is required for midgut elongation during mouse development.

Developmental Dynamics, 239(3), 941–953. <https://doi.org/10.1002/dvdy.22212>

Yamamoto-Shiraishi, Y. I., & Kuroiwa, A. (2013). Wnt and BMP signaling cooperate with Hox in

the control of Six2 expression in limb tendon precursor. *Developmental Biology*, 377(2),

363–374. <https://doi.org/10.1016/j.ydbio.2013.02.023>

Yang, Q., Xue, S.-L., Chan, C. J., Rempfler, M., Vischi, D., Maurer-Gutierrez, F., Hiiragi, T.,

Hannezo, E., & Liberali, P. (2021). Cell fate coordinates mechano-osmotic forces in

intestinal crypt formation. *Nature Cell Biology*, 23(7), 733–744.

<https://doi.org/10.1038/s41556-021-00700-2>

Yang, Y., Paivinen, P., Xie, C., Krup, A. L., Makela, T. P., Mostov, K. E., & Reiter, J. F. (2021).

Ciliary Hedgehog signaling patterns the digestive system to generate mechanical forces

driving elongation. *Nature Communications* 2021 12:1, 12(1), 1–14.

<https://doi.org/10.1038/s41467-021-27319-z>

Yin, W., Kim, H.-T., Wang, S., Gunawan, F., Li, R., Buettner, C., Grohmann, B., Sengle, G., Sinner, D., Offermanns, S., & Stainier, D. Y. R. (2019). Fibrillin-2 is a key mediator of smooth muscle extracellular matrix homeostasis during mouse tracheal tubulogenesis. *European Respiratory Journal*, 53(3), 1800840. <https://doi.org/10.1183/13993003.00840-2018>

Respiratory Journal, 53(3), 1800840. <https://doi.org/10.1183/13993003.00840-2018>

Yu, J., Carroll, T. J., & McMahon, A. P. (2002). Sonic hedgehog regulates proliferation and differentiation of mesenchymal cells in the mouse metanephric kidney. *Development*, 129(22), 5301–5312.

Zacchetti, G., Duboule, D., & Zakany, J. (2007). Hox gene function in vertebrate gut morphogenesis: The case of the caecum. *Development*, 134(22), 3967–3973.

<https://doi.org/10.1242/dev.010991>

Zakany, J., Darbellay, F., Mascrez, B., Necsulea, A., & Duboule, D. (2017). Control of growth and gut maturation by HoxD genes and the associated lncRNA Haglr. *Proceedings of the National Academy of Sciences of the United States of America*, 114(44), E9290–E9299.

<https://doi.org/10.1073/pnas.1712511114>

Zákány, J., & Duboule, D. (1999). Development: Hox genes and the making of sphincters. *Nature*, 401(6755), 761–762. <https://doi.org/10.1038/44511>

Zhang, W., Herrera, C., Atluri, S. N., & Kassab, G. S. (2005). The Effect of Longitudinal Pre-Stretch and Radial Constraint on the Stress Distribution in the Vessel Wall: A New Hypothesis. In *MCB* (Vol. 2, Issue 1).

Zhang, Y., Bailey, D., Yang, P., Kim, E., & Que, J. (2021). The development and stem cells of the esophagus. *Development (Cambridge)*, 148(6).

<https://doi.org/10.1242/DEV.193839/237849>

Zhao, J., Chen, X., Yang, J., Liao, D., & Gregersen, H. (2007). Opening angle and residual strain in a three-layered model of pig oesophagus. *Journal of Biomechanics*, 40(14), 3187–3192.

<https://doi.org/10.1016/j.jbiomech.2007.04.002>

Zorn, A. M., & Wells, J. M. (2009). Vertebrate endoderm development. *Annu Rev Cell Biol*, 25, 221–251. <https://doi.org/10.1146/annurev.cellbio.042308.113344.Vertebrate>